Dynamics and Shapes of Galaxies: Orbit Modeling of Triaxial Galaxies Hosting Supermassive Black Holes

by

Matthew E. Quenneville

A dissertation submitted in partial satisfaction of the

requirements for the degree of

Doctor of Philosophy

in

Physics

in the

Graduate Division

of the

University of California, Berkeley

Committee in charge:

Professor Chung-Pei Ma, Chair
Associate Professor Jessica Lu
Associate Professor Daniel Kasen

Summer 2022

Dynamics and Shapes of Galaxies: Orbit Modeling of Triaxial Galaxies Hosting Supermassive Black Holes

Abstract

Dynamics and Shapes of Galaxies: Orbit Modeling of Triaxial Galaxies Hosting Supermassive Black Holes

by

Matthew E. Quenneville

Doctor of Philosophy in Physics

University of California, Berkeley

Professor Chung-Pei Ma, Chair

Elliptical galaxies display a wide variety of photometric and kinematic features. Supermassive black holes are thought to lie in the centers of all elliptical galaxies, with masses that exhibit tight correlations with the masses and velocity dispersions of their hosts. Measurement of these correlations in the local universe underpin our understanding of the growth of supermassive black holes throughout cosmic time. These measurements can only be as precise as our measurements of the underlying supermassive black hole masses and host galaxy properties.

The most massive ellipticals exhibit photometric and kinematic signatures of triaxiality. While axisymmetric dynamical modeling has been most prevalent over the past decades, triaxial orbit modeling allows models to capture the orbital complexity that the more general geometry allows. The limited number of direct tests of triaxial models have revealed biased shape recoveries and inconsistencies with axisymmetric models.

This dissertation begins by addressing the inconsistency between axisymmetric and triaxial models. Starting from the most commonly used existing triaxial orbit code, the axisymmetric limit is approached in a careful manner in order to acheive consistent and stable results. An updated version of this code is introduced which is about twice as fast and does not suffer from the same spurious minima that have been observed in the literature. This version is applied to fast-rotating massive elliptical galaxy NGC 1453.

I then proceed to the triaxial case. I demonstrate that the existing code uses kinematics that are incorrect, and describe several other improvements to the code and the way it is typically applied. A novel search strategy is used to explore the six dimensional parameter space more accurately and with far fewer expensive model evaluations than previously used grid based searches. This methodology is applied to obtain a simultaneous measurement of the triaxial shape, dark matter halo, stellar mass-to-light ratio, and central black hole mass

of NGC 1453.

Next, the updated code is validated against mock galaxy data. The code updates have dramatically improved the precision of the code. When used to measure the triaxial shape of a mock galaxy, the axis ratios p and q are recovered with far more accuracy and precision than would be suggested by any previously reported triaxial recovery tests.

Finally, I turn from dynamical modeling to examining photometry of massive elliptical galaxies. I present new measurements of K-band total magnitudes and half-light radii for a volume limited sample of ~ 100 galaxies. These new, more accurate values are used to study the scaling relations among massive ellipticals. The resulting relations are consistent with a picture in which massive ellipticals form through dissipationless mergers. As the relationship between total luminosity and velocity dispersion are found to be poorly fit by a single power law, this suggests that the $M_{\rm BH} - L$ relation is likely to be a better predictor of central black hole mass than the $M_{\rm BH} - \sigma$ relation for high mass ellipticals.

To my parents

Contents

List of Figures

List of Tables

Acknowledgments

First of all, I would like to thank my advisor, Professor Chung-Pei Ma. Thank you for all of your guidance and encouragement. I am extremely grateful for the direction and knowledge that you have provided for the past six years. Thank you as well to Professors Jessica Lu, Daniel Kasen, and Eliot Quataert for serving on my qualifying exam and dissertation committees. Throughout my degree, I have been fortunate to work with many talented and brilliant collaborators. I have had the pleasure of learning from collaborations with Professors John Blakeslee, Jonelle Walsh, and Jenny Greene among others. I am also particularly thankful to Emily Liepold, Jacob Pilawa, and Irina Ene for discussions and ideas that have greatly shaped the research that I have done. I am also grateful to have had the opportunity to collaborate with Melanie Veale, Shaunak Modak, and Philipp Kempski. I acknowledge the support of the Natural Sciences and Engineering Research Council of Canada (NSERC).

I would not be where I am today without the many teachers and mentors who inspired and nurtured my love of physics. I particularly thank Mr. Johnson, Professor Dugan O'Neil, and Professor David Sivak. Thank you Micah, Sam, and Jon helping me make it through the ups and downs of the past six years. Finally, thank you Mom, Dad, and Vince for all of your love and support throughout the years.

Chapter 1

Introduction

1.1 Galaxies

Our understanding of the universe has advanced in tandem with technological advancements that have allowed astronomers to map the night sky more precisely. Telescopes have revealed an enormous variety of objects in exquisite detail that are entirely invisible with the naked eye. The recognition that many of these objects are galaxies beyond our own Milky Way galaxy has revolutionized our understanding of the true scale of the universe.

Galaxy Morphologies

Galaxies have been observed with a wide variety of characteristics. In order to begin to understand these characteristics, it is natural to classify galaxies according to their shapes, or morphologies. The Hubble sequence classifies galaxies into three broad categories: spirals, ellipticals, and lenticulars.

Spirals are characterized by a flattened disk-like shape, often with a central bulge-like structure. Within the plane of the disk, stars are arranged to form the spiral arms that give these galaxies their name. Elliptical galaxies, on the other hand, are largely featureless in comparison. These galaxies appear smooth and have observed surface brightness distributions that have roughly elliptical level surfaces (isophotes). Lenticular galaxies are intermediate between these two classifications, consisting of both a central elliptical-like bulge as well as an extended flattened disk. Galaxies that do not fall into any of these classifications are broadly classified as irregular. The term early-type galaxy (ETG) is used to refer collectively to elliptical and lenticular galaxies, while the term late-type galaxy refers to spirals and irregulars [1].

While elliptical galaxies do not exhibit the elaborate structures observed in late-type galaxies, they are nevertheless fascinating systems with diverse structure and dynamics. These galaxies span many orders of magnitude in total mass, and many of the most massive galaxies in the universe fall under this classification. These elliptical galaxies are the focus of this dissertation.

Photometric Observations

Photometric observations can reveal a wealth of information about ellipitical galaxies. Most such information is based on measuring the surface brightness (SB) or flux density per unit area of the galaxy in a given passband. This surface brightness is largest near the center of the galaxy and decreases away from the center with roughly elliptical isophotes.

From this SB profile, many other properties can be determined. For example, if the distance to the galaxy is known, a total luminosity can be derived. Elliptical galaxies span an enormous range in total luminosity, and many of the most luminous observed galaxies are ellipticals. Many other photometric properties are found to correlate with this total luminosity.

A characteristic length scale can be inferred for the galaxy from the size of the isophote containing half of the galaxy's total light. This is referred to as the half-light radius. On average, galaxies with larger luminosities tend to have larger half-light radii. This can be quantified either through the luminosity-size relation or the closely related Kormendy relation [2].

In addition to global photometric properties like the total luminosity and half-light radius, the SB profile itself is rich with information. For many ellipticals, the SB profile as a function of isophotal semi-major axis, R, is well described by a Sérsic profile:

$$I(r) = I_e \exp\left(-b_n\left[(R/R_e)^{1/n} - 1\right]\right), \tag{1.1}$$

where R_e is the profile half-light radius, I_e is the surface brightness at $R = R_e$, n is a parameter known as the Sérsic index that describes the degree of central concentration of the profile [3]. b_n is a numerical factor that depends on n and can be calculated by numerically inverting:

$$\gamma(2n; b_n) = \frac{1}{2}\Gamma(2n), \tag{1.2}$$

where Γ represents the Gamma function and γ represents the lower incomplete Gamma function. The best-fit Sérsic index, n, is observationally found to increase with total luminosity [4]. In many of the most luminous ellipticals, the true SB profile is overestimated by a Sérsic profile [5]. In these galaxies the central SB profile flattens, exhibiting a central core. These central cores stand in contrast to less luminous ellipticals which tend to have steep central SB cusps [6].

Beyond the SB profile, the shapes of the isophotes themselves can be examined. Isophotes tend to be more round for highly luminous ellipticals, and more flattened for less luminous ellipticals [7, 8]. As well, the isophotal position angle (PA) on the sky tends to be constant with R for less luminous ellipticals, while many of the most massive ellipticals exhibit twists in PA with R [9]. Despite their name, the isophotes of many ellipticals are observed to deviate from perfectly elliptical shapes. These deviations can be quantified through the lowest order fourier component a_4, with $a_4 < 0$ giving "boxy" isophotes and $a_4 > 0$ giving "disky" isophotes [10]. This deviation also correlates with total luminosity with isophotes in more luminous ellipticals appearing more boxy and isophotes in less luminous ellipticals appearing more disky [11, 12].

Spectroscopic Observations

Spectroscopic data can be used to gain information about the internal motions of distant galaxies. When light emitted from a star is plotted against wavelength, clear absorption lines appear in the spectrum. These lines are due to gas in the stellar atmosphere absorbing light at specific wavelengths governed by atomic or molecular transition energies. When the star is moving towards or away from the observer, these absorption lines will be shifted due to the Doppler effect. By comparing absorption line positions to their known wavelengths at rest, the component of the stars velocity along the line-of-sight can be inferred.

In the Milky Way and some other very nearby galaxies, individual stars can be resolved and individual stellar velocities (along the line-of-sight) can be inferred. In most galaxies, however, individual stars cannot be resolved. In this case, the combined spectrum of a group of stars within an area on the sky can be measured. This spectrum can be regarded as a convolution of an average rest-frame stellar spectrum with the line-of-sight velocity distribution (LOSVD) of the stars.

Spectroscopic measurements are essential for studying galaxies as they allow us to measure internal motions of galaxies. In turn, this allows us to learn about the gravitational forces acting within these galaxies giving us direct insight into the mass distributions within these galaxies.

Much like with photometric observations, data from spectroscopic observations can be used to produce many different kinematic measurements. One common global kinematic measurement is the width of the LOSVD, referred to as velocity dispersion, as measured within a single aperture. In some cases, this aperture size is set by the instrument used for measurement. It is also common to use an aperture that covers the half-light isophote of the galaxy [13].

The velocity dispersion along the line-of-sight, σ correlates closely with total luminosity. This correlation is known as the Faber-Jackson relation [14]. In fact, ellipticals are found to lie on a thin plane in the three dimensional (L, R_e, σ) space. This relationship is known as the Fundamental Plane [15].

Many modern telescopes are equipped with an integral field spectrograph (IFS) [16, 17]. An IFS allows for measurement of spectra within small bins at numerous positions within the field of view. When used for spectroscopic galaxy observations, this allows astronomers to measure the LOSVD as a function of position on the sky plane. This allows for much more detailed measurements of internal stellar motions than a single aperture.

Galactic rotation appears as a differential average velocity between the two sides of a galaxy. The amount of rotation is often quantified as the ratio between rotation speed V and velocity dispersion σ. This ratio strongly correlates with galaxy luminosity: typically $V/\sigma \lesssim 0.1$ for the most luminous ellipticals, while V/σ can be up to ~ 0.8 for lower luminosity ellipticals [7].

In practice, LOSVDs are not perfectly gaussian. Deviations from gaussianity are typically quantified through Gauss-Hermite (GH) moments $h_1, h_2, h_3, ...$ V and σ can be chosen such that $h_1 = h_2 = 0$, meaning $h_3, h_4, ...$ are typically used to quantify deviation from a gaussian

distribution [18].

Triaxiality

Information about 3-dimensional galaxy shapes can be inferred from both photometric and spectroscopic data. However, since we can only observe the galaxy's light as projected along the line-of-sight, complete knowledge of the galaxy's shape is not possible from photometry alone.

Perhaps the most obvious indication of the galaxy's intrinsic shape are the shapes of its projected isophotes. Almost all elliptical galaxies appear at least somewhat flattened in projection. The lack of galaxies that appear perfectly round suggests that real galaxies tend not to be perfectly spherical.

A less obvious photometric indication of intrinsic galaxy shape arises from the relative alignment of a galaxies isophotes. For a perfectly axisymmetric intrinsic shape, all isophotes will appear perfectly aligned in position angle when viewed along any line-of-sight. If a galaxy has a triaxial intrinsic shape, however, this need not be the case. Even if a galaxy's 3-dimensional luminosity distribution is stratified on ellipsoidal surfaces that all have the same principal axes, the isophotes can appear to twist in projection. These twists arise if the axis ratios vary with radius (or more precisely, if the triaxiality varies) [19]. Isophotal twists have been observed in many galaxies [9]. The presence of isophotal twists, however, appears to be highly correlated with galaxy luminosity. Lower luminosity galaxies tend to have regular, aligned isophotes, while isophotal twists are much more common among more massive galaxies [8].

While twisting isophotes suggest that the galaxy is intrinsically triaxial, triaxial galaxies do not necessarily have isophotes that twist. The degree of isophotal twisting will depend strongly on the line-of-sight that the galaxy is observed along. As well, galaxies that have a fixed triaxiality with radius will not have twisting isophotes [20].

By combining kinematic and photometric data, far more can be inferred about galaxy intrinsic shapes [21]. For a perfectly oblate axisymmetric galactic potential and distribution function, the projected velocity field will be perfectly aligned with the projected major axis. Further, the resulting kinematics will be symmetric across the major axis and anti-symmetric across the minor axis. This is due to the azimuthal symmetry of orbits within an axisymmetric potential. Any deviation from this symmetry suggests an intrinsic galaxy shape that deviates from oblate axisymmetry.

In triaxial galaxies, multiple orbit families are allowed[22, 23, 24, 25]. In addition to the short-axis tubes that are present in oblate axisymmetric galaxies, long-axis tube are also present, which rotate about the galaxy's major axis. This allows for the angular momentum vector to be misaligned with respect to the galaxy's minor axis, and projected velocity fields that need not be aligned with the principal axes of the projected SB distribution. As well, orbital populations that vary with distance from the galaxy center can result in projected velocity maps with rotation directions that vary with radius. Kinematically decoupled cores (KDCs) are extreme examples of this phenomenon where there is a central cluster of stars

with an entirely different rotation direction than the rest of the galaxy [11, 26]. Such kinematic misalignments and twists have been observed in real galaxies. Much like photometric twists however, they are far more prevalent in more luminous galaxies [27].

While these features are relatively intuitive and visible in the kinematic and photometric data, the combination of photometric and kinematic IFS data are likely to contain far more information than this about galaxy shape and alignment. More detailed dynamical modeling is needed to take advantage of this information.

Supermassive Black Holes

Supermassive black holes are ubiquitously found in the centers of elliptical galaxies [28]. Initial evidence for these enormous objects arose from the observation of extremely luminous emission from the centers of many distant galaxies, known as active galactic nuclei (AGN) [29, 30]. This emission can be so bright as to outshine entire galaxies. The source of this emission is now recognized as radiation resulting from matter accreting onto central SMBHs.

Along with a growing sample of observed AGN, there is a plethora of more direct evidence for SMBHs in the local universe as well. The strongest evidence for the existence of an SMBH comes from the center of our own Milky Way galaxy. By following the trajectories of individual stars near the galactic center over years, the influence of a central dark object with a mass of about $4 \times 10^6\ M_\odot$ can be measured [31]. This central dark object's size must be comparable to its Schwarzschild radius - much denser than any known astrophysical object other than a black hole. Black holes have been detected in other galaxies through their gravitational influence on nearby luminous matter - typically stars, gas, or astrophysical masers [32].

In recent years, the Event Horizon Telescope (EHT) collaboration has used very-long-baseline interferometry together with an array of ground-based telescopes from around the world to directly image the centers of both M87 (a nearby massive elliptical galaxy) and our own Milky Way galaxy with resolutions comparable to the SMBH event horizons [33, 34]. In both cases, the resulting images were entirely consistent with previously dynamically determined SMBH masses [35, 36]. This provides an important independent verification of the dynamical measurements of these SMBHs.

More massive SMBHs tend to lie at the centers of more massive galaxies. Among the sample of dynamically determined SMBH masses, there are tight correlations between SMBH mass, $M_{\rm BH}$, and both total lumionsity and velocity dispersion. Decades of studies have shown these scaling relations to hold over several orders of magnitude in $M_{\rm BH}$ (eg. [37, 28, 38, 32]). Typically, central SMBHs account for $\sim 0.2\%$ of the total mass of the galaxy. As such the SMBH has a significant dynamical effect on stars within a small volume at the galaxy's center, referred to as the SMBH's sphere of influence. The tight correlation between $M_{\rm BH}$ and global galactic properties such as σ and L is therefore surprising. This has led to suggestions that central SMBHs may play a key role in galaxy evolution, affecting their growth and star formation through feedback processes [39].

The local population of SMBHs where dynamical $M_{\rm BH}$ measurements can be performed presents key insights into the population of SMBHs elsewhere in the universe. These local SMBH measurements are used to calibrate $M_{\rm BH}$ estimations in AGNs where measurements have much larger intrinsic uncertainties [40]. Therefore, a complete understanding of the local SMBH population is vital to our understanding of SMBH growth throughout cosmic time. The most massive SMBHs are particularly important as these are thought to be relics of the most luminous AGNs in the early universe.

1.2 Dynamical Modeling

Distribution Functions

The stellar distribution function (DF) $f(\vec{x}, \vec{v})$ describes the mass distribution of stars within the phase space $(\vec{x}, \vec{v})$. The stellar density is therefore related to f by:

$$\rho_*(\vec{x}) = \int f(\vec{x}, \vec{v}) \mathrm{d}\vec{v}. \tag{1.3}$$

Assuming the stars do not collide and that they interact solely via gravitational forces, the system has no dissipation and must therefore obey the Liouville equation:

$$\frac{\partial f}{\partial t} + \frac{\partial f}{\partial \vec{x}} \cdot \dot{\vec{x}} + \frac{\partial f}{\partial \vec{v}} \cdot \dot{\vec{v}} = 0. \tag{1.4}$$

Assuming that the distribution function is stationary, and assuming the stars are subject to a total potential $\Phi(\vec{x})$ gives the stationary Collisionless Boltzmann Equation (CBE) [41]:

$$\vec{v} \cdot \frac{\partial f}{\partial \vec{x}} - \frac{\partial \Phi}{\partial \vec{x}} \cdot \frac{\partial f}{\partial \vec{v}} = 0. \tag{1.5}$$

The potential is generated by the stellar density, combined with any additional contributions to the mass such as dark matter or a central black hole. The potential must follow Poisson's equation:

$$\nabla^2 \Phi(\vec{x}) = \rho_*(\vec{x}) + \rho_{\rm ext}(\vec{x}), \tag{1.6}$$

where $\rho_{\rm ext}(\vec{x})$ is any additional mass component.

While the CBE itself has many useful applications, it is also common to instead work with velocity moments of this equation, referred to as Jeans equations. The 0th velocity moment equation is given by simply integrating equation (1.5) over velocity, giving:

$$\begin{aligned} 0 &= \int \sum_i \left(v_i \frac{\partial f}{\partial x_i} - \frac{\partial \Phi}{\partial x_i} \frac{\partial f}{\partial v_i} \right) \mathrm{d}\vec{v} \\ &= \sum_i \frac{\partial}{\partial x_i} \left(\rho_* \overline{v_i} \right), \end{aligned} \tag{1.7}$$

where we have used index notation for clarity, and $\overline{v_i}$ represents the expectation value of v_i at a given position.

The 1st velocity moment equations are obtained by multiplying equation (1.5) by velocity, and integrating over all velocities:

$$\begin{aligned} 0 &= \int \sum_i \left(v_i \cdot \frac{\partial f}{\partial x_i} \right) v_j \mathrm{d}\vec{v} - \int \sum_i \left(\frac{\partial \Phi}{\partial x_i} \frac{\partial f}{\partial v_i} \right) v_j \mathrm{d}\vec{v}, \\ &= \sum_i \left(\frac{\partial}{\partial x_i} \int f v_i v_j \mathrm{d}\vec{v} - \frac{\partial \Phi}{\partial x_i} \int v_j \frac{\partial f}{\partial v_i} \mathrm{d}\vec{v} \right) \end{aligned} \tag{1.8}$$

where index notation has been used for the sake of clarity. Using the divergence theorem and setting the boundary terms to 0 gives:

$$0 = \left(\sum_i \frac{\partial}{\partial x_i} \left(\rho_* \overline{v_i v_j} \right) + \frac{\partial \Phi}{\partial x_j} \rho_* \right). \tag{1.9}$$

The Jeans equations are then given by subtracting $\langle v_j \rangle$ times equation 1.7 from equation 1.9 leading to:

$$\begin{aligned} 0 &= \sum_i \left(\frac{\partial}{\partial x_i} \left(\rho_* \overline{v_i v_j} \right) - \overline{v_j} \frac{\partial}{\partial x_i} \left(\rho_* \overline{v_i} \right) \right) + \frac{\partial \Phi}{\partial x_j} \rho_* \\ &= \sum_i \left(\frac{\partial}{\partial x_i} \left(\rho_* \sigma_{ij}^2 \right) + \rho_* \overline{v_i} \frac{\partial \overline{v_j}}{\partial x_i} \right) + \frac{\partial \Phi}{\partial x_j} \rho_*, \end{aligned} \tag{1.10}$$

where $\sigma_{ij}^2 = \overline{(v_i - \overline{v_i})(v_j - \overline{v_j})}$ is the velocity dispersion tensor.

Virial Theorem

Multiplying equation (1.9) by x_j, integrating over positions, and summing over j gives:

$$\begin{aligned} 0 &= \sum_j \int \left(\sum_i \frac{\partial}{\partial x_i} \left(\rho_* \overline{v_i v_j} \right) + \frac{\partial \Phi}{\partial x_j} \rho_* \right) x_j \mathrm{d}\vec{x} \\ &= \sum_j \int \left(\rho_* \overline{v_j^2} + \frac{\partial \Phi}{\partial x_j} \rho_* \right) \mathrm{d}\vec{x}. \end{aligned} \tag{1.11}$$

The first term in this equation can be recognized as twice the total kinematic energy, K, while the second can be recognized as the total potential energy, W, giving the scalar virial theorem:

$$0 = 2K + W. \tag{1.12}$$

This relationship can be used to estimate mass. Defining the gravitational radius radius $r_g = GM^2/|W|$ where M is the total mass of the galaxy and writing the kinematic energy

term as $K = \frac{1}{2}M\langle v^2\rangle$ (where $\langle v^2\rangle$ represents the expectation value of v^2 over both velocity and position) gives:

$$M = \frac{r_g \langle v^2\rangle}{G}. \tag{1.13}$$

While r_g and $\langle v^2\rangle$ are not directly observable, if we regard R_e and σ_e^2 as proxies for these two variables, this suggests the scaling:

$$M = c\frac{R_e\sigma_e^2}{G}, \tag{1.14}$$

where the proportionality constant c can be set by observations. Cappellari et al. [13] and Cappellari et al. [42] find that $c = 5$ gives a reasonable estimator of the total mass. Assuming a fixed mass-to-light ratio, equation (1.14) gives an expected scaling for the fundamental plane in the (L, R_e, σ_e) space.

While the virial theorem allows for rough mass estimation, even more can be learned by using a more complex modeling procedure that utilizes high quality IFS data that is now available for many nearby galaxies.

Jeans Modeling

Jeans modeling uses the velocity moment equations derived in section 1.2 in order to estimate the observed root-mean-square velocity as a function of position on the sky. In its most commonly used form, the potential and distribution function are assumed to be axisymmetric. Then, re-writing (1.9) in cylindrical coordinates gives:

$$\begin{aligned} \frac{\nu\overline{v_R^2} - \nu\overline{v_\phi^2}}{R} + \frac{\partial(\nu\overline{v_R^2})}{\partial R} + \frac{\partial(\overline{v_R v_z})}{\partial z} &= -\nu\frac{\partial\Phi}{\partial R} \\ \frac{\nu\overline{v_R v_z}}{R} + \frac{\partial(\nu\overline{v_z^2})}{\partial z} + \frac{\partial(\nu\overline{v_R v_z})}{\partial R} &= -\nu\frac{\partial\Phi}{\partial z}, \end{aligned} \tag{1.15}$$

where $\nu = \rho/\Upsilon$ is a stellar luminosity density obtained by assuming a fixed mass-to-light ratio, Υ. The third equation for the ϕ component is identically 0. Taking the density and potential to be known, the four unknowns $\overline{v_R^2}$, $\overline{v_z^2}$, $\overline{v_\phi^2}$, and $\overline{v_R v_z}$ are related by the two equations (1.15). These two equations alone do not provide enough information to specify a unique solution. Instead, this set of equations can be closed by including additional assumptions on these unknowns.

Cappellari [43] suggested using the assumptions that the tensor $\overline{v_i v_j}$ be aligned in cylindrical coordinates (ie. $\overline{v_R v_z} = 0$, and that the anisotropy is constant in the sense that $\overline{v_R^2} = b\overline{v_z^2}$. These two assumptions together with the two equations (1.15) thus provide the four constraints needed to specify the four unknowns.

A trial potential is given by specifying by a deprojected stellar luminosity density, stellar mass-to-light ratio, central SMBH mass, and possibly a dark matter halo. Given this trial potential, a value for the anisotropy parameter b, and the assumed stellar luminosity density,

the velocity moments $\overline{v_\phi^2}$, $\overline{v_R^2}$, and $\overline{v_z^2}$ can be calculated. By projecting along the line-of-sight, the resulting model can be compared to the observed mean-square velocity along the line-of-sight for each bin with an LOSVD measurement. The goodness-of-fit can then be compared for different trial potentials in order to obtain a best-fit model. Cappellari [43] gives general expressions that can be computed using a single numerical quadrature by assuming a flexible parameterization of the luminosity density that allows for a unique deprojection. This allows for fast evaluation of these models, making them both fast and easy to use.

Unlike the virial theorem, this method allows for constraints to be put on multiple individual mass components such as the stellar mass-to-light ratio, SMBH mass, and dark matter halo. However, its major shortcoming is the strictness of the assumptions that have been made. Real galaxies appear to have variations in velocity anisotropy, with central regions that are tangentially biased or isotropic and outer regions that are radially biased. This differs from the constant anistropy parameter, b, assumed here. Further, the assumptions that $\overline{v_R v_z} = 0$ and $\overline{v_R^2} = b\overline{v_z^2}$ dramatically limit the allowed orbital configurations.

Cappellari [44] presents an alternative version of these expressions using similar arguments, but with spherical coordinates in place of cylindrical coordinates. In a similar manner to the cylindrical case, the four velocity moments $\overline{v_\phi^2}$, $\overline{v_r^2}$, $\overline{v_\theta^2}$, and $\overline{v_r v_\theta}$ are determined by the two non-trivial velocity moment equations (1.9) and the assumptions that $\overline{v_r v_\theta} = 0$ and $\overline{v_r^2} = \frac{\overline{v_\theta^2}}{1-\beta}$. While this suffers from similar short-comings to the cylindrical version, running models with both sets of assumptions on orbital anistropy can help to quantify the systematic uncertainty that comes from imposing these restrictions. Both of these Jeans modeling techinques have seen wide-spread use.

Schwarzschild Orbit Modeling

Schwarzschild orbit modeling allows for more freedom in the model DF than the Jeans models previously described. The original ideas behind these models were laid out by Schwarzschild [45]. In order to generate a model, a model potential is first chosen. Next, a large number of orbits are integrated within the potential, and their positions are recorded throughout the orbit. Non-negative weights are then chosen for these orbits such that the weighted sum of the individual orbital mass distributions reproduces the original assumed stellar mass density. This results in a self-consistent DF for the original model. In the original Schwarzschild [45], this method was used to find a self consistent triaxial galaxy model, showing that such triaxial configurations can indeed be in equilibrium.

Schwarzschild [23] improved on this implementation further. In order to have as much model flexibity as possible, a wide variety of orbits should be provided to the model. Schwarzschild [23] demonstrated that for a somewhat realistic potential, orbit initial conditions sampled in a pair of 3-dimensional subspaces of the full 6-dimensional phase space gave a sufficient orbit sampling in triaxial potentials.

The next major step forward for this modeling technique came in a series of papers that adapted Schwarzschild's method of generating equilibrium models in order to directly model

data from real galaxies. Rix et al. [46] provided the first example of a direct fit to real galaxy data. In this paper, a spherical model of elliptical galaxy NGC 2434 was constructed using techniques based on Schwarzschild's method. The mass density was chosen to be a combination of the spherically deprojected SB, together with a dark matter halo. The orbital weights were then chosen to fit both the deprojected stellar density as well as the observed kinematics as parameterized through GH moments. The likelihood of each model was then determined based on the χ^2 statistic, quantifying the goodness of fit for each model. Using this technique Rix et al. [46] showed that a constant mass-to-light ratio was insufficient to accurately reproduce the observed kinematics of NGC 2434. Instead, a dark matter halo was needed to accurately match the outer velocity dispersion.

van der Marel et al. [47] and Cretton et al. [48] extended this technique to construct axisymmetric models. van der Marel et al. [47] presented axisymmetric Schwarzschild models of elliptical galaxy M32 were presented. These models demonstrate that the central velocity dispersion is not able to be matched unless a central dark mass concentration, consistent with an SMBH, is included in the potential. They estimate the central dark object to have a mass of $(3.4 \pm 0.7) \times 10^6 M_\odot$. Cretton et al. [48] outlines the details of the modeling implementation.

Since these original papers, axisymmetric Schwarzschild modeling has become widely adopted as the most reliable stellar-dynamical mass modeling method. This same implementation has been used to measure numerous central black hole masses (eg. [49, 50, 51, 13, 52]). Other implementations have since arisen (eg. Gebhardt et al. [53] and Valluri, Merritt, and Emsellem [25]) and been used to measure a large sample of central SMBH masses (eg. [54, 55, 56, 57, 58]).

Triaxial Orbit Modeling

Despite Schwarzschild's initial application of orbit superposition to constructing triaxial models in 1978, it was not until van den Bosch et al. [59] that the first effort to infer parameters from real galaxy data using triaxial models was published. van den Bosch et al. [59] outlined the detailed implementation of this triaxial orbit code, and applied it to infer the mass-to-light ratio and triaxial shape of elliptical galaxy NGC 4365. The shape recovery of this code was then tested on a mock triaxial galaxy, with multiple additional tests in van den Bosch and van de Ven [60]. These papers concluded that the shape could be accurately recovered, but with an uncertainty estimate that is significantly larger than suggested by the commonly used criterion. This alternative method of uncertainty estimation, discussed further in chapter 4, is now widely used in the literature for triaxial shape recovery. Ven, De Zeeuw, and Van Den Bosch [61] studied the ability for these orbit models to recover the true DF within a known triaxial potential. The recovered DF was found to be qualitatively consistent with the true DF.

This code has seen wide-spread use since its introduction. In addition to measure triaxial galaxy shapes (eg. [59, 62, 63, 64, 65]), it has also been used to determine central SMBH masses in triaxial galaxies (eg. [66, 67, 68, 69]).

Another widespread use case has been to perform "nearly" axisymmetric modeling. The shape is set to be nearly axisymmetric in the sense of having an intermediate-to-major axis ratio that is close to 1. This reduces the dimension of the parameter space to be explored. This method has been used for several $M_{\rm BH}$ determinations (eg. [70, 71, 72, 73, 74]).

Despite its widespread use, several papers have reported shortcomings and inconsistencies between this code and other methods. Ahn et al. [74] found that when the code was used to generate "nearly" axisymmetric models, the best-fit $M_{\rm BH}$ in ultracompact dwarf galaxy M59-UCD3 was consistent with 0 in contrast to multiple other modeling methods which preferred $M_{\rm BH} = (4.2^{+2.1}_{-1.7}) \times 10^6\ M_\odot$. More recently, den Brok et al. [69] found a similar result for their triaxial models of PGC 046832. In terms of shape recovery, Jin et al. [75] reported a bias in recovered axis ratios of 0.07 for the intermediate-to-major axis ratio and 0.14 for the minor-to-major axis ratio. Biases of this size can result in models with significantly different triaxial shapes and alignments.

In addition to potential biases on other mass parameters, measurements of triaxial galaxy shapes are needed to recover the intrinsic orbital structure of galaxies. The allowed orbit families depend strongly on the galaxy's shape [61]. As well, the brightest galaxy in a cluster is thought to be well-aligned with the underlying dark matter halo [76]. Alignment of a triaxial dark matter halo with respect to the line-of-sight is a major source of systematic uncertainty in mass estimations from gravitational lensing [77]. Understanding and constraining the intrinsic shapes of these galaxies may be useful for reducing these uncertainties.

1.3 Outline

This dissertation takes significant steps towards an understanding of the shapes of these most massive SMBHs and their host galaxies. In chapter 2, I present a modified version of the van den Bosch et al. [59] orbit modeling code capable of modeling axisymmetric systems. Allowing modeling of axisymmetric systems and triaxial systems within the same modeling framework allows for consistency checks between the two cases. The ability for this code to accurately recover SMBH masses is validated on a simple mock dataset. This version represents a significant improvement over the common practice in the field of using nearly axisymmetric models which can lead to significant biases in recovered SMBH masses. Additional improvements were also made to the code that extend beyond the axisymmetric case, including a reduction in computing time of about 50%.

In chapter 3, I build upon the results of chapter 2 to present a further updated version of the fully triaxial van den Bosch et al. [59] code and describe a general search strategy for the triaxial parameter space. This version corrects significant errors in model kinematics allowing for stable parameter recovery. The search strategy described requires far fewer expensive model evaluations than commonly used grid-based strategies. This search strategy is then applied to massive elliptical galaxy NGC 1453 to obtain a simultaneous measurement of its central SMBH, mass-to-light ratio, dark matter halo, and 3-dimensional shape.

Chapter 4 presents a validation of this final code version. I present a new code for generating mock galaxy observations. This code is then used to generate both axisymmetric and triaxial galaxy models to validate both the axisymmetric and triaxial versions of the updated orbit modeling code. Unlike previous shape recovery tests with triaxial galaxy models which have adopted ad hoc confidence levels, I have employed consistent confidence level estimation between the axisymmetric and triaxial cases. The improvements outlined in prior chapters resulted in recovered parameters that are dramatically more accurate than any prior published recovery tests.

While chapters 2, 3, 4 address dynamical modeling of individual massive ellipticals, chapter 5 explores the photometric properties of the local population of massive elliptical galaxies. This chapter presents deep infrared images and measurements of the scaling relations for the most luminous volume-limited sample of galaxies in which these relations have been measured. Our results are consistent with the conclusion that massive ellipticals form from dissipationless mergers, suggesting that the $M_{\rm BH} - L$ relation will be a better predictor of central SMBH mass than the $M_{\rm BH} - \sigma$ relation for these galaxies.

Chapter 2

Modeling of Axisymmetric Galaxies

With the goal of measuring shapes of triaxial galaxies, it makes sense to start with the simpler case: axisymmetry. While axisymmetric orbit models have been utilized for decades, these models are manifestly axisymmetric. The azimuthal symmetry is used to reduce the orbit integration to 2-dimensions, and the resulting kinematics are manifestly bisymmetric. This is qualitatively different than the "nearly axsiymmetric" models that have been run in several cases in the literature. In fact, Ahn et al. [74] found that while manifestly axisymmetric models preferred a non-zero $M_{\rm BH}$, consistent with Jeans modeling, nearly axisymmetric models within the van den Bosch et al. [59] preferred no central black hole. In early tests, I found similar behavior for models of NGC 1453. This chapter explores the process of generating axisymmetric models within a triaxial orbit modeling code. This chapter was originally published as:

Matthew E. Quenneville, Christopher M. Liepold, and Chung-Pei Ma. "Dynamical Modeling of Galaxies and Supermassive Black Holes: Axisymmetry in Triaxial Schwarzschild Orbit Superposition Models". In: *The Astrophysical Journal, Supplement* 254.2, 25 (June 2021), p. 25. DOI: 10.3847/1538-4365/abe6a0. arXiv: 2005.00542 [astro-ph.GA].

2.1 Introduction

The orbit superposition method of Schwarzschild [45] enables efficient construction of self-consistent and equilibrium mass models of galaxies. The basic procedure consists of two steps: integrating a representative set of orbits in a static triaxial gravitational potential, and finding weights for these orbits such that their superposition reproduces the assumed mass distribution.

The orbit superposition method has been extended to include kinematic information and used to determine mass distributions in real galaxies, starting with studies such as Pfenniger [79], Richstone and Tremaine [80, 81], and Rix et al. [46]. From the quality of the fit to both kinematic and photometric data, this method can be used to assess the relative likelihood

of a range of mass models and to determine best-fit mass parameters such as $M_{\rm BH}$, stellar mass-to-light ratios, galaxy shapes, and dark matter halo parameters.

Due to the large number of orbits needed to sample the relevant phase space, the orbit superposition method is computationally expensive. To reduce the number of orbits and the dimensions of the model parameter space, a few orbit-based numerical codes have been developed for axisymmetric systems (e.g., [48, 53, 82, 25, 13]). Many dynamical measurements of $M_{\rm BH}$ from stellar kinematics have been obtained using these axisymmetric orbit codes.

Triaxiality allows for more general galaxy shapes and additional orbit types, but modeling orbits in triaxial potentials comes at the cost of increased complexity and computation time. van den Bosch et al. [59] presented a triaxial orbit-based code capable of comparing directly to observations, using an orbital sampling scheme based on Schwarzschild [23]. Ven, De Zeeuw, and Van Den Bosch [61] performed recovery tests of this code for analytically tractable triaxial potentials (excluding central black holes). Only a handful dynamical determinations of $M_{\rm BH}$ have been obtained using triaxial models from this code [83, 67, 84]. Several additional $M_{\rm BH}$ were determined using this code in the (nearly) axisymmetric limit [70, 71, 72, 73, 74]. This code has also been used to construct axisymmetric and triaxial galaxy models to determine stellar dynamics and dark matter distributions for a wide range of galaxies (e.g., [62, 63, 65]). Vasiliev and Valluri [85] recently presented a new triaxial orbit-based code using a different method for phase space sampling and orbit initialization; the method was tested on mock data but had not been applied to real data.

An important test of the orbit superposition codes is the ability to produce consistent results between an axisymmetric code and a triaxial code in the axisymmetric limit. We note that the code by van den Bosch et al. [59] is written for triaxial potentials and "is not capable of making a perfectly axisymmetric model" [83]. Studies that attempt to run it near axisymmetry and then compare with results from axisymmetric codes have reached conflicting conclusions. For instance, van den Bosch and de Zeeuw [83] used their triaxial code to construct (nearly) axisymmetric models for M32 and NGC3379, and found the mass-to-light ratios and $M_{\rm BH}$ to be consistent with those from earlier studies using axisymmetric codes ([47, 86, 50] for M32; [53, 51] for NGC 3379). Ahn et al. [74], on the other hand, found a puzzling global χ^2 minimum at $M_{\rm BH} = 0$ while using this triaxial code to perform axisymmetric modeling of the ultracompact dwarf galaxy M59-UCD3. They found this minimum to be inconsistent with the best-fit non-zero $M_{\rm BH}$ from Jeans modeling and the axisymmetric orbit code of Cappellari et al. [13].

It is the purpose of our recent work [87] and this paper to investigate how to modify the van den Bosch et al. [59] code to enable it to handle properly both axisymmetric and triaxial systems. Since no galaxy in nature is likely to be exactly axisymmetric, it may appear that we are taking a step backwards in examining the axisymmetric limit of a triaxial code. While our next goal is indeed to adopt the more realistic triaxial potentials, we believe that one critical test of a triaxial code is its behavior in the simpler, axisymmetric limit. Such a study – the main goal of this paper – is a particularly important step in the quest for dynamical $M_{\rm BH}$ measurements in view of the facts that almost all existing $M_{\rm BH}$ measurements have been obtained assuming exact axisymmetry, and that the aforementioned recent comparison

of axisymmetric and triaxial codes have led to unresolved conflicting results.

In Liepold et al. [87], we described a set of recipes and code changes for achieving axisymmetry. We then performed proper axisymmetric orbit modeling using the revised code to obtain a new $M_{\rm BH}$ measurement for the massive elliptical galaxy NGC 1453, a fast rotator in the MASSIVE survey [88] well suited for axisymmetric orbit modeling. Similar to Ahn et al. [74], we had encountered difficulties in constraining $M_{\rm BH}$ in NGC 1453 when we used the original code with comparable settings. Through extensive testing, we came to two main conclusions: (1) higher Gauss-Hermite moments (beyond the typically used h_4) of the line-of-sight velocity distributions (LOSVDs) are needed to fully constrain the orbital weights, and (2) the orbit libraries need to be modified to satisfy axisymmetry. The use of higher moments is described in detail in Liepold et al. [87]. Here, we focus on the construction of axisymmetric orbit libraries in a triaxial orbit code.

In this paper, we provide a full discussion of the required steps to axisymmetrize the model and the various modifications that we have implemented to the triaxial code by van den Bosch et al. [59]. The code was never given a name; we will refer to it as the TriOS ("Triaxial Orbit Superposition") code from this point on. In Section 2.2, we provide some background information about the implementation of the orbit superposition method in this code. We focus on four topics that are pertinent to subsequent discussions: the three major orbit types in a triaxial potential (Section 2.2), orbit sampling and initialization (Section 2.2), orbit integration (Section 2.2), and parameters used to quantify triaxial shapes (Section 2.2).

In Section 2.3, we give an in-depth discussion of the three main ingredients for axisymmetry listed in Section 4.1 of Liepold et al. [87]: axisymmetrization of short-axis tube orbits (Section 2.3), criteria for how to exclude long-axis tube orbits (Section 2.3), and exclusion of box orbits (Section 2.3).

We have made additional improvements and corrections to the code (Section 2.4). We identify a subset of slowly precessing quasi-planar orbits that are misclassified and are "mirrored" improperly in the orbit library (Section 2.4). We correct an issue with the zero point of the logarithmic potential for the dark matter halo that would otherwise render energy conservation checks ineffective in the code (Section 2.4). We are able to speed up the total runtime of a mass model by a factor of 2 to 3 by a simple modification to how the point spread function convolution is implemented in the code (Section 2.4). An improvement in setting the intrinsic mass grid used to constrain stellar density profiles is described in Section 2.4. Finally, we illustrate the effects of these changes in the case of NGC 1453 (Section 2.5).

Three appendices are included as well. Appendix A derives a simple analytic criterion for the existence of long-axis tube orbits within a model. Appendix B outlines a change in the thin orbit finding algorithm that must be made to the TriOS code in order to generate the correct orbit sampling. Finally, Appendix C presents a mock recovery test demonstrating the ability of our revised TriOS code to recover the input mass parameters.

2.2 Orbit Modeling Background

A summary of the implementation of the Schwarzschild orbit superposition method in the TriOS code is given in Section 4 of Liepold et al. [87]. Here we focus on the topics relevant for subsequent discussions of axisymmetry (Section 2.3) and code modifications (Section 2.4).

In this paper, we use a Cartesian coordinate system in which the x, y, and z axes are directed along the intrinsic major, intermediate, and minor axes of the galaxy, respectively. The z-axis is therefore the symmetry axis of an oblate axisymmetric potential, and the x-axis is the symmetry axis of a prolate axisymmetric potential. We focus on oblate axisymmetric systems in this paper, although our discussions can be easily modified for the prolate axisymmetric case.

Orbit Types in a Triaxial Potential

In a static triaxial gravitational potential, time invariance is the only global continuous symmetry of the Hamiltonian, H. By Noether's theorem, this symmetry gives rise to conservation of energy as the only "classical" integral of motion. This conservation law restricts the allowed phase space for a given orbit from the full six phase space dimensions to a five dimensional subspace defined by the energy $H = E$. An integral that reduces the allowed phase space dimension in this way is referred to as an isolating integral.

Numerical studies have revealed that orbits in many potentials often conserve two additional "non-classical" isolating integrals of motion [45], which we refer to as I_2 and I_3. These additional integrals do not typically have simple analytical expressions nor correspond to global symmetries of H. Orbits that conserve three (or more) isolating integrals of motion are referred to as regular. These regular orbits often fall into one of three main orbit types: short axis tubes, long axis tubes, and boxes.

Both types of tubes have a fixed sense of rotation. For short-axis tubes, the component of angular momentum along the potential's minor axis, L_z, does not change sign. Similarly, for long-axis tubes, the component of angular momentum along the potential's major axis, L_x, does not change sign. For box orbits, all three components of angular momentum change sign, leaving no fixed sense of rotation. Box orbits also have the property of touching the equipotential surface, $\Phi(x, y, z) = E$, at some point during their trajectory. Intermediate axis tube orbits are typically unstable in triaxial models [89].

A triaxial system generally admits all three of these main orbit types. For oblate axisymmetric systems, the orbit structure is simpler because L_z is an integral of motion, and only short-axis tubes are present. Similarly, for prolate axisymmetric systems, L_x is an integral of motion and only long-axis tubes are present.

Orbit Sampling and Initialization

The set of initial conditions (referred to as a start space) should sample over all orbit types supported by the potential. Even though regular orbits in a triaxial potential conserve energy

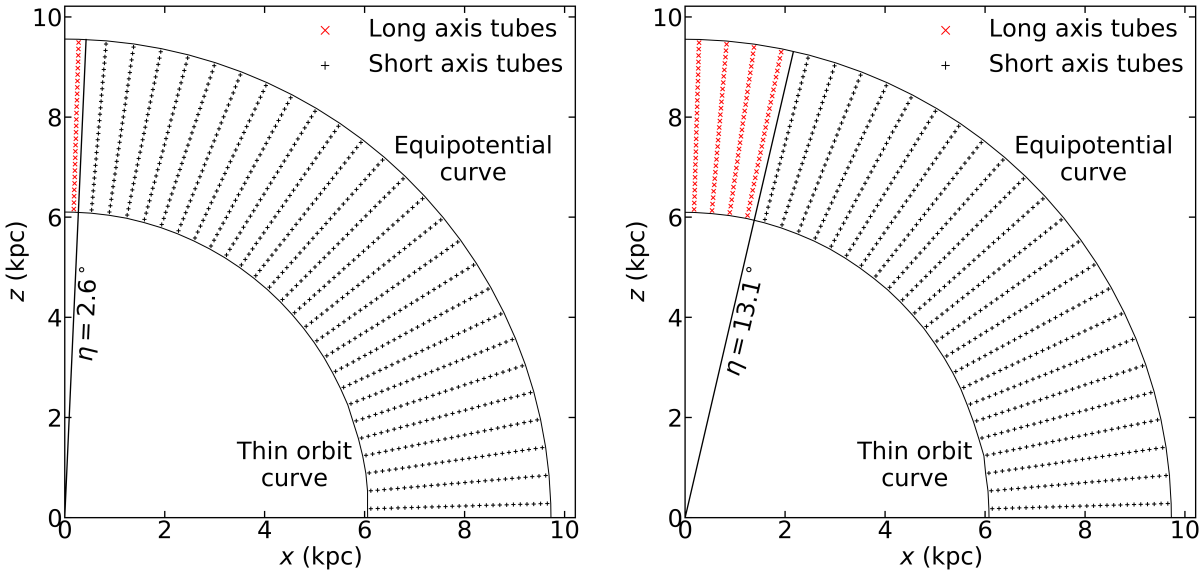

Figure 2.1: Two examples of the initial orbit locations in the x-z start space. Two nearly axisymmetric models for massive elliptical galaxy NGC 1453 are shown: (left) triaxiality parameter $T = 0.002$, (luminosity weighted) axis ratio $p = 0.9997$, and viewing angles $(\theta, \phi, \psi) = (89°, 45°, 90.001°)$; (right) $T = 0.05$, $p = 0.993$, and $(\theta, \phi, \psi) = (89°, 45°, 90.026°)$. Both models have the best-fit $M_{\rm BH}$, mass-to-light ratio, and dark matter halo from Liepold et al. [87] and assume the orbit sampling parameters $(N_\Theta, N_R, N_{\rm Dither}) = (9, 9, 3)$ (see Section 2.3). In each panel, one energy is shown, where the energy is chosen such that the potential is dominated by the stellar mass. Each symbol represents the initial location for a single trajectory, which are bundled with adjacent trajectories to form one dithered orbit. The long-axis tubes (red crosses) are all contained within the angle η of the z-axis for both values of T, where η and T are related by Equation (2.2). In general, more triaxial potentials contain a larger fraction of long-axis tubes in the x-z start space.

plus two additional integrals of motion, the non-classical integrals of motion, I_2 and I_3, may not be the same quantities for each orbit type [90, 41]. Thus, for a given energy, each orbit type can be sampled by a 2D start space, but the start spaces for the different orbit types cannot necessarily be combined into a single 2D start space.

Schwarzschild [23] argued that a 4D space can guarantee that all orbit types of a given energy are sampled, and further suggested that a pair of 2D start spaces is sufficient for sampling phase space in realistic galaxy potentials. The first of these start spaces, the x-z start space, is defined by sampling over a grid of points in the x-z plane, and setting $y = v_x = v_z = 0$ and v_y from $v_y^2 = 2[E - \Phi(x, 0, z)]$ for a given E. For simplicity, v_y is taken to be positive and a second copy is added to the orbit library with the velocity direction flipped. Two examples of this x-z start space are shown in Figure 2.1.

Typically, tube orbits will pass through the positive quadrant of the x-z plane perpendicularly at two points, separated by the thin orbit curve (see Figure 2.1). Orbits launched along that curve will perpendicularly pass through the plane at a single point, so the curve can be found by iteratively launching orbits at different radii to identify those which pass through the x-z plane in a thin curve (see Appendix B). Each orbit in the x-z start space passes once inside and once outside the thin-orbit radius, so the code avoids double counting by initializing orbits only between the thin-orbit curve and the equipotential where $E = \Phi(r)$, as shown by the crosses in the examples in Figure 2.1. All three main orbit types pass through this start space.

The second 2D start space proposed by Schwarzschild [23] is referred to as the stationary start space. In this start space, orbits are started from rest on the equipotential surface and are sampled over solid angle. Since tube orbits never come to rest, box orbits will be the only main orbit family in this start space. By combining the x-z start space that samples mainly tube orbits with the stationary start space that samples mainly box orbits, Schwarzschild [23] suggests that any remaining unsampled region of phase space is likely to be small.

The TriOS code is designed for static triaxial potentials that possess reflection symmetry along each of the three principal axes. Under this assumption, any orbital property only needs to be calculated in one octant; it can then be "mirrored" into the other seven octants by symmetry. Taking advantage of this symmetry, the code initializes orbits only in one octant ($x, y, z > 0$) and integrates only these orbits. Seven additional copies of each orbit are then created by simply mirroring along the three axes. The details are described in Section 4.5 of van den Bosch et al. [59] and the mirroring scheme is given in Table 2 there. A key feature to note in Table 2 is that the exact mirror procedure (i.e., how the signs of the velocity components are flipped in each octant) depends on whether the orbit is a short-axis tube, long-axis tube, or box. The orbits therefore must be classified first.

To classify an orbit, the code determines how the angular momentum components change sign over the course of its integrated trajectory and uses these rules: (1) short-axis tubes, if L_x and L_y flip signs while L_z does not, (2) long-axis tubes, if L_y and L_z flip signs while L_x does not, and (3) box orbits, if all three angular momentum components change signs. The velocities are mirrored in order to maintain the orbit's sense of rotation. If an orbit does not fall into any of these categories, its velocity is mirrored to have zero angular momentum.

Orbit Integration

The TriOS code uses the `DOP853` explicit Runga-Kutta integrator with order 8(5,3). The integrator performs adaptive time stepping to ensure that the relative error in the positions and velocities are below a set threshold, typically 10^{-5}. After each orbit is integrated, a relative energy tolerance is used to check energy conservation. If the change in energy exceeds this tolerance (typically set to 10%), it is re-integrated with a smaller integration error threshold.

The default integration time for each orbit is 200 dynamical times, where a dynamical time is set to the period of a closed elliptical orbit of the same energy. To enforce smooth-

ness of the recovered distribution function, the orbital initial conditions can be "dithered" by combining $N^3_{\rm Dither}$ trajectories corresponding to nearby initial conditions. By merging trajectories in this way, each orbit represents a small volume of the start space rather than a single point. This results in smoother orbital properties without a significant memory increase, since only the bundled orbital properties are stored.

After integration, the trajectory of each orbit is interpolated onto a set of points (typically 50,000) that are uniformly spaced in time. These interpolated points are then stored and used for computing orbital properties. Once the orbit libraries are constructed, weights are found for each orbit to reproduce the observed surface brightness (SB) distribution, the LOSVDs, and intrinsic 3D mass distribution.

Viewing Angles, Axis Ratios, and Triaxiality

Three viewing angles (θ, ϕ, ψ) can be used to relate the intrinsic and projected coordinate systems of a triaxial galaxy [21]. The two angles θ and ϕ describe the orientation of the observer's line of sight with respect to the intrinsic axes of the galaxy. The angle ψ specifies the remaining degree of freedom – rotation of the galaxy around the line of sight. The angle $\psi = 90°$ corresponds to an oblate axisymmetric potential. In the oblate axisymmetric limit, θ is the inclination with $\theta = 90°$ corresponding to edge-on, and ϕ describes rotations about the symmetry axis.

These three viewing angles are related to the intrinsic axis ratios p and q, where $p = b/a$ is the intrinsic intermediate-to-major axis ratio, $q = c/a$ is the intrinsic minor-to-major axis ratio, and a, b, c are the lengths of the three principal axes of a triaxial system (with $c \leq b \leq a$). A third parameter, $u = a'/a$, represents a compression factor due to projection, where a' is the major axis of the projected shape on the sky; $u = 1$ corresponds to the intrinsic major axis lying in the plane of the sky, while $u = p$ corresponds to the intrinsic intermediate axis lying in the plane of the sky. These quantities obey the inequality $0 \leq q \leq p \leq u \leq 1$. The relationship between the viewing angles, intrinsic axis ratios and observed axis ratio is given in Equations (7)-(10) of van den Bosch et al. [59]. In addition, a triaxiality parameter is often used:

$$T = \frac{1 - p^2}{1 - q^2}\,. \tag{2.1}$$

This parameter ranges from 0 for oblate axisymmetry to 1 for prolate axisymmetry, with values in between indicating a triaxial shape.

The oblate axisymmetric limit can be achieved by setting either $p = 1$ or $\psi = 90°$, but for numerical reasons, the code does not run when ψ is exactly 90°. As we discussed in Liepold et al. [87] and elaborate below (Section 2.3), axisymmetry in the code can be achieved only with carefully chosen values of ψ or p.

2.3 Ingredients for Achieving Axisymmetry

In this section, we discuss a number of steps that need to be taken to generate orbit-superposition models in the oblate axisymmetric limit using the TriOS code. It is straightforward to modify these steps for the prolate axisymmetric limit. In Appendix C, we test the modified TriOS code on a mock dataset showing that we can accurately recover input parameters.

Axisymmetrize Short-Axis Tube Orbits

As we described in Section 2.2, a triaxial potential exhibits reflection symmetry along each principal axis, allowing the TriOS code to initialize orbits in only one octant of the x-z start space. These orbits are then mirrored via eight-fold reflections about the principal axes into each of the other seven octants. This setup is not meant for axisymmetric systems, in which the orbit library should respect azimuthal symmetry about the symmetry axis.

To enable modeling axisymmetric systems, we have implemented an axisymmetrized version of the orbit library by creating 80 copies of each short-axis tube orbit in the original loop library: 40 copies rotated evenly through an angle 2π about the short axis with velocities rotated to preserve L_z, and another 40 copies generated by flipping the sign of z and v_z in each of the 40 rotations. We choose 40 rotations, as this gives several copies per quadrant, with a comparable density to the start space grid sampling. Once we perform this operation, it is unnecessary to perform the eight-fold reflections in the original code. A similar rotation scheme was tested on mock data with no central SMBH in Hagen, Helmi, and Breddels [91].

The net result of our axisymmetrization process is to create a library of short-axis tube orbits in the TriOS code that samples the azimuthal angle uniformly with effectively equal orbital weights. In order for this procedure to be justified, the library should consist solely of short axis-tubes. In the next section, we show how to ensure that no long-axis tubes occur in this library.

Exclude Long-Axis Tube Orbits

In an oblate axisymmetric potential, the long-axis tube orbits become unstable since there is no longer a single preferred long axis. These orbits therefore should not be present in the orbit library. [1]

As we discussed in Section 2.2, the potential is oblate axisymmetric when ψ is set to 90° exactly, and long-axis tubes should be absent in this limit. For numerical reasons, however, the code does not run when ψ is set to 90° within machine accuracy. Prior work using this code for black hole mass measurements in the axisymmetric limit chose either $|\psi - 90°|$ between 0.001° and 0.01° [72, 74], or an axis ratio of $p = 0.99$ [70, 71, 73]. As we first pointed

[1] Similarly, in the case of a prolate axisymmetric potential, the short-axis tube orbits become unstable and should be absent.

out in Liepold et al. [87], some of these values may not have been close enough to the desired axisymmetric values to exclude long-axis tubes. Here we provide a detailed explanation.

We use two examples of the x-z start space in Figure 2.1 to illustrate how long-axis tube orbits are initialized in the code. As shown in Appendix A, long-axis tube orbits in many realistic triaxial potentials are confined to pass through the x-z start space within an angle η from the z-axis. The angle η depends on the shape of the potential, and we find the relation between η and the triaxiality parameter T (Equation 2.1) to be well approximated by

$$\eta = \tan^{-1}\sqrt{\frac{T}{1-T}}\,. \tag{2.2}$$

This is demonstrated in Figure 2.1 where the black line at angle η separates the short-axis tube orbits (black crosses) from the long-axis tube orbits (red crosses). As the potential becomes more oblate axisymmetric ($T = 0.05$ in the right panel vs. $T = 0.002$ in the left panel), η becomes smaller and the area in the x-z start space occupied by long-axis tubes shrinks. To effectively achieve oblate axisymmetry, η needs to be small enough so that no orbits are sampled within an angle of η of the positive z-axis. Two additional mass models with higher triaxiality, ($T = 0.25$ and 0.75) are shown in Appendix A and Figure A.1. Equation (2.2) again provides an excellent approximation for the angle demarcating the long-axis and short-axis tube orbits in the x-z start space.

Whether orbits are sampled within the angle η on the x-z plane depends on the input parameters. For a given energy, the code starts the orbits on a grid of N_R radii between the inner and outer thin orbit radii and N_Θ angles between 0° and 90° in the positive quadrant on the x-z plane [59]. The code further allows for dithering, where $N^3_{\rm Dither}$ nearby initial conditions, adjacent in (E, R, Θ), are bundled together to improve the phase space sampling. Orbits are therefore sampled at a total of $N_\Theta \times N_{\rm Dither}$ angles, where the first angle from the z axis is chosen to start at half of the grid spacing (i.e., at an angle of $(\pi/2)/(2N_\Theta N_{\rm Dither})$ from the z-axis). The criterion to satisfy oblate axisymmetry is therefore

$$\frac{1}{2N_\Theta N_{\rm Dither}}\frac{\pi}{2} \gtrsim \eta. \tag{2.3}$$

The two examples of NGC 1453 shown in Figure 2.1 have $N_\Theta = N_R = 9$, $N_{\rm Dither} = 3$, and 27×27 orbits initialized in the x-z start space. The orbits closest to the z-axis are therefore at an angle of $\approx 1.67°$ away. These orbits lie within the demarcation angle η of Equation (2.2) for either model in Figure 2.1: $\eta = 2.56°$ for $T = 0.002$ (left) and $\eta = 12.9°$ for $T = 0.05$ (right). Both models therefore violate Equation (2.3) and contain long-axis tubes. This provides the physical explanation for our statement in Liepold et al. [87] that even $|\psi - 90°|$ as small as 0.001 (left panel) is not sufficiently close to 90° to achieve axisymmetry in our models.

To extend the discussion beyond the two specific mass models shown in Figure 2.1, we illustrate in Figure 2.2 the relation between T and ψ for nearly axisymmetric models of NGC 1453 (top panel), and the corresponding fraction of long-axis tubes that are initialized

in the x-z plane (bottom panel). The inclination angle θ is assumed to be 89° here, and the shaded band indicates the additional dependence of T on ϕ. Figure 2.2 shows that $T \lesssim 5 \times 10^{-4}$ is needed to exclude long-axis tube orbits in this case. The corresponding requirement on ψ is $|\psi - 90°| \lesssim 8.7 \times 10^{-6}$ for $\phi \sim 1°, 89°$ and $|\psi - 90°| \lesssim 2.5 \times 10^{-4}$ for $\phi \sim 45°$. We advocated $|\psi - 90°| = 10^{-9}$ in Liepold et al. [87], which safely excluded all long-axis tube orbits.

Earlier work using the code in the near axisymmetric limit does not typically satisfy the criterion in Equation (2.3). For M59-UCD3, Ahn et al. [74] used $(\theta, \phi, \psi) = (85°, -49.99°, 89.99°)$, which we find to correspond to $T = 0.004$ and $\eta = 3.64°$. The orbit sampling parameters were not explicitly given for the runs using the triaxial code. Assuming the same parameters used in their runs with the axisymmetric orbit code ($N_\Theta = 8, N_{\rm Dither} = 6$), we find that the innermost ray would be at an angle of 0.94° from the z-axis, which is well inside $\eta = 3.64°$, and therefore violates the criterion in Equation (2.3).

For M60-UCD1 [70], NGC 1271 [71], and Mrk 1216 [73], each paper quoted an axis ratio of $p = 0.99$. The minimum possible triaxiality with this value of p is $T = 1 - p^2 = 0.0199$ (in the unrealistic limit of a razor-thin disk with $q = 0$), leading to a minimum η of 8.1°. For NGC 1271 and Mrk 1216, $N_{\rm Dither} = 5$ was used, while N_Θ was set to 8 and 9 respectively. Thus, orbits were sampled starting at 1.125° and 1° away from the z-axis, indicating that neither satisfies the criterion in Equation (2.3). For M60-UCD1, not enough information is given about the orbit sampling to determine whether the criterion is satisfied. However, for typical orbital sampling parameters quoted above, the criterion in Equation (2.3) would not be satisfied.

The modeling of the NGC 1277 black hole used $N_\Theta = 9$ and $N_{\rm Dither} = 5$ [72]; the innermost ray of initial orbits therefore lies at 1° from the positive z-axis. The complete shape information was not given in the paper, but private communication indicated that $(\theta, \phi, \psi) = (75.3°, 71.6°, 90.001°)$ was used. We find this set of viewing angles to correspond to $T = 0.0002$ and $\eta = 0.85°$, narrowly satisfying the criterion in Equation (2.3).

We note that the presence of the long-axis tube orbits in the orbit library does not necessarily imply that they receive significant weights after fitting to observational constraints for a given galaxy. Direct tests would need to be performed for each galaxy to assess the impact of these orbits on previous work.

Exclude Box Orbits

As we discussed in Section 2.2, all orbits in the (oblate) axisymmetric limit conserve L_z. Box orbits in this limit have $L_z = 0$ and therefore have similar properties as the tube orbits with small L_z. In this case, as long as angular momentum is sufficiently sampled by the tube orbits, there is no need to include box orbits explicitly.

The TriOS code devotes an entire library to box orbits and initializes them in the stationary start space (Section 2.2). One can modify the code to exclude this library when needed. We use a simpler approach without changing the code itself: we skip running the orbit integration routine `orblib_f.f90` for the stationary start space, and replace the box library

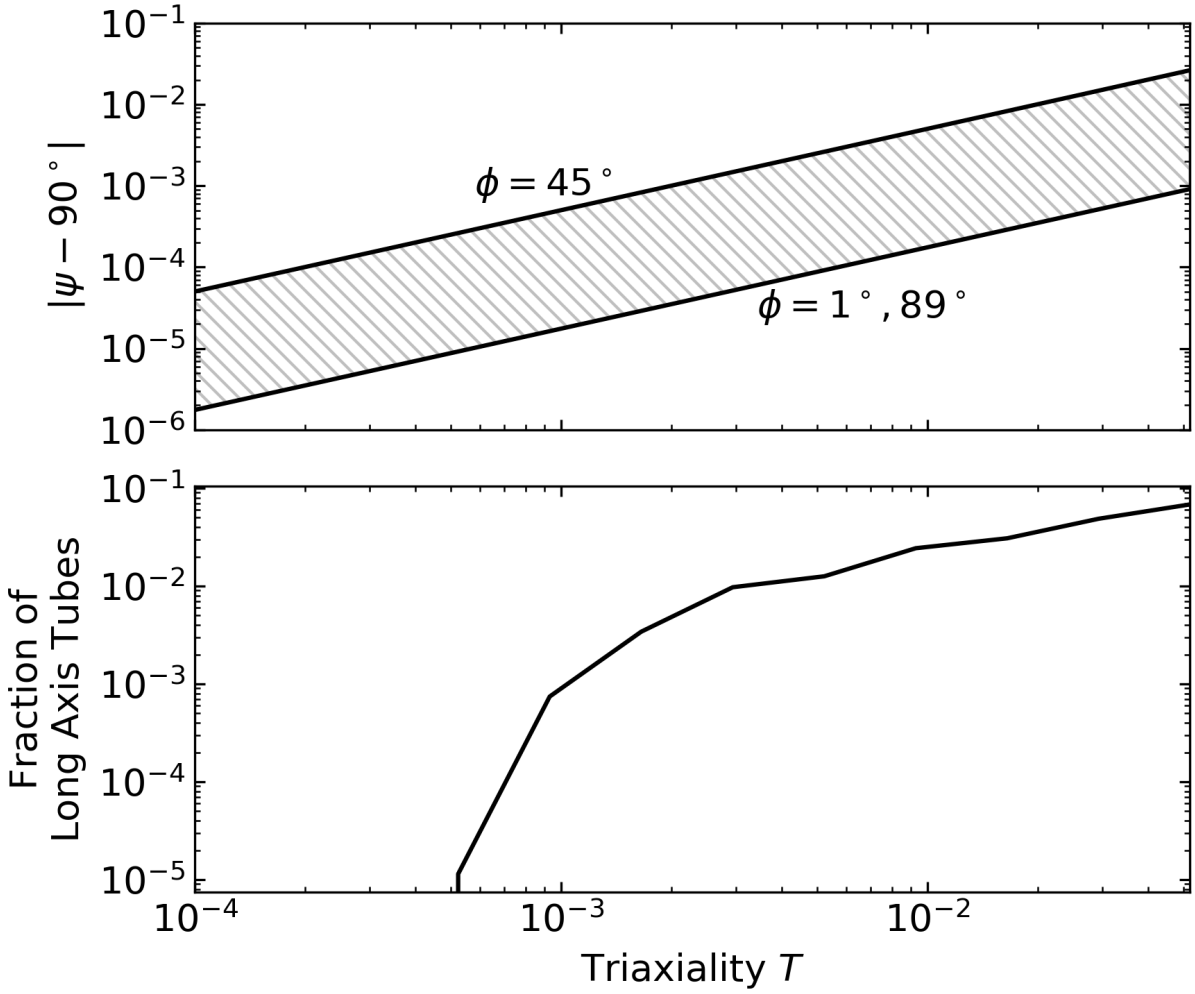

Figure 2.2: (Top panel) Relationship between the viewing angle ψ and the triaxiality of the deprojected stellar density. Exact oblate axisymmetry has $T = 0$ and $\psi = 90.0°$. The other viewing angle θ is taken to be 89°, and ϕ is varied from 1° to 89°. (Bottom panel) Fraction of long-axis tube orbits in the x-z start space as a function of the triaxiality of the stellar density near the oblate axisymmetric limit. The same mass model and orbit sampling parameters for NGC 1453 shown in Figure 2.1 is assumed here. In this example, long-axis tube orbits begin to appear when T is as small as $\sim 5 \times 10^{-4}$, or $|\psi - 90°|$ as small as $\sim 9 \times 10^{-6}$, and the fraction of these orbits increases monotonically as the potential becomes more triaxial, reaching $\sim 6\%$ at $T = 0.05$.

with a copy of the x-z library in the input file for the weight-finding routine `triaxnnls.f90`. These modifications typically reduce the total computation time of the original code by more than half.

While box orbits are unnecessary in the axisymmetric limit, they also should be harmless and not affect the results if included. As a test, we have run our revised code including the box library for comparison. Since the box orbits launched at different azimuthal angles are allowed to have different weights in the triaxial code, we have to impose an additional constraint of equal weights to enforce axisymmetry in the box library. Once these weights are forced to be equal, we indeed find similar results as the case when the box library is excluded altogether. The case where the box library weights are free to differ between azimuthal angles is discussed in Section 2.5. To reduce computational cost, we recommend excluding the stationary start space for axisymmetric models.

For a triaxial potential, we note that box orbits can also occur in the x-z start space (e.g., Figure 1 of [23]). However, the region in the x-z start space that would generate box orbits shrinks as the potential becomes increasingly axisymmetric. When exact axisymmetry is reached, only the orbits that begin exactly on the equipotential surface in the x-z start space have $L_z = 0$ (since they have zero initial velocities) and are box orbits. The TriOS code does not sample orbits lying exactly on the equipotential curve in the x-z start space, so the number of box orbits will shrink to 0 as axisymmetry is approached. In other orbit-based codes that assume axisymmetry from the start, the $L_z = 0$ orbits also are not usually sampled, as they are presumed to be represented by the tube orbits with small but non-zero L_z (e.g., [48, 82]).

2.4 Additional Code Fixes and Improvements

We have made several modifications in the TriOS code in addition to those described in Section 2.3. These modifications include corrections, improvements and speedups that are general to the code regardless of the issue of axisymmetry. We describe these changes in this section.

Correct Orbit Misclassifications

As we described in Section 2.2, the TriOS code assumes the triaxial potential to possess reflection symmetry along each of the three principal axes and integrates only orbits that are initialized in one octant of space to save computation time. It then uses an eight-fold reflection scheme to generate seven more copies of each orbit. How the orbits are "mirrored" depends on whether the orbit is classified as a short-axis tube, long-axis tube, or box orbit.

We have discovered that the mirroring scheme in the original code misclassifies a subset of orbits for which the angular momenta vary on timescales slower than the integration time. We find this to happen in at least two situations. First, in nearly oblate axisymmetric models, many box orbits in the stationary start space tend to be misclassified as short axis

tubes due to the near conservation of L_z. Because L_z varies slowly, it may not change sign throughout the integration time. However, these orbits have very low angular momentum, so it is unlikely that mirroring these orbits to preserve L_z would cause significant issues in the models themselves.

The second situation occurs in regions of space where the potential is nearly spherical, e.g., deep within the SOI of an SMBH, or in the outer part of a galaxy where a (spherical) dark matter dominates the potential. Some orbits in these regions follow quasi-planar rosettas or Keplerian-like ellipses with nearly constant angular momentum vectors, consistent with prior studies of orbits near a central point mass [92, 93, 94]. For the subset of orbits with precession time longer than the integration time, no component of their angular momentum changes sign over the entire integrated trajectories. These orbits therefore do not fall into any of the categories listed above and are mirrored incorrectly to have no net angular momentum.

These quasi-planar orbits will not be significant in most Schwarzschild models, as they are only present at extreme radii. We checked this in our models of NGC 1453, with the properly axisymmetrized code as described in Section 2.3 using the lowest four Gauss-Hermite kinematic moments as constraints. In this model, we find that $\sim 10\%$ of the total weight after orbital weight minimization is assigned to orbits that would have been quasi-planar in the original version of the code ($\sim 10\%$ of the mass within the Mitchell apertures and $\sim 2\%$ of the mass within the GMOS apertures). These relatively low percentages suggest a minimal effect on the model for NGC 1453.

We expect the issues with orbit integration time and misclassification to be more severe for galaxies with data that resolve well within the black hole's sphere of influence (SOI), or well beyond the stellar half-light radius, e.g., M87 and the Milky Way black hole. The effect is also likely to be more significant if the galaxy has a net rotation at these radii.

We find a further issue with orbit classification in the orbital composition information outputted in the file `intrinsic_moments.out`. This file reports the mass fraction of box orbits for each bin in the intrinsic spatial grid described in Section 2.4. In this case, however, all orbits that are neither long-axis tubes or short axis-tubes are grouped together as box orbits. Since this includes the quasi-planar orbits discussed above, the reported fraction of true box orbits may be overestimated.

In our revised code for axisymmetric systems, these orbit misclassification issues are not present because we manually assign all orbits as short-axis tubes and exclude all other orbit types. We will discuss further these quasi-planar orbits in triaxial systems in Section 2.6.

Fix Zero-point Issues with the Logarithmic Halo

A logarithmic potential is often used to approximate the dark matter halo in prior orbit modeling work. The spherical version of a logarithmic halo is given by

$$\Phi(r) = \frac{1}{2} V_c^2 \ln\left(R_c^2 + r^2\right) + \Phi_0 \,, \tag{2.4}$$

where R_c is the core radius, and V_c is the circular velocity at large r:

$$V_c(r) = \frac{V_c\, r}{\sqrt{R_c^2 + r^2}}\,. \tag{2.5}$$

The zero point Φ_0 can in principle be chosen arbitrarily; the original code set $\Phi_0 = 0$. In practice, we find the choice of $\Phi_0 = 0$ and the use of physical units such as kilometers for all distances to create numerical problems. The cause is simple: unlike other commonly used dark matter potentials such as Hernquist [95] and Navarro, Frenk, and White [96] that are negative at all locations and approach 0 at large r, the logarithmic potential with $\Phi_0 = 0$ is positive everywhere and grows unbounded at large r. Thus, for the other potentials, $|\Phi(r)|$ can be interpreted as the local maximum kinetic energy for a bound orbit, but the orbital binding energy is infinite in the logarithmic potential. Furthermore, with the choice of $\Phi_0 = 0$, $|\Phi(r)|$ is much larger than the kinetic energy for all orbits in a logarithmic halo. This is because the central potential energy value, $\Phi(0) = V_c^2 \ln(R_c)$, is much larger than the maximum possible kinetic energy sampled by the orbits, which is $\Phi(r_{\max}) - \Phi(0)$, where $r_{\max}$ is the largest equipotential radius of any orbit in a model.

To illustrate this point, we plot the ratio of $|\Phi(r)|$ and $|\Phi(r_{\max}) - \Phi(0)|$ for the best-fit logarithmic dark matter halo of NGC 1453 [87] in Figure 2.3 (dotted curve). Additional contributions to the potential from the stars and black hole reduce the value of the potential energy and help lower this ratio (dot-dashed and dashed solid curves), but the ratio is well above unity for all relevant radii in all cases.

An unintended consequence of this large central offset is that even a $\sim 100\%$ change in the kinetic energy would contribute to only a tiny fraction of the total energy and would be difficult to detect. The energy conservation checks in the code are therefore effectively not performed for most orbits. While these numbers are worrying, we did not find the choice of $\Phi_0 = 0$ to affect significantly the best-fit mass parameters of NGC 1453 in Liepold et al. [87]. The reason for this particular case is that the orbit integrator happened to be accurate enough to satisfy the energy conservation tolerance (set to the default 10%) even when this conservation criterion was unchecked. There is, however, no guarantee that this would be true for other galaxies or for parameters outside the ranges that we had explored.

To ensure energy conservation is checked in the code for the logarithmic potential, we choose a different zero point

$$\Phi_0 = -\Phi(r = 2r_{\max})\,, \tag{2.6}$$

so that $\Phi(r)$ is negative for the entire allowed radial range of the orbits and approaches 0 outside the largest equipotential radius $r_{\max}$. The resulting ratio of $|\Phi(r)|$ to $|\Phi(r_{\max}) - \Phi(0)|$ for the best-fit model of NGC 1453 is shown by the solid line in Figure 2.3.

Our choice of Φ_0 in Equation (2.6) also removes another issue that we have encountered with the original code: the orbit start space was sometimes not calculated correctly for mass models in which the black hole is either absent or has small mass compared to the stellar component and the logarithmic halo. As discussed in Section 2.2 and shown in Figure 2.1, the x-z start space of Schwarzschild [23] requires finding equipotential curves in the x-z

plane. The code locates it by finding the equipotential radius for each of a series of angles in the plane. For each angle, the equipotential radius is found via bisection with a relative tolerance that is typically taken between 10^{-7} and 10^{-5}. For $\Phi_0 = 0$, this tolerance again is not enforcing the intended accuracy level due to the large central value of Φ. For NGC 1453, this issue exists only for a few central equipotential radii and thus did not have a significant impact on our results.

Speed Up Point Spread Function Implementation

The point spread function (PSF) of the relevant observations needs to be incorporated into a mass model before the model is fitted to data to determine the orbital weights. The TriOS code approximates the effect of the PSF by perturbing each trajectory at every stored time step with a pair of δx and δy randomly drawn from the PSF, which is assumed to be a single or multiple Gaussian functions. This scheme involves a large number of operations since an orbit is typically stored at 50,000 points along the trajectory (see Section 2.2), and up to $\sim 10^6$ orbits can be used to represent a single mass model.

The code generates each orbit perturbation by drawing two independent numbers, k_x and k_y, from a uniform distribution over the interval $(-1, 1)$ repeatedly until a pair with $k \equiv |\vec{k}| < 1$ is found. The perturbations $\delta x = \frac{k_x}{k}\sqrt{-2\ln(k^2)}$ and $\delta y = \frac{k_y}{k}\sqrt{-2\ln(k^2)}$ are then normally distributed. This large number of operations is not easily vectorized and is computed sequentially.

We are able to speed up this process significantly using instead the Box-Muller transform, which is easily vectorized. In this scheme, we draw a pair of independent numbers A and B from the uniform distribution over $(0, 1)$ and then construct the normal distribution with $\delta x = \sqrt{-2\ln A}\cos(2\pi B)$ and $\delta y = \sqrt{-2\ln A}\sin(2\pi B)$. We have tested that the resulting distributions of displacements are consistent with analytical PSFs to within the counting error from the finite number of timesteps, and the consistency increases as expected when the number of timesteps increases.

To benchmark the amount of speedup gained by our scheme, we note that PSF convolution is one of several operations performed in the orbit library construction subroutine `orblib_f.f90` in the code. This subroutine first integrates the orbits and generates the necessary reflected or rotated copies of the orbits about the symmetry axes (see Section 2.3). It then computes each orbit's contribution to the 3D mass grid and projects each orbit onto the sky plane. The projected trajectories are then perturbed according to the PSF as described above. Finally, the subroutine determines each orbit's contribution to each observed kinematic aperture on the sky and stores the associated LOSVDs. The tasks performed in this subroutine consume the bulk ($> 90\%$) of the total runtime of the code (for one mass model); much of the remaining time is spent on performing minimizations to find optimal orbital weights.

To our surprise, our timing analysis of the various tasks executed in this subroutine (using $N_{\rm Dither} = 5$ and NGC 1453 as a test case) shows that the PSF portion of the code (before implementing orbit axisymmetrization in Section 2.3) takes up $\sim 55\%$ of the run time,

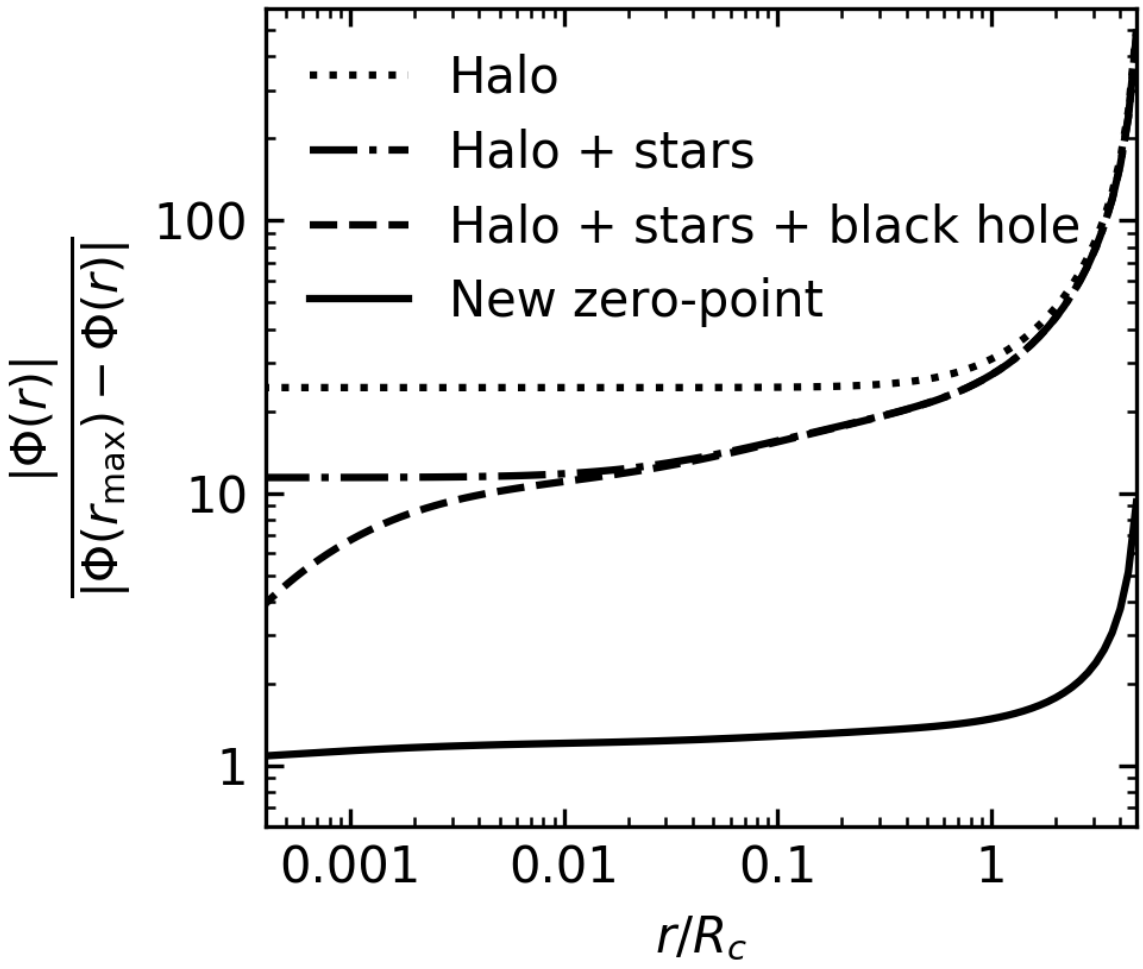

Figure 2.3: Illustration of the issue with setting the zero-point of the logarithmic potential to $\Phi_0 = 0$ in Equation (2.4), as is assumed in the original code. As an example, we use the best-fit mass model for NGC 1453 in Liepold et al. [87] with a logarithmic dark matter halo of $R_c = 15$ kpc and $V_c = 633$km s^{-1}. The ratio of the potential energy to the maximum kinetic energy is plotted for this halo (dotted), halo plus stars (dot-dashed), and all three mass components (dashed). When this ratio is much larger than 1, as is shown for a large range of radius, even large errors in the kinetic energy would have little effect on the total energy. Energy conservation is therefore effectively not enforced in the original code for a logarithmic potential. The solid line shows the same ratio with all three mass components included, but with the halo zero point set according to Equation 2.6.

while the orbit integration itself only contributes $\sim 20\%$, and sky projections contributes the remaining $\sim 25\%$. When we switch to the vectorized Box-Muller transform, the computation time for the PSF step becomes negligible. We are therefore able to reduce the total runtime of the code by a factor of ~ 2 in this test.

The speedup is even more dramatic in our axisymmetrized version when the orbits are copied azimuthally (Section 2.3). In this case, 80 (instead of 8) copies of each orbit are projected onto the sky and perturbed by the PSF. We find $\sim 70\%$ of runtime is spent on the PSF portion with the original scheme, while our new scheme reduces the runtime by a factor of ~ 3.

Improve Intrinsic 3D Mass Grid

The TriOS code uses an intrinsic 3D spatial grid to constrain the stellar component in a model to reproduce the 3D stellar density profile deprojected from the photometry of a galaxy. The code calculates the mass contributed by each orbit as it passes through a spatial bin and records this information during the stage of orbit library construction. At the subsequent stage of orbital weight optimization, the superposition of the orbits is required to match the input mass profile within a pre-specified precision (typically 1%) in each bin.

In each octant of this 3D spatial grid, the code uses azimuthal and polar bins for the two angles, each linearly spaced between 0 and 90°. The radial bins are logarithmically spaced between $r_{\rm min}$ and $r_{\rm max}/2$, where $r_{\rm min}$ and $r_{\rm max}$ are the innermost and outermost equipotential radii used to determine the orbital energies sampled in the model. The innermost bin is then extended down to $r = 0$ and the outermost is extended out to $100 r_{\rm max}$.

For the outer boundary of the innermost mass bin, we find it preferable not to base the value on $r_{\rm min}$, which is used for a different purpose of specifying the innermost equipotential radius for sampling orbital energy. Instead, we modify the code to make it an independent parameter, which we set to be of similar scale as the PSF of the photometric data since these are the data used to constrain the deprojected 3D mass density. To ensure that sufficient orbits are used to represent the innermost mass bins, we recommend that $r_{\rm min}$ be set to be smaller than the outer boundary of the innermost mass bin. In the case of NGC 1453, we set the outer boundary of the innermost mass bin to be $0.03''$ and set $r_{\rm min}$ to $0.01''$.

For similar reasons, we allow the outermost mass bin's edges to also be set independently from the outermost equipotential radius, $r_{\rm max}$. The remaining bin boundaries are then logarithmically sampled between the outer boundary of the innermost bin and the inner boundary of the outermost bin.

2.5 A Case Study: NGC 1453

We use the massive elliptical galaxy NGC 1453 reported in Liepold et al. [87] to illustrate the effects of the modifications described thus far. In Liepold et al. [87], we demonstrated that using more than 4 Gauss-Hermite moments was essential for obtaining robust constraints on

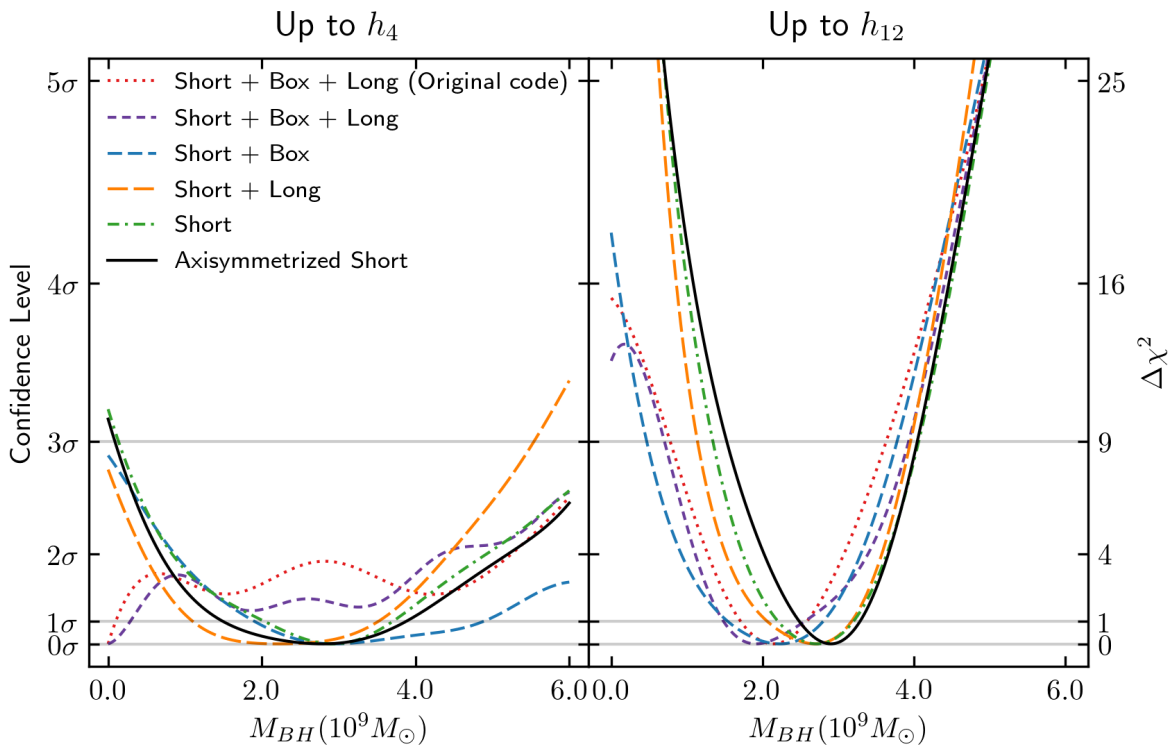

Figure 2.4: Illustration of the changing $M_{\rm BH}$ constraints in NGC 1453 as the orbit model goes through the step-by-step axisymmetrization procedure described in Sections 2.3 and 2.4. The starting case (red dotted) uses the original code with typical (near) axisymmetric parameters assumed in the literature ($\psi = 90.001°$; see Section 2.5 for details). The end case (black solid) uses our final axisymmetrized code including all changes from Sections 2.3 and 2.4. The four intermediate curves have all the code fixes described in Section 2.4, but have different combinations of orbit types according to Sections 2.3 and 2.3. The left panel is for models with orbital weights chosen by fitting to the first four Gauss-Hermite moments of the LOSVDs determined from kinematic data, as is typical in the literature. The right panel uses 12 moments as constraints and shows tighter constraints on $M_{\rm BH}$, as is reported in Liepold et al. [87]. The 1D χ^2 in $M_{\rm BH}$ is obtained by marginalizing over the stellar mass-to-light ratio using a smoothed 2D χ^2 landscape generated by Gaussian Process regression with a squared-exponential covariance function [97]. The dark matter halo is fixed to the best-fit logarithmic halo in Liepold et al. [87].

the model LOSVDs. Below we examine the effects in both the 4-moment and 12-moment cases, with the latter being our chosen configuration. We stress that the 4-moment case is included here only for comparison purposes since this is the typical configuration used in the literature. We have found the 4-moment case to lead to unconstrained higher moments and spurious features in the LOSVDs for NGC 1453 (Figs. 10 and 11 of Liepold et al. [87]); the resulting χ^2 in this case should therefore not be trusted.

Fitting up to h_4

We begin with the case labeled "up to h_4" and "original Leiden version" in Figure 12 of Liepold et al. [87]. This case is run with the original code, $N_{\rm Dither} = 3$, $N_\Theta = 9$, and the viewing angles $(\theta, \phi, \psi) = (89°, 45°, 90.001°)$, corresponding to a nearly oblate axisymmetric potential with a triaxiality parameter of $T = 0.002$. As we discussed in Section 2.3, these parameters are chosen to resemble those used in earlier studies, and the models include both the x-z and stationary start spaces and contain all three major types of orbits: short-axis tubes, long-axis tubes and box orbits. The left panel of Figure 2.1 illustrates the starting locations of both short- and long-axis tube orbits in the x-z start space for one energy in this configuration.

The 1D χ^2 as a function of $M_{\rm BH}$ (marginalized over the mass-to-light ratio) is shown in the left panel of Figure 2.4 (red dotted curve). As first shown in Liepold et al. [87], the favored model in this case contains no black hole. The χ^2 minimum at $M_{\rm BH} = 0$ here resembles the finding for the dwarf galaxy M59-UCD3 by Ahn et al. [74], which also used four Gauss-Hermite moments as constraints and a set of viewing angles with a similar deviation from axisymmetry.

Applying the code changes described in Section 2.4 results in minor changes in the χ^2 contour for NGC 1453 (purple short dashed curve in Figure 2.4), but the $M_{\rm BH} = 0$ minimum remains. In the next step, we exclude the box orbits and long-axis tube orbits as described in Section 2.3. The box orbits are eliminated by the simple procedure in Section 2.3. To remove the long-axis tube orbits, we choose a galaxy shape that is sufficiently axisymmetric, as discussed in Section 2.3. For NGC 1453, we simply change ψ from 90.001° to $(90+10^{-9})°$, as was done in Liepold et al. [87]. This new value is far enough from 90.0° to avoid numerical issues in the code but is close enough to 90.0° so that all of our orbits lie outside the long-axis tube region in the x-z start space shown in Figure 1.

The effect of excluding these orbits on the best-fit parameter values for NGC 1453 is significant. The preferred $M_{\rm BH}$ is changed from 0 to $2.8 \times 10^9 M_\odot$ (green dot-dashed curve in Figure 2.4a). Before their removal, box orbits generally accounted for less than 10-35% of total mass, while long axis tube orbits accounted for less than 2%. Removing box orbits (orange long dashed curve in Figure 2.4a) has a significant effect on $M_{\rm BH}$ because box orbits starting at different azimuthal angles are not forced to have equal weights in the original code (Section 2.3). Removing the long-axis tubes (blue dashed curve in Figure 2.4a) has a significant impact likely due to their ability to fit minor-axis rotation in triaxial potentials.

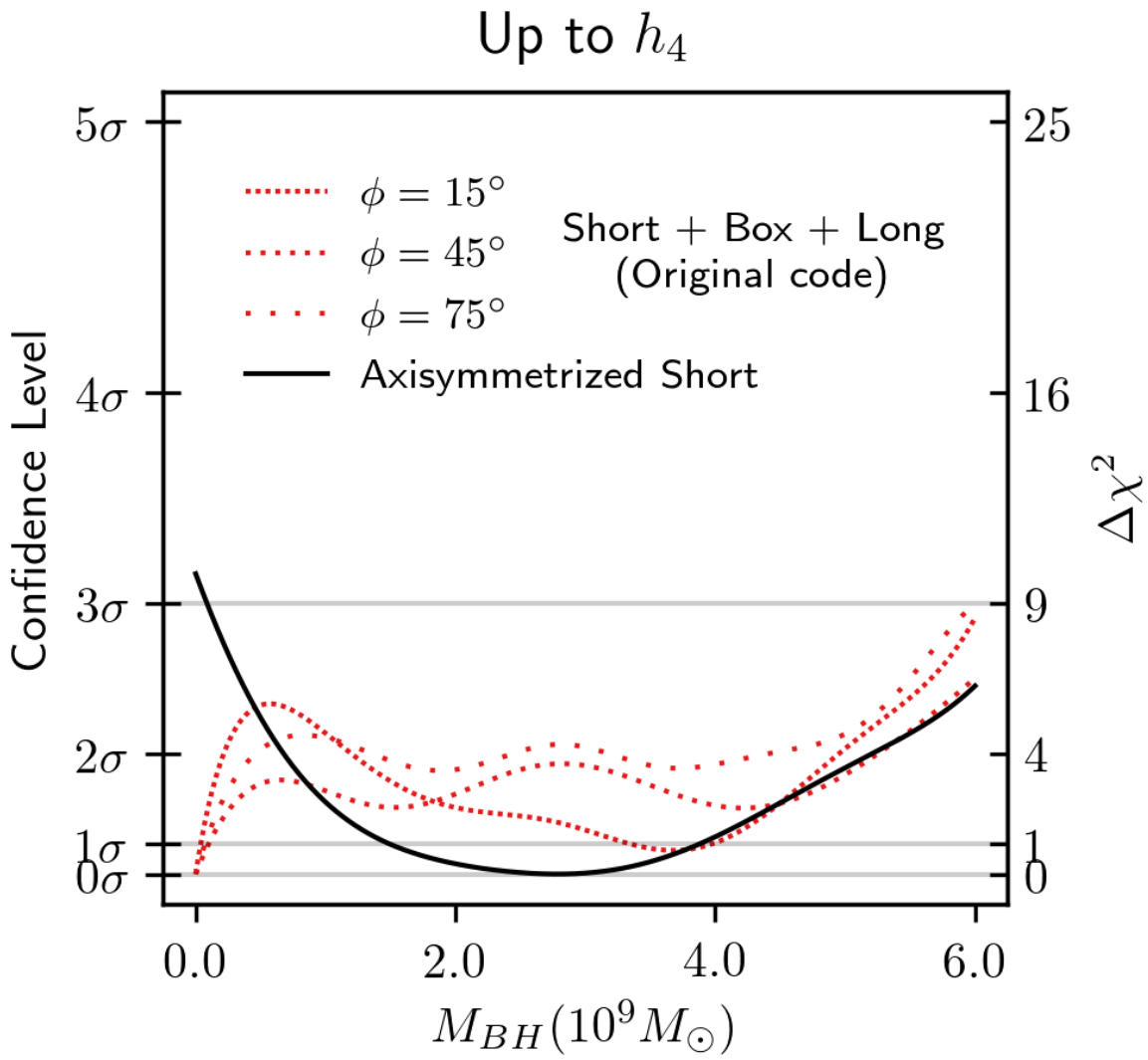

Figure 2.5: Same as the left panel of Figure 2.4 but showing the azimuthal dependence of the original code when ψ is chosen to be 90.001° and all three main orbit types are included (red curves). Our final axisymmetrized code does not depend on ϕ and obeys azimuthal symmetry.

In addition to excluding the box and long-axis tubes, we describe in Section 2.3 the need to enforce axisymmetry in the code by generating many azimuthally rotated copies of each short-axis tube in the x-z start space. For NGC 1453, we find that the main effect on the χ^2 contour of this axisymmetrization procedure is to widen the minimum (black solid curve in Figure 2.4a), as a broader range of orbital weights are able to fit the mass constraint for each mass model.

The results presented thus far with the original version of the code all assumed a viewing angle of $\phi = 45°$. When the model galaxy is perfectly axisymmetric, this angle is irrelevant and the resulting χ^2 landscape should be independent of ϕ. As a test, we have repeated the run with the original code (using four Gauss-Hermite moments) with two other values of ϕ (15° and 75°) while keeping all other parameters fixed. The resulting χ^2 as a function of $M_{\rm BH}$ for the three values of ϕ are shown in Figure 2.5. The dependence on ϕ indicates that the mass models are indeed not consistent with axisymmetry. All three values of ϕ exhibit the same preference for $M_{\rm BH} = 0$.

Fitting up to h_{12}

We now examine models in which the orbital weights are constrained to fit the first 12 Gauss-Hermite moments of the observed LOSVDs for NGC 1453. The first 8 moments are measured from spectroscopic observations, while the 9th-12th moments are set to 0 with an error bar based on the lower moments, as described in detail in Liepold et al. [87]. Even without any of the modifications described in this paper, Liepold et al. [87] showed that the original code performed better when 12, rather than 4, moments were used as constraints. The right panel of Figure 12 in Liepold et al. [87] illustrated how the best-fit black hole mass moved from $M_{\rm BH} = 0$ for 4 moments (green curve) to $M_{\rm BH} = 2.2 \times 10^9 M_\odot$ for 12 moments (black curve). The result from the original code, however, was highly dependent on the number of input moments and showed no convergence even at 12 moments. By contrast, after the orbit and code modifications were implemented, the main effect of increasing the constraining kinematic moments was to tighten the error bars while leaving the best-fit values largely unchanged (left panel of Figure 12 in Liepold et al. [87]).

Here we examine the progression of changes after each of the key modifications described in Sections 2.3 and 2.4 is implemented, all for the case of using 12 moments as constraints. The right panel of Figure 2.4 shows that implementing the code fixes described in Section 2.4 (purple dot-dot-dashed curve) and removing long-axis tubes (blue dot-dashed curve) move the best-fit $M_{\rm BH}$ by $\sim 10\%$ in comparison to $M_{\rm BH} \sim 2.2 \times 10^9 M_\odot$ from the original code (red dotted curve). Removing the box orbits increases $M_{\rm BH}$ to $\sim 2.9 \times 10^9 M_\odot$ (orange dot-dash-dashed and green dashed curve). The subsequent axisymmetrization of short-axis tubes (Section 2.3) has essentially no effect (black solid curve).

To ensure that the number of orbits included in the modeling is sufficient, we tested the effect of increasing the number of orbits. We increased the density of energy sampling by a factor of 4, from 40 energy values to 160 over the same range. With 4 times the number

of orbits, the best-fit $M_{\rm BH}$ changed by less than 3%, and the 1σ error changed by less than 10%, demonstrating that our results do not depend on the exact number of orbits used.

2.6 Conclusion

We have presented a revised version of the triaxial orbit superposition code by van den Bosch et al. [59], which we refer to as the TriOS code, that is capable of properly modeling axisymmetric systems. The original code was designed for triaxial systems with (discrete) reflection symmetry along each of the three principal axes. The setup was not capable of modeling exactly axisymmetric systems in which the orbit library should respect (continuous) azimuthal symmetry about the symmetry axis.

We have implemented two main changes needed for modeling axisymmetric systems within the triaxial code: excluding all orbit types that are not allowed in an axisymmetric model, and enforcing axisymmetry among the allowed orbits. In the case of oblate axisymmetry, our recipe involves (1) axisymmetrizing the short-axis tube orbits by creating multiple copies of the orbits rotated about the symmetry axis (Section 2.3), (2) setting the viewing angle ψ to be sufficiently close to 90° to allow no long-axis tube orbits (Section 2.3), and (3) excluding the stationary start space used to generate box orbits (Section 2.3).

We have made further improvements and corrections to the code in general. We discussed an issue with slowly precessing quasi-planar orbits that are misclassified and are "mirrored" improperly in the orbit library (Section 2.4). We also corrected a problem with the logarithmic halo implementation that prevented checking energy conservation of the integrated orbits (Section 2.4). We achieved a factor of 2 to 3 speedup in the runtime of the code by adopting a different algorithm for modeling PSF convolution (Section 2.4). Finally, we allowed the orbit sampling and mass constraints to be set independently (Section 2.4).

For NGC 1453, we found the shape of the χ^2 contours for $M_{\rm BH}$ to vary significantly as we went through the step-by-step axisymmetrization procedure described in this paper (Figure 2.4). As we described in Liepold et al. [87], the orbit models favored no black holes when we used the original code with typical (near) axisymmetric parameters in the literature and four Gauss-Hermite moments to constrain the stellar LOSVDs. In contrast, we obtained a well constrained non-zero $M_{\rm BH}$ using our final axisymmetrized code including all the changes described in Sections 2.3 and 2.4.

One issue that warrants further investigation in triaxial models is the equilibrium behavior of quasi-planar orbits in regions where the potential is nearly spherical, e.g., well within a SMBH's SOI, or far outside the galaxy's effective radius in a spherical dark matter halo. As we discussed in Section 2.4, the subset of quasi-planar orbits with precession times longer than the integration time has a nearly constant $\vec{L}$ and is misclassified and mirrored incorrectly in the original code. Furthermore, the integration time for these orbits is not long enough to fill the allowed volume of phase space. For axisymmetric systems, we resolve these issues in our revised code described in this paper by including only short-axis tubes and enforcing axisymmetry in the orbits, while preserving L_z.

We also expect the severity of the orbit integration issue to vary from system to system: the better a SMBH's SOI is resolved by the available kinematic data, the more care is needed to test orbital integration time because quasi-planar orbits occupy a large fraction of the orbit library, and more orbits are deeper in the SMBH's potential and hence have longer precession times. For the NGC 1453 SMBH studied in Liepold et al. [87] and here, since our kinematic data do not reach deep inside the SOI, orbits in our mass models with precession time exceeding 200 dynamical times account for less than 4% of luminosity within the central arcsecond. The integration issue (and the resulting misclassification) therefore does not significantly impact our results, as is evidenced by the similarity between the solid black and green dashed curves in Figure 2.4. We expect a different situation for better resolved systems such as the M87 and Milky Way SMBHs.

In future work, a straightforward solution to ensure that quasi-planar orbits are representative of their equilibrium distributions is to extend the default integration time of 200 dynamical times in the code. Our preliminary tests suggest that integrating the orbits up to ~ 10 times longer is computationally feasible, but this may still be insufficient for the orbits closest to the SMBH and in the outermost part of the galaxy where the precession times are slowest. A more reliable treatment of these orbits would be needed.

Acknowledgements

We thank Jonelle Walsh for useful discussions and a critical reading of the manuscript, and Karl Gebhardt for discussions about mock tests. We also thank the anonymous referee for their helpful comments and suggestions. M.E.Q. acknowledges the support of the Natural Sciences and Engineering Research Council of Canada (NSERC), PGSD3-517040-2018. C.-P.M. acknowledges support from NSF AST-1817100, HST GO-15265, HST AR-14573, the Heising-Simons Foundation, the Miller Institute for Basic Research in Science, and the Aspen Center for Physics, which is supported by NSF grant PHY-1607611. This work used the Extreme Science and Engineering Discovery Environment (XSEDE) at the San Diego Supercomputing Center through allocation AST180041, which is supported by NSF grant ACI-1548562.

Chapter 3

Modeling of Triaxial Galaxies

Having demonstrated the ability of our updated code to recover stable and reliable $M_{\rm BH}$ values in the axisymmetric case, I now proceed to examine the triaxial case. The triaxial case is significantly more complex than the axisymmetric case. This chapter presents significant improvements and corrections to the van den Bosch et al. [59] code, improved search and modeling strategies for the triaxial case, and an application of this version to simultaneously measure the triaxial shape, dark matter halo, mass-to-light ratio, and central black hole mass in the massive elliptical galaxy NGC 1453. This chapter was originally published as:

Matthew E. Quenneville, Christopher M. Liepold, and Chung-Pei Ma. "Triaxial Orbit-based Dynamical Modeling of Galaxies with Supermassive Black Holes and an Application to Massive Elliptical Galaxy NGC 1453". In: *The Astrophysical Journal* 926.1, 30 (Feb. 2022), p. 30. DOI: 10.3847/1538-4357/ac3e68. arXiv: 2111.06904 [astro-ph.GA].

3.1 Introduction

Elliptical galaxies exhibit a wide range of isophotal shapes and surface brightness profiles. There is an intrinsic uncertainty in inferring the 3D stellar luminosity density from the observed 2D isophotes on the sky. When stellar kinematics from spectroscopic observations are combined with photometric information, stronger constraints can be placed on the intrinsic 3D shapes of elliptical galaxies (e.g., Binney [21] and Franx, Illingworth, and de Zeeuw [99]). An idealized galaxy obeying exact axisymmetry would, by construction, have a regular surface brightness distribution without any isophotal twists and have perfectly aligned photometric and kinematic axes. Triaxial systems, on the other hand, can have isophotal twists, misaligned photometric and kinematic axes, and other spatially varying kinematic features absent in an axisymmetric system. This consideration led Binney [21] to argue that triaxiality is common among elliptical galaxies.

Since then, a more detailed picture has emerged. Elliptical galaxies with lower stellar mass ($M_* \lesssim 10^{11.5} M_\odot$) tend to exhibit properties typical of axisymmetry [e.g., 100, 20, 101,

102]. Comparatively, elliptical galaxies with higher mass ($M_* \gtrsim 10^{11.5} M_\odot$) typically exhibit photometric twists, slow or no rotation, and misalignments between the photometric and kinematic axes, suggesting triaxial intrinsic shapes [e.g., 103, 104, 105, 106, 27, 8, 107]. Thus, it is vital to understand the role of triaxiality in dynamical galaxy modeling, particularly in studying massive elliptical galaxies and their central black holes in the local universe.

The most massive SMBHs observed in the nearby universe lie in centers of some of the most massive nearby elliptical galaxies [88]. However, few triaxial SMBH mass ($M_{\rm BH}$) measurements have been published thus far, perhaps because of the complexity in orbital structures, high-dimensional parameter space, and the associated computational cost required to model stellar orbits in triaxial potentials. To date, all published $M_{\rm BH}$ measurements based on triaxial orbit modeling have been performed using the code initially presented in van den Bosch et al. [59]. This code was first applied to determine the intrinsic shapes and $M_{\rm BH}$ of two fast-rotating elliptical galaxies M32 and NGC 3379 [83]. In this work, M32 was found to be near oblate axisymmetry with $M_{\rm BH} = (2.4 \pm 1.0) \times 10^6 M_\odot$, fully consistent with $M_{\rm BH}$ from earlier axisymmetric models [47, 86, 50]. NGC 3379, on the other hand, was found to be moderately triaxial, and the inferred $M_{\rm BH} = (4 \pm 1) \times 10^8 M_\odot$ was double the value derived from axisymmetric models [53, 51]. In a subsequent application to the S0 galaxy NGC 3998 [67], the best-fit model was found to be moderately triaxial although oblate axisymmetry was not ruled out.

Feldmeier-Krause et al. [84] applied the van den Bosch et al. [59] code to the nuclear star cluster and SMBH at the Galactic center. The cluster shape was strongly triaxial, and the inferred $M_{\rm BH}$ was consistent within $1\,\sigma$ of the values inferred from the orbit of the S2 star [31, 108].

More recently, den Brok et al. [69] used the van den Bosch et al. [59] code to model PGC 046832. This galaxy exhibits dramatic twists, and the resulting models preferred strong variations in triaxiality. However, while axisymmetric models suggested a central black hole mass of $6 \times 10^9 M_\odot$, the triaxial models prefer models with no central black hole. Instead they report an upper bound on the central black hole mass of $2 \times 10^9 M_\odot$. This differs significantly from the value determined from axisymmetric models.

In addition to these published triaxial $M_{\rm BH}$ values, the van den Bosch et al. [59] code has been used to determine several $M_{\rm BH}$ in the nearly axisymmetric limit [70, 71, 72, 73, 74]. It has also been used to estimate the intrinsic triaxiality of galaxies under the assumption of a fixed $M_{\rm BH}$ [e.g., 59, 109, 110, 62, 63, 111, 65].

We have been revamping the van den Bosch et al. [59] code for a systematic study of the SMBHs and other mass components in the $\sim$ 100 most massive local early-type galaxies in the MASSIVE survey [88]. As a first step, we introduced a version of the code capable of achieving the exact axisymmetric limit [87, 78]. The original van den Bosch et al. [59] code was (intentionally) not built to respect axisymmetry, but it had been used to perform (nearly) axisymmetric orbit modeling, leading to unexplained inconsistencies when the resulting $M_{\rm BH}$ values were compared to those from axisymmetric orbit codes (e.g., Ahn et al. [74]). Our axisymmetrized version of the code has bridged this gap and now enables dynamical modeling of galaxies using stellar orbits that properly obey axisymmetry.

We applied our axisymmetrized code to NGC 1453, a fast-rotating elliptical galaxy in the MASSIVE survey, and obtained a significant detection of its SMBH with $M_{\rm BH} = (2.9 \pm 0.4) \times 10^9\ M_\odot$ [87]. Models without black holes were excluded at the 8.7σ level.

For clarity, we refer to the original code (which was unnamed) by the citation van den Bosch et al. [59], and refer to our versions as the TriOS (Triaxial Orbit Superposition) code.

In this paper, we move beyond the axisymmetric limit of Quenneville, Liepold, and Ma [78], and present a triaxial version of the TriOS code and a first application of this code. This triaxial TriOS code differs in a number of major ways from the original van den Bosch et al. [59] code. We have implemented these changes to correct a number of bugs and issues that we uncovered during extensive tests of the original code for triaxial potentials. As a start, we correct a major error in the orbit construction part of the code that incorrectly flips some velocity components for the tube orbits. Our tests indicate that for most viewing angles, correcting this mistake has a significant impact on the resulting orbital kinematics and galaxy model parameter recovery within the code. Other major changes include (i) modifying the acceleration table used for orbit integration to gain a significant speedup in runtime, (ii) resolving issues with insufficient orbit sampling that can result in spurious shape preferences, and (iii) using a more uniform mass binning scheme to eliminate frequent problems in satisfying mass constraints. Details of these changes are described in Section 3.4.

In addition to these code changes, we introduce a new set of shape parameters in this paper (Section 3.3) that are chosen to improve the efficiency of parameter searches in triaxial galaxy shapes and orientations. These parameters strike a balance between sampling in galaxy intrinsic shape and galaxy orientation, and result in fewer unrealistically flat galaxy shapes. To place these new parameters in context, we provide a summary (Section 3.2) of the parameters used in previous work to describe a triaxial galaxy's intrinsic and observed axis ratios, the relations of viewing angles and sky projections, and how an observed surface brightness is deprojected to obtain a 3D intrinsic shape within the TriOS code.

We apply our triaxial TriOS code to NGC 1453 in the final part of the paper (Section 3.5). Since triaxial modeling typically involves at least five parameters (three for shapes and at least two for mass parameters), we introduce an efficient new search strategy for sampling this multi-dimensional parameter space. This new strategy does not rely on direct grid searches used in previous orbit modeling studies. Instead, we apply nested Latin hypercube sampling to a 6D parameter space and are able to converge to a best-fit model for NGC 1453 with an order-of-magnitude fewer sample points. The resulting best-fit triaxial model is compared to the best-fit axisymmetric model from Liepold et al. [87].

3.2 Modeling a Triaxial Galaxy

In this section we summarize the information relevant for modeling a triaxial galaxy, e.g., coordinate systems, intrinsic and apparent shape parameters, viewing angles, and sky projections.

Intrinsic Shapes and Axis Ratios

To describe the 3D structure of a galaxy, we use a Cartesian coordinate system centered at the galaxy's nucleus, in which the x, y, and z axes are directed along the intrinsic major, intermediate, and minor axes of the galaxy, respectively. The z-axis is therefore the symmetry axis of an oblate axisymmetric galaxy, and the x-axis is the symmetry axis of a prolate axisymmetric galaxy.

It is convenient to use a different coordinate system to describe properties projected on the sky. We follow the standard practice and take the x' and y' axes of this coordinate system to be along the major and minor axes of the projected surface brightness distribution of a galaxy. The z' axis is along the line-of-sight.

We use a, b, c to denote the lengths of the three principal axes of a triaxial ellipsoidal isodensity surface, assuming $c \leq b \leq a$. We use a' and b' to denote the lengths of the (observed) major and minor axes of the projected ellipse on the sky. Four useful axis ratios are

$$p = \frac{b}{a}\,, \quad q = \frac{c}{a}\,, \quad u = \frac{a'}{a}\,, \quad q' = \frac{b'}{a'}\,, \tag{3.1}$$

where p is the intrinsic intermediate-to-major axis ratio, q is the intrinsic minor-to-major axis ratio, u represents a compression factor between the intrinsic major axis and the apparent major axis on the sky due to projection, and q' is the flattening of the projected shape. These quantities obey the inequalities

$$\begin{aligned} & 0 \leq c \leq b' \leq b \leq a' \leq a\,, \\ \text{or} \qquad & 0 \leq q \leq uq' \leq p \leq u \leq 1\,. \end{aligned} \tag{3.2}$$

The upper and lower limits of u correspond to the intrinsic major axis lying in the plane of the sky ($u = 1$ or $a' = a$) and the intrinsic intermediate axis lying in the plane of the sky ($u = p$ or $a' = b$), respectively.

The commonly used triaxiality parameter is

$$T = \frac{a^2 - b^2}{a^2 - c^2} = \frac{1 - p^2}{1 - q^2}\,, \tag{3.3}$$

which ranges between 0 for an oblate axisymmetric shape ($a = b$), and 1 for a prolate axisymmetric shape ($b = c$), with values between 0 and 1 indicating a triaxial shape.

Viewing Angles and Sky Projections

A line of sight between an observer and a galaxy is specified by two viewing angles (θ, ϕ), where θ and ϕ are the usual polar angles in the galaxy's intrinsic (x, y, z) coordinate system. Thus, $\theta = 0^\circ$ is for a line of sight along the intrinsic minor axis (i.e., a face-on view down the z-axis), and $\theta = 90^\circ$ is for lines of sight in the $x - y$ plane (i.e., an edge-on view with the intrinsic minor axis in the sky plane). Similarly, $\phi = 0^\circ$ is for lines of sight in the $x - z$ plane

(i.e., the intrinsic intermediate axis is in the sky plane), and $\phi = 90°$ is for lines of sight in the $y - z$ plane (i.e., the intrinsic major axis is in the sky plane).

Given a triaxial 3D density stratified on similar concentric ellipsoids, the viewing angle θ and ϕ are sufficient to project the 3D shape and determine the 2D projected coordinate system (x', y'). To de-project an observed 2D shape on the sky, however, a third angle, ψ, is needed to completely specify the intrinsic coordinate system. This third angle ψ specifies the remaining degree of freedom once θ and ϕ are fixed – a rotation of the galaxy around the line of sight. More precisely, ψ is defined as the angle between the y' axis, and the line defined by the intersection of the $x' - y'$ and $x - y$ planes. When $\psi = 0°$, the $x - y$ plane and $x' - y'$ plane intersect along the y' axis; when $\psi = 90°$, the $x - y$ plane and $x' - y'$ plane intersect along the x' axis.

Together, the three angles (θ, ϕ, ψ) uniquely specify the orientation of the intrinsic axes with respect to the projected axes. If the 3D density is stratified on similar concentric ellipsoidal surfaces, the axis ratios (p, q, u) of Equation (3.1) can be uniquely determined from the projected surface brightness and (θ, ϕ, ψ) using the equations from Appendix A of de Zeeuw and Franx [112].

Deprojecting Observed Surface Brightness

Within the TriOS code, the 3D stellar density distribution is described by a sum of multiple Gaussian components of varying widths and axis ratios using the Multi-Gaussian Expansion (MGE) scheme [113]. To determine these components, one first fits a 2D MGE to the observed surface brightness of the galaxy. Each MGE component is allowed to have its own projected flattening q' to account for radially varying ellipticity in the observed isophotes. In addition, each MGE component can have a different position angle (PA) to accommodate any observed isophotal twists.

In general, the deprojection of a 2D surface brightness distribution to give a 3D triaxial luminosity density is not unique. MGE is a parametric method of choosing one particular 3D density for a given 2D surface brightness and set of intrinsic axes. Non-parametric deprojection methods have also recently been developed for triaxial galaxies in de Nicola et al. [114], but the TriOS code is not yet capable of using these deprojections.

For a set of (θ, ϕ, ψ) that specifies the alignment of the galaxy's intrinsic principle axes (x, y, z), one can determine the deprojection of each MGE component that shares these principle axes (if a valid deprojection exists). This deprojection is unique due to the assumption that each 2D gaussian corresponds with a 3D gaussian density with similar concentric ellipsoidal surfaces of constant density. The axis ratios p and q of each deprojected MGE component can have their own values. The triaxiality parameter T, on the other hand, has the convenient property that it is identical for all MGE components when the components share the same PA (i.e., no isophotal twists).[1]

[1]This is valid as long as the line-of-sight does not lie in a principal plane of the triaxial shape. If it does, then all aligned 3D ellipsoids will have parallel or perpendicular PAs when viewed in projection, and

3.3 New Parameters for Triaxial Space Sampling

Prior practice

As discussed in Section 3.2, either (p, q, u) or (θ, ϕ, ψ) can be used to specify the shape of a triaxial galaxy and its sky projections. One can in principle search in either space when running orbit models to determine a galaxy's intrinsic shape and mass parameters. In practice, however, prior triaxial orbit modeling studies favored (p, q, u) over the angles. In these studies, the orbit models were typically run for a grid of regularly spaced values of (p, q, u) [e.g., 60, 83, 67, 75]. In a few other triaxial studies, u was fixed to some value close to 1 while the parameter search was conducted over p and q in a regular 2D grid [e.g., 110, 62, 63]. Since $u \sim 1$ corresponds to the intrinsic major axis lying close to the sky plane, these studies did not search over all allowed viewing angles.

The argument used by van den Bosch and van de Ven [60] for favoring conducting parameter searches in (p, q, u) rather than (θ, ϕ, ψ) is that a change in the angles can result in either a very small or very large change in axis ratios, depending on the angles being explored. We note, however, that the converse is also true: a change in the axis ratios can result in either a very small or very large change in the principal axes' alignment, depending on the values of these ratios. Two models with similar axis ratios, but viewed along very different lines of sight, can result in very different observables. An optimal sampling should consider both the intrinsic shape and the alignment of the line of sight.

Properties of new parameters

Here we propose a new set of variables to parameterize a galaxy's intrinsic triaxial shape and its sky projections. The advantages of conducting parameter searches in these variables over either (p, q, u) or (θ, ϕ, ψ) during triaxial orbit modeling will be discussed in Section 3.3.

For the first shape parameter, we choose the triaxiality parameter T (Equation 3.3). We define the next two parameters with forms analogous to T:

$$\begin{aligned} T &= \frac{a^2 - b^2}{a^2 - c^2} = \frac{1 - p^2}{1 - q^2}\,, \\ T_{\rm maj} &\equiv \frac{a^2 - a'^2}{a^2 - b^2} = \frac{1 - u^2}{1 - p^2}\,, \\ T_{\rm min} &\equiv \frac{b'^2 - c^2}{b^2 - c^2} = \frac{(uq')^2 - q^2}{p^2 - q^2}\,, \end{aligned} \tag{3.4}$$

where $T_{\rm maj}$ parameterizes the length of the projected major axis, a', relative to its allowed limits a and b, and $T_{\rm min}$ parameterizes the length of the projected minor axis, b', relative

differences in T cannot be inferred from differences in projected PA. We do not consider any models with lines-of-sight lying directly in the principal planes.

to its allowed limits b and c. It then follows from the inequalities in Equation (3.2) that $(T, T_{\rm maj}, T_{\rm min})$ form a unit cube, i.e.,

$$\begin{aligned} 0 \leq T \leq 1\,, \\ 0 \leq T_{\rm maj} \leq 1\,, \\ 0 \leq T_{\rm min} \leq 1\,. \end{aligned} \tag{3.5}$$

The limiting cases represented by each face of the unit cube has the following physical significance: (i) $T = 0$ and 1 correspond to oblate axisymmetric ($a = b$ or $p = 1$) and prolate axisymmetric ($b = c$ or $p = q$) shapes, respectively; (ii) $T_{\rm maj} = 0$ and 1 correspond to the intrinsic major axis lying in the sky plane ($a' = a$ or $u = 1$) and the intrinsic intermediate axis lying in the sky plane ($a' = b$ or $u = p$), respectively; (iii) $T_{\rm min} = 0$ and 1 correspond to the intrinsic minor axis lying in the sky plane ($b' = c$ or $uq' = q$) and the intrinsic intermediate axis lying in sky ($b' = b$ or $uq' = p$), respectively. While both the $T_{\rm maj} = 1$ and $T_{\rm min} = 1$ planes correspond to the intrinsic intermediate axis in the sky plane, they represent two complementary ranges of viewing angles such that b is equal to the projected *major* axis a' for $T_{\rm maj} = 1$, whereas b is equal to the projected *minor* axis b' for $T_{\rm min} = 1$.

Equation (3.4), along with the requirement that $q > 0$, yields the inequality

$$\frac{(1-T)T_{\rm min}}{1 - TT_{\rm maj}} < q'^2\,, \tag{3.6}$$

implying that for an observed axis ratio q' on the sky, only the $(T, T_{\rm maj}, T_{\rm min})$ region satisfying the inequality has valid deprojections. When the projected shape is flattened ($q' < 1$), some models within the unit cube will result in negative (and thus invalid) values of the squared minor axis length, c^2. This volume surrounds the line $(T, T_{\rm maj}, T_{\rm min}) = (T, 1, 1)$, which does not have a valid deprojection for any flattened projected shape.

Relating $(T, T_{\rm maj}, T_{\rm min})$ to old parameters

While Equations (3.4) relate our new parameters to (p, q, u), it is often useful to do the inverse and convert a given set of $(T, T_{\rm maj}, T_{\rm min})$ to (p, q, u). To do so, we use these sequential expressions

$$\begin{aligned} 1 - q^2 &= \frac{1 - q'^2}{1 - (1-T)T_{\rm min} - q'^2 TT_{\rm maj}}\,, \\ 1 - p^2 &= T(1 - q^2)\,, \\ 1 - u^2 &= T_{\rm maj}(1 - p^2)\,. \end{aligned} \tag{3.7}$$

For a given set of $(T, T_{\rm maj}, T_{\rm min})$, these equations define the deprojection from an observed MGE component with flattening, q', to its 3D shape parameters, (p, q, u).

Similarly, it is useful to convert $(T, T_{\rm maj}, T_{\rm min})$ to the angles (θ, ϕ, ψ):

$$\begin{aligned} \cos^2\theta &= T_{\rm min}(1 - T\,T_{\rm maj})\,, \\ \tan^2\phi &= \frac{1 - T_{\rm maj}}{T_{\rm maj}} \frac{1 - T_{\rm min}}{1 - T_{\rm min}(1-T)}\,, \\ \tan^2\psi &= \frac{[1 - T_{\rm min}(1-T)]\,(1 - T\,T_{\rm maj})(1 - T_{\rm min})}{T^2(1 - T_{\rm maj})T_{\rm maj}\,T_{\rm min}}\,. \end{aligned} \tag{3.8}$$

We choose to use the branch where $0° \le \theta \le 90°$, $0° \le \phi \le 90°$, and $90° \le \psi \le 180°$, though other equivalent branches exist as well.[2] The inverse expressions relating $(T, T_{\rm maj}, T_{\rm min})$ and (θ, ϕ, ψ) are given in Appendix D.

Equations (3.7) and (3.8), as well as Equations (D.1) and (D.2), follow directly from the definitions in Equation (3.4), and the general expressions for the deprojection of a triaxial density that is stratified on similar, concentric ellipsoids [e.g., 112, discussed further in appendix D]. Furthermore, since Equation (3.8) and its inverse Equation (D.2) make no reference to the observed flattening, the same set of values $(T, T_{\rm maj}, T_{\rm min})$ can be used for a density that is composed of multiple such components with different flattening values. Thus, $(T, T_{\rm maj}, T_{\rm min})$ and (θ, ϕ, ψ) are simply different parameterizations of the same space. Equations (3.7) and (3.8), along with the equations listed in Appendix D, make no reference to the MGE formalism and are applicable to any triaxial system that meets these conditions. The existence and uniqueness of a valid deprojection are not affected by the choice of shape space parameterization outside the principal planes.

To illustrate the properties of $T_{\rm maj}$ and $T_{\rm min}$, we plot a set of lines of constant $T_{\rm maj}$ and $T_{\rm min}$ in a galaxy's intrinsic coordinate system x, y, and z in Figure 3.1. The corner points $(T_{\rm maj}, T_{\rm min}) = (1, 0)$, $(0, 0)$, and $(0, 1)$ correspond to viewing angles along the short, intermediate, and long axes, respectively. The point $(T_{\rm maj}, T_{\rm min}) = (1, 1)$ represents a line of sight lying along the line $\theta = \eta = \tan^{-1}(\sqrt{T/(1-T)})$ in the $x - z$ plane, which only results in a valid model for round projected shapes. For flattened shapes, there are no valid deprojections for lines of sight within a solid angle surrounding this direction. This non-deprojectable region increases in size, as the projected shape becomes flatter.

Advantages of $T, T_{\rm maj}$ and $T_{\rm min}$

The parameters T, $T_{\rm maj}$, and $T_{\rm min}$ have a number of desirable properties. First, as Figure 3.1 illustrates, $T_{\rm maj}$ and $T_{\rm min}$ change relatively uniformly with the line-of-sight direction. This is in contrast to the axis ratio space, (p, q, u), in which tiny changes can result in large differences in the angles. For example, models with $p = 0.99$ and a fixed q would undergo a $90°$ rotation in ϕ when u is varied from 0.99 to 1.

Similarly, the galaxy shape varies much more uniformly with $(T, T_{\rm maj}, T_{\rm min})$ than with (θ, ϕ, ψ). Again, tiny changes in the latter can result in large differences in galaxy shape. For

[2] For instance, if one prefers $0° \le \psi \le 90°$ and $0° \le \theta \le 90°$, then ϕ obeys $-90° \le \phi \le 0°$.

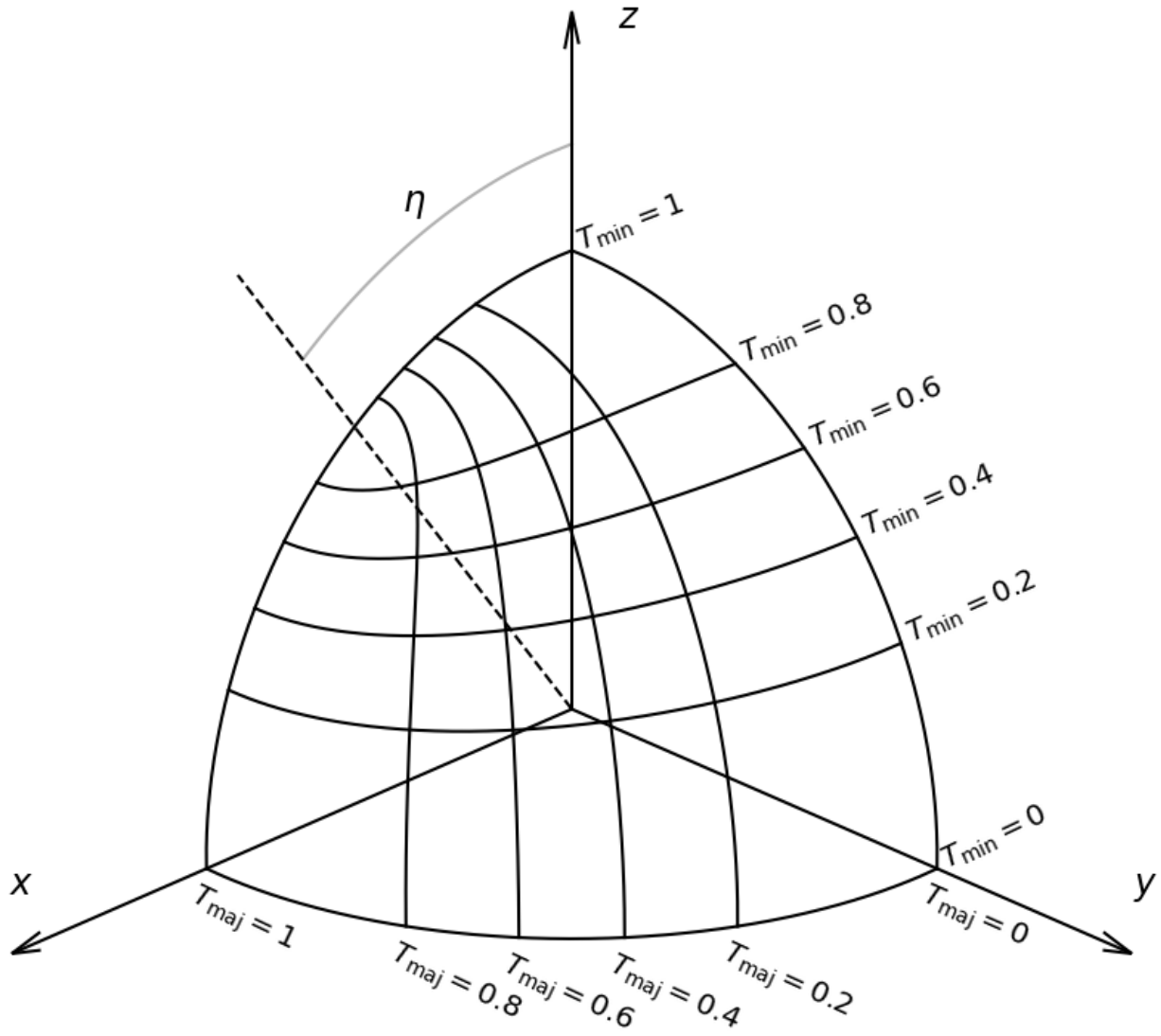

Figure 3.1: Isocontours of the new shape parameters, $T_{\rm maj}$ and $T_{\rm min}$, in a galaxy's coordinate system, where the x, y, and z axes are chosen to be the intrinsic major, intermediate, and minor axes, respectively. The triaxiality parameter, T, is assumed to be 0.35 here. The parameters $T_{\rm maj}$ and $T_{\rm min}$ are seen to change relatively uniformly with the line-of-sight direction, resulting in fewer unrealistically flattened models near non-deprojectable regions (see text).

example, when an observed surface brightness (without isophotal twists) is deprojected into a 3D ellipsoidal shape with principle axes defined by $(\theta, \phi, \psi) = (89°, 45°, 90°)$, Equation (A2) shows that the resulting 3D shape has $T = 0$, i.e., it is oblate axisymmetric. As ψ is increased from 90° by only $\sim 1°$, however, the deprojected shape varies drastically, with oblate axisymmetry at $\psi = 90°$ to prolate axisymmetry at $\psi \sim 91°$, with the full range of triaxialities lying in between. From Equation (A2) with $\phi = 45°$, we find prolate axisymmetry ($T = 1$) to occur when $\psi - 90° = (90°/\pi) \arctan\left(2\cos\theta/\sin^2\theta\right)$ on our chosen branch. As θ approaches 90°, the value of ψ that gives prolate axisymmetry approaches 90°. For $\theta = 89°$ (and $\phi = 45°$), prolate axisymmetry occurs at $\psi = 90.99985°$.

The behavior in the example above arises from coordinate singularities in the (θ, ϕ, ψ) space. When the line-of-sight is chosen to lie in a principal plane (i.e., $\cos(\theta) = 0, 1$ or $\sin(2\phi) = 0$), it is impossible for continuous photometric twists to arise in projection as triaxiality is varied. One consequence of this is that the only valid values of ψ are 0° or 90°, meaning it is no longer an independent parameter. Thus, (θ, ϕ, ψ) are insufficient to fully specify the 3D projection. The parameters $(T, T_{\rm maj}, T_{\rm min})$, on the other hand, have no such singularity. In the above example, the proximity of the chosen value of θ to 90° causes the rapid shift in shape with ψ.

Another desirable property of $T_{\rm maj}$ and $T_{\rm min}$ is that, similar to T (see Section 3.2), they do not vary among MGE components with different axis ratios, so long as there are no isophotal twists.

This invariant property can be explained by identifying $T_{\rm maj}$ and $T_{\rm min}$ as the shifted and rescaled versions of the conical coordinates, $\mu_{\rm pro}$ and $\nu_{\rm pro}$ within the galaxy's intrinsic coordinate system [115], where $\mu_{\rm pro} = a'^2$ and $\nu_{\rm pro} = b'^2$. Since the coordinate surfaces of $\mu_{\rm pro}$ and $\nu_{\rm pro}$ are the same for all MGE components, the shifted and scaled quantities $T_{\rm maj}$ and $T_{\rm min}$ do not vary between components.

The advantages of T, $T_{\rm maj}$, and $T_{\rm min}$ are especially clear for systems not far from axisymmetry. Towards oblate axisymmetry ($T \approx 0$), we have $T_{\rm min} \approx \cos^2\theta$ and $T_{\rm maj} \approx \cos^2\phi$. Thus, a uniform sampling in $\sqrt{T_{\rm min}}$ and $\sqrt{T_{\rm maj}}$ will result in a nearly uniform sampling in the cosines of the inclination and the azimuthal angle. The same behavior holds towards prolate axisymmetry ($T \approx 1$) since the roles of $T_{\rm maj}$ and $T_{\rm min}$ are simply switched if the x and z axis labels are interchanged. Thus, for nearly axisymmetric galaxies, a uniform sampling in $(T, \sqrt{T_{\rm maj}}, \sqrt{T_{\rm min}})$ results in fewer unrealistically flattened models.

3.4 Code Corrections and Improvements

In this section, we describe the key corrections, improvements, and speedups made to the van den Bosch et al. [59] code. See Section 4 of Quenneville, Liepold, and Ma [78] for other general changes that we had implemented (regardless of axisymmetry).

Position	Long-axis tube	Short-axis tube	Intermediate-axis tube
(x, y, z)	(v_x, v_y, v_z)	(v_x, v_y, v_z)	(v_x, v_y, v_z)
$(-x, y, z)$	$(-v_x, v_y, v_z)$	$(v_x, -v_y, \boldsymbol{-v_z})$	$(v_x, \boldsymbol{-v_y}, -v_z)$
$(x, -y, z)$	$(\boldsymbol{-v_x}, v_y, -v_z)$	$(-v_x, v_y, \boldsymbol{-v_z})$	$(v_x, -v_y, v_z)$
$(x, y, -z)$	$(\boldsymbol{-v_x}, -v_y, v_z)$	$(v_x, v_y, -v_z)$	$(-v_x, \boldsymbol{-v_y}, v_z)$
$(-x, -y, z)$	$(\boldsymbol{v_x}, v_y, -v_z)$	$(-v_x, -v_y, v_z)$	$(v_x, \boldsymbol{v_y}, -v_z)$
$(-x, y, -z)$	$(\boldsymbol{v_x}, -v_y, v_z)$	$(v_x, -v_y, \boldsymbol{v_z})$	$(-v_x, v_y, -v_z)$
$(x, -y, -z)$	$(v_x, -v_y, -v_z)$	$(-v_x, v_y, \boldsymbol{v_z})$	$(-v_x, \boldsymbol{v_y}, v_z)$
$(-x, -y, -z)$	$(-v_x, -v_y, -v_z)$	$(-v_x, -v_y, -v_z)$	$(-v_x, -v_y, -v_z)$

Table 3.1: Corrected mirroring scheme of the three types of tube orbits in our TriOS code. Boldfaced velocity components have the opposite signs from the original scheme in Table 2 of van den Bosch et al. [59]. These components were flipped incorrectly in the original code.

Correct orbital mirroring mistakes

The TriOS code is written for a static triaxial potential that is symmetric under reflection along each of the three principal axes of a triaxial system. Under this assumption, any orbital property only needs to be calculated in one octant of the orbit space; it can then be "mirrored" into the other seven octants by symmetry.

Taking advantage of this symmetry, the code initializes orbits in only one octant ($x, y, z > 0$) and integrates only these orbits. Seven additional copies of each orbit are then created by simply mirroring along the three axes. The recipe for how to flip the signs of the velocity components is given in Table 2 of van den Bosch et al. [59]. The exact procedure depends on whether the orbit is a short-axis tube, long-axis tube, or box. These orbits are classified as follow: throughout its trajectory, an orbit is labelled a box orbit if all three components of its angular momentum (L_x, L_y, L_z) change sign, and a tube orbit if exactly one component of angular momentum maintains its sign. The tube orbits are further classified according to the angular momentum component that maintains its sign, i.e., a long-axis (i.e. x-axis) tube maintains the sign of its L_x, an intermediate-axis (y-axis) tube maintains the sign of L_y, and a short-axis (z-axis) tube maintains the sign of L_z. Orbits that don't fall into the tube or box orbit classifications are flipped in the same way as box orbits.

We discovered that the tube orbits are incorrectly flipped for four of the eight octants in Table 2 of van den Bosch et al. [59]. We indicate the incorrect components in boldface and give the corrected expressions in Table 3.1. The mistakes are such that the mirrored positions and velocities are inconsistent with one another, and the two do not combine to give a valid trajectory. A consequence of these mistakes is that the magnitude of each component of $\vec{L}$ is not always preserved by the mirroring, as it should be, and the resulting $|\vec{L}|$ is also not preserved. For instance, for the short-axis tube flip, the original recipe would change the amplitudes of L_x and L_y for 4 of the 8 copies, and the resulting total L would not be

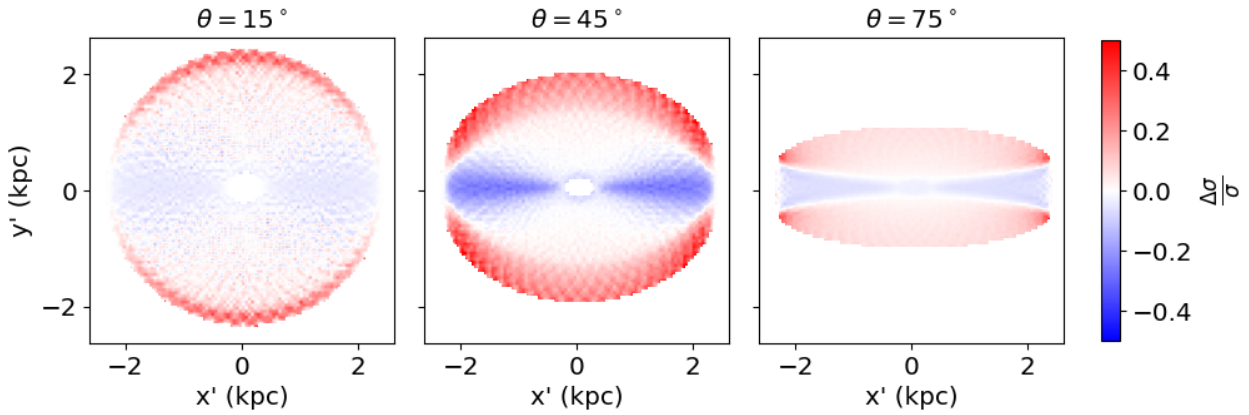

Figure 3.2: Illustration of the impact of the incorrect mirroring scheme in the van den Bosch et al. [59] code. We plot the fractional error between the incorrect and corrected schemes (see Table 1) in the kinematic map of the line-of-sight velocity dispersion, σ, for a single orbit. The orbit is chosen from the $x-z$ start space of a triaxial model with $T = 6\times10^{-6}$ for NGC 1453, but it is representative of typical short-axis tubes in a triaxial potential. Each panel represents a different viewing inclination angle θ. The fractional error is largest near $\theta = 45°$, reaching beyond 50% for some parts of the orbit.

preserved. Similarly, L_y and L_z are incorrect for 4 copies of the long-axis tubes, and L_x and L_z are incorrect for 4 copies of the intermediate-axis tubes.

To illustrate the impact of the incorrect orbital flips, we plot the error in the line-of-sight velocity dispersion, σ, for a single short-axis tube orbit for three different viewing angles in Figure 3.2. We first integrate the trajectory of this orbit within the potential and then compute the 7 mirrored copies using the original and corrected flips in Table 3.1. The fractional difference in the projected σ between the two schemes is then plotted for three different values of viewing inclination angle θ. The errors vary across the plane of the sky and exceed 50% for $\theta = 45°$. For this orbit, the incorrect flip scheme tends to under-predict σ along the galaxy's projected major axis and over-predict σ near the edges. The orbit shown in Figure 3.2 is typical of short-axis tubes in triaxial potentials. Long-axis tube orbits exhibit similar error patterns when the appropriate axis labels are switched. While the pattern of velocity dispersion error is different for each orbit, systematic errors with magnitudes of $10\%-100\%$ are typical, with peak errors of over 1600% in some cases for orbital inclinations near 45°.

To assess further the impact of the incorrect flips, we perform full orbit modeling for a grid of triaxial models for NGC 1453 using the original and then the corrected scheme.

Overall, when the correct flips are used, we find that χ^2 is lowered by a wide range of values depending on the triaxiality and viewing angles. For instance, the value of χ^2 can decrease by more than 100 for strongly triaxial models, while it can change by less than 5 or even increase slightly for other models. The overall χ^2 landscape is therefore significantly altered by our corrections.

Due to the symmetry of the tube orbits, the errors in the orbital flips can cancel out when the galaxy is viewed along a principal axis. Nearly axisymmetric models that are viewed edge-on or face-on will be similarly unaffected. Outside of these special cases, the orbital kinematics have significant errors. The incorrect flips were not used in our axisymmetric modeling of NGC 1453 [87, 78] since we used an axisymmetrization procedure in place of the flips in the TriOS code.

The discussion above is relevant only for tube orbits. For box orbits, we find the flips given in Table 2 of van den Bosch et al. [59] to be correct. However, in addition to this set of 8 mirrored orbits, we choose to include 8 more orbits for each point in the stationary start space (defined in section 3.4) that correspond to enforcing time reversal symmetry for the box orbits. This addition ensures that box orbits have the expected even parity in their line-of-sight velocity distributions (LOSVDs). In the cases that we have examined, these orbits already have small enough odd LOSVD components that this change makes very little difference.

Modify acceleration table for significant speedup

In order to speed up orbital integration, the orbit code pre-computes a lookup table of acceleration values over a spatial grid and performs a trilinear interpolation to closely approximate the true acceleration. If an orbit passes outside the radial range of this grid, the acceleration is then computed from scratch, which is multiple orders of magnitude slower than interpolating values from the lookup table. It is therefore prudent to choose the extent of the grid wisely because even a small number of orbits passing outside the table's coverage can dominate the total runtime and unnecessarily increase the computation time of the entire orbit library.

We have noticed that some orbits can indeed pass outside the radial range used in the original code and result in a significant slow down. To eliminate this situation, we have made a simple modification to the radial range used for the acceleration table. In van den Bosch et al. [59], the acceleration is pre-computed over a grid spanning the radial range

$$\begin{aligned} r_{\rm interp,min} &= \min\left[0.1 \times \min\left(\sigma_i'\right), 0.01\, r_{\rm min}\right], \\ r_{\rm interp,max} &= \max\left[6 \times \max\left(\sigma_i\right), 1.05\, r_{\rm max}\right], \end{aligned} \tag{3.9}$$

where σ_i' is length of the semi-major axis of the ith projected MGE component, σ_i is the length of the semi-major axis of the corresponding intrinsic MGE component, and $r_{\rm min}$ and $r_{\rm max}$ are the innermost and outermost orbital equipotential radii in the model. Thus, the lowest and highest energy orbits included in the model have energies $\Phi(x = r_{\rm min}, y = 0, z = 0)$ and $\Phi(x = r_{\rm max}, y = 0, z = 0)$, where Φ is the gravitational potential of the model.

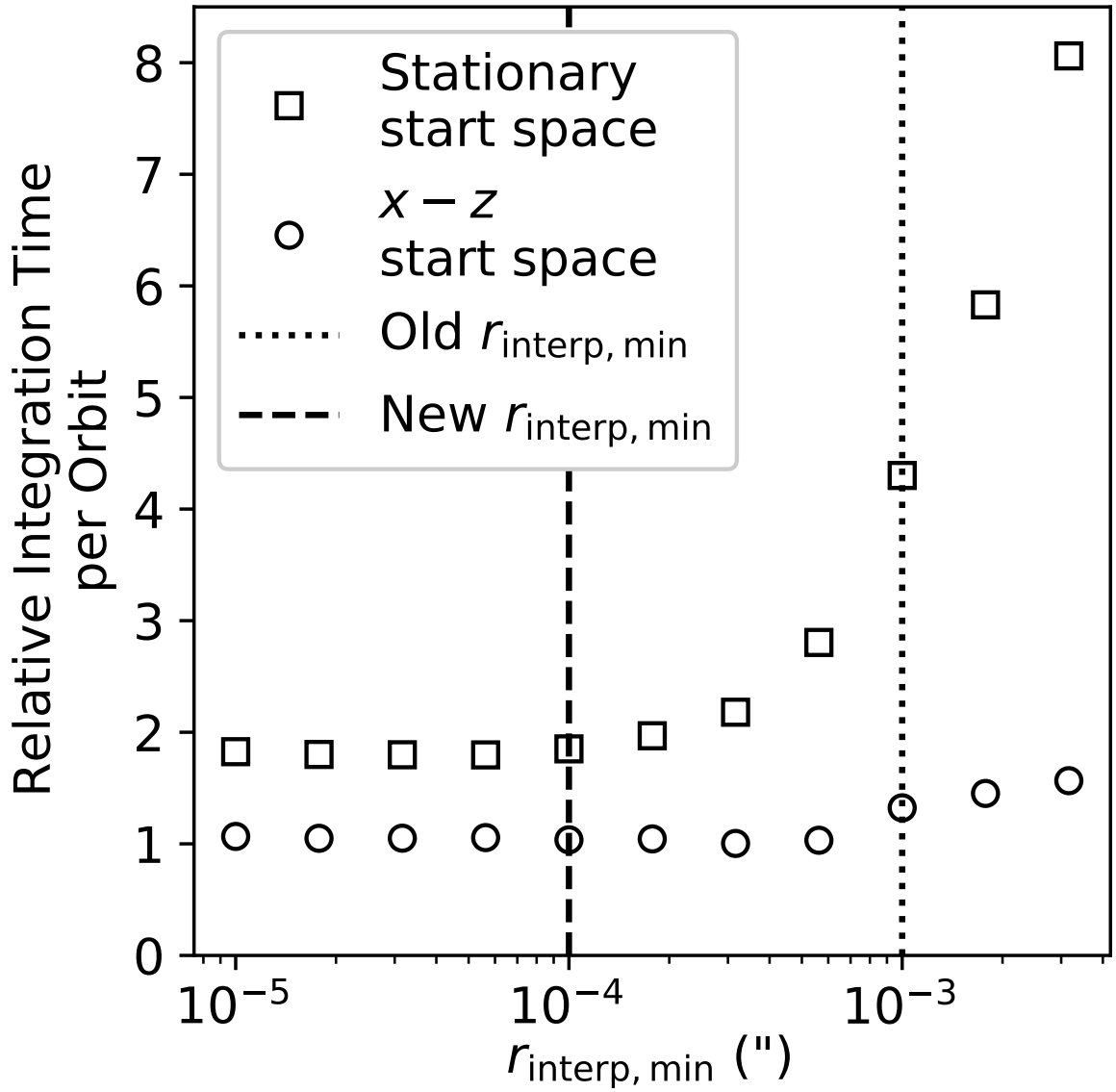

Figure 3.3: Average orbital integration time (per orbit) as a function of the inner interpolation radius, $r_{\mathrm{interp,min}}$, used to tabulate the accelerations. The stationary start space contains mostly box orbits that pass near the galaxy center. The box orbit integration time increases drastically with $r_{\mathrm{interp,min}}$, and the value used in the van den Bosch et al. [59] code is typically not small enough to minimize the integration time.

In practice, we find that the second conditions in Equation (3.9) typically determine the range of the acceleration table, i.e., $r_{\rm interp,min} = 0.01\,r_{\rm min}$ and $r_{\rm interp,max} = 1.05\,r_{\rm max}$. The outer boundary is never exceeded because energy conservation prevents orbits from passing outside $r_{\rm max}$ and therefore $r_{\rm interp,max}$. The inner boundary of $r_{\rm interp,min} = 0.01\,r_{\rm min}$, however, can be problematic because centrophilic box orbits can pass well within $0.01\,r_{\rm min}$. The `DOP853` Runga-Kutta integrator in the TriOS code uses adaptive timesteps, tuning them to minimize errors in the position and velocity between timesteps. In this scheme many acceleration evaluations are required in regions of the trajectory where the timestep is smaller, namely, when the trajectory passes closest to the central black hole where the orbits are most likely to reach below $0.01\,r_{\rm min}$. The fraction of acceleration evaluations within this boundary is somewhat model-dependent and may be higher when box orbits are launched from well within the SMBH's sphere of influence because the potential felt by those orbits is largely spherical and supportive of highly centrophilic box orbits. For a typical case of $r_{\rm min} = 0.1''$ and $r_{\rm interp,min} = 0.01\,r_{\rm min} = 0.001''$, we find as many as a sixth of the acceleration evaluations during the box orbit integrations to lie outside the lookup table. This minority of acceleration evaluations take up more than 50% of the total time when constructing the orbit library.

To enable a more efficient use of the acceleration table, we choose to decouple $r_{\rm interp,min}$ and $r_{\rm interp,max}$ from $r_{\rm min}$ and $r_{\rm max}$ which are used to determine the range of orbital energy sampling. When $r_{\rm interp,min}$ is allowed to be smaller than $0.01\,r_{\rm min}$, we find the total time to integrate orbits can be reduced by a factor of a few, with a negligible change in accuracy. This speed-up is illustrated in Figure 3.3. As the acceleration table is extended to smaller radii, fewer orbits fall outside the radial coverage of the table, and the average integration time for box orbits drops significantly with decreasing $r_{\rm interp,min}$. For the example shown in Figure 3.3, choosing $r_{\rm interp,min} \sim 0.0001''$ would reduce the orbit integration time by a factor of $\gtrsim 2$ compared with the original setting of $r_{\rm interp,min} = 0.01\,r_{\rm min} = 0.001''$. Since energy conservation prevents orbits from passing outside $r_{\rm max}$, setting $r_{\rm interp,max}$ to be slightly larger than $r_{\rm max}$ minimizes the integration time while maximizing the interpolation accuracy.

Since we don't typically vary the interpolation boundaries by more than 1 dex, the density of points in the interpolation grid does not change dramatically, and we find that the accuracy of the interpolated potential is sufficient. However, if the boundaries are changed more drastically, the number of radial interpolation points should be adjusted to maintain the desired accuracy.

Resolve issues with insufficient orbit sampling

The TriOS code samples orbit initial conditions from two separate spaces, referred to as start spaces [23, 59]. In the first start space ("stationary start space"), all orbits start from rest on the equipotential surface for a given energy. This start space contains only box, box-like, and chaotic orbits.

The second start space ("$x-z$ start space") contains mainly tube orbits and samples orbits in the $x-z$ plane, with velocity vectors pointing along the y-axis. As illustrated in

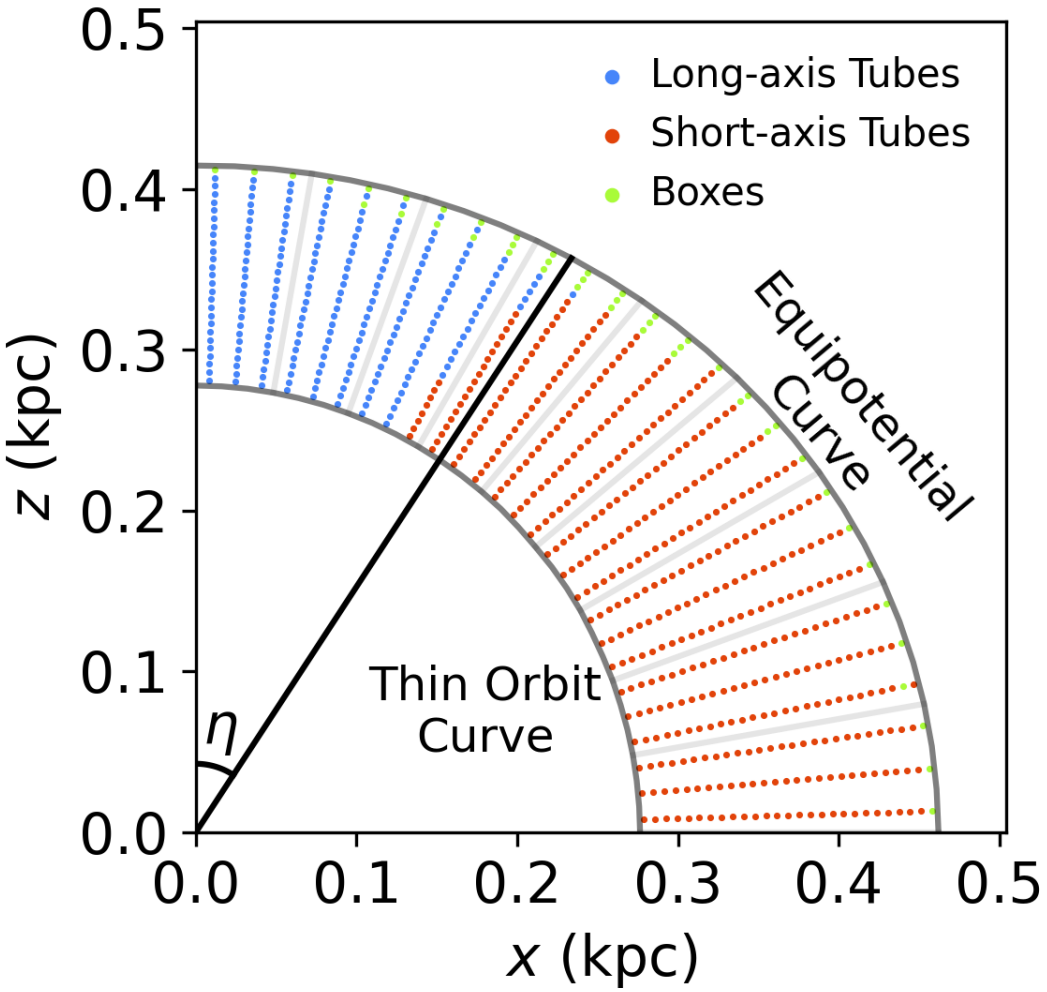

Figure 3.4: An example of the initial orbit locations in the $x - z$ start space for a single energy value in the triaxial TriOS code. Orbits are launched from within the thin-orbit curve (inner grey arc) and equipotential curve (outer grey arc). The orbit initial conditions are sampled with $N_{\mathrm{I}_2} = 9$ radial rays uniformly spaced in the polar angle from the z-axis to the x-axis, $N_{\mathrm{I}_3} = 9$ points along each ray, and $N_{\mathrm{dither}} = 3$ to further improve the sampling, resulting in a total of 27×27 orbits. Each of the 27×27 color dots indicates the initial locations of an orbit (color coded by the type of orbits). The black line at angle η (see text) approximates the boundary between long-axis and short-axis tube orbits within this start space. Model χ^2 values are sensitive to the alignment between the angle η and orbit cell boundaries.

Figure 3.4, orbits of a given energy in this space are sampled over the region bounded by the equipotential and thin-orbit curves. Typically, $N_{\mathrm{I}_2} = 9$ rays of orbits are sampled uniformly in polar angles from 0 to $\pi/2$ in the positive x and z quadrant; along each ray, $N_{\mathrm{I}_3} = 9$ orbits are uniformly spaced between thin-orbit curves and equipotential curve. Additionally, the code allows for dithering, where orbits with N_{dither} adjacent initial conditions in each dimension are integrated and then bundled together to form each of the 9×9 orbits in order to improve phase space sampling. Figure 3.4 illustrates the case of $(N_{\mathrm{I}_2}, N_{\mathrm{I}_3}, N_{\mathrm{dither}}) = (9, 9, 3)$, where 27×27 tube orbits are launched in the positive quadrant of the $x - z$ start space for a given energy.

For a triaxial model, the short-axis tubes (red points in Figure 3.4) and long-axis tubes (blue points) occupy two regions of the $x - z$ start space separated by the focal curve. As derived in Appendix A of Quenneville, Liepold, and Ma [78], the focal curve is roughly approximated by a line at angle

$$\eta = \tan^{-1} \sqrt{\frac{T}{1 - T}} \,. \tag{3.10}$$

Thus, as T increases from 0 to 1, the focal curve moves smoothly from the z-axis to the x-axis, and the composition of the tube orbits changes from being all short-axis tubes (for an oblate axisymmetric potential) to all long-axis tubes (for a prolate axisymmetric potential).

When orbits are well sampled, model properties such as the goodness-of-fit (χ^2) should vary smoothly as η (and hence T) is varied. In our test runs for NGC 1453, however, we find that on top of a smooth variation, χ^2 varies periodically with T with a frequency matching the spacing between dithered orbits, $(\pi/2)/N_{\mathrm{I}_2}$, resulting in multiple spurious local minima at different values of T. Further testing reveals that these local minima arise from insufficient orbit sampling: as T increases, the focal curve approximated with η crosses rays of orbits in a periodic manner, resulting in the artificial oscillations in χ^2 with that same period. Since the periodic behavior is coherent as other model parameters are changed, it can have a significant impact on the recovered value of T and its uncertainty. Other parameter values are mainly impacted through their correlations with T.

We are able to eliminate the spurious oscillations in χ^2 vs. T by increasing N_{I_2}, which increases the number of radial rays in the $x - z$ start space and therefore improves the sampling in the polar angle. For the models presented in Section 3.5, we find that increasing N_{I_2} from the default value of 9 to 15 and beyond removes the oscillations and also yields convergent results. We choose $N_{I_2} = 18$ for the $x - z$ start space.

We do not find similar issues for the other start space. Nonetheless, we increase N_{I_2} to 18 for the stationary start space as well so as to maintain equal sizes for the tube and box orbit libraries. In summary, we use $(N_E, N_{I_2}, N_{I_3}, N_{\mathrm{dither}}) = (40, 18, 9, 3)$ for both start spaces. This results in a total $40 \times 18 \times 9 \times 3^3 \times 3 = 524,880$ integrated orbits in each galaxy model, where the last factor of 3 accounts for the 3 orbit libraries (the $x - z$ start space, its time-reversed copy, and the stationary start space).

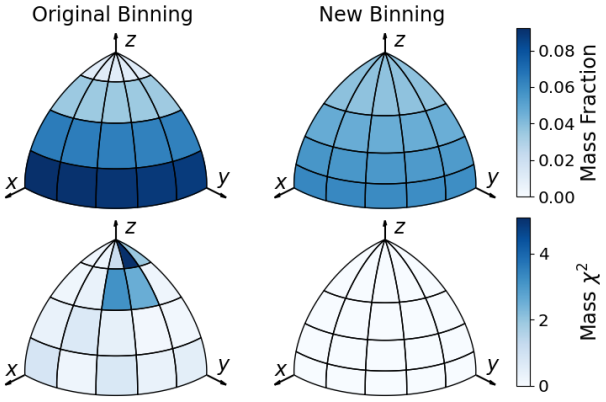

Figure 3.5: Comparison of the original (left) and new (right) mass binning scheme in the TriOS code. The top row shows that the bins near the $x-y$ plane contain far more mass than the bins near the z axis due to the significant difference in bin volume in the original scheme (top left). Our new binning scheme evens out the mass considerably (top right). The color scale here indicates the fraction of mass that falls within a given angular bin, summed over radius. The bottom row shows an example of the resulting χ^2 in the mass fits for a triaxial galaxy for the two binning schemes. The color scale here indicates χ^2 from attempting to fit a particular mass model, summed over radius. Only the 3D mass distribution is fit, with an error of 1% assumed on each bin. The most significant contributions to the mass χ^2 are from bins near the z-axis that contain very little mass. The triaxial mass model shown here has $M_{\rm BH} = 2.9 \times 10^9 M_\odot$, $M^*/L_{\rm F110W} = 2.0$, $T = 0.10$, $q = 0.96q'$, $T_{\rm maj} = 0.95$, and $T_{\rm min} = 0.12$.

Improve intrinsic mass binning scheme

In addition to kinematic constraints, the TriOS code enforces self-consistency of the mass model by requiring that the orbital weights be chosen to reproduce an input mass distribution (e.g., deprojected surface brightness profile of a galaxy). This is done by binning the mass in spherical coordinates (r, θ, ϕ), and requiring that the mass in each bin be reproduced to within a pre-specified precision (typically 1%). van den Bosch et al. [59] uses linearly spaced bins between 0° and 90° for θ and ϕ, and logarithmically spaced bins between $r_{\rm min}$ and $r_{\rm max}/2$ for r, where $r_{\rm min}$ and $r_{\rm max}$ are the innermost and outermost equipotential radii discussed in Section 3.4.

In the axisymmetrized TriOS code [78], we changed the radial binning scheme above to ensure sufficient orbits are used to represent the innermost and outermost mass bins. During our subsequent tests for triaxial systems, however, we noticed occasional problems with mass misfits in which a handful mass bins would have difficulty satisfying the 1% precision and/or contribute disproportionately high values to the total χ^2 of the galaxy model under examination. We are able to trace the problem to uneven bin sizes in θ used

in the original code: the bins near the poles contained much less mass, as shown in the left panel of Figure 3.5. Because of this, the mass near the z axis was subject to much more stringent constraints than elsewhere, leading to frequent difficulties in satisfying the 1% fitting criterion. Even in the absence of kinematic constraints, spurious variations would arise in the χ^2 landscape, as illustrated in the right panel of Figure 3.5. The more oblate ($T \lesssim 0.1$) and round ($q \gtrsim 0.9q'$) systems are more prone to this issue.

We find that this mass misfitting problem can be easily resolved by using mass bins linearly spaced in $\cos(\theta)$ and ϕ, rather than in θ and ϕ. The resulting bins at a given radius then occupy the same volume, and the mass in each bin is much more uniform, with the bin-to-bin variations representing the galaxy's intrinsic deviation from spherical symmetry. Correspondingly, the pre-specified mass constraint criterion is enforced more uniformly.

For clarity, we have chosen to illustrate the mass misfitting issue in Figure 3.5 without imposing any kinematic constraints. When kinematic constraints are added in full orbit modeling (see Section 3.5), the total χ^2 returned by the code includes contributions from fits to the masses as well as kinematics. In this case, models with significant mass misfits due to uneven binning schemes would have disproportionately larger χ^2 values, leading to potential biases in the recovered galaxy parameters.

3.5 Triaxial Orbit Models of NGC 1453

NGC 1453

We apply the updated TriOS code described in the previous section to NGC 1453, a massive elliptical galaxy targeted by the MASSIVE survey [88]. In Liepold et al. [87], we performed orbit modeling of NGC 1453 using the axisymmetrized TriOS code. We refer the reader to that paper for a detailed description of the input kinematic and photometric data. In brief, the stellar kinematics are measured over 135 spatial bins from our high-spatial resolution Gemini GMOS IFS data [116, 107] and wide-field McDonald Mitchell IFS data [103, 104, 105]. The first eight Gauss-Hermite moments are measured from the IFS spectra and used to constrain the stellar LOSVD in each kinematic bin; see Figure 4 of Liepold et al. [87].

The MGE components representing the galaxy's mass distribution (see Section 3.2) are obtained from deprojections of our *HST* WFC3 photometry [8]. Here we use the same input data but relax the assumption of axisymmetry in the orbit models. In order to ensure that all trajectories within the model are representative of their equilibrium distributions, we integrate each orbit in the $x-z$ start space for 2000 times the orbital period for a thin tube orbit of the same energy. For orbits in the stationary start space, we integrate for 200 times the orbital period, as is typical of previous studies using the van den Bosch et al. [59] code.

Due to the regular isophotes of NGC 1453 (Figure 5 of Liepold et al. [87]), we use the same PA for all MGE components and do not model isophotal twists. This is a common simplifying assumption [e.g., 83, 67, 84] and it enables us to explore the galaxy's shape using the new scheme outlined in Section 3.3.

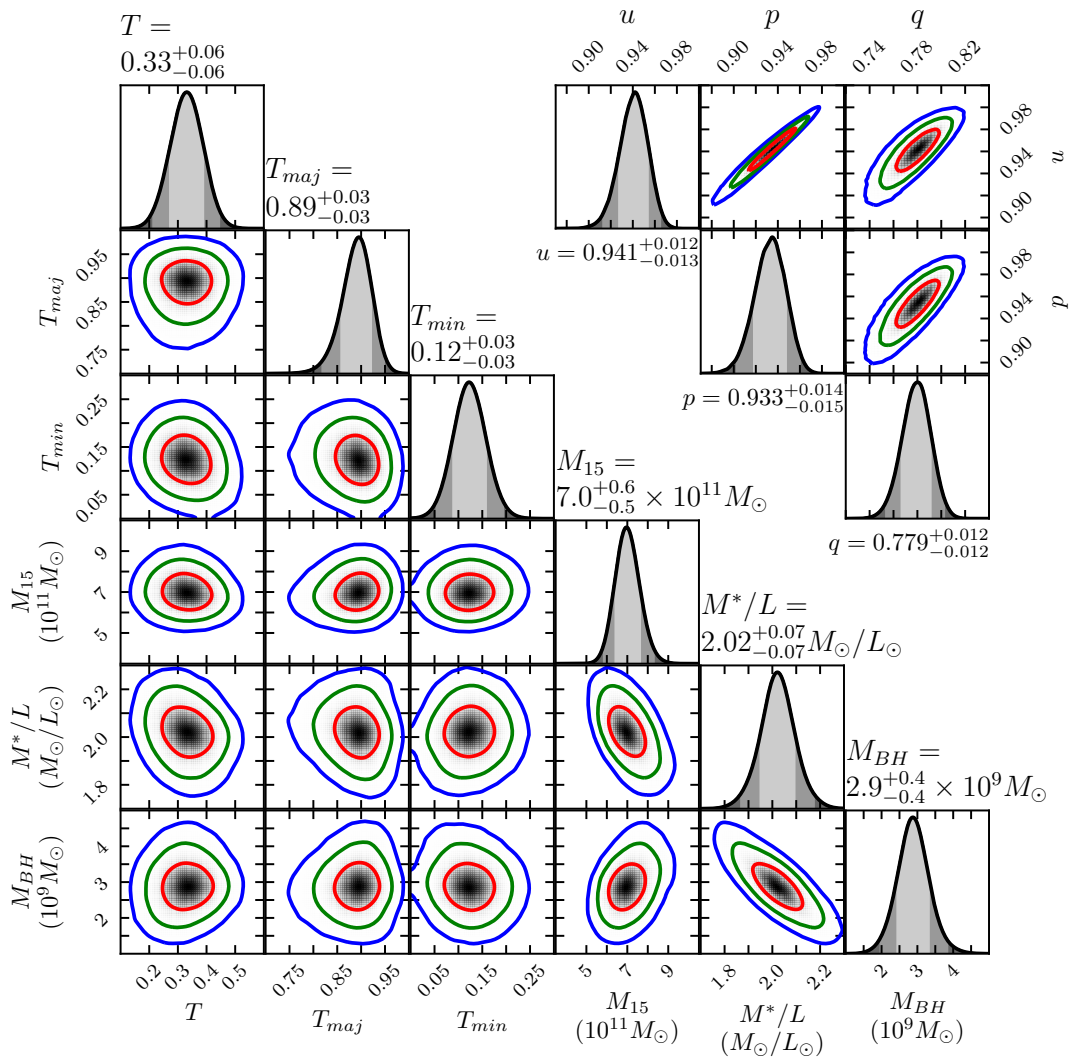

Figure 3.6: (Left) 6D likelihood landscape for orbit models of NGC 1453. As described in the text, the models are sampled in T, $\sqrt{T_{\rm maj}}$, $\sqrt{T_{\rm min}}$, $M_{\rm BH}$, $M^*/L_{\rm F110W}$, and M_{15}, and the 1D and 2D likelihood landscapes are obtained by marginalizing over a smoothed 6D landscape generated by Gaussian process regression. The red, green, and blue curves represent the 1σ, 2σ, and 3σ contours, respectively. (Right) 3D likelihood in axis ratio space, (p, q, u), marginalized over $M_{\rm BH}$, $M^*/L_{\rm F110W}$, and M_{15}. All three axis ratios are significantly correlated with one another, in particular between p and u. This degeneracy is significantly reduced when our new shape parameters T, $T_{\rm maj}$, and $T_{\rm min}$ are used.

For the distance to NGC 1453, we adopt our new determination of 51.0 Mpc from the MASSIVE-WFC3 project [8] using the surface-brightness fluctuation technique [117]. At this distance, 1″ is 245 pc for a flat ΛCDM model with a matter density of $\Omega_m = 0.315$ and a Hubble parameter of $H_0 = 70$km s^{-1} Mpc^{-1}.

Parameter Search Using Latin Hypercube Sampling

We conduct the search for the best-fit galaxy shape in the new triaxial parameters $(T, T_{\rm maj}, T_{\rm min})$ introduced in Section 3.3. The dark matter halo is modeled as a logarithmic potential. We parameterize it through its mass within 15 kpc, M_{15}, which is roughly the central radius of the outermost kinematic bins, following Liepold et al. [87]. As in Liepold et al. [87], we fix the scale radius of the dark matter halo to 15 kpc. Combining the three shape parameters with the three mass parameters $M_{\rm BH}$, $M^*/L_{\rm F110W}$, and M_{15}, we sample the 6D parameter space of galaxy models.

We determine the best-fit parameters by minimizing a χ^2 that includes terms for each LOSVD moment within each aperture, the projected light within each aperture, as well as the binned 3D mass density in order to enforce self-consistency for the stellar density. For each model, the best-fit set of weights are used to calculate the χ^2 differences between models. Lipka and Thomas [118] recently suggested that recovery of the inclination of axisymmetric models can be biased unless the intrinsic flexibility of the models is accounted for. However, a triaxial exploration of model flexibility is beyond the scope of the present study.

Instead of conducting model searches on a regular grid as was done in previous studies, we use the more efficient method of Latin hypercube sampling [119]. There are many techniques for ensuring spatial uniformity in multidimensional spaces. We adopt the scheme described in Deutsch and Deutsch [120], as implemented in the `LHSMDU` python package [121]. This procedure results in models that span a more continuous range of values than a regular grid, and are more uniformly spaced than random sampling. This approach allows a more representative sampling of the 6 dimensions with many fewer points than a regular grid.

We initially use a hypercube consisting of 1000 models spanning the range of $M^*/L_{\rm F110W} \in [1.7, 2.3]$, $M_{15} \in [3.5, 10.5] \times 10^{11} M_\odot$, and $M_{\rm BH} \in [1, 5] \times 10^9 M_\odot$, and the full range between 0 and 1 for $(T, \sqrt{T_{\rm maj}}, \sqrt{T_{\rm min}})$. Of these models, 927 resulted in valid deprojections. We then use a rejection-based scheme to choose subsequent sets of model points. A Gaussian process interpolation of the 6-dimensional χ^2 surface is computed from the previously-run models. We use this interpolation to estimate the χ^2 for $O(10^4)$ points chosen using the LHS scheme described above in the original volume and select points where the estimated χ^2 is within $\Delta\chi^2 = 20.06$ (3σ for 6 parameters) of the estimated global minimum. To avoid premature optimization we perform this routine 10 times where random subsets of half of all previously-run models are used to build the interpolation function. With this scheme we select roughly 1000 model points which are expected to lie near the global χ^2 minimum to evaluate with the TriOS code. We perform two iterations of this rejection scheme, yielding roughly 3000 total model evaluations.

The resulting 6D likelihood landscape is shown in Figure 3.6. To determine the best-fit value and uncertainties, we fit the χ^2 landscape using Gaussian process regression with a squared-exponential covariance function [97]. To make the 2D contours shown in Figure 3.6, we transform this smoothed surface from $(T, \sqrt{T_{\rm maj}}, \sqrt{T_{\rm min}})$ to $(T, T_{\rm maj}, T_{\rm min})$, or (p, q, u). The marginalized 1D likelihood is also shown for each parameter. The shapes of the 2D contours in Figure 3.6 clearly demonstrate that $(T, T_{\rm maj}, T_{\rm min})$ do not have the strong degeneracy apparent in (p, q, u).

The standard values of $\Delta\chi^2 = 1, 4, 9$ are used to define the 1σ, 2σ, and 3σ confidence intervals for 1 degree of freedom when considering the marginalized landscape for each variable individually. For the 2D contours, we use the values for 2 degrees of freedom, giving $\Delta\chi^2 \approx 2.3, 6.2, 11.8$. This is different from most previous work using the van den Bosch et al. [59] code, where typically $\Delta\chi^2 = \sqrt{2N_{\rm obs}}$ is used to define the 1σ confidence interval, where $N_{\rm obs}$ is the number of apertures on the sky, multiplied by the number of moments fitted within each aperture. This value is chosen to represent the intrinsic noise in the χ^2 values for each model, and is much larger than our values. However, while this is true when the input data are varied according to its noise level as discussed in Vasiliev and Valluri [85], the noise level in the χ^2 values between models are significantly smaller when the input data are fixed.

Best-fit Triaxial Model

The best-fit values and the uncertainties for each NGC 1453 parameter are listed in Table 3.2. For each parameter, all other dimensions have been marginalized over. The best-fit $M_{\rm BH}$ is consistent with the value determined from axisymmetric modeling in Liepold et al. [87]. The value of $M^*/L_{\rm F110W}$ has shifted down slightly, but is still consistent within 2σ of the axisymmetric value.

The best-fit shape, on the other hand, is inconsistent with axisymmetry. It is useful to compare our best-fit values of $p = 0.93$ and $q = 0.78$ with those inferred statistically from the observed distributions of ellipticity and misalignment angle between the kinematic and photometric axes for 49 slowly-rotating massive elliptical galaxies with measurable kinematic axes in the MASSIVE survey [27]. In that sample, 56% of the galaxies have $p > 0.9$ with a mean value of 0.88, and the mean value of q is 0.65. Our best-fit shape for NGC 1453 indicates this fast-rotating galaxy is relatively oblate like the MASSIVE slow rotators and is slightly less flattened than the mean of that population.

The orbital composition of the best-fit triaxial model is shown in Figure 3.7 (top panel). Long-axis tubes and box orbits – two orbit types that are present only in triaxial potentials – together account for $\sim 30\%$ of the orbital weights in the inner part and $\sim 45\%$ in the outer part of NGC 1453. Quasi-planar orbits account for a small fraction of the total mass at small and large radii and are excluded from the plot. While long-axis tubes contribute a significant fraction of the mass, the projected model has fairly little minor axis rotation, due in part to the LOS being close to the intrinsic major axis.

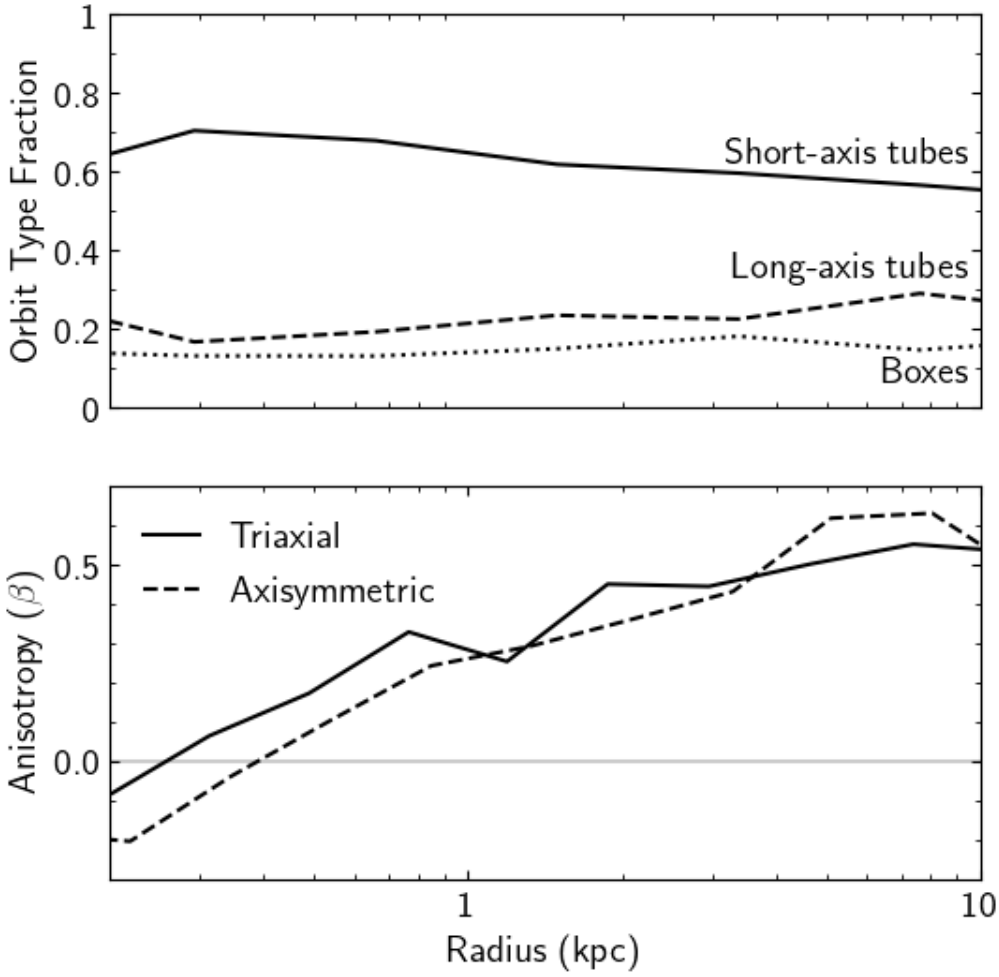

Figure 3.7: Orbital composition (top) and velocity anisotropy (bottom) of the best-fit triaxial model of NGC 1453 as a function of radius. Short-axis tubes (solid) are dominant throughout the model, with significant contributions from long-axis tubes (dashed) and box orbits (dotted) that are present only in triaxial potentials. The velocity anisotropy parameter, β, has a similar radial profile for the best-fit triaxial (solid) and axisymmetric (dashed) models, being mildly tangentially anisotropic in the inner part and becoming more radially anisotropic in the outer part.

Parameter	Value
$M_{\rm BH}$ $(10^9 M_\odot)$	2.9 ± 0.4
$M^*/L_{\rm F110W}$ $(M_\odot/L_\odot)$	2.02 ± 0.07
M_{15} $(10^{11} M_\odot)$	$7.0^{+0.6}_{-0.5}$
T	0.33 ± 0.06
$T_{\rm maj}$	0.89 ± 0.03
$T_{\rm min}$	0.12 ± 0.03
u	$0.941^{+0.012}_{-0.013}$
p	$0.933^{+0.014}_{-0.015}$
q	0.779 ± 0.012
θ (°)	73 ± 3
ϕ (°)	19 ± 3
ψ (°)	$92.7^{+0.7}_{-0.8}$

Table 3.2: Best-fit triaxial model parameters for NGC 1453 from the 6D likelihood landscape in Figure 3.6. For each parameter, all other dimensions have been marginalized over.

The orbital velocity anisotropy of the best-fit model (bottom panel of Figure 3.7) is mildly tangential ($\beta < 0$) in the inner part and becomes increasingly radial outward. The radial profile has a similar shape to the axisymmetric model presented in Liepold et al. [87].

Triaxial vs. Axisymmetric Best-fit Models

The best-fit triaxial model presented above matches the observed kinematics significantly better than the best-fit axisymmetric model in Liepold et al. [87].

Even though the best-fit χ^2 values in the two cases – 493.0 for axisymmetric versus 382.7 for triaxial – differ by ~ 110, they should not be compared directly because triaxial potentials require a new library of box orbits, and different numbers of orbits are used (6480 independent weights for axisymmetric versus 19440 for triaxial). Nonetheless, within triaxial modeling, our best-fit triaxiality of $T = 0.33$ is preferred over nearly oblate axisymmetric models with $T \approx 0$ at a confidence level of about 5σ. To understand why non-axisymmetric models are favored, we examine the 2D maps of V and the lowest 3 even Gauss-Hermite moments in the GMOS data in Figure 3.8 (first row). We recall that axisymmetric models by construction produce only bisymmetric kinematics about the photometric major axis on the sky, meaning that the LOSVDs would be symmetric for points mirrored across the projected major axis and anti-symmetric for points mirrored across the projected minor axis. Any observed systemic deviation from bisymmetry would then indicate triaxiality.

For this reason, we decompose each GMOS moment map into a bisymmetrized component (second column) and a non-bisymmetrized component (third column). The latter exhibits clear systemic deviations from bisymmetry. The most obvious feature is the residual minor

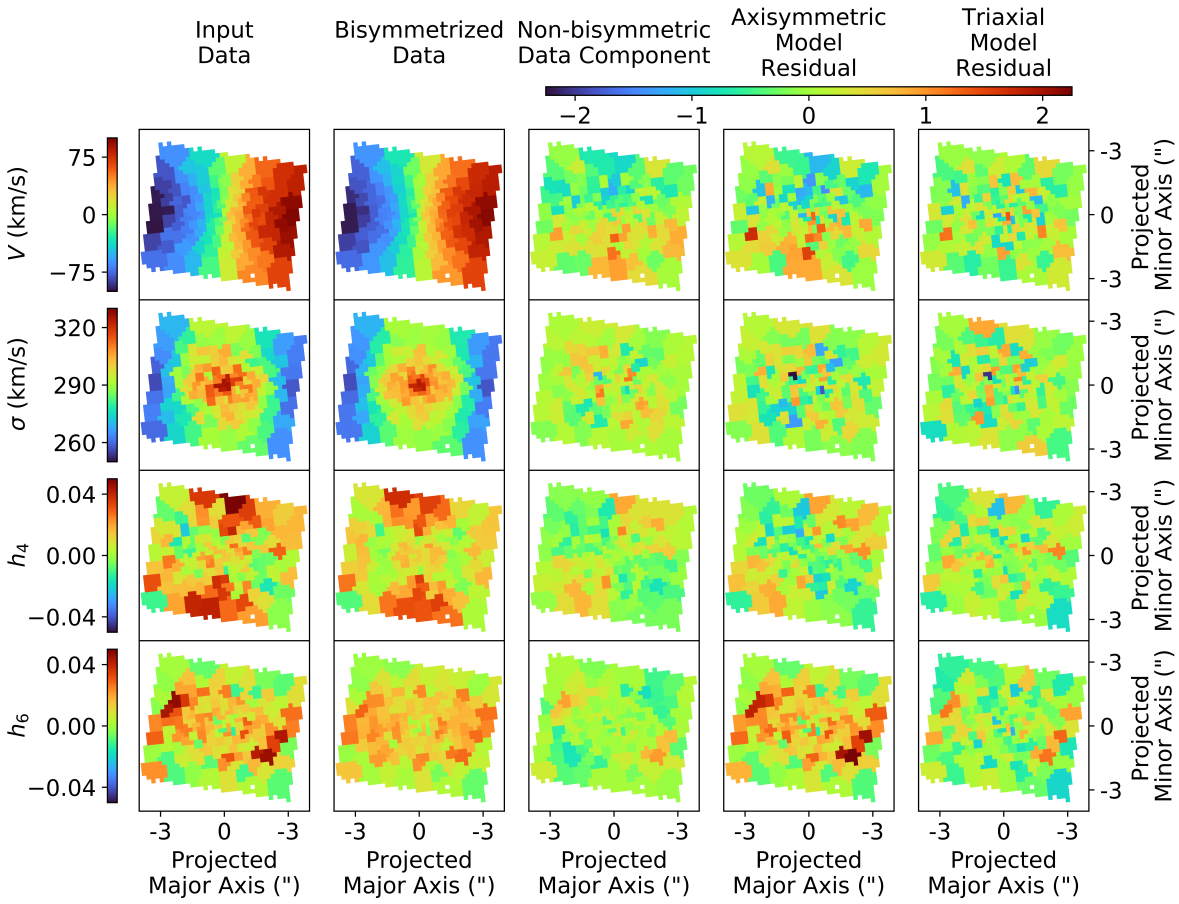

Figure 3.8: Maps of the stellar kinematics from the Gemini GMOS IFS in 135 spatial bins of the central $5'' \times 7''$ of NGC 1453. Four velocity moments are shown (from top down): V, σ, h_4 and h_6. The maps are oriented such that the horizontal and vertical axes are aligned with the galaxy's projected major and minor photometric axes, respectively. The data (first column) are decomposed into a bisymmetric component (second column) and a non-bisymmetric component (third column). To accentuate systematic patterns, we plot the non-bisymmetric component normalized by the moment uncertainty. Since an axisymmetric model can only produce bisymmetric kinematic maps, the residuals from the best-fit axisymmetric model (fourth column) show similar patterns to the bisymmetrized residuals. h_6 shows additional residuals that are consistent with bisymmetry, but unable to be fit by an axisymmetric model. A triaxial model (right column) is able to capture most of the systematic behaviour in the input map, resulting in largely random residuals. The residuals have been normalized by the moment uncertainty.

axis rotation indicative of kinematic misalignment. These maps assume a bisymmetrization along the projected photometric major axis used by our dynamical models, with a PA of 28.5°. The residual pattern persists and can not be "rotated away" even if the PA is within uncertainties in the PA determination determined from the isophotal profile from [8]. An axisymmetric model (consistent with the photometry) would be incapable of fitting these non-bisymmetric features in the data. To confirm this point, we plot the residual maps (fourth column) between the GMOS data and the best-fit axisymmetric model of Liepold et al. [87]. Indeed, the axisymmetric model exhibits similar residual patterns as in the data (third column). In comparison, the best-fit triaxial model is able to fit these non-bisymmetric features to a large extent, producing essentially random residuals (fifth column).

Figure 3.8 indicates that the preference for triaxiality is driven by the non-axisymmetric features in the NGC 1453 kinematics. Even though the non-bisymmetric features are somewhat subtle, they lead to detectable triaxiality, which we find to be best fit with $p = 0.933$, $q = 0.779$, and $T = 0.33$. Thus, despite being a fast rotator with regular isophotal and kinematic features, NGC 1453 is best fit by a triaxial model. This is further evidence for widespread triaxiality in massive elliptical galaxies.

Importantly, however, the best-fit black hole mass $M_{\rm BH} = 2.9 \times 10^9 M_\odot$ is unchanged from that in the axisymmetric model. The stellar mass-to-light ratio and dark matter mass within 15 kpc agree to within a 1σ confidence level.

3.6 Conclusions

In this paper we have presented a revised code and a revamped approach for performing dynamical modeling of triaxial galaxies and their central SMBHs using the orbit superposition technique. We discussed a new triaxial version of the TriOS code that is capable of modeling triaxial systems while avoiding several shortcomings of the original van den Bosch et al. [59] code. As a first application of this code, we performed triaxial orbit modeling of the massive elliptical galaxy NGC 1453 and presented the best-fit galaxy shape and mass parameters. This work complements Liepold et al. [87] and Quenneville, Liepold, and Ma [78], in which we introduced a properly axisymmetrized version of the TriOS code.

We discovered and corrected a major error in the orbit kinematics in the van den Bosch et al. [59] code: the tube orbits had wrong signs in certain mirrored velocity components in the orbit library (Table 1), resulting in incorrect projected kinematics. The magnitude of the kinematic errors varies spatially and depends on the viewing angles (Figure 3.2). This issue impacts all triaxial models that are not viewed along a principal axis, and all nearly axisymmetric models that are not viewed edge-on. How this error affects the best-fit galaxy shapes and mass parameters would have to be assessed on a galaxy-by-galaxy basis by rerunning the models with the corrected orbital flips in Table 1. In the case of NGC 1453, we find the χ^2 landscapes to be altered drastically, with χ^2 values changing non-uniformly by more than 100 for some models.

Following Quenneville, Liepold, and Ma [78], we continued to find ways to speed up the code. In this updated version of the TriOS code, we achieved another significant speedup (of up to ~ 50 %; Figure 3.3) in orbit integration time by a simple extension of the interpolation table used to evaluate orbit accelerations (Section 3.4). The reduction in integration time is particularly pronounced for centrophilic orbits.

We have made two other adjustments in the code that significantly improve the sampling of long-axis tube orbits (Section 3.4) and enforce more uniformly the 3D mass constraints (Section 3.4). After these changes, the behavior of χ^2 vs. T (triaxiality parameter) no longer exhibits spurious oscillations, and the orbit code is able to find reasonable solutions for some mass models that were previously strongly disfavored.

The rest of this paper is devoted to new and improved strategies for searching the multi-dimensional parameter space required to specify triaxial galaxy models. We introduced a new set of shape parameters (Section 3) as well as a novel sampling technique (Section 3.4), which together lead to a remarkable gain in parameter searching efficiency. Searching in the new parameters T, $T_{\rm maj}$, and $T_{\rm min}$ (Equation 3.3) avoids significant non-uniformities associated with other parameters used in earlier work. Our Latin hypercube sampling scheme results in an order-of-magnitude reduction in needed sampling points compared with conventional grid searches.

We applied the TriOS code and triaxial sampling scheme to the fast-rotating massive elliptical galaxy NGC 1453 in the MASSIVE survey (Section 5). NGC 1453 has a relatively small twist in the isophotes, and the kinematic and photometric axes are nearly aligned. Despite these properties that are typically invoked to justify the use of axisymmetric orbit codes, we find the best-fit model to have a triaxiality value of $T = 0.33$, with intrinsic axis ratios $p = 0.933$ and $q = 0.779$. This best-fit triaxial model is able to match the observed kinematic maps significantly better than the best-fit axisymmetric model in Liepold et al. [87]. The improvement is mainly due to the ability of triaxial models to account for non-bisymmetric features in the data (Figure 3.8). Most other galaxies in the MASSIVE survey exhibit less (or no) rotation and more twists in their photometric and kinematic maps compared to NGC 1453. This is further evidence that massive elliptical galaxies have triaxial intrinsic shapes.

$M_{\rm BH}$ in the best-fit triaxial model for NGC 1453 is unchanged from the value measured with the axisymmetrized TriOS code from Liepold et al. [87]. Among the many dozens of stellar dynamical $M_{\rm BH}$ measurements in local galaxies (e.g., McConnell and Ma [38]), NGC 1453 is only one of a handful galaxies whose central SMBH is studied with the full triaxial orbit modeling technique not limited to axisymmetry. In four other galaxies (Section 1), M32 had consistent $M_{\rm BH}$ from axisymmetric and triaxial modeling, the NGC 3379 $M_{\rm BH}$ increased by a factor of ~ 2 when axisymmetry was relaxed, the PGC 046832 $M_{\rm BH}$ decreased enough to be consistent with 0, while NGC 3998 was only modeled with the triaxial code so no comparison can be made. All four systems were modeled with the original van den Bosch et al. [59] code, which used the incorrect mirroring scheme. Triaxial orbit modeling of more galaxies is needed for a full assessment of the systematic effects on stellar dynamical $M_{\rm BH}$ measurements when the commonly-made assumption of axisymmetry is relaxed.

Acknowledgements

We thank Shaunak Modak and Jonelle Walsh for useful discussions. M.E.Q. acknowledges the support of the Natural Sciences and Engineering Research Council of Canada (NSERC), PGSD3-517040-2018. C.-P.M. acknowledges support from NSF AST-1817100, HST GO-15265, HST AR-14573, the Heising-Simons Foundation, the Miller Institute for Basic Research in Science, and the Aspen Center for Physics, which is supported by NSF grant PHY-1607611. This work used the Extreme Science and Engineering Discovery Environment (XSEDE) at the San Diego Supercomputing Center through allocation AST180041, which is supported by NSF grant ACI-1548562.

Chapter 4

Recovery Tests on Mock Galaxy Observations

With the code improvements and modeling strategies of the previous sections in hand, I now validate this code using mock galaxy data. Previous such validations have used far more conservative uncertainty estimations than comparable validations for axisymmetric models. Significant biases have also been found in recovered shape. In this chapter, we re-examine this validation in the context of the improved version of the code, as described in the previous chapters.

4.1 Mock Generation Framework

In this section, I describe the code pipeline that I have written to go from a stellar distribution function to mock photometric and IFU data inputs for the TriOS code. Generating galaxy models therefore requires selecting a total potential and a stellar DF that obey eq. (1.5). In order to be maximally flexible with respect to the choice of distribution function, I have chosen to estimate the projected galactic properties numerically by sampling directly from the DF via Markov chain Monte Carlo (MCMC) sampling. Phase space points are sampled from the DF, which can then be binned into image pixels or IFU apertures. While the required number of samples varies depending on the required accuracy of the model, I have found about 10^8 particles to be adequate for realistic cases.

Given the N-body samples from the chosen DF, a distance and viewing angles must be chosen for the mock observation. With these in hand, mock photometric data is generated by binning the N-body samples into a uniform grid according to their coordinates within the sky plane. The resolution and field-of-view for this mock image should be chosen to be roughly representative of realistic image data such as from HST or CFHT. These points can also be convolved with a gaussian photometric PSF before binning. This mock image is then run through the MGE pipeline in order to extract an MGE fit.

Like the mock photometric data, the mock IFU data is generated by first binning the

N-body points on a uniform grid to imitate uniform lenslets or fibers. Again, the resolution and FOV should be chosen to be comparable to realistic IFU instruments such as GMOS or KCWI. These lenslets can then be merged to form the apertures that will be fed into the TriOS code. This can either be done by forming annular bins, or by voronoi binning based on an estimated signal-to-noise ratio in each bin based on the flux. With the kinematic apertures decided, LOSVDs can then be constructed for each aperture. The GH moments can either be fitted in a least-squares sense to the LOSVD, or estimated directly from the N-body points. Moments from the two methods were found to be consistent.

Outside of the discreteness due to the finite number of MCMC samples, the resulting kinematics are extremely and smooth free of noise. Thus, observational noise needs to be added to the mock observations. Schwarzschild modeling results differ significantly if no additional noise is added [25]. Detailed modeling of the uncertainties in moments extracted from real spectra is beyond the scope of this thesis. Instead we assume gaussian noise on each moment, as is typically assumed in modeling. We further validated that adding uniform gaussian noise to the bins of the LOSVD resulted in moment values that were largely consistent with adding noise directly to the moments. It is often useful to perform orbit modeling with multiple draws of this gaussian noise to ensure that results are not due to random fluctuations within the noise.

4.2 Spherical Models

Before proceeding to axisymmetric and triaxial models, it is useful to consider the simpler case of spherical symmetry. One method of finding solutions to equations (1.5) and (1.6) is to impose an assumption on the form of f. It will be useful to define the relative potential:

$$\Psi = -\Phi(\vec{x}) + \Phi_0 \tag{4.1}$$

and the relative energy:

$$\mathcal{E} = -E + \Phi_0, \tag{4.2}$$

where Φ_0 is a constant chosen such that $f = 0$ when $\mathcal{E} \leq 0$. One common method of finding a valid DF is to assume that the DF is ergodic - namely, f depends only on the relative energy $\mathcal{E}$.

If the potential and stellar density are assumed to be spherical, an ergodic DF can be found with a relatively simple form, as outlined by Eddington [122]. These assumptions allow us to simplify the integral in equation (1.3). Since $\vec{v}$ enters $\mathcal{E}$ and therefore f only through its magnitude v, we can perform the integration over directions of $\vec{v}$ as:

$$\rho_*(r) = 4\pi \int_0^\infty v^2 f(\mathcal{E}) \mathrm{d}v. \tag{4.3}$$

Changing the variable of integration from v to $\mathcal{E}$ gives:

$$\rho_*(r) = 4\pi \int_0^{\Psi(r)} f(\mathcal{E}) \sqrt{2(\Psi - E)} \mathrm{d}\mathcal{E}, \tag{4.4}$$

where it is assumed that Φ_0 is chosen such that $f = 0$ when $\mathcal{E} \leq 0$. Because $\Psi(r)$ is a monotonic function of r, we can regard Ψ instead of r as the independent variable. If we do this and differentiate the previous equation with respect to Ψ, we get:

$$\frac{\partial \rho_*}{\partial \Psi} = 4\pi \int_0^{\Psi} \frac{f(\mathcal{E})}{\sqrt{2(\Psi - E)}} \mathrm{d}\mathcal{E}. \tag{4.5}$$

Integrals of the form

$$g(x) = \int_0^x \frac{h(t)}{(x-t)^{\alpha}} \mathrm{d}t, \tag{4.6}$$

with $0 < \alpha < 1$ are said to be of "Abel" form and can be inverted relatively simply to give

$$h(t) = \frac{\sin \pi\alpha}{\pi} \int_0^t \frac{g(x)}{(t-x)^{(1-\alpha)}} \mathrm{d}x. \tag{4.7}$$

Using this Abel inversion formula with $\alpha = 0.5$, we obtain the result given by Eddington:

$$f(\mathcal{E}) = \frac{1}{\sqrt{8}\pi^2} \frac{\mathrm{d}}{\mathrm{d}\mathcal{E}} \int_0^{\mathcal{E}} \frac{1}{\sqrt{\mathcal{E} - \Psi}} \frac{\partial \rho_*}{\partial \Psi} \mathrm{d}\Psi. \tag{4.8}$$

For any given potential and stellar density, this equation gives a physically valid DF so long as $f(\mathcal{E}) \geq 0$ for all values of $\mathcal{E}$.

These ergodic models are isotropic, in the sense that the DF does not depend on the direction of the velocity vector. However, these models can be generalized to be anisotropic, with a DF that depends on both $\mathcal{E}$ and the angular momentum L. The DF can be written relatively simply if the DF is chosen to be of the form $f(\mathcal{E}, L) = L^{-2\beta} f_1(\mathcal{E})$, where β is a parameter controlling the degree of anisotropy. Another popular choice is to write the DF as $f(Q) = f(\mathcal{E} - \frac{L^2}{2r_a^2})$, where r_a is a length scale over which the anistropy varies. These are referred to as Osipkov-Merritt models [123, 124].

4.3 Hunter-Qian Models

Theoretical Background

While useful for some specific systems, the spherical models described in the previous section are unable to represent many of the non-spherical stellar systems observed in nature. Most galaxies appear flattened on the sky, indicating that these galaxies are not spherical.

Another useful class of models can be obtained by assuming the galaxy potential and stellar distribution function to be axisymmetric. Eddington's solution for spherical potentials was generalized to axisymmetric models with a DF that depends on both $\mathcal{E}$ and L_z by Hunter and Qian [125]. If the potential has reflective symmetry along the z axis, then Ψ is a monotonic function of z^2 at fixed R^2. Thus, ρ can be regarded as a function of R^2 and Ψ

instead of R^2 and z^2. This is in analogy with the spherical case, where ρ was regarded as a function of Ψ instead of r. Writing this density as $\rho(\Psi, R^2)$, the Hunter-Qian (HQ) solution involves the analytic continuation of this density to complex inputs which we write as $\tilde{\rho}$. For a given axisymmetric potential and stellar density, there is a unique stellar DF that is even in L_z. Models that are not even in L_z can be obtained by taking the odd part of the distribution function to equal the product of f_e and any function with magnitude less than 1 that is odd in L_z. The unique even stellar DF is given by:

$$f_e(E, L_z) = \frac{1}{\sqrt{8}\pi^2 i} \frac{\partial}{\partial \mathcal{E}} \int_{\Psi_\infty}^{[\Psi_{\rm env}(\mathcal{E})+]} \frac{1}{\sqrt{\xi - \mathcal{E}}} \tilde{\rho}_1 \left[\xi, \frac{L_z^2}{2(\xi - \mathcal{E})}\right] \mathrm{d}\xi. \tag{4.9}$$

A subscript 1 (2) on a function indicates a derivative with respect to its first (second) argument. Ψ_∞ indicates the value of the potential as $|\vec{x}| \to \infty$, and $\Psi_{\rm env}(\mathcal{E})$ is the potential evaluated on the circular orbit with relative energy $\mathcal{E}$. For simplicity, we choose Ψ_0 such that $\Psi_\infty = 0$, and do not consider potentials where $\Psi_\infty = -\infty$. The integration is along a contour in the complex ξ plane beginning at $\xi = \Psi_\infty$ below the real axis, continuing below the real axis until passing through the real axis at $\xi = \Psi_{\rm env}(\mathcal{E})$, and returning to $\xi = \Psi_\infty$ above the real axis. Following Qian et al. [126], we choose the contour to be elliptical with the form:

$$\xi = \frac{1}{2}\Psi_{\rm env}(\mathcal{E})(1 + \cos\theta) + ih \sin\theta, \quad -\pi \leq \theta \leq \pi. \tag{4.10}$$

The parameter h describing the width of the contour should be chosen to be sufficiently small so as to not enclose any complex conjugate singularities, but sufficiently large so as to not come near the singularities on the real-axis. An example of this contour is shown in figure 4.1.

The analogy between the axisymmetric and spherical cases is apparent in the similarity between the forms of equations (4.8) and (4.9).

A more useful form for evaluation of this integral is:

$$f_e(E, L_z) = \frac{1}{\sqrt{8}\pi^2 i} \int_{\Psi_\infty}^{[\Psi_{\rm env}(\mathcal{E})+]} \frac{1}{\sqrt{\xi - \mathcal{E}}} \tilde{\rho}_{11} \left[\xi, \frac{L_z^2}{2(\xi - \mathcal{E})}\right] \mathrm{d}\xi, \tag{4.11}$$

where $\tilde{\rho_{11}}$ can be evaluated as

$$\tilde{\rho}_{11}(\xi, R^2) = \frac{\rho_{22}(R^2, z^2)}{[\Psi_2(R^2, z^2)]^2} - \frac{\rho_2(R^2, z^2)\Psi_{22}(R^2, z^2)}{[\Psi_2(R^2, z^2)]^3}, \tag{4.12}$$

where z^2 is regarded as a function of ξ and R^2 which can be evaluated numerically. At a given point on the contour, $R^2 = \frac{L_z^2}{2(\xi - \mathcal{E})}$, and thus z^2 is given by the numerical solution of

$$\xi = \Psi\left[\frac{L_z^2}{2(\xi - \mathcal{E})}, z^2\right], \tag{4.13}$$

such that z^2 is real at $\xi = \Psi_{\rm env}(\mathcal{E})$ and follows from analytic continuation for the remainder of the contour.

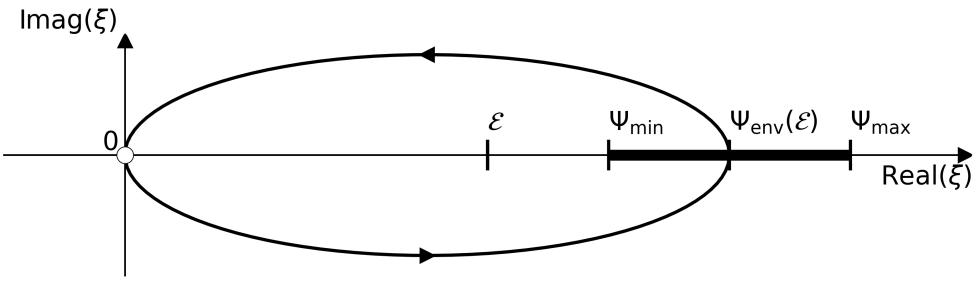

Figure 4.1: Integration contour for Hunter-Qian models with $\Psi_\infty = 0$ for a given $\mathcal{E}$ and L_z. The elliptical contour starts from 0 below the real axis, passes through the real axis at $\xi = \Psi_{\rm env}(\mathcal{E})$, and returns to 0 above the real axis. The shaded region of the real line indicates values of ξ which are physically allowed values of the potential at this $\mathcal{E}$ and L_z. The minimum and maximum physically allowed values of the potential are indicated by $\Psi_{\rm min}$ and $\Psi_{\rm max}$.

Double Power-law Models

While the equations described above apply more generally, we now consider the specific case of stellar density models of the form:

$$\rho(m^2) = \rho_0 \left(\frac{m}{b}\right)^\alpha \left(1 + \frac{m^2}{b^2}\right)^\beta, \quad m^2 = R^2 + z^2/q^2 \tag{4.14}$$

where ρ_0 is a characteristic density, b is a characteristic length, q is the model flattening, and α and β are parameters controlling the inner and outer power law slopes. To roughly model the central region of a giant elliptical galaxy, we choose $\rho_0 = 9.46 \times 10^{10}\ M_\odot {\rm kpc}^{-3}$, $b = 0.29$ kpc, $q = 0.85$, $\alpha = -0.57$, and $\beta = -1.0$. This density has a central power-law cusp with slope -0.57 and an outer slope of -2.57. We consider models with a central black hole for which we choose $M_{\rm BH} = 3.0 \times 10^9\ M_\odot$. In order to evaluate $f_e(\mathcal{E}, L_z)$ using the results of the previous section, each term in equation (4.12) needs to be evaluated for this potential and stellar density model. The necessary density derivatives are:

$$\begin{aligned} \rho_2(m^2) &= \rho'(m^2)/q^2 \\ &= \frac{\rho(m^2)}{q^2} \frac{\alpha b^2 + (\alpha + 2\beta) m^2}{2m^2(m^2 + b^2)} \end{aligned} \tag{4.15}$$

and

$$\begin{aligned}\rho_{22}(m^2) &= \rho''(m^2)/q^2 \\ &= \frac{\rho(m^2)}{q^4}\frac{(\alpha-2)\alpha b^4 + (2\alpha^2-4\alpha+4\alpha\beta)m^2b^2 + (\alpha^2-2\alpha+4\alpha\beta-4\beta+4\beta^2)m^4}{4m^4(m^2+b^2)^2}.\end{aligned} \tag{4.16}$$

The stellar potential can be calculated by numerical quadrature for complex inputs as:

$$\begin{aligned}\Psi^*(R^2,z^2) =& \frac{2\pi Gq}{e}\left\{\arcsin e\int_{R^2+z^2/q^2}^{\infty}\rho(m^2)dm^2\right. \\ &\left. + \int_0^{\infty}\rho(U)\left[\frac{R^2}{(1+u)^2}+\frac{z^2}{(q^2+u)^2}\right]\arcsin\frac{e}{\sqrt{1+u}}\mathrm{d}u\right\},\end{aligned} \tag{4.17}$$

where

$$U = \frac{R^2}{1+u}+\frac{z^2}{q^2+u}, \tag{4.18}$$

and $e = \sqrt{1-q^2}$. Equation (4.17) holds so long as the integrals converge at large radii which we find to be true for the models that we consider. The derivatives of this potential can be calculated by numerical quadrature as:

$$\Psi_2^*(R^2,z^2) = -\pi Gq\int_0^{\infty}\frac{\mathrm{d}u}{(1+u)(q^2+u)^{3/2}}\rho(U) \tag{4.19}$$

$$\Psi_{22}^*(R^2,z^2) = -\pi Gq\int_0^{\infty}\frac{\mathrm{d}u}{(1+u)(q^2+u)^{5/2}}\rho'(U). \tag{4.20}$$

The total potential is given by the stellar contribution added to that of the black hole:

$$\begin{aligned}\Psi(R^2,z^2) &= \Psi^*(R^2,z^2)+\frac{GM_{\rm BH}}{\sqrt{R^2+z^2}} \\ \Psi_2(R^2,z^2) &= \Psi_2^*(R^2,z^2)-\frac{1}{2}\frac{GM_{\rm BH}}{(R^2+z^2)^{3/2}} \\ \Psi_{22}(R^2,z^2) &= \Psi_{22}^*(R^2,z^2)+\frac{3}{4}\frac{GM_{\rm BH}}{(R^2+z^2)^{5/2}}.\end{aligned} \tag{4.21}$$

Numerical Implementation

In order to evaluate the HQ distribution function, we use a similar scheme to that outlined in Qian et al. [126]. For a given value of $(\mathcal{E}, L_z)$, the integration is performed via Gauss quadrature. Beginning on the real axis at $\xi = \Psi_{\rm env}(\mathcal{E})$, the (complex) value of z^2 is evaluated from equation (4.13) at each subsequent point via Newton's method using the previous point's z^2 value as an initial guess. The integrand is then evaluated using (4.12). The integral is calculated cumulatively by adding the Guass quadrature weight multiplied by the

integrand for each point. The contribution to the integral falls off as ξ approaches 0. We thus terminate the integration when the weighted integrand falls below 10^{-6} of the cumulative integral value.

In practice, this procedure is too computationally demanding to evaluate the DF directly during MCMC sampling. Instead, we evaluate the DF on a grid of $\mathcal{E}$ and $\eta = L_z/L_c(\mathcal{E})$, where $L_c(\mathcal{E})$ is the angular momentum of a circular orbit at relative energy $\mathcal{E}$. Intermediate values are then interpolated linearly between values of $\log f_e$ on the grid points. For $\mathcal{E}$ values larger than those in the interpolation table, we use an approximation to the DF. For large $\mathcal{E}$, the even DF is approximately given by:

$$f_e(\mathcal{E}, L_z) = \frac{\rho_0 q^{-\alpha}}{(2\pi B)^{3/2}} \left(\frac{E - \Psi_0^*}{B}\right)^{-\alpha-3/2} \frac{\Gamma(1-\alpha)}{\Gamma(-\alpha-1/2)} {}_3F_2(\frac{1-\alpha}{2}, 1-\frac{\alpha}{2}, -\frac{\alpha}{2}; -\alpha-\frac{1}{2}, \frac{1}{2}; e^2\eta^2), \tag{4.22}$$

where $B = \frac{GM_{\rm BH}}{b}$ is a characteristic energy scale, Γ is the Γ-function, and ${}_3F_2$ is a generalized hypergeometric function. The smallest value of $\mathcal{E}$ in the interpolation table is chosen such that f_e is roughly described by a power-law for the smallest $\mathcal{E}$ in the table. We then extrapolate values beyond the table as a power law for each value of η within the table.

With this interpolation scheme, I sampled 10^8 points using the potential parameters outlined in the previous section. Since the DF depends only on $\mathcal{E}$ and L_z, the MCMC sampling can be performed in the four dimensional space (R, z, v_ϕ, v_T) where v_ϕ is the azimuthal component of velocity, and v_T is the component perpendicular to the azimuthal direction. The DF needs to be multiplied by a Jacobian determinant given by $J = (2\pi R)(2\pi v_T)$. 6-dimensional phase space points can be calculated by drawing two angles ϕ and ϕ_v between 0 and 2π, where ϕ is the azimuthal angle in cylindrical coordinates and ϕ_v describes the angle of v_T within the meridional plane. In order to increase the sampling with negligible computation costs, we sample 10 different values of these angles for each 4-dimensional point in order to obtain a total of 10^9 N-body points. Following Qian et al. [126], we choose the odd part of the DF to be:

$$f_o(\mathcal{E}, L_z) = (2F-1)\frac{\tanh\left[a\eta/2\right]}{\tanh[a/2]} f_e(\mathcal{E}, L_z), \tag{4.23}$$

with the two parameters set to $F = 1$ and $a = 5.5$. We then project the model along an inclination angle of $\theta = 50°$. We take the galaxy to be at a distance to be 51.0 Mpc. We use a mock IFU with a resolution of 0.1 arcseconds and a 5 arcsecond field-of-view, and assume a gaussian PSF with a standard deviation of $0''.5$. Within each bin, we fit the first 8 GH moments, and apply gaussian noise of magnitude 0.03 in each moment $(h_1 - h_8)$. The resulting kinematics are shown in figures 4.2 and 4.3. The mass-to-light ratio for the model is taken to be 1 $M_\odot/L_\odot$.

Recovery

In order to determine best-fit parameters for these HQ mock observations via Schwarzschild modeling, a latin hypercube was used to sample the 3 dimensional $(M_{\rm BH}, M/L, \theta)$ space.

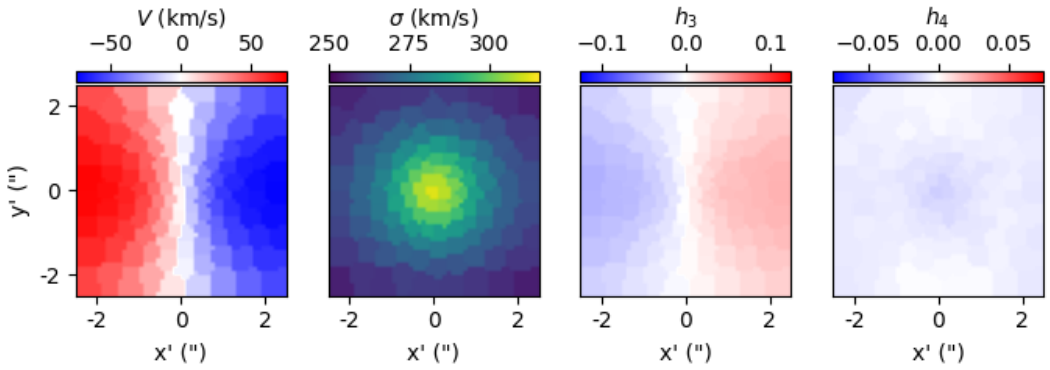

Figure 4.2: Noiseless kinematic maps for the HQ models described in the text.

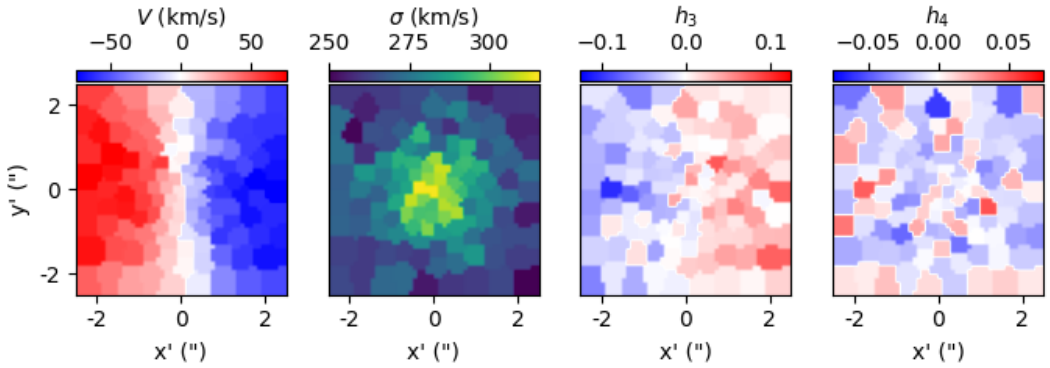

Figure 4.3: Kinematic maps for the HQ models described in the text for a given noise realization.

$M_{\rm BH}$ was sampled between 0 and 6×10^9 $M_\odot$, M/L was sampled between 0.4 and 1.4, and $\cos\theta$ was sampled from 0 up to the maximum deprojectable value for the MGE. Sampling in $\cos\theta$ is equivalent to sampling in $\sqrt{T_{\rm min}}$ for the oblate axisymmetric case. For each set of parameters, the stellar potential was determined by deprojecting the surface brightness from the MGE, and multiplying by the mass-to-light ratio. Within each trial potential consisting of the stellar mass and $M_{\rm BH}$, a library of orbits was integrated following the same procedure as 2. The orbit library consists of $40 \times 9 \times 9$ orbits, each composed of 3^3 trajectories with dithered starting positions.

Following 2, the stationary start space is not included since the models are taken to be axisymmetric. The two viewing angles that were not sampled directly were set to $(\phi, \psi) = (45°, (90 + 10^{-7})°)$ in order to exclude long-axis tube orbits from the model. Each orbit was rotated 40 times in ϕ in order to enforce axisymmetry within the orbit library.

Orbital weights were determined by minimizing a χ^2 function that includes contributions from the GH moments within each kinematic aperture, the projected mass within each kinematic aperture, and the intrinsic mass distribution. The resulting χ^2 values were interpolated in 3D using a Gaussian process regression. A likelihood was then calculated from this landscape as $p = e^{-\chi^2/2}$, before marginalizing to obtain the 2D likelihood contours and 1D likelihoods shown in figure 4.4. The true values of $M_{\rm BH}$ and M/L are both well within the 1σ confidence intervals. The inclination θ, however, is far beyond the 1σ confidence interval, with the Schwarzchild models strongly preferring edge-on inclinations.

While figure 4.4 shows the likelihood landscape for a single realization of noise in the GH moments of the mock observation, this procedure can be repeated for multiple realizations of the noise to ensure that the results are consistent. This is shown in figure 4.5. The results are extremely consistent between noise realizations. Namely, the $M_{\rm BH}$ and M/L are recovered very well with 1σ confidence intervals that are somewhat conservative, while θ is consistently biased towards 90° indicating a preference for edge-on models.

4.4 Triaxial Abel Models

While the HQ models described previously are excellent for testing the recovery of black hole mass and mass-to-light ratio in axisymmetric models, recovery of triaxial shape requires mock triaxial galaxy data with a known input galaxy shape and alignment. For this purpose, we use the triaxial Abel models described in Ven, De Zeeuw, and Van Den Bosch [61], based on the models originally described in Dejonghe and Laurent [127] and extended in Mathieu and Dejonghe [128].

Stackel Potentials

Stackel potentials are a class of potentials for which orbital dynamics can be expressed in relatively simple analytic forms. We first must define a set of confocal ellipsoidal coordinates

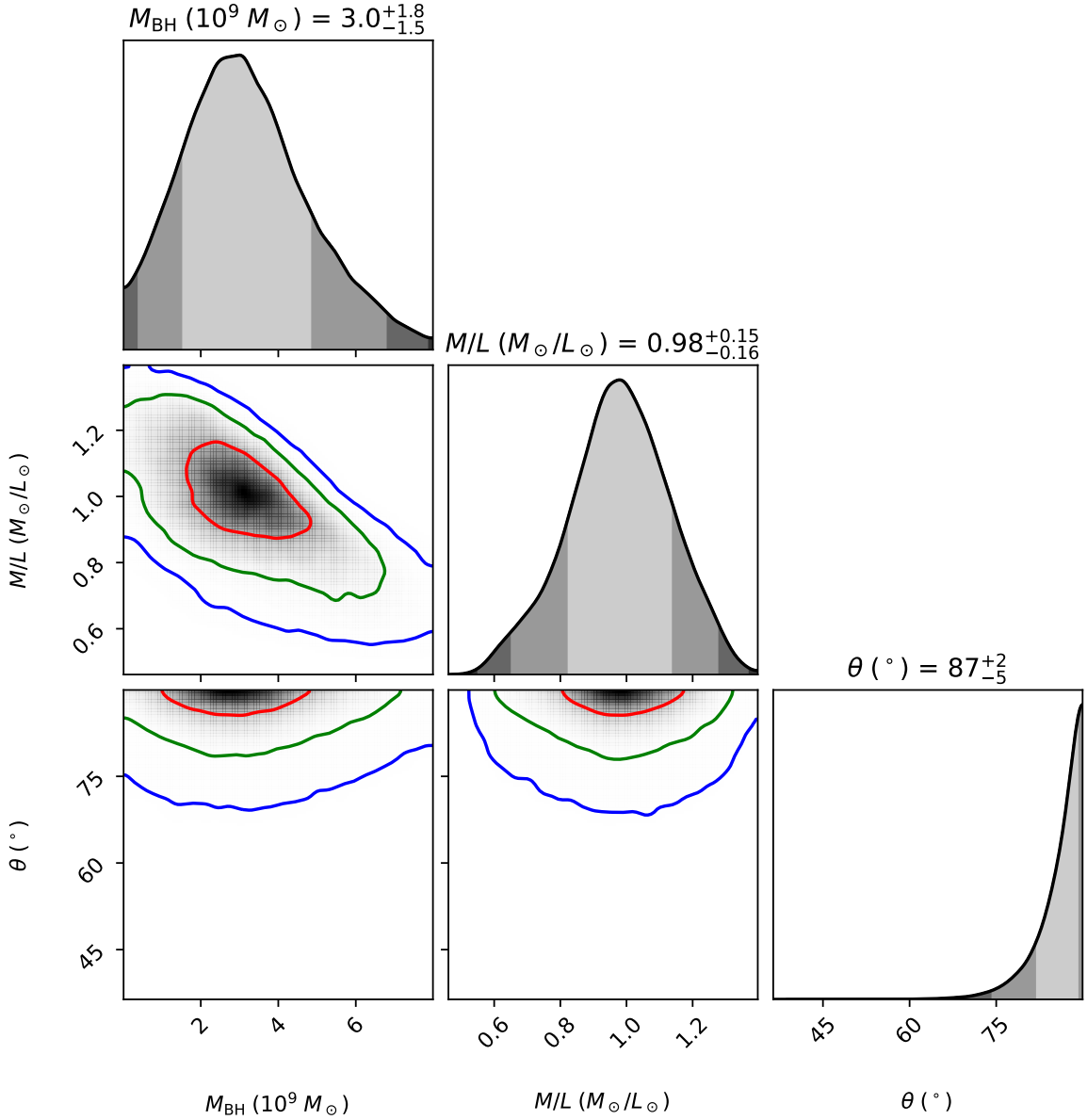

Figure 4.4: 3D likelihood landscape for orbit models of the Hunter-Qian model described in the text. The models are sampled in $M_{\rm BH}$, M/L, and θ. The 1D and 2D likelihood landscapes are obtained by marginalizing over a smoothed 3D landscape generated by Gaussian process regression. The red, green, and blue curves represent the 1σ, 2σ, and 3σ contours, respectively. $M_{\rm BH}$ and M/L are consistent within 1σ, while the inclination recovery exhibits a clear bias towards edge-on models.

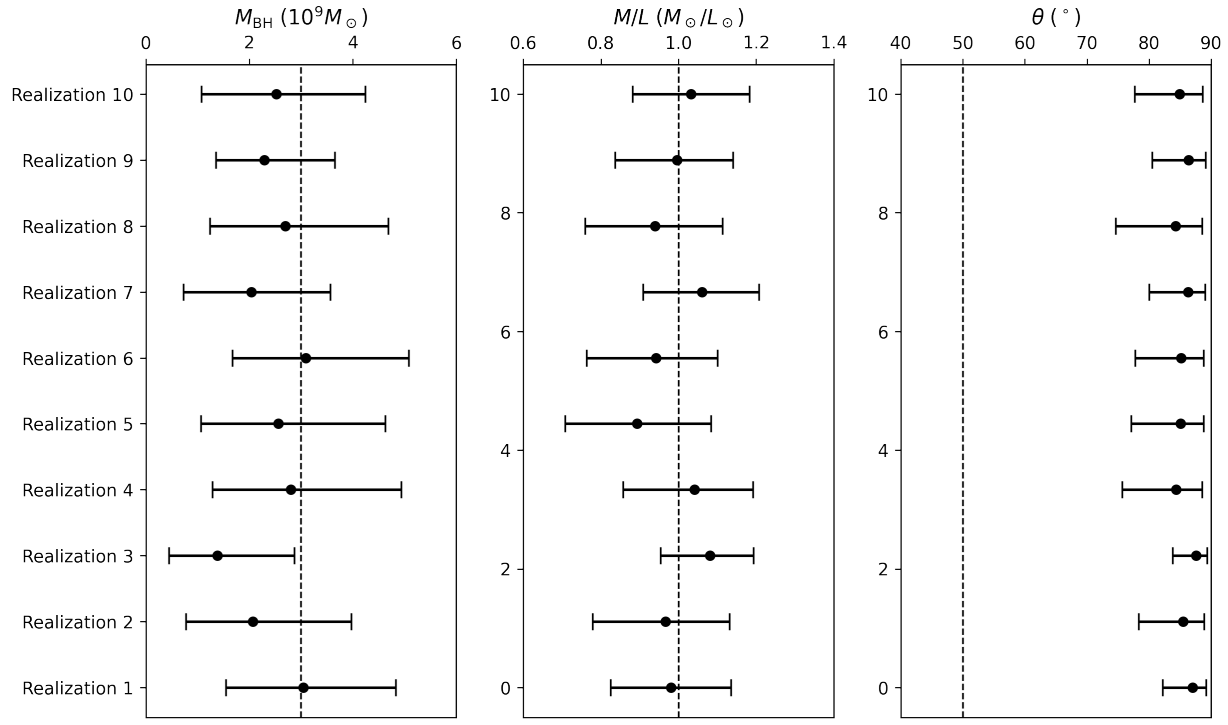

Figure 4.5: 1D marginalized 1σ confidence intervals for orbit model parameters of the Hunter-Qian model described in the text. The 1D confidence intervals are obtained by marginalizing over a smoothed 3D landscape generated by Gaussian process regression. The estimated uncertainties are somewhat conservative on $M_{\rm BH}$ and M/L, while the inclination θ is clearly biased towards edge-on.

(λ, μ, ν) as the three roots for τ in the expression:

$$\frac{x^2}{\tau+\alpha} + \frac{y^2}{\tau+\beta} + \frac{z^2}{\tau+\gamma} = 1, \tag{4.24}$$

where (x, y, z) are the normal cartesian coordinates, and α, β, and γ are constants such that $-\gamma \leq \nu \leq -\beta \leq \mu \leq -\alpha \leq \lambda$. The inverse transformation is given by:

$$\begin{aligned} x^2 &= \frac{(\lambda+\alpha)(\mu+\alpha)(\nu+\alpha)}{(\alpha-\beta)(\alpha-\gamma)} \\ y^2 &= \frac{(\lambda+\beta)(\mu+\beta)(\nu+\beta)}{(\beta-\gamma)(\beta-\alpha)} \\ z^2 &= \frac{(\lambda+\gamma)(\mu+\gamma)(\nu+\gamma)}{(\gamma-\alpha)(\gamma-\beta)}. \end{aligned} \tag{4.25}$$

Thus, each point in confocal ellipsoidal coordinates (λ, μ, ν) represents 8 points in cartesian coordinates $(\pm x, \pm y, \pm z)$.

A Stackel potential is then defined as having the form:

$$\Phi_{\rm S}(\lambda, \mu, \nu) = \frac{U(\lambda)}{(\lambda - \mu)(\lambda - \nu)} + \frac{U(\mu)}{(\mu - \nu)(\mu - \lambda)} + \frac{U(\nu)}{(\nu - \lambda)(\nu - \mu)}, \tag{4.26}$$

where $U(\tau)$ is an arbitrary smooth function for $\tau = \lambda, \mu, \nu$.

It will prove useful to introduce an expression for a divided difference of $U(\tau)$ following Hunter and de Zeeuw [129]. We define the first order divided difference of $U(\tau)$ as:

$$U[\tau_1, \tau_2] = \frac{U(\tau_1) - U(\tau_2)}{\tau_1 - \tau_2}. \tag{4.27}$$

Higher order divided differences can then be defined recursively in terms of lower order divided differences as:

$$U[\tau_1, \tau_2, \ldots] = \frac{U[\tau_1, \ldots] - U[\tau_2, \ldots]}{\tau_1 - \tau_2}. \tag{4.28}$$

Such divided differences are symmetric in their arguments. Direct calculation reveals that equation (4.26) can be re-written as a second order divided difference:

$$\Phi_S(\lambda, \mu, \nu) = U[\lambda, \mu, \nu]. \tag{4.29}$$

The mass density that generates this potential follows from Poisson's equation as:

$$\rho_S(\lambda, \mu, \nu) = \frac{1}{4\pi G} \nabla^2 \Phi(\lambda, \mu, \nu). \tag{4.30}$$

For such a potential, the triaxiality parameter is defined as:

$$T = \frac{\beta - \alpha}{\gamma - \alpha}. \tag{4.31}$$

The utility of these potentials follows from the fact that the Hamilton-Jacobi equation separates in the coordinates (λ, μ, ν) for potentials of the form (4.26). This allows us to write the three integrals of motion analytically as:

$$\begin{aligned} E &= \frac{1}{2}(v_x^2 + v_y^2 + v_z^2) + U[\lambda, \mu, \nu] \\ I_2 &= \frac{1}{2}L_z^2 + \frac{1}{2}TL_y^2 + \frac{1}{2}(\alpha - \beta)v_x^2 + (\alpha - \beta)x^2 U[\lambda, \mu, \nu, -\alpha] \\ I_3 &= \frac{1}{2}L_x^2 + \frac{1}{2}(1 - T)L_y^2 + \frac{1}{2}(\gamma - \beta)v_z^2 + (\gamma - \beta)z^2 U[\lambda, \mu, \nu, -\gamma]. \end{aligned} \tag{4.32}$$

In order to classify these orbits, it is useful to define the effective potential:

$$\Phi_{\rm eff}(\tau) = \frac{I_2}{\tau + \alpha} + \frac{I_3}{\tau + \gamma} - G(\tau). \tag{4.33}$$

is defined as:

$$G(\tau) = -\frac{U(\tau) - \frac{\tau+\gamma}{\gamma-\alpha}U(-\alpha) + \frac{\tau+\alpha}{\gamma-\alpha}U(-\gamma)}{(\tau+\alpha)(\tau+\gamma)}. \tag{4.34}$$

For $\tau = y^2 - \beta \geq -\beta$, $-G(y^2 - \beta)$ is the value of the potential along the intermediate axis. Assuming the density ρ_S that generates this potential is centrally concentrated and has finite central density, $G(\tau)$ decreases monotonically with τ, $G(\tau)$ falls off slower than $1/\tau$ as $\tau \to \infty$, and $G(\tau)$ is either finite at $\tau = -\gamma$ or diverges slower than $1/\tau + \gamma$ [22].

Under this assumption, the potential supports four major orbit families: box orbits, inner long-axis tube orbits, outer long-axis tube orbits, and short-axis tube orbits. Bounded motion is allowed at a given position so long as:

$$\begin{aligned} E &\geq \Phi_{\text{eff}}(\lambda) \\ E &\geq \Phi_{\text{eff}}(\mu) \\ E &\leq \Phi_{\text{eff}}(\nu) \\ E &\leq 0. \end{aligned} \tag{4.35}$$

At a given position, each constraint in equation (4.35) represents a plane in the (E, I_2, I_3) integral space. The volume in this space is therefore a tetrahedron bounded by these four planes, which we denote as $\mathcal{T}_{\lambda\mu\nu}$. This volume is shown in figure 4.6. With this definition of the effective potential in hand, orbits can be classified relatively simply according to the scheme outlined in table 4.1.

	$I_2 < 0$	$I_2 > 0$
$E < \Phi_{\text{eff}}(-\beta)$	Inner Long-axis Tube orbit	Outer Long-axis Tube orbit
$E > \Phi_{\text{eff}}(-\beta)$	Box orbit	Short-axis tube orbit

Table 4.1: Orbit classification within a Stackel potential.

Abel Distribution Functions

Following Dejonghe and Laurent [127], we define our triaxial DF to depend only on a variable S which can be written as:

$$S = -E + wI_2 + uI_3. \tag{4.36}$$

This choice is analogous to the ansatz chosen for axisymmetric Osipkov-Merritt models, where the DF depends only a variable $Q = -E - \frac{L^2}{2r_a^2}$. The magnitudes of w and u can thus be considered as characteristic inverse squared distances at which the orbital anisotropy changes.

Under the assumption of a DF that depends only on S, self-consistency is only possible in the spherical case [130]. However, following Ven, De Zeeuw, and Van Den Bosch [61], we

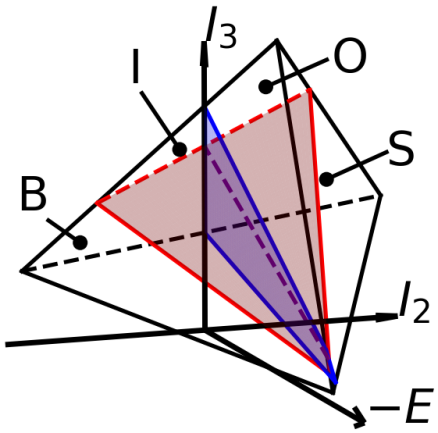

Figure 4.6: Volume in integral space that is accessible by orbits at a given position, $\mathcal{T}_{\lambda\mu\nu}$. The four orbit types, separated by the blue and red planes, are indicated by I (inner long-axis tube orbits), O (outer long-axis tube orbits), B (box orbits), and S (short-axis tube orbits).

will choose the DF to roughly approximate the total mass near the center and underestimate the total mass at larger distances, roughly approximating the effect of dark matter in real galaxies.

The DFs described in Ven, De Zeeuw, and Van Den Bosch [61] can sample only a subset of the volume $\mathcal{T}_{\lambda\mu\nu}$. This allowed subset, $\mathcal{S}_{\lambda\mu\nu}$, is defined by the additional contraint that S must be greater than some minimum value, $S_{\rm lim}$. This value is given by:

$$S_{\rm lim} = \begin{cases} -U[-\alpha, 1/u - \gamma, -\gamma] & u \geq 0 \text{ and } \frac{U[-\alpha,1/u-\gamma,-\gamma]}{\beta-\alpha} \leq w \leq \frac{u}{1-(\gamma-\alpha)u} \\ -U[-\alpha, 1/w - \alpha, -\gamma] & w \geq 0 \text{ and } u \leq \frac{w}{1+(\gamma-\alpha)w} \\ w(\beta-\alpha)\Phi_0 & \text{otherwise,} \end{cases} \tag{4.37}$$

where $\Phi_0 = U[-\alpha, -\beta, -\gamma]$ is the central value of the potential. In order to have a non-zero volume of $\mathcal{S}_{\lambda\mu\nu}$ at the origin, we must have $u \leq \frac{1}{\gamma-\beta}$ and $w \geq -\frac{1}{\beta-\alpha}$.

With these definitions in hand, we define our distribution function to have the form:

$$f_\delta(S) = \left(\frac{S - S_{\rm min}}{-\Phi_0 - S_{\rm min}}\right)^\delta \quad \text{within } \mathcal{T}_{\lambda\mu\nu} \text{ and } S \geq S_{\rm min} \geq S_{\rm lim}. \tag{4.38}$$

In this expression, $S_{\rm min}$ and δ are constants, with δ being non-negative. The DF is 0 outside the volume $\mathcal{T}_{\lambda\mu\nu}$ and for $S < S_{\rm min}$.

As written, equation (4.38) describes a distribution function that includes no rotation; all four orbit families are included with equal prograde and retrograde weights for tube components. Components consisting of a single orbit type can be constructed by imposing constraints from table 4.1.

Since each integral in equation (4.32) is quadratic in velocities, they are invariant under time reversal. Thus, prograde and retrograde components for each tube orbit type correspond to the same values of (E, I_2, I_3). Therefore, in order to introduce rotation, unequal weights must be assigned based on the sign of L_z for short-axis tube orbits, or L_x for long-axis tube orbits. Following Ven, De Zeeuw, and Van Den Bosch [61], we refer to these DFs as triaxial Abel models.

Isochrone Potentials

Thus far in this section, all results have applied for any function $U(\tau)$, so long as it is generated by a density $\rho_S(\lambda, \mu, \nu)$ that is centrally concentrated and finite at the origin. We now specify the choice of U to be:

$$U(\tau) = -GM\sqrt{\tau}(\tau + \beta). \tag{4.39}$$

Since $\tau \geq -\gamma$, this expression is valid so long as $\gamma \leq 0$. Since equation (4.24) is invariant under shifts of the form $\alpha, \beta, \gamma, \tau \to \alpha - \Delta, \beta - \Delta, \gamma - \Delta, \tau + \Delta$, the parameter γ can always be chosen to be non-positive without loss of generality.

The resulting potential is:

$$\Phi_S(\lambda,\mu,\nu) = -GM\frac{\sqrt{\lambda\mu}+\sqrt{\mu\nu}+\sqrt{\nu\lambda}-\beta}{(\sqrt{\lambda}+\sqrt{\mu})(\sqrt{\mu}+\sqrt{\nu})(\sqrt{\nu}+\sqrt{\lambda})}, \tag{4.40}$$

and the third-order divided difference that enters equation (4.32) is:

$$U[\lambda,\mu,\nu,\sigma] = GM\frac{\sqrt{\lambda\mu\nu}+\sqrt{\mu\nu\sigma}+\sqrt{\nu\sigma\lambda}+\sqrt{\sigma\lambda\mu}-\beta(\sqrt{\lambda}+\sqrt{\mu}+\sqrt{\nu}+\sqrt{\sigma})}{(\sqrt{\lambda}+\sqrt{\mu})(\sqrt{\lambda}+\sqrt{\nu})(\sqrt{\lambda}+\sqrt{\sigma})(\sqrt{\mu}+\sqrt{\nu})(\sqrt{\mu}+\sqrt{\sigma})(\sqrt{\nu}+\sqrt{\sigma})}. \tag{4.41}$$

The function $G(\tau)$ that enters the effective potential in equation (4.33) is:

$$G(\tau) = \frac{GM}{\sqrt{-\alpha}+\sqrt{-\gamma}}\left(\frac{\sqrt{\tau}(\sqrt{-\alpha}+\sqrt{-\gamma})+\sqrt{\alpha\gamma}-\beta}{\sqrt{\tau}(\sqrt{-\alpha}+\sqrt{-\gamma})+\sqrt{\alpha\gamma}+\tau}\right). \tag{4.42}$$

The mass density that generates this potential is given in Appendix C of de Zeeuw and Pfenniger [131] as:

$$\begin{aligned}\rho(\lambda,\mu,\nu) = \frac{M}{4\pi}&\frac{1}{Z^3(XY-Z)^3}\\ &\times\Big\{\left[(\beta-\alpha-\gamma)(Y^2+XZ)+(\alpha\beta-\beta^2+2\alpha\gamma+\beta\gamma)(X^2+Y)\right]Z^3\\ &\quad-3\alpha\beta\gamma Z^2(X^3+Z)+\alpha\beta^2\gamma X(X^2Y^2+X^3Z-3XYZ+3Z^2)\Big\},\end{aligned} \tag{4.43}$$

where:

$$\begin{aligned}X &= \sqrt{\lambda}+\sqrt{\mu}+\sqrt{\nu}\\ Y &= \sqrt{\lambda\mu}+\sqrt{\mu\nu}+\sqrt{\nu\lambda}\\ Z &= \sqrt{\lambda\mu\nu}.\end{aligned} \tag{4.44}$$

Numerical Implementation

We take a significantly different implementation approach to van den Bosch and van de Ven [60]. While the projected properties of these models can be calculated in a relatively simple numerical manner, we instead elect to sample the DF directly with an MCMC as outlined in section 4.1. In this case, we sample in the 6 dimension space $(\lambda,\mu,\nu,v_x,v_y,v_z)$. In order to account for the change cartesian and ellipsoidal coordinates, the distribution function must be multiplied by the Jacobian determinant, which is given by:

$$J = \frac{(\lambda-\mu)(\lambda-\nu)(\mu-\nu)}{8\sqrt{(\lambda+\alpha)(\lambda+\beta)(\lambda+\gamma)(\mu+\alpha)(\mu+\beta)(\mu+\gamma)(\nu+\alpha)(\nu+\beta)(\nu+\gamma)}}. \tag{4.45}$$

For each trial phase space point, it is verified that the point lies within the volume $\mathcal{T}_{\lambda\mu\nu}$ and that $S \geq S_{\min}$. If the DF is specified to consist of only a subset of orbit types, then the

trial point must lie within the associated subvolume of $\mathcal{T}_{\lambda\mu\nu}$ according to the constraints in table 4.1. If the trial point lies within the allowed volume, the log distribution function and Jacobian determinant are evaluated.

Each phase space point can be mapped to 16 points in cartesian phase space: one position in each octant of configuration space, together with its time-reversed (velocity mirrored) copy. Weights are assigned to these 16 points depending on the desired rotation fraction of these orbits. If the component is non-rotating, all 16 points receive equal weights. For a purely rotational short-axis tube component for example, the 8 weights with $L_z > 0$ would receive equal weights while the 8 with $L_z < 0$ would receive no weight. These phase space points are then used to calculate a stellar luminosity MGE and stellar kinematics.

In addition to the phase space points, a separate set of MCMC points are drawn from the density distribution (4.43) in order to fit an MGE to the mass distribution. We choose to study a triaxial model similar to those studied in van den Bosch and van de Ven [60]. We take a set of ellipsoidal coordinates with $(\alpha, \beta, \gamma) = (-0.94, -0.70, -0.40)$, which gives comparable axis ratios to the triaxial models explored in van den Bosch and van de Ven [60]. This gives a triaxiality parameter of $T = 0.45$. We adopt a triaxial Isochrone Potential with $M = 10^{11} M_{\odot}$. The stellar distribution function is then taken to be stratified on planes of constant S defined by parameter values $u = \frac{-0.5}{-\alpha}$ and $w = \frac{-0.5}{-\alpha}$ for $S \geq S_{\min} = S_{\lim}$. The models are projected along a line-of-sight directed along $(\theta, \phi) = (60^{\circ}, 60^{\circ})$. We take the mock galaxies to be at a distance to be 20.0 Mpc. We use a mock IFU with a resolution of 1.0 arcseconds and a $40'' \times 30''$ field-of-view.

I consider two distinct DFs within this potential. The first is composed of a non-rotating componenent with a relative weight of 0.8 (filling the entire volume $\mathcal{S}_{\lambda\mu\nu}$) and a purely prograde short-axis rotating component with a relative weight 0.2 (filling the subset of $\mathcal{S}_{\lambda\mu\nu}$ that consists of short-axis tube orbits). This DF, referred to as DF1 here, is the same as the "ST2" model explored in van den Bosch and van de Ven [60]. The surface brightness and kinematic maps for DF1 are shown in 4.7. The model kinematics have been randomly perturbed with a gaussian distribution of width 0.03 for each GH moment. V and σ were perturbed by a gaussian distribution with width $0.03\sqrt{2}\sigma$.

The projected kinematics of DF1 exhibit fairly little kinematic misalignment, similar to NGC 1453. However, DF1 rotates more slowly than NGC 1453, and is more representative of the slow rotators that are common among high mass ellipticals. h_4 is consistently negative throughout the field of view. The model exhibits a mild misalignment between the mass and luminosity distributions.

The second DF that I consider replaces a quarter of the short-axis tube component with a long-axis tube component. The complete model thus consists of a non-rotating componenent with a relative weight of 0.8 (filling the entire volume $\mathcal{S}_{\lambda\mu\nu}$), a purely prograde short-axis rotating component with a relative weight 0.15 (filling the subset of $\mathcal{S}_{\lambda\mu\nu}$ that consists of short-axis tube orbits), and a purely prograde long-axis rotating component with a relative weight of 0.05 (filling the subset of $\mathcal{S}_{\lambda\mu\nu}$ that consists of long-axis tube orbits). This DF is referred to as DF2. The kinematics for this model, perturbed with gaussian noise in the same manner as DF1, are shown in 4.8. The same random seed was used for DF1 and DF2

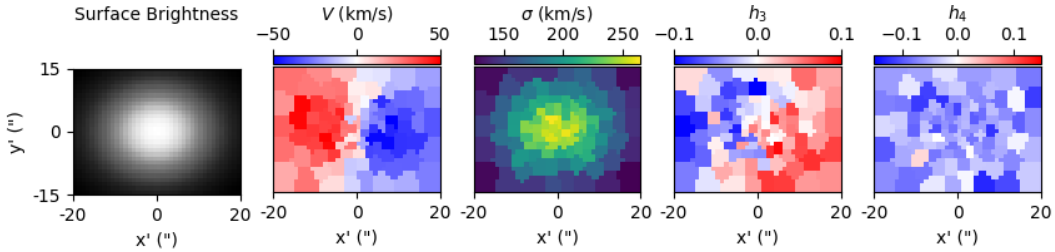

Figure 4.7: Kinematic maps for the DF1 Abel model described in the text for a given noise realization.

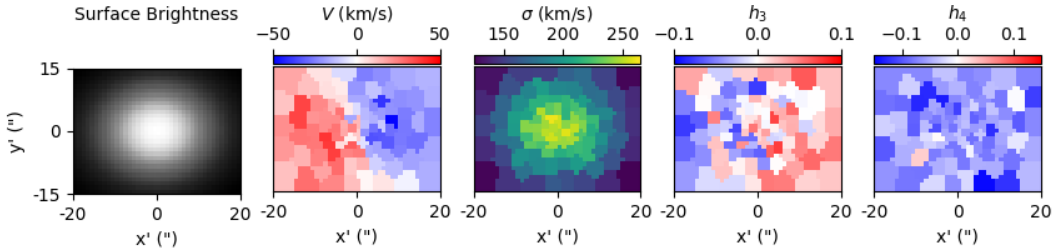

Figure 4.8: Kinematic maps for the DF2 Abel model described in the text for the same noise realization as figure 4.7.

in order to compare more directly.

The projected kinematics of DF2 exhibit a large kinematic misalignment, similar to NGC 57 Ene et al. [116]. The kinematics look qualitatively similar to DF1 beyond the first moment. By testing both of these models, we can study whether strong kinematic misalignments result in tighter constraints on the underlying triaxial shape. The model exhibits a mild misalignment between the mass and luminosity distributions. A mass-to-light ratio of $1 M_\odot/L_\odot$ is assumed for both DF1 and DF2.

Recovery

In order to test the recovery of these models within the TriOS code, a similar search strategy to chapter 3 was used. The 4-dimensional $(M/L, T, \sqrt{T_{\rm maj}}, \sqrt{T_{\rm min}})$ space was sampled with a latin hypercube. M/L was sampled from 0.7 to 1.3, while $(T, \sqrt{T_{\rm maj}}, \sqrt{T_{\rm min}})$ was sampled over the unit cube. For each point in the latin-hypercube, a set of viewing angles were calculated using (3.8) on the branch $0° \leq \theta \leq 90°$, $0° \leq \phi \leq 90°$, $90° \leq \psi \leq 180°$. Since the mass density MGE has no twists, the deprojected mass density does not depend on the

choice of branch. For each set of viewing angles, the mass density MGE was then deprojected (when such a deprojection is valid according to equation (3.6)).

A library of orbits was then integrated within the potential for each potential based on the start-space outlined in 3.4. $40 \times 18 \times 9$ orbits were used in each orbit library for a total $3 \times 40 \times 18 \times 9$ orbits. Each orbit was dithered 3^3 times.

Next, the surface brightness MGE was deprojected for each mass model. Since the luminosity density is misaligned relative to the mass density, the deprojected luminosity density will depend on the choice of branch. Thus, for each deprojected mass density, there are two possible sets of viewing angles and thus two possible deprojected luminosity densities. We denote the branch with $0° \leq \theta \leq 90°$, $0° \leq \phi \leq 90°$, $90° \leq \psi \leq 180°$ as branch 1. Branch 2 is then taken to be related to branch 1 via $(\phi, \psi) \rightarrow (-\phi, 180° - \psi)$ such that $0° \leq \theta \leq 90°$, $-90° \leq \phi \leq 0°$, $0° \leq \psi \leq 90°$. The misalignment between the projected mass and luminosity densities results in a smaller region of valid deprojections for the lumionsity than the mass alone.

Finally, orbital weights can be chosen to best reproduce the mock observations. For each branch of each model, the weights are found using a non-negative least squares (NNLS) solver to minimize a χ^2 value that includes contributions from each GH moment for each kinematic aperture. The projected and intrinsic luminosity distributions are included in the χ^2 value with an assumed 1% uncertainty. For each branch, we employ a Gaussian process interpolation with a Matern covariance kernel with ν parameter of 3/2 to the 4-dimensional χ^2 values [132]. Then, taking each model to have a likelihood of $p = e^{-\chi^2/2}$, we use a Markov Chain Monte-Carlo procedure to sample points from this likelihood function in order to marginalize the likelihood to give 2-dimensional contours and 1-dimensional distributions. This marginalized likelihood is shown on branch 1 for a single noise realization for DF1 and DF2 in figures 4.9 and 4.10 respectively. This branch contains the true deprojection for the input model and has a best fitting model that is significantly preferred over the best-fit in branch 2 for both DFs.

I performed the same fitting and marginalization procedure for 5 separate realizations of noise in the GH moments. Since branch 1 was significantly preferred over branch 2 in each case, we present only the confidence intervals for branch 1. The branch 2 landscapes are qualitatively similar in shape. The same random seed was used for the noise in the two DFs. The marginalized 1σ confidence intervals are shown in figures 4.11 and 4.12 for the two DFs.

Overall, the model parameters are recovered well. For DF1, the true value is contained within the 1σ confidence interval for 4/5 realizations for T, 2/5 realizations for $\sqrt{T_{\rm maj}}$, and 1/5 realizations for $\sqrt{T_{\rm min}}$. For DF2, the true value is contained within the 1σ confidence interval for 4/5 realizations for T, 3/5 realizations for $\sqrt{T_{\rm maj}}$, and 2/5 realizations for $\sqrt{T_{\rm min}}$. Between the two DF models, only one realization of a single shape parameter ($\sqrt{T_{\rm min}}$ for realization 5 of DF1) lies beyond 3σ of the true value. For both DF1 and DF2, the estimated 1σ confidence intervals are largely representative of the true variation in recovered values of the shape parameters. In either case, the mass-to-light ratio is consistently overestimated by about 5%.

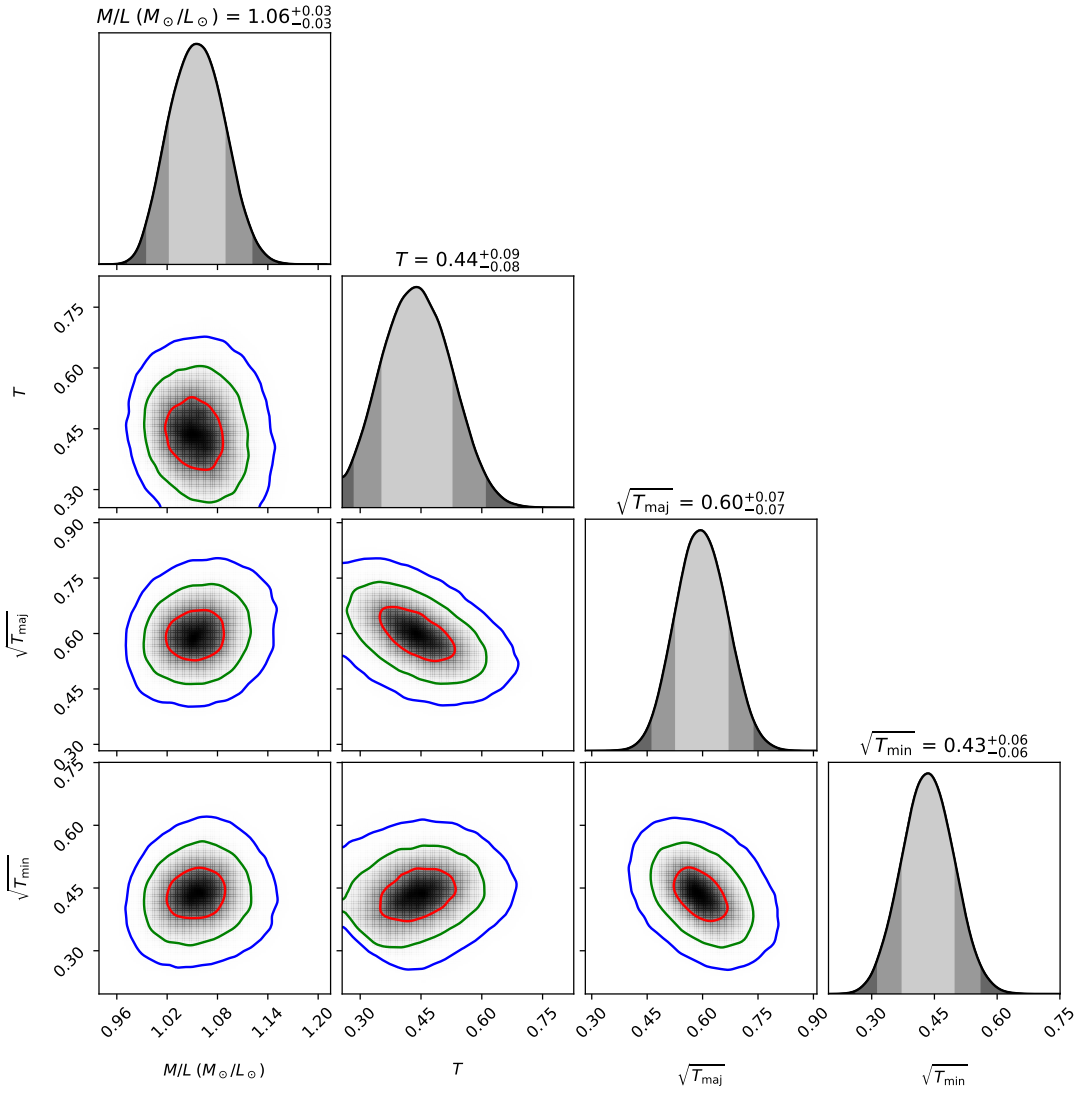

Figure 4.9: 4D likelihood landscape for orbit models of the trixaial Abel model DF1 described in the text. The models are sampled in M/L, T, $\sqrt{T_{\rm maj}}$, $\sqrt{T_{\rm min}}$, and deprojected using viewing angles lying in branch 1. The 1D and 2D likelihood landscapes are obtained by marginalizing over a smoothed 4D landscape generated by Gaussian process regression. The red, green, and blue curves represent the 1σ, 2σ, and 3σ contours, respectively. $\sqrt{T_{\rm maj}}$ and $\sqrt{T_{\rm min}}$ are within 1σ of their true values of 0.47 and 0.53 respectively. M/L and T are within 2σ of the true values of 1.0 and 0.45 respectively.

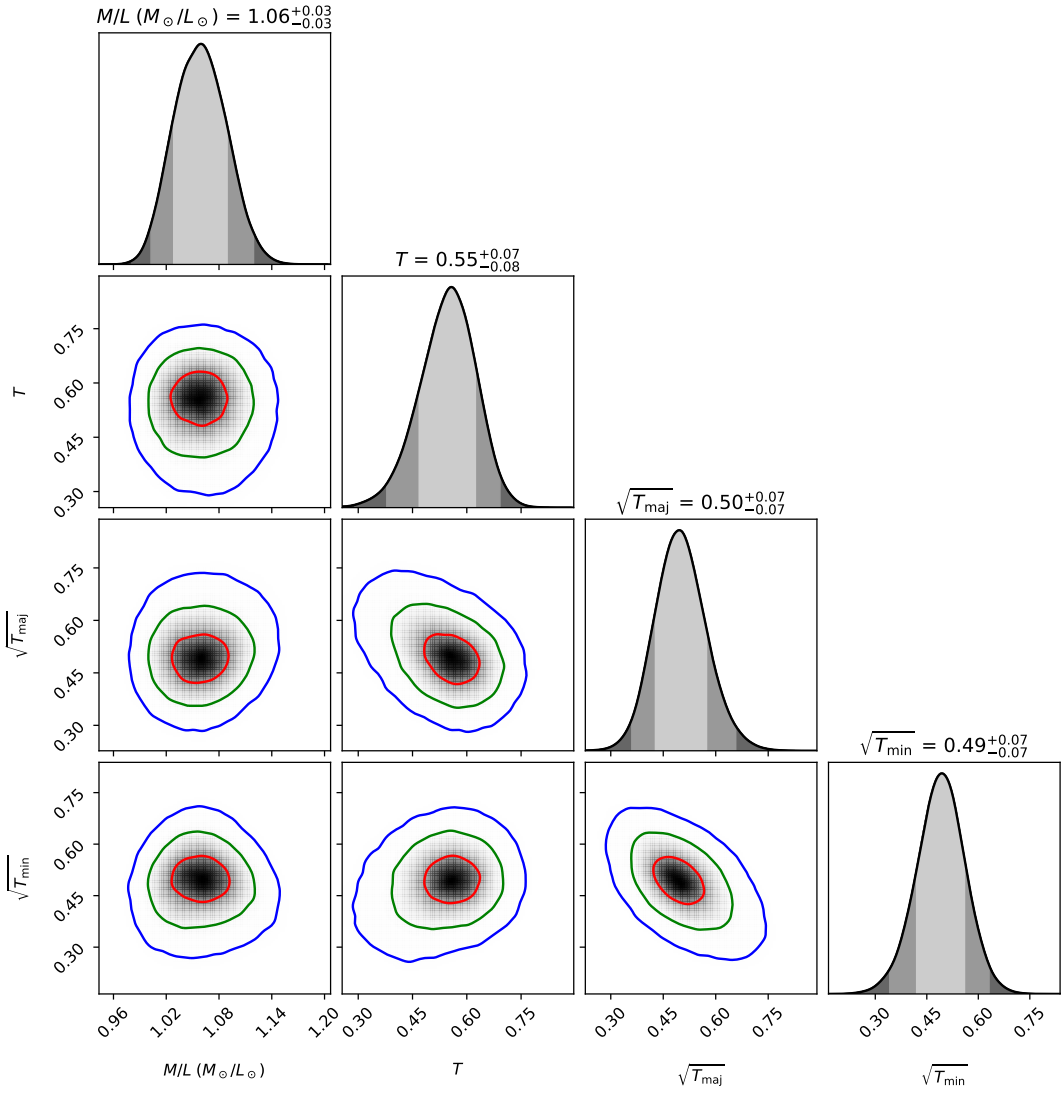

Figure 4.10: 4D likelihood landscape for orbit models of the trixaial Abel model DF2 described in the text. The models are sampled in M/L, T, $\sqrt{T_{\rm maj}}$, $\sqrt{T_{\rm min}}$, and deprojected using viewing angles lying in branch 1. The 1D and 2D likelihood landscapes are obtained by marginalizing over a smoothed 4D landscape generated by Gaussian process regression. The red, green, and blue curves represent the 1σ, 2σ, and 3σ contours, respectively. $\sqrt{T_{\rm maj}}$ and $\sqrt{T_{\rm min}}$ are within 1σ of their true values of 0.47 and 0.53 respectively. M/L and T are within 2σ of the true values of 1.0 and 0.45 respectively.

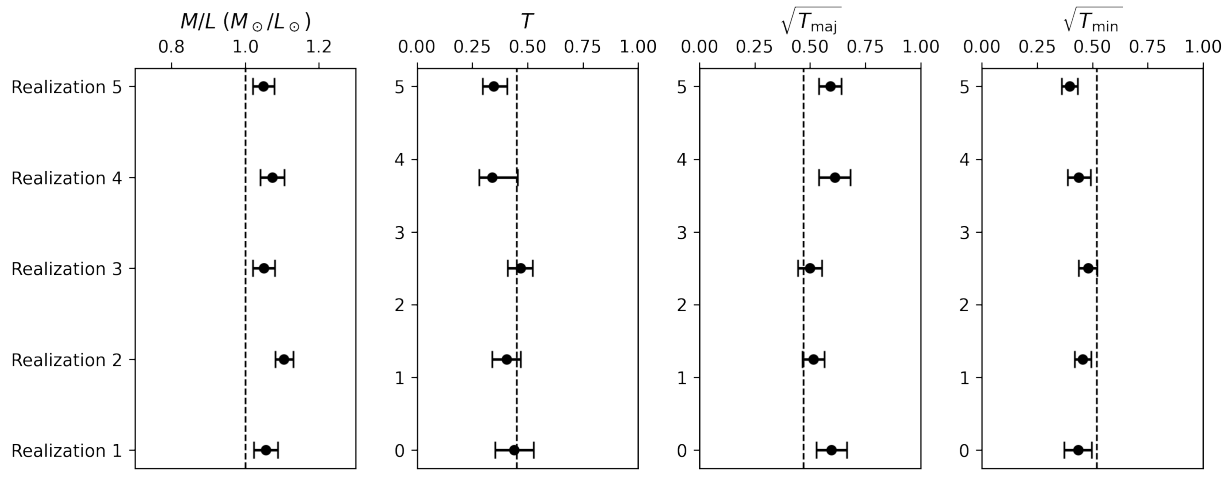

Figure 4.11: 1D marginalized 1σ confidence intervals for orbit model parameters of the triaxial Abel model DF1 described in the text, deprojected with viewing angles lying in branch 1. The 1D confidence intervals are obtained by marginalizing over a smoothed 4D landscape generated by Gaussian process regression. While M/L is consistently overestimated by about 5% ($\sim 2\sigma$), the deviations in the shape parameters are of order 1σ.

4.5 Discussion

Confidence Criteria

Schwarzschild modeling has been widely used to estimate mass distributions in galaxies for several decades. The majority of such work has involved axisymmetric galaxy models. For axisymmetric modeling, the most common method of determining 1σ confidence intervals for a given parameter is to find the maximum and minimum values of this parameter among models with $\Delta\chi^2 < 1$. This method is based on the assumption of a likelihood for each model given by $e^{-\chi^2/2}$, together with the assumption that this likelihood is roughly gaussian near the best-fit value (ie. χ^2 is roughly parabolic).

Throughout this thesis, I have employed a related, but somewhat more general method of determining confidence intervals. In order to relax the assumption of gaussianity near the best-fit value, we instead seek to construct the likelihood as a function of all input parameters. We find gaussian process regression to be a stable, reliable method of determining a smooth interpolation between parameter values in these spaces. We then perform a MCMC in order to sample from this likelihood function. The best-estimate for each parameter is taken to be the median value from these MCMC samples, and the confidence interval is taken to be the range between the 16th and 84th percentiles of the distribution in each parameter.

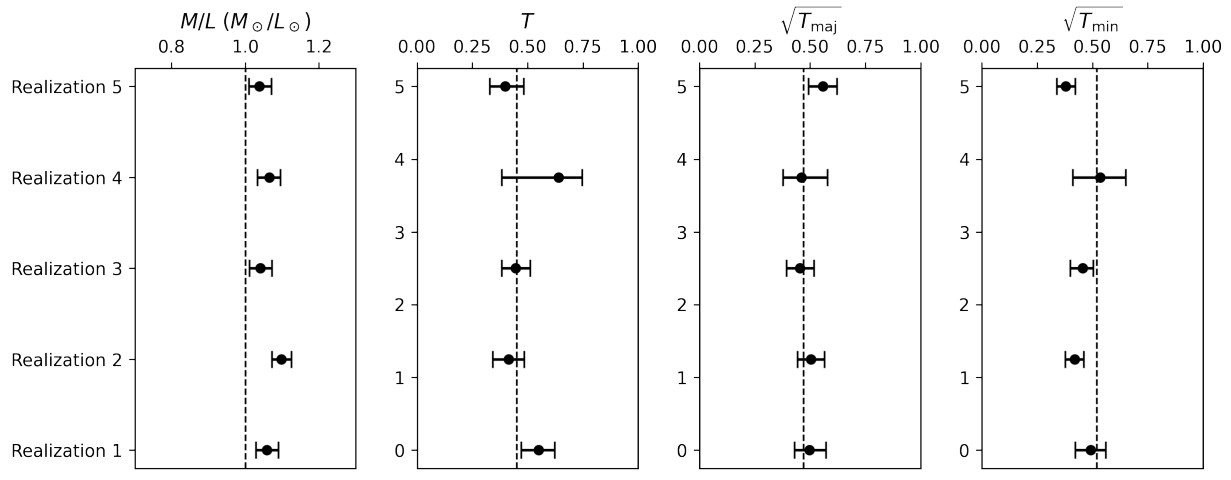

Figure 4.12: 1D marginalized 1σ confidence intervals for orbit model parameters of the triaxial Abel model DF2 described in the text, deprojected with viewing angles lying in branch 1. The 1D confidence intervals are obtained by marginalizing over a smoothed 4D landscape generated by Gaussian process regression. While M/L is consistently overestimated by about 5% ($\sim 2\sigma$), the deviations in the shape parameters are of order 1σ.

This method stands in contrast with most other triaxial orbit modeling. The most commonly used method for triaxial models is based on van den Bosch et al. [59] and van den Bosch and van de Ven [60], though several variations exist. This method is based on the idea that the noise in the χ^2 values themselves is large compared to the $\Delta\chi^2 < 1$ levels that are typically used. This noise level is estimated as $\sqrt{2(N_{\rm kin} - N_{\rm par})}$, where $N_{\rm kin}$ is the number of kinematic constraints in the model (ie. the number of kinematic apertures times the number of GH moments included for each aperture) and $N_{\rm par}$ is the number of mass parameters that are explored (eg. M/L, shape parameters, etc.). Since $N_{\rm kin} \gg N_{\rm par}$ for Schwarzschild models, this noise level is approximated as $\sqrt{2N_{\rm kin}}$, and the 1σ confidence interval for a given parameter is taken to be the range between the maximum and minimum values of this parameter among models with $\Delta\chi^2 < \sqrt{2N_{\rm kin}}$. This criterion was validated in van den Bosch and van de Ven [60], where it was found that recovered parameter values did indeed differ from their true values by roughly the scale set by this criterion. Confidence intervals determined via this method are significantly larger than those determined using the method that I have employed throughout this thesis.

The choice to use a different confidence interval criterion than most previous triaxial models is based on the following argument. For a fixed set of input kinematics, we do not find the χ^2 values of our models to have noise at a scale of $\sqrt{2N_{\rm kin}}$. For a fixed set of input kinematics, the only statistical noise is due to the PSF convolution which is performed by

randomly perturbing projected positions according to a parameterized PSF model. This results in noise levels of $\sim 1 \ll \sqrt{N_{\rm kin}}$. While there are likely to be systematic uncertainties associated with this modeling method, these would certainly would not be well estimated by the assumption of gaussianity used to arrive at $\sqrt{2N_{\rm kin}}$. The χ^2 values do indeed vary on the scale of $\sqrt{N_{\rm kin}}$ when the input kinematics are varied according to their uncertainties, but this is mainly an overall shift in the landscape - the $\Delta\chi^2$ between any two models tends to be much smaller than this estimate.

Ultimately, the correct choice of confidence interval should be the one that best represents deviations from the true parameter values. Further, chapters 2 and 3 outlined several issues with the code that was used to perform the original tests in van den Bosch and van de Ven [60]. The tests performed in this section allow us to compare these two criteria with the updated version of the code. The confidence intervals on the mass averaged axis ratios (u, p, q) are shown in figures 4.13 and 4.14 for several realizations of noise on the input kinematics of DF1 and DF2 respectively. The axis ratios are calculated for the models presented in figure 4.11 and 4.11 by luminosity averaging the axis ratios over the deprojected mass MGE for each model. The black points and errorbars indicate the 1σ confidence intervals calculated via the 16th and 84th percentiles of MCMC samples from a smoothed likelihood function. The red points and errorbars indicate the 1σ confidence intervals calculated as the range of models with $\Delta\chi^2 < \sqrt{2N_{\rm kin}}$. The errorbars in red are excessively conservative. The black errorbars are more representative of the deviations of the black points from the true parameter values.

Reliability of Estimated Parameters

In most cases, the tests described in this section indicate that the statistical uncertainties, as estimated via MCMC samples from a smoothed likelihood function, are representative of actual deviations from the input parameter values. The main exceptions to this for the triaxial Abel models are the $\sim 5\%$ overestimate of M/L and a slight $\sim 1\%$ overestimate of q (or underestimate of $\sqrt{T_{\rm min}}$ by about 0.1). These biases are both of order $\lesssim 2\sigma$.

It is illustrative to compare these tests to those performed in van den Bosch and van de Ven [60]. In that paper, parameter estimates were found to differ from the true values by amounts comparable to the $\Delta\chi^2 < \sqrt{2N_{\rm kin}}$ confidence interval. Given that our deviations are significantly smaller, this suggests that the improvements to the code outlined in chapters 2 and 3 have improved the precision dramatically.

The model DF1 is a particularly direct comparison to van den Bosch and van de Ven [60], as it is equivalent to their ST2. It is important to note that the comparison is not perfect, as the number of kinematic bins is significantly different (I use far fewer bins) and the moment noise is somewhat different between the two analyses. The binning of van den Bosch and van de Ven [60] is not entirely specified, but it is apparent by comparing to figure 4 of van den Bosch and van de Ven [60] that their input kinematics appear to much smoother. One would therefore expect less noise in their parameter estimates than ours. Reading off values from figure 4 of van den Bosch and van de Ven [60], the recovered p value appears to be

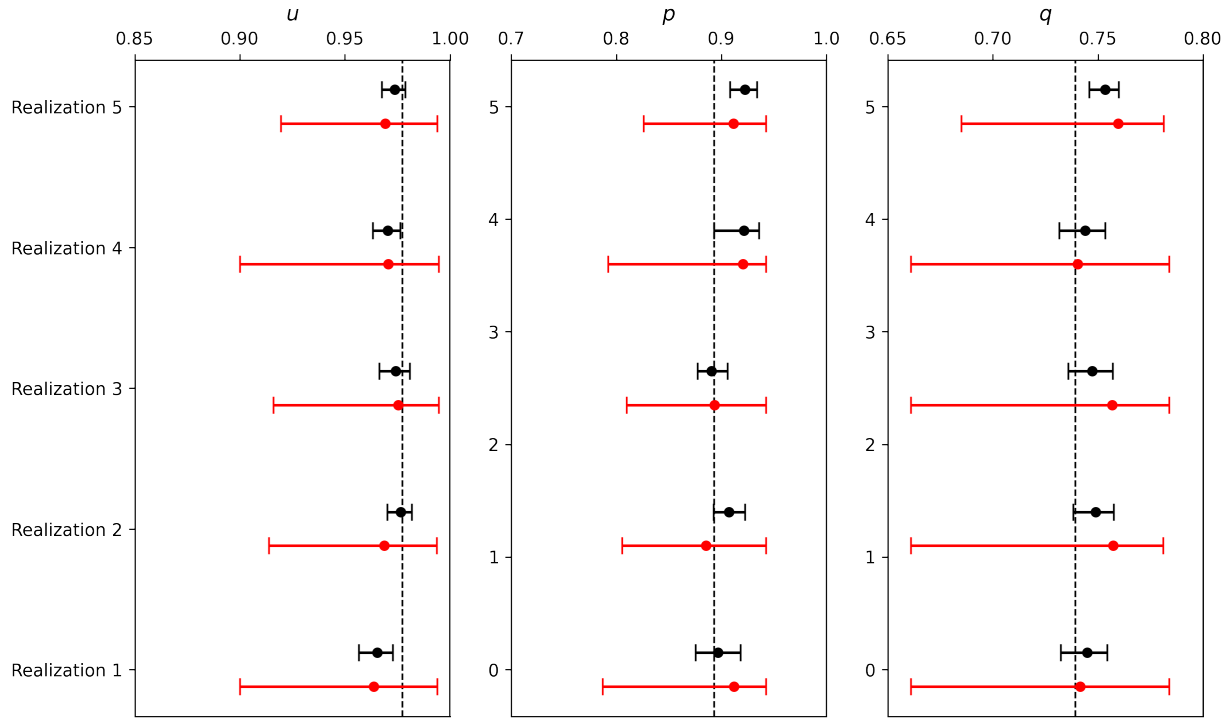

Figure 4.13: 1D marginalized 1σ confidence intervals for luminosity averaged axis ratios of the trixaial Abel model DF1 described in the text, deprojected with viewing angles lying in branch 1. The 1D confidence intervals in black are obtained by marginalizing over a smoothed 4D landscape generated by Gaussian process regression. The 1D confidence intervals in red are determined using the criterion laid out in van den Bosch and van de Ven [60]. The black confidence intervals are a more accurate representation of the deviation from the true parameter values than the red confidence intervals which are overly conservative.

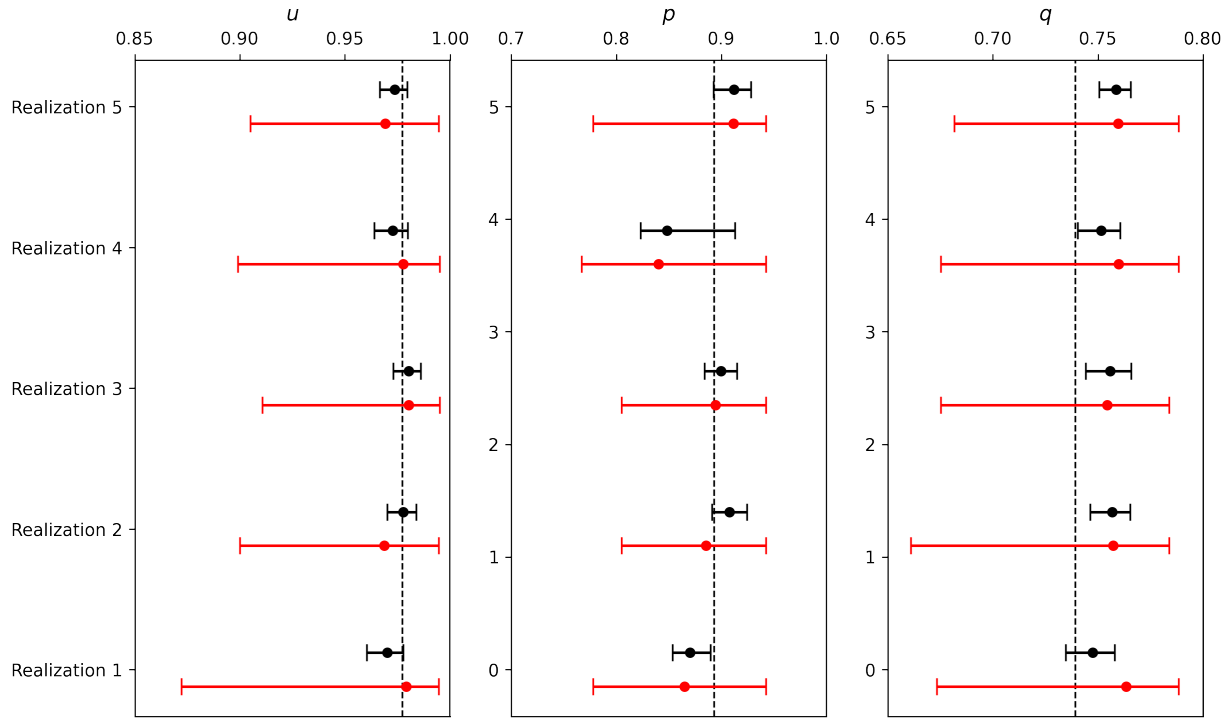

Figure 4.14: 1D marginalized 1σ confidence intervals for luminosity averaged axis ratios of the trixaial Abel model DF2 described in the text, deprojected with viewing angles lying in branch 1. The 1D confidence intervals in black are obtained by marginalizing over a smoothed 4D landscape generated by Gaussian process regression. The 1D confidence intervals in red are determined using the criterion laid out in van den Bosch and van de Ven [60]. The black confidence intervals are a more accurate representation of the deviation from the true parameter values than the red confidence intervals which are overly conservative.

overestimated by 0.08, and the q value appears to be overestimated by about 0.07. These deviations are comparable to the red confidence intervals shown in figure 4.13.

Another point of comparison comes from Jin et al. [75]. In their case, using mock galaxies from the Illustris simulation, they find recovered estimates of p and q to have biases of order 0.07 and 0.14 respectively. Again, these biases are comparable to the red confidence intervals and significantly larger than the black confidence intervals, or any potential bias in our recovered axis ratios.

Another point of comparison is offered by Thater et al. [133]. The authors of this paper concluded that fixing the orbit mirroring bug according to table 3.1 did not have a significant impact on the recovered parameter values. However, figure 4 in this paper shows that the recovered shape parameters differ between the two versions by amounts that are comparable to or larger than their confidence interval based on the $\Delta\chi^2 < \sqrt{2N_{\rm kin}}$ criterion.

The results presented here are consistent in that the recovered value for model DF1 differs from van den Bosch and van de Ven [60] by an amount comparable to the $\Delta\chi^2 < \sqrt{2N_{\rm kin}}$ criterion. However, our conclusion is significantly differnt. Our results demonstrate instead that this confidence interval is overly conservative, and that deviations on this scale indicate dramatic differences in recovered models. We find the updated version of the TriOS code to be able to recover parameter values with $\sim 3-5$ times the precision suggested by the $\Delta\chi^2 < \sqrt{2N_{\rm kin}}$ criterion.

Further evidence for this conclusion is provided by Pilawa et al. [134]. In this case, the recovered inclination from models of massive elliptical galaxy NGC 2693 using the updated version of the code outlined in this dissertation was consistent within 1σ of the inclination inferred from the central dust disk.

The most obvious recovery bias in our tests is in the inclination of the axisymmetric HQ mocks. Edge-on Schwarzschild models are strongly preferred over the true inclination of $\theta = 50°$. This is consistent with several previous papers such as Krajnović et al. [135] and Cappellari et al. [13] which found that Schwarzschild models can place constraints on inclination that may not be reliable. This effect was further explored in Lipka and Thomas [118], who found similar biases towards edge-on inclinations when assigning a likelihood to each model according to $e^{-\chi^2/2}$. By estimating and accounting for the effective number of degrees of freedom for each model, they find that the inclination can indeed be recovered.

Lipka and Thomas [118] go on to suggest that this effect will impact the triaxial case as well. While the fully triaxial case is likely to benefit from a model selection framework that accounts for model flexibility, our results indicate that the problem is not as severe as in the axisymmetric case, at least for the triaxial Abel models explored here. The relatively small upwards bias in M/L and downwards bias in $T_{\rm min}$ (equivalent to a bias towards edge-on) are consistent with the direction of bias observed in Lipka and Thomas [118] for axisymmetric models.

In addition to the sources of systematic uncertainty explored here, real data is likely to give rise to further complications. One major source of uncertainty that we have not addressed is in extraction of the LOSVDs from spectra. This relies on accurate modeling and fitting of stellar templates which can have strong effects on recovered GH moments.

Accurate extraction of kinematics and modeling of their uncertainties is thus essential to obtain accurate estimates of galactic shapes and dynamical masses.

Acknowledgements

Thank you to Shaunak Modak for his work on the Hunter-Qian model implementation.

Chapter 5

Scaling Relations of Massive Ellipticals

While the previous chapters demonstrate how to use photometric and spectroscopic data to constrain stellar density profiles and central SMBHs in elliptical galaxies, this chapter focuses on what can be learned from photometric data alone. Photometric data is much more easily accessible for large galaxy samples. Measuring accurate total magnitudes among massive ellipticals is an important step towards quantifying the $M_{\rm BH} - L$ relation. As well, scaling relations can offer insights into the formation history of galaxies, which are intimately connected with the growth of SMBHs in their centers. For example, variations in formation history with mass can result in curvature in the Faber-Jackson relation. If the Faber-Jackson relation is curved, the power law $M_{\rm BH} - \sigma$ and $M_{\rm BH} - L$ relations must necessarily predict different $M_{\rm BH}$ values for some galaxies. In this chapter, I obtain total magnitudes and luminosities for a volume limited sample of the most massive nearby elliptical galaxies, and explore the scaling relations of this sample. This chapter is taken from a manuscript that is currently in preparation for publication that was co-authored with John P. Blakeslee, Chung-Pei Ma, and Jenny E. Greene. Image stacking was performed by Stephen D. J. Gwyn. Preliminary data analysis was performed by Stephanie Ciccone and Blanka Nyiri.

5.1 Introduction

By studying the properties of nearby massive early-type galaxies (ETGs), we can learn about their evolutionary histories. The growth history of these galaxies can leave measurable impacts on their observed properties. Many of these properties are found to be strongly correlated: the Size-Luminosity (SL) relation describes the correlation between a galaxy's half-light radius (R_e) and its total luminosity (L), and the Faber-Jackson (FJ) relation describes a correlation between a galaxy's velocity dispersion (σ) and total luminosity. These and other scaling relations provide insight into the formation and growth histories of early-type galaxies [e.g., 136, 137, 138, 42].

In order determine the slopes and intercepts of these scaling relations, accurate and precise measurements are needed of the velocity dispersions, half-light radii, and total luminosities. Velocity dispersions were reported for a large subset of the MASSIVE galaxies in Veale et al. [105]. In this paper, we measure the half-light radii and total luminosities for ~ 100 galaxies in the MASSIVE survey for which we have obtained deep, wide-field K-band imaging.

The MASSIVE survey is an ongoing effort to measure and characterize the properties of the most massive nearby ETGs [88]. The full sample comprises 116 galaxies with K-band magnitude < -25.3 mag as measured in the 2MASS extended source catalog, corresponding to stellar masses $M^* \gtrsim 10^{11.5} M_\odot$. The survey is volume limited within a distance of about 100 Mpc in the northern sky. These massive ETGs contain supermassive black holes (SMBHs) at their centers. One of the major goals of the MASSIVE survey is to dynamically model these galaxies and measure their central SMBH masses. Thus, we have obtained wide-field spectroscopic data from the Mitchell IFS [103, 105] as well as high-resolution spectroscopic data from the GMOS IFU [116] to study the kinematics of these galaxies. We have also obtained high resolution photometry from the Hubble Space Telescope's Wide Field Camera 3.

Accurate total luminosities and half-light radii are key to many science goals of the MASSIVE survey. Half-light radii provide a natural scale for each galaxy that have many uses, including studies of both stellar dynamics [116] and the stellar initial mass function [139]. Total luminosities are needed to study the M–L relation, one of the most commonly used local SMBH-host scaling relations [38].

The total magnitude and half-light radii of ETGs can be deduced from their surface brightness profiles. Imaging in the K-band is particularly useful since it accurately traces the stellar populations within ETGs and minimizes extinction due to dust. K-band imaging already exists for the MASSIVE galaxies from the 2MASS extended source catalog (XSC). However, total magnitudes from the XSC have been found to be systematically too faint. The half-light radii from the 2MASS XSC tend to be systematically smaller than other estimates, perhaps due to the underestimate of the total luminosity. This may be due to a combination of extrapolation from insufficiently deep photometry [e.g., 6, 32] and systematic issues in the 2MASS analysis pipeline [140].

In Section 5.2, we describe the CFHT WIRCam data, the data reduction process, and the process for determining total luminosities and half-light radii from the reduced images. In Section 5.3, we compare the resulting parameter values to those from 2MASS, and demonstrate the systematic bias in total luminosities from 2MASS. We analyze the SL and FJ relations in Section 5.5 and Section 5.6 respectively. We then compare these relations to previous analyses from the literature, and discuss their implications about galaxy formation and evolution.

5.2 Observations and Reductions

CFHT WIRCam Observations

The selection of galaxies for the MASSIVE survey is described in detail by Ma et al. [88] and is based on 2MASS photometry combined with distances estimated from the the 2MASS galaxy redshift survey [141]. To obtain improved estimates of the photometric and structural parameters for the MASSIVE sample, we targeted the galaxies for deep wide-field near-infrared imaging with the Wide-field InfraRed Camera [WIRCam; 142] on the Canada-France-Hawaii Telescope (CFHT). We chose to use the K band for these observations because it traces the old populations that make up most of the stellar mass in these galaxies, and it minimizes dust extinction. Priority was given to the subset of 72 MASSIVE galaxies with absolute $M_K < -25.5$ mag, as these were also the priorty targets for the integral field spectroscopy.

The observations presented here were conducted by CFHT staff in Queued Service Observation over a series of semesters from late 2014 to early 2017. The focal plane of WIRCam contains four HAWAII-2RG detectors imaged at a pixel scale of $0''.307$ pix^{-1}, so that each detector covers $10'.2 \times 10'.2$. They are arranged in a square mosaic with $\sim 0'.6$ gaps between the detectors. The full field of view thus spans approximately $20'.8$ square.

We used the "WIRCam Dithering Pattern 5" (WDP5) sequence that successively places the target on each of the four detectors array of the mosaic, and then steps through the sequence five times, ensuring small offsets of about $1''$ between subsequent placements of the target on the same detector, for a total of 20 exposures. For the first two semesters of the program, we executed this pattern twice in succession with individual exposures of 20 s, followed by a WDP3 sequence (stepping through all four chips 3 times) with exposures of 10 s to avoid saturation. This gave total on-target exposure times of 920 s for extremely deep images. With overheads, the executime time was 24 minutes per target, not including slew.

However, by analyzing the images, we found that this amount of exposure was excessive for our purpose. Tests showed the results were not significantly affected when using half of the exposure stack, as systematic effects in the sky estimation become dominant. In addition, we found that in good seeing conditions, the centers of some galaxies could saturate even in 10 s exposures (these were later reobserved). We therefore adopted a revised observing strategy that consisted of a single "long" WDP5 sequence with 20 s exposures followed by another "short" sequence with 3 s exposures to ensure that none of the galaxies saturated in the center. The resulting total exposure time was thus 460 s per galaxy. Under typical conditions, this approach yielded a 3-σ surface brightness limit of $\mu_K \approx 23.0$ AB mag arcsec^{-2}, roughly 2.5 mag fainter than 2MASS. Repeat observations showed that there were no systematic differences between the results obtained with the original and revised observing strategies.

In all, we obtained high quality imaging for 98 MASSIVE survey galaxies, but for the luminous galaxy pair NGC 545 & NGC 547, our standard photometric analysis procedure did not yield reliable results because their isophotes are so strongly overlapping. Thus, in this work, we present new photometric and structural parameter measurements for a total

of 96 galaxies.

Image Processing

Standard detrending of the WIRCam exposures was performed by the IDL Interpretor of WIRCam Images ('I'iwi) processing pipeline at CFHT.[1] 'I'iwi identifies and flags saturated pixels, corrects the pixel intensities for nonlinearity effects, performs bias and dark current subtraction, divides by the normalized flat field, and then masks the known bad pixels. It also performs initial sky subtraction using offset fields; the sky level estimation is improved during the stacking process.

The sets of detrended exposures for each galaxy observation were then processed with the WIRWolf imaging stacking pipeline [143]. WIRWolf performs automatic photometric and astrometric calibration by matching the detected sources in each WIRCam exposure against the 2MASS catalog data. After this initial iteration, it then matches the stellar magnitudes for each exposure to a master catalogue generated from the full set of images in the stack. This procedure results in an internal photometric accuracy typically better than 0.003 mag for each exposure relative to all the others. WIRWolf also refines the relative background levels of each detector in each exposure at this stage. It then uses SWarp [144] to resample and stack the images onto a fixed grid with a default pixel size of $0''.3$ (very close to the average raw pixel scale of WIRCam). It then performs a final absolute photometric calibration by comparing the source magnitudes in the stack image against the magnitudes from 2MASS.

According to the online documentation for WIRWolf,[2] the absolute photometric accuracy of the stacked WIRCam images is typically 0.02 mag in the J and H bands and 0.03 mag for the K band because there are generally fewer sources that are of sufficient signal-to-noise in 2MASS and not saturated in the WIRCam K-band images. We checked the photometric calibrations by running SExtractor [145] on our stacked K-band images to extract point source magnitudes and then comparing to 2MASS. Any sources that had poor quality flags or that appeared to be saturated were omitted from the comparison. We confirmed that the mean photometric offsets determined from the stacked images with respect to 2MASS are accurate within a scatter of 0.03 mag. This is small compared the scatter in the comparison of the total magnitudes of our sample galaxies (see Section 5.3). Thus, we do not find any reason to adjust the photometric calibrations derived by WIRWolf. However, for consistency with 2MASS, we convert from AB to Vega magnitudes by subtracting 1.88 mag following the WIRWolf online documentation.

In some of the images, a cross-shaped pattern is apparent, centered on a star that was used for guiding the telescope during the observation. This pattern indicates a deficit of light within the columns and rows containing the star. In these cases, we mask the affected rows and columns within the image. In a few cases, the galaxy itself was used for guiding,

[1] https://www.cfht.hawaii.edu/Instruments/Imaging/WIRCam/IiwiVersion1Doc.html

[2] https://www.cadc-ccda.hia-iha.nrc-cnrc.gc.ca/en/wirwolf/

resulting in a cross pattern on the galaxy nucleus. These observations could not be used, and we reobserved the galaxies in subsequent runs, explicitly instructing the software to avoiding guiding on sources within a 30″ radius of the galaxy center. In addition, some very bright stars can producing a bleeding effect, giving an excess of light along the entire column containing the star. In these cases, we also masked the affected column.

In addition to the above problems relating to stars in the images, vertical bands of variable bias levels appeared in the WIRCam data in 2016A, and CFHT implemented a correction by subtracting the median of each column. However, due to the extended nature of our targets, this did not work well for our data and resulted in significant deficits of light above and below the galaxy. We corrected for this by aggressively masking the main galaxy and all other foreground sources above the local background, and then subtracting the median values from each column determined near the top and bottom of the image. This essentially removed the correction applied by CFHT. We then requested the observatory to process all subsequent data without applying that correction. The vertical bias bands tend to average out in the stacked image.

5.3 Galaxy Parameter Measurements

Curve of Growth Analysis

We determine the total magnitude and half-light radius of each galaxy from the stacked image using the galaxy photometry package ARCHANGEL [146]. Specifically, we use the *profile*, *sky_box*, *bdd*, and *el* routines within ARCHANGEL. Figure 5.1 illustrates the basic procedure using the galaxy NGC 393 as an example. The steps in the procedure are discussed in more detail below.

The *profile* routine produces an elliptical isophotal profile from an input image. It begins by determining an approximate sky level in the image. Sky boxes are scattered around the edge of the image. After discarding boxes that differ from the mean by more than 4 standard deviations, the mean intensity value from these boxes is then taken as the sky intensity. The uncertainty on the sky value is taken to be the standard deviation of this mean. The routine then searches for sources in the image that exceed the sky level by a given number of standard deviations and masks them.

Next, the routine performs the elliptical isophote fitting. The resulting ellipses are shown in the top right panel of Figure 5.1 for NGC 393. Ellipses are first fit to the isophotes of the cleaned image. The ellipticities and position angles of the ellipses are allowed to vary with radius. Any drastic changes between adjacent ellipses are smoothed out to generate a more regular profile. Then, any pixels along each isophote that differ from the mean intensity by more than 4 standard deviations are masked. Then, ellipses are fitted to this new cleaned image, and the process is repeated to obtain a final cleaned image. A final set of ellipses are fitted to the final cleaned image and the profile is smoothed once again. This results in an isophotal profile for the image.

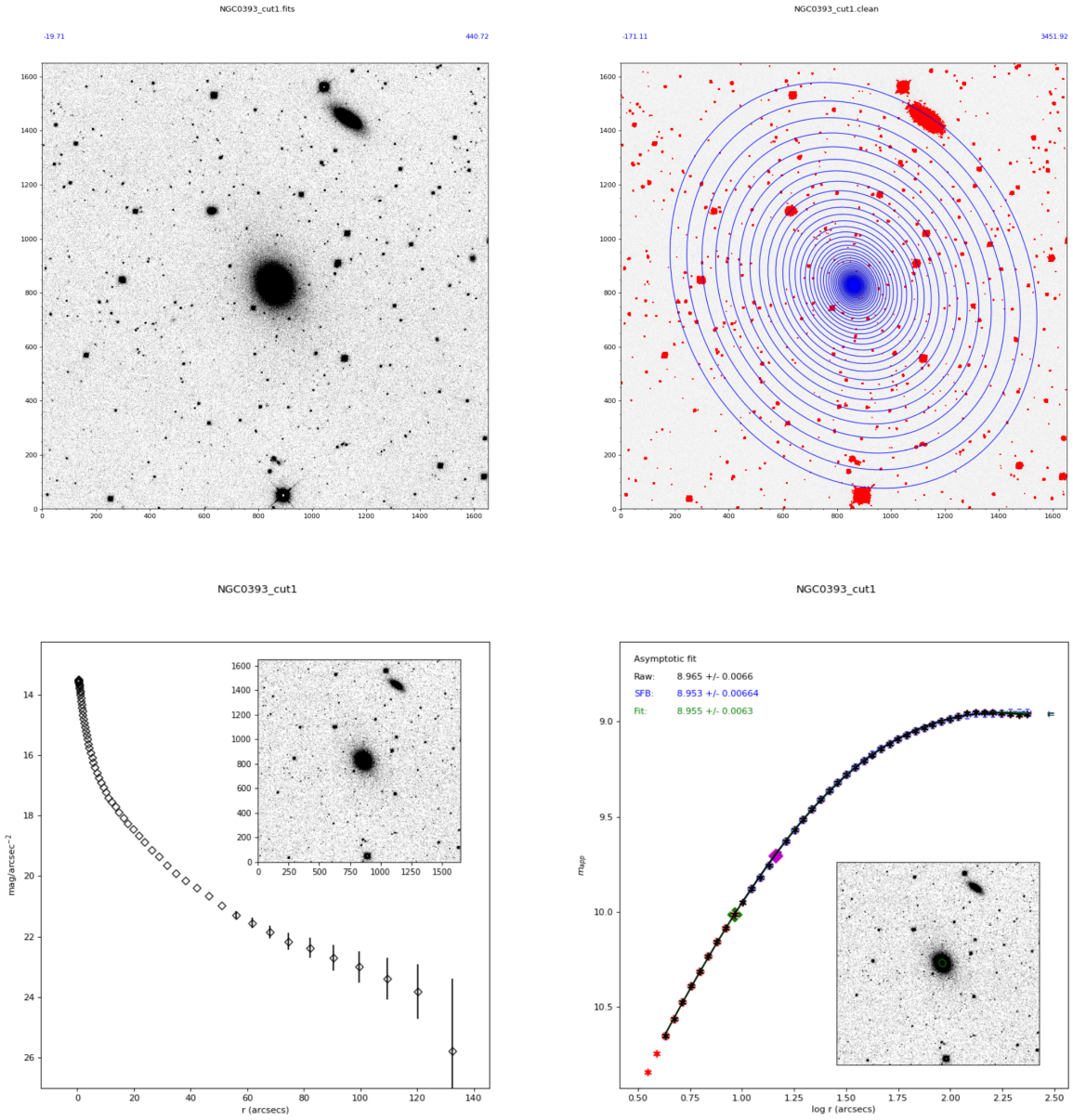

Figure 5.1: Output plots from the ARCHANGEL pipeline for elliptical galaxy NGC 393. (Top left) The original CFHT WIRCam image. (Top right) Elliptical isophotes overlaid on the image, with masked regions in red. (Bottom left) Surface brightness profile as a function of radius. (Bottom right) Curve of growth, showing the enclosed magnitude as a function of isophotal semi-major axis. After iterating to improve the sky estimate, the program converges on a total K magnitude for the galaxy of 8.95 mag. The magenta diamond marks the empirically-determined half-light radius.

In order to get an improved estimate of the sky value, we use the *sky_box* routine on the cleaned image. This routine scatters boxes that are 20 pixels by 20 pixels around the image, using the fitted isophotes to avoid the galaxy light. We find that re-fitting the sky value with the cleaned image results in a more robust determination than the preliminary fit performed in the *profile* routines

The *bdd* routine takes the sky value and isophotal profile and determines the corresponding surface brightness profile. The surface brightness profile for NGC 393 is shown in the bottom left panel of Figure 5.1. Parametric fits to this surface brightness profile can also be performed.

Finally, the *el* routine performs aperture photometry using the elliptical isophotes. The routine begins by filling in the masked pixels in the image with values interpolated from the isophotal profile. Then, the total luminosity within each elliptical isophote is calculated from this interpolated image. The curve of total luminosity or magnitude versus isophotal semimajor axis (shown in the bottom right panel of Figure 5.1) is referred to as a curve-of-growth. Near the edge of the image, galaxy light can be dominated by sky noise. In this case, directly summing the pixels within each isophote can lead to unreliable values. To obtain a more reliable estimate, the aperture luminosities are instead estimated by interpolating the 1D surface brightness profile. This reduces noise near the outer edge of the curve of growth.

If the galaxy light is fully contained within the field of view of the image and the sky is accurately estimated, the curve of growth will flatten at large radii. In some cases, the curve of growth does not flatten for our images. This happens in our images of 14 galaxies. Since these galaxies appear to be fully contained within the image frame, we adjust the sky value within its uncertainty in order to force the curve of growth to flatten at large radii.

Once the curve of growth visually flattens, the outer end of the curve of growth is then fit with a rational function given by a ratio of two polynomials of degree 2 as described in Schombert [146] in order to capture the asymptotic behaviour. This fit is then evaluated at the outermost fitted isophote to estimate the total luminosity. The semi-major axis of the elliptical isophote containing half the total galaxy light is then determined by interpolating the curve of growth. We also interpolate the surface brightness profile to determine the semi-minor axis (and thus the observed axis and ellipticity) of the half-light isophote.

The main photometric parameters that we consider in this paper are the total absolute K-band magnitude M_K (or, equivalently, the K-band luminosity L_K) and the semi-major axis half-light radius R_e (or, alternatively, the circularized version $R_{e,\mathrm{circ}}$). Table 5.1 lists our measurements of these photometric parameters as well as other properties of the MASSIVE survey galaxies. The following sections discuss these measurements in more detail.

Total Magnitudes

We compare our total K-band magnitudes derived with Archangel to those from the 2MASS Extended Source Catalog (XSC). For apparent K-band magnitude, we use 2MASS parameter k_m_ext. This is the K-band magnitude measured within a 20 mag/arcsec^2 isophotal aperture, extrapolated beyond the aperture via a Sérsic fit.

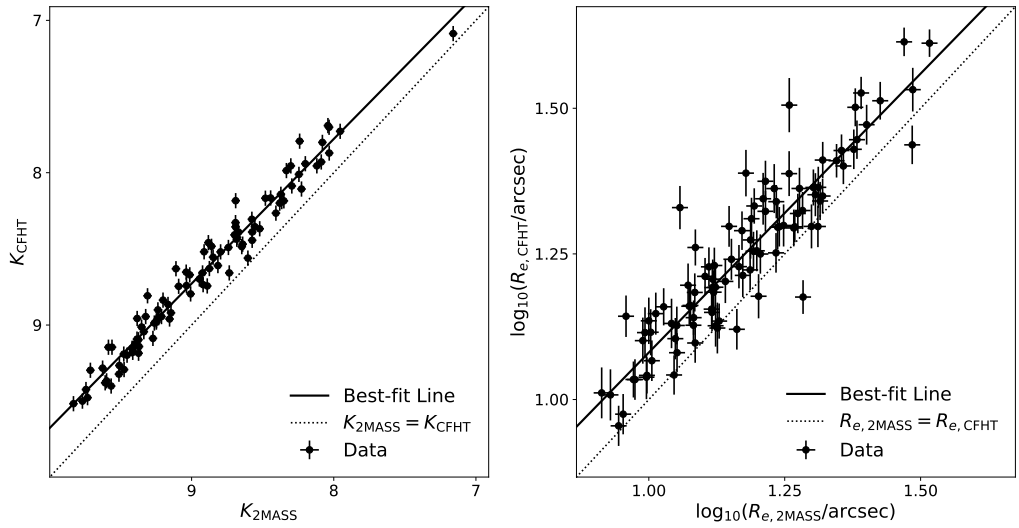

Figure 5.2: Comparison of photometric properties measured with CFHT to 2MASS values. (a) Total K-band magnitudes. (b) K-band half-light radii.

The galaxy magnitudes measured from the CFHT curve of growth are systematically brighter than the corresponding magnitudes from the 2MASS survey. This is demonstrated in the left panel of Figure 5.2. The best-fit linear relation between the apparent K-band magnitudes from CFHT and 2MASS is given by

$$(K^{\rm CFHT} - 9) = b_K(K^{\rm 2MASS} - 9) + a_K\,, \tag{5.1}$$

where the best-fit values of these parameters are $a_K = -0.273^{+0.009}_{-0.010}$ and $b_K = 0.949^{+0.019}_{-0.018}$ from *LinMix*. The slope is mildly inconsistent with unity. $K^{\rm CFHT}$ has an average scatter of 0.09 about this relation. On average, $K^{\rm CFHT}$ is brighter than $K^{\rm 2MASS}$ by 0.27 ± 0.01 mag.

Schombert and Smith [140] reported a bias in total magnitudes extracted from the 2MASS XSC. The surface brightness profiles extracted from 2MASS are systematically too dim, particularly at larger radii. The source of this discrepancy was determined to be an issue with the 2MASS sky subtraction scheme. The surface brightness profiles, which are used to determine aperture and total magnitudes, were found to be too dim by a uniform shift in intensity for each galaxy. Consequently, total J magnitudes from 2MASS were found to be systematically too faint by an average of 0.33 mag. These authors did not provide a direct comparison for the K band, but their discussion suggests that the size of the offset should be similar.

The offset that we measure at $K_{\rm 2MASS} \sim 10$ mag is 0.32 ± 0.02 mag, consistent the result of Schombert and Smith [140] in the J band. However, we find the slope of the

relation between $K_{\rm CFHT}$ and $K_{\rm 2MASS}$ to be less than 1, meaning the offset between the two sets of magnitudes decreases for the brightest galaxies in our sample. For example, $K_{\rm CFHT} - K_{\rm 2MASS} \sim -0.18$ mag at $K_{\rm 2MASS} \approx 7.5$ mag. For giant ellipticals, this corresponds to $J_{\rm 2MASS} \approx 8.5$ mag. Examination of Figure 12 from Schombert and Smith [140] reveals that the offset for the brightest $\sim$2 mag of their comparison with 2MASS is significantly smaller than the quoted mean and is approximately $J - J_{\rm 2MASS} \sim -0.2$ mag, which is very similar to what we find in our K-band comparison.

Comparable 2MASS magnitude offsets have been observed in other samples as well. Ríos-López et al. [147] use Galfit to measure total extrapolated magnitudes from 2MASS images for 101 bright, nearby galaxies, including 20 early-type galaxies. They find no significant offset with respect to the 2MASS XSC total magnitudes for late-type galaxies, but they do find significant offsets for the smaller sample of early-type galaxies. In the K-band, they report a mean offset of 0.34 ± 0.07 mag; however, the scatter is large, and the sample includes several intrinsically faint nearby galaxies, including two Local Group dwarf ellipticals. If we limit the comparison to the subsample of 17 early-type galaxies $\gtrsim 10$ Mpc to make it more similar to our sample, then the weighted offset is 0.36 ± 0.08 mag, with a scatter of 0.32 mag and a median offset of 0.27 mag. The scatter is several times larger than we find, but the offset agrees with our result.

Läsker, Ferrarese, and Van De Ven [148], again using Galfit to do 2-D parametric modeling, measure extrapolated K-band magnitudes from CFHT/WIRCam data for a sample of 35 nearby galaxies of all morphological types with well-measured central black hole masses. These authors report several versions of the total magnitudes, including magnitudes derived from a single Sérsic model, a "standard bulge plus disk" model, and an "improved" model that adds structural components (up to six in some cases) to the standard model until the residuals over the field are judged visually to be at an acceptable level. They quote an average offset of 0.34 mag for their the total magnitudes from their "improved" models with respect to 2MASS, in the sense that 2MASS is too faint.

If we omit the spirals and consider only the 31 galaxies that Läsker, Ferrarese, and Van De Ven [148] classify as either elliptical or S0, then the mean offset (unweighted, as the authors do not provide uncertainties) with respect to the magnitudes from their "improved" models is 0.34 mag, the scatter is 0.28 mag, and the median offset is 0.25 mag. However, we note that for this subset of early-type galaxies, the standard bulge+disk models in Läsker, Ferrarese, and Van De Ven [148] give better agreement with the 2MASS total magnitudes, with a scatter of 0.20 mag, or 40% less than the scatter given by their "improved models." Using this set of model magnitudes, the mean magnitude offset for the 31 early-types is 0.27 ± 0.04 mag, and the median offset is also 0.27 mag. This is identical to the mean offset that we find with respect to 2MASS, but the scatter in our comparison is a factor of two lower.

Four of the galaxies in the MASSIVE survey were studied in Läsker, Ferrarese, and Van De Ven [148]: NGC 4486 (M87), NGC 4649 (M60), NGC 5252, and NGC 7052. Of these, we obtained new CFHT data for NGC 5252 and NGC 7052, which were processed as described in Section 5.2. For NGC5252, our K-band total magnitude is 0.27 mag brighter than the

result from their standard model, and 0.13 mag fainter than their "improved" model (which is 0.40 mag brighter than 2MASS). For NGC 7052, our measurement is 0.09 mag fainter than their standard model, and they do not make any improvements to that model. Thus, from this very small direct comparison, the offsets are consistent with the scatter.

We conclude that our measured offset of 0.27 ± 0.01 mag with respect to the K-band total magnitude from the 2MASS XSC agrees well with previous studies. The scatter we find of 0.09 mag is considerably less than previous comparisons using parametric modeling. Finally, for the subset of early-type galaxies in Läsker, Ferrarese, and Van De Ven [148], the standard bulge+disk models appear to give more robust magnitudes than the "improved" models.

Half-light Radius

The half-light radii derived from CFHT can be compared to those of the 2MASS XSC. 2MASS measured the semi-major axis of the half-light elliptical isophote in 3 different bands (listed as parameters j_r_eff, h_r_eff, and k_r_eff). We take the K-band half-light radius, k_r_eff, to compare to our CFHT K-band photometry.

The effective radii derived from CFHT are systematically larger than those from 2MASS. This is shown in the right panel of fig. 5.2. The best-fit power-law relation between the 2MASS and CFHT half-light radii is given by:

$$\log_{10}\left(\frac{R_e^{\mathrm{CFHT}}}{10^{1.2}\ \mathrm{arcsec}}\right) = b_{R_e}\log_{10}\left(\frac{R_e^{\mathrm{2MASS}}}{10^{1.2}\ \mathrm{arcsec}}\right) + a_{R_e}, \tag{5.2}$$

where the best-fit values of these parameters are $a_{R_e} = 0.072 \pm 0.006$ and $b_{R_e} = 0.96 \pm 0.04$. The slope is consistent with unity to within 1σ. R_e^{CFHT} has a mean scatter of 0.06 dex about this relation. On average, the half-light radii from CFHT range are a factor of $10^{0.072} = 1.18$ times larger than from 2MASS. Since half-light radii are derived from total magnitudes, a shift in a total magnitude value will translate into a shift in the half-light radius. Thus, the offsets reported in half-light radius correlate with the offsets in magnitude between our CFHT data and 2MASS.

In some contexts, it is useful to consider the geometric, or circularized radius of the half-light isophote. The ellipticity of the half-light isophote is needed to determine this from the major axis. We compare the elliptical axis ratios of our isophotes to those reported by 2MASS. For this, we use the sup_ba parameter from the 2MASS catalog. Our average observed flattening is in excellent agreement with 2MASS. There is no significant shift between the two. The CFHT values display a scatter of 0.06 about the 2MASS values.

Table 5.1: (1) Galaxy name. (2) Angular semi-major axis of the half-light elliptical isophote from K-band CFHT imaging. (3) Angular semi-major axis of the half-light elliptical isophote from 2MASS in K-band (*k_r_eff*). (4) Ellipticity of the half-light elliptical isophote from K-band CFHT imaging. (5) Ellipticity of the 3-σ elliptical isophote from 2MASS in the combined J+H+K-band image (1-*sup_ba*). (6) Total K-band apparent magnitude from CFHT imaging. (7) Total K-band apparent magnitude from 2MASS. (8) Distance, as reported in Jensen et al. [117] where available (indicated by *), otherwise from Ma et al. [88]. (9) Total K-band absolute magnitude based on CFHT imaging. (10) Semi-major axis of the half-light elliptical isophote from K-band CFHT imaging, converted to physical units using the adopted distance. (11) Geometric radius of the half-light elliptical isophote from K-band CFHT imaging, in physical units. (12) Velocity dispersion within the half-light radius as reported by Veale et al. [105], where the radius comes from the NSA where available or 2MASS corrected to agree with NSA on average. (13) Central velocity dispersion [105]

Name	R_e (")	$R_e^{\rm 2MASS}$ (")	ϵ	$\epsilon^{\rm 2MASS}$	K (mag)	$K^{\rm 2MASS}$ (mag)	D (Mpc)	M_K (mag)	R_e (kpc)	$R_{e,\rm circ}$ (kpc)	σ_e (km/s)	σ_c (km/s)
(1)	(2)	(3)	(4)	(5)	(6)	(7)	(8)	(9)	(10)	(11)	(12)	(13)
NGC0057	16.91	14.65	0.14	0.2	8.42	8.68	66.9*	-25.73	5.48	5.07	251	289
NGC0080	21.04	16.39	0.11	0.08	8.66	8.92	81.9	-25.93	8.35	7.9	222	248
NGC0128	14.99	19.22	0.5	0.7	8.37	8.52	59.3	-25.51	4.31	3.04		
NGC0227	13.65	10.0	0.35	0.24	8.75	9.09	75.9	-25.66	5.02	4.05		
NGC0315	25.7	22.15	0.26	0.24	7.73	7.96	68.1*	-26.46	8.48	7.31	341	348
NGC0383	22.11	16.23	0.13	0.16	8.17	8.48	66.1*	-25.95	7.09	6.59	257	290
NGC0393	14.5	11.93	0.17	0.18	8.95	9.23	85.7	-25.73	6.03	5.49		
NGC0410	21.11	19.18	0.26	0.26	8.2	8.38	61.3*	-25.76	6.27	5.39	247	291
NGC0467	19.49	14.84	0.05	0.08	8.67	9.01	75.8	-25.74	7.16	6.98		
PGC04829	9.01	8.8	0.26	0.34	9.48	9.73	99.0	-25.56	4.33	3.71		
NGC0499	13.2	14.52	0.36	0.36	8.66	8.74	69.8	-25.58	4.47	3.57	266	274
NGC0507	31.75	23.98	0.15	0.08	7.96	8.3	61.7*	-26.01	9.5	8.74	257	274
NGC0533	29.63	25.16	0.25	0.24	8.17	8.44	72.8*	-26.15	10.46	9.08	258	280
NGC0545							79.0				231	249
NGC0547		29.58		0.28		8.49	75.5				232	259
NGC0665	13.27	13.37	0.24	0.38	8.63	8.88	62.3*	-25.37	4.01	3.49	164	206
UGC01332	18.79	15.39	0.24	0.3	9.19	9.48	99.2	-25.85	9.04	7.87	253	248
NGC0708	34.04	30.59	0.3	0.4	8.44	8.57	61.5*	-25.53	10.15	8.49	219	206

Name	R_e	R_e^{2MASS}	ϵ	ϵ^{2MASS}	K	K^{2MASS}	D	M_K	R_e	$R_{e,circ}$	σ_e	σ_c
	(")	(")			(mag)	(mag)	(Mpc)	(mag)	(kpc)	(kpc)	(km/s)	(km/s)
(1)	(2)	(3)	(4)	(5)	(6)	(7)	(8)	(9)	(10)	(11)	(12)	(13)
UGC01389	13.03	9.84	0.14	0.34	9.28	9.63	99.2	-25.76	6.27	5.83		
NGC0741	25.17	22.8	0.18	0.36	8.09	8.3	69.6*	-26.14	8.49	7.71	289	292
NGC0777	16.69	15.36	0.18	0.1	8.19	8.37	68.0*	-25.99	5.5	4.98	291	324
NGC0890	23.14	20.5	0.39	0.38	8.01	8.24	45.6*	-25.31	5.11	4.0	194	207
NGC0910	19.83	14.05	0.08	0.16	8.84	9.2	77.9*	-25.64	7.49	7.17	219	236
NGC0997	11.66	10.13	0.14	0.18	9.16	9.42	90.4	-25.66	5.11	4.73	215	267
NGC1016	19.7	18.48	0.05	0.08	8.31	8.58	85.9*	-26.37	8.2	8.01	279	286
NGC1060	19.9	17.7	0.23	0.14	7.94	8.2	53.8*	-25.77	5.19	4.54	271	310
NGC1066	19.79	18.56	0.2	0.2	8.74	8.89	67.4	-25.46	6.47	5.78		
NGC1132	24.42	18.12	0.36	0.34	8.99	9.26	97.6	-25.98	11.56	9.25	218	239
NGC1129	41.12	29.49	0.22	0.2	7.79	8.24	66.2*	-26.35	13.2	11.69	259	241
NGC1167	22.35	20.88	0.17	0.22	8.47	8.64	53.7*	-25.24	5.82	5.31	172	188
NGC1226	15.95	13.83	0.16	0.18	8.94	9.21	85.7	-25.78	6.63	6.08	229	274
IC0310	13.41	12.08	0.05	0.04	8.92	9.14	71.0*	-25.39	4.62	4.5	205	218
NGC1272	25.77	20.89	0.04	0.02	8.36	8.69	71.0*	-25.95	8.87	8.69	250	285
UGC02783	9.44	8.97	0.11	0.16	9.09	9.27	85.8	-25.63	3.93	3.7	266	292
NGC1453	19.76	17.26	0.19	0.14	7.95	8.12	51.2*	-25.62	4.91	4.43	272	312
NGC1497	13.39	13.27	0.34	0.4	9.29	9.48	87.8	-25.49	5.7	4.63	190	234
NGC1600	27.93	24.15	0.33	0.26	7.69	8.04	71.7*	-26.6	9.71	7.97	293	346
NGC1573	17.86	17.14	0.29	0.34	8.35	8.56	63.5*	-25.7	5.5	4.62	264	288
NGC1684	23.02	17.01	0.29	0.24	8.33	8.69	62.8*	-25.68	7.01	5.91	262	295
NGC1700	16.34	14.89	0.27	0.28	7.93	8.09	52.2*	-25.67	4.13	3.52	223	236
NGC2208	21.86	17.16	0.43	0.32	8.65	9.04	84.1	-26.02	8.91	6.7	255	268
NGC2256	26.76	22.62	0.19	0.2	8.39	8.67	79.4	-26.15	10.3	9.27	259	240
NGC2274	18.0	15.8	0.12	0.1	8.44	8.68	69.1*	-25.79	6.03	5.66	259	288
NGC2258	19.82	19.92	0.21	0.24	8.11	8.23	57.0*	-25.71	5.48	4.86	254	293
NGC2320	16.27	12.69	0.42	0.3	8.55	8.85	89.4	-26.22	7.05	5.35	298	340
UGC03683	14.11	13.07	0.21	0.26	8.96	9.15	85.1	-25.72	5.82	5.18	257	257

Name	R_e	R_e^{2MASS}	ϵ	ϵ^{2MASS}	K	K^{2MASS}	D	M_K	R_e	$R_{e,circ}$	σ_e	σ_c
	(")	(")			(mag)	(mag)	(Mpc)	(mag)	(kpc)	(kpc)	(km/s)	(km/s)
(1)	(2)	(3)	(4)	(5)	(6)	(7)	(8)	(9)	(10)	(11)	(12)	(13)
NGC2332	13.51	11.01	0.36	0.34	9.12	9.39	89.4	-25.66	5.86	4.69	224	254
NGC2340	32.58	26.65	0.44	0.44	8.46	8.88	79.9*	-26.08	12.62	9.42	235	232
UGC03894	14.3	13.05	0.1	0.12	9.19	9.37	97.2	-25.77	6.74	6.38	255	297
NGC2418	14.46	11.87	0.21	0.12	8.7	8.94	74.1	-25.66	5.19	4.61	217	245
NGC2456	15.27	12.15	0.25	0.24	9.52	9.83	107.3	-25.65	7.94	6.86		
NGC2492	10.82	9.43	0.22	0.16	9.37	9.6	97.8	-25.6	5.13	4.53		
NGC2513	17.97	15.58	0.19	0.2	8.49	8.74	71.1*	-25.78	6.2	5.57	253	280
NGC2672	20.86	18.8	0.15	0.28	8.18	8.35	66.2*	-25.93	6.7	6.17	262	273
NGC2693	15.04	15.92	0.27	0.26	8.56	8.6	71.0*	-25.7	5.18	4.43	296	327
NGC2783	24.47	15.09	0.4	0.44	8.94	9.32	101.4	-26.09	12.03	9.28	264	252
NGC2832	23.12	20.08	0.25	0.18	8.41	8.7	105.2	-26.71	11.79	10.25	291	327
NGC2892	15.57	13.09	0.03	0.08	9.01	9.35	101.1	-26.04	7.63	7.5	234	237
NGC2918	11.0	9.92	0.32	0.22	9.4	9.57	102.3	-25.65	5.46	4.51		
NGC3158	20.44	15.45	0.18	0.16	8.52	8.8	91.5*	-26.29	9.07	8.23	289	301
NGC3209	14.04	10.3	0.26	0.24	9.04	9.34	94.6	-25.84	6.44	5.55	247	288
NGC3332	16.99	13.2	0.14	0.08	9.1	9.37	89.1	-25.66	7.34	6.82		
NGC3343		12.68		0.32		9.57	93.8					
NGC3462	12.03	11.27	0.25	0.2	9.14	9.37	99.2	-25.85	5.79	5.0	214	233
NGC3562	13.9	9.08	0.2	0.16	8.96	9.38	101.0	-26.08	6.81	6.09	241	250
NGC3615	13.05	10.08	0.34	0.34	9.2	9.45	101.2	-25.83	6.4	5.2	232	268
NGC3805		9.4		0.26		9.3	99.4				225	266
NGC3816		13.76		0.4		9.6	99.4				191	212
NGC3842		15.62		0.18		9.08	87.5				231	262
NGC3862		11.12		0.08		9.49	99.4				228	248
NGC3937		12.53		0.24		9.42	101.2				243	292
NGC4055		8.63		0.12		9.76	107.2					
NGC4065		9.42		0.14		9.69	107.2					
NGC4066		10.36		0.16		9.81	107.2					

Name	R_e	$R_e^{\rm 2MASS}$	ϵ	$\epsilon^{\rm 2MASS}$	K	$K^{\rm 2MASS}$	D	M_K	R_e	$R_{e,\rm circ}$	σ_e	σ_c
	(")	(")			(mag)	(mag)	(Mpc)	(mag)	(kpc)	(kpc)	(km/s)	(km/s)
(1)	(2)	(3)	(4)	(5)	(6)	(7)	(8)	(9)	(10)	(11)	(12)	(13)
NGC4059		10.26		0.14		9.75	107.2					
NGC4073		25.27		0.34		8.49	85.0				292	316
NGC4213	15.59	13.26	0.16	0.24	9.38	9.61	101.6	-25.67	7.68	7.05		
NGC4472		56.11		0.09		5.4	16.7				258	292
NGC4486		41.46		0.01		5.81	16.7					
NGC4555	12.72	11.19	0.26	0.16	8.86	9.17	103.6	-26.22	6.39	5.48	277	328
NGC4649		42.14		0.11		5.74	16.5					
NGC4816	21.49	15.63	0.2	0.14	9.3	9.71	99.1*	-25.69	10.33	9.22	207	217
NGC4839		21.89		0.34		9.2	91.2				275	261
NGC4874	33.59	24.58	0.07	0.1	8.48	8.86	99.1*	-26.5	16.14	15.59	258	251
NGC4889	26.89	23.83	0.36	0.36	8.27	8.41	99.1*	-26.72	12.92	10.33	337	370
NGC4914	17.77	16.04	0.4	0.38	8.49	8.65	67.1*	-25.65	5.78	4.47	225	233
NGC5129	17.41	14.19	0.34	0.32	8.97	9.25	107.5	-26.19	9.07	7.36	222	260
NGC5208	10.82	9.37	0.61	0.58	9.27	9.51	105.0	-25.85	5.51	3.42	235	270
PGC047776		8.49		0.2		9.73	103.8					
NGC5252	15.28	13.16	0.58	0.5	9.5	9.77	103.8	-25.59	7.69	4.99		
NGC5322	27.37	30.52	0.32	0.34	7.09	7.16	31.5*	-25.41	4.18	3.46	239	246
NGC5353		17.95		0.56		7.62	34.8				225	277
NGC5490	11.02	11.13	0.18	0.18	8.73	8.92	71.4*	-25.54	3.81	3.44	282	349
NGC5557	19.8	17.38	0.16	0.14	7.8	8.08	49.2*	-25.66	4.72	4.34	223	279
IC1143	10.92	9.9	0.1	0.14	9.32	9.51	97.3	-25.64	5.15	4.9		
UGC10097	10.18	8.5	0.3	0.26	9.09	9.38	91.5	-25.72	4.52	3.77		
NGC6223	21.35	11.41	0.32	0.2	8.63	9.11	86.7	-26.07	8.98	7.4	238	274
NGC6364	10.27	8.19	0.16	0.22	9.42	9.74	105.3	-25.7	5.24	4.81		
NGC6375	12.5	12.17	0.13	0.1	9.18	9.41	95.8	-25.76	5.81	5.4	187	226
UGC10918	18.24	12.18	0.17	0.14	8.81	9.31	100.2	-26.25	8.86	8.05	249	247
NGC6442	12.62	9.75	0.21	0.12	9.15	9.59	98.0	-25.84	6.0	5.35		
NGC6482	13.82	12.09	0.3	0.36	8.14	8.37	51.8*	-25.46	3.47	2.91	291	305

Name	R_e	R_e^{2MASS}	ϵ	ϵ^{2MASS}	K	K^{2MASS}	D	M_K	R_e	$R_{e,circ}$	σ_e	σ_c
	(")	(")			(mag)	(mag)	(Mpc)	(mag)	(kpc)	(kpc)	(km/s)	(km/s)
(1)	(2)	(3)	(4)	(5)	(6)	(7)	(8)	(9)	(10)	(11)	(12)	(13)
NGC6575	14.43	10.65	0.26	0.28	9.15	9.56	106.0	-26.0	7.41	6.38	234	264
NGC7052	22.47	20.25	0.5	0.5	8.39	8.57	61.9*	-25.61	6.74	4.77	266	298
NGC7242	40.9	32.84	0.31	0.28	7.99	8.33	79.6*	-26.56	15.79	13.09	283	255
NGC7265	32.02	18.13	0.21	0.22	8.18	8.69	82.8	-26.44	12.85	11.39	206	230
NGC7274	15.71	11.81	0.08	0.06	8.9	9.24	82.8	-25.72	6.31	6.05	244	259
NGC7386	16.09	13.11	0.29	0.3	9.15	9.42	99.1	-25.85	7.73	6.5	273	312
NGC7426	13.64	13.47	0.36	0.34	8.61	8.82	80.0	-25.94	5.29	4.22	219	284
NGC7436	19.82	20.47	0.07	0.1	8.8	9.01	106.6	-26.37	10.24	9.89	263	280
NGC7550	16.9	12.9	0.08	0.1	8.52	8.91	72.7	-25.83	5.96	5.71	224	270
NGC7556	23.03	18.93	0.24	0.2	8.98	9.25	103.0	-26.09	11.5	10.02	243	253
NGC7618	13.4	11.26	0.32	0.28	8.74	9.04	76.3	-25.74	4.96	4.07	265	292
NGC7619	23.7	16.39	0.22	0.18	7.7	8.03	46.6*	-25.66	5.35	4.73	277	325
NGC7626	21.92	20.66	0.15	0.12	7.87	8.03	46.6*	-25.49	4.95	4.57	250	269
NGC7681		12.39		0.22		9.22	96.8					

5.4 Fitting the Scaling Relations

Uncertainties

In order to study the relationships between the photometric parameters determined in the previous Section and other galaxy properties, we need to estimate the uncertainties on these measurements. For most of our galaxy images, the dominant source of uncertainty is due to the sky determination. By comparing sky estimates from the automated *sky_box* routine, manually placed sky boxes and the asymptotic intensity of the isophotal profile, we find that our sky estimates result in values of K with an uncertainty of about $\delta K = 0.05$ mag. The uncertainty in the half-light radius is dominated by the uncertainty in the sky determination. We thus assume the uncertainties in these two measurements to be perfectly correlated. We measure the slope of the curve-of-growth (aperture magnitude versus logarithm of aperture semi-major axis) at $\log(R_{e,\mathrm{app}})$, $S = \left|\frac{\mathrm{d}K(R)}{\mathrm{d}\log(R)}\right|_{\log(R_{e,\mathrm{app}})}$ and assign a corresponding uncertainty on $\log(R_{e,\mathrm{app}})$ of $\delta\log(R_{e,\mathrm{app}}) = S\delta K$. This results in a median uncertainty on $R_{e,\mathrm{app}}$ of about 8%. We therefore adopt a covariance matrix on these quantities given by:

$$\mathrm{Cov}(\log(R_{e,\mathrm{app}}), K) = \begin{pmatrix} (S\delta K)^2 & -S(\delta K)^2 \\ -S(\delta K)^2 & (\delta K)^2 \end{pmatrix} \tag{5.3}$$

The corresponding absolute quantities, R_e and M_K or L, will also have correlated uncertainties. This covariance arises for two reasons: the measurements of the apparent magnitude K and angular size $R_{e,\mathrm{app}}$ are strongly correlated, and the intrinsic quantities R_e and M_K both depend on the distance. The total covariance matrix between these two quantities is given by:

$$\begin{aligned} &\mathrm{Cov}(\log(R_e), M_K) \\ &\quad = \mathrm{Cov}(\log(R_{e,\mathrm{app}}), K) + (\delta\log D)^2 \begin{pmatrix} 1 & -5 \\ -5 & 25 \end{pmatrix} \\ &\quad = \begin{pmatrix} (S\delta K)^2 + (\delta\log D)^2 & -S(\delta K)^2 - 5(\delta\log D)^2 \\ -S(\delta K)^2 - 5(\delta\log D)^2 & (\delta K)^2 + 25(\delta\log D)^2 \end{pmatrix} \end{aligned} \tag{5.4}$$

For our given uncertainties, this results in a mean correlation coefficient between the uncertainties on $\log(R_e)$ and M_K of about 0.87. Ignoring the correlation between the apparent quantities and only including the correlation due to the distance estimation would still result in a median correlation of 0.39 for galaxies with distances measured via SBF and 0.76 for galaxies with distances measured via group-corrected flow velocities.

Linear Fitting Procedure

Since our data can have correlated uncertainties in both the dependent and independent variables, as well as a selection on absolute magnitude, M_K, a robust fitting procedure is needed in order to obtain reliable results.

The fitting procedure we use throughout this paper is the *LinMix* procedure outlined in Kelly [149]. This procedure constructs a likelihood function for the data, in which the distribution of the independent variable is modeled as a mixture of gaussian functions. The dependent variable is then assumed to be drawn from a gaussian distribution centered on a linear relation with respect to the independent variable. The main strengths of this procedure are its explicit model for the data, and its ability to account for both selection effects and covariances between the uncertainties on the dependent and independent variables. It also returns samples from the posterior distribution over parameters, allowing for a clearer interpretation of the fit uncertainties. For each parameter, we report a marginalized 1D best-fit value and uncertainty. The best-fit value is determined as the 50th percentile of the 1D distribution of samples, while the 1σ uncertainties are determined from the 16th and 84th percentiles.

Velocity Dispersions and Conversion to Physical Parameters

To explore relations among the physical properties of the galaxies in our sample, we require a set of reliable distances. We use distances from Jensen et al. [117], where available. These distances are derived using surface brightness fluctuations (SBF) in WFC3 Hubble Space Telescope images, and have a median uncertainty of 3.9%. For galaxies not studied in Jensen et al. [117], we use the values reported in the first MASSIVE paper, Ma et al. [88]. In some cases, these distances were derived using SBF. Where SBF distances were not available, distances from group-corrected flow velocities were used. In the following, we adopt a 4% uncertainty on SBF derived distances, and a 10% uncertainty on those derived from group-corrected flow velocities.

We also use the velocity dispersion values reported in Veale et al. [105]. Mainly, we use the velocity dispersion measured within the central fiber of the Mitchell IFU, σ_c. We also use σ_e, which is measured via a luminosity-weighted average of σ for fibers within a radius $R_{e,\mathrm{NSA}}$ of the galaxy center[3]. Here, $R_{e,\mathrm{NSA}}$ is the half-light radius reported by the NASA-Sloan Atlas (NSA), based on the SDSS DR8 catalogue [150]. Where values from NSA were not available, values from 2MASS were used and corrected for the relative slope and offset between the two using equation 4 of Ma et al. [88]. We do not attempt to correct these values to the newly determined radii reported above. In the following, we adopt a 5% uncertainty on both σ_c and σ_e values.

5.5 Size-Luminosity Relation

The size-luminosity (SL) relation describes an observed correlation between the projected size and total luminosity of early-type galaxies. The projected size is quantified through the

[3]Note that this luminosity-weighted average is not the same as determining the velocity dispersion for a single spectrum with radius $R_{e,\mathrm{NSA}}$. For slow-rotating galaxies, the difference is very minor. For fast-rotating galaxies, the difference can be significant.

	Sample	$a_{\rm SL}$	$b_{\rm SL}$	$\epsilon_{\rm SL}$
(1)	MASSIVE	0.634 ± 0.018	$0.90^{+0.10}_{-0.11}$	0.100 ± 0.008
(2)	ATLAS$^{\rm 3D}$	0.52 ± 0.02	0.41 ± 0.03	$0.143^{+0.007}_{-0.006}$
(3)	MASSIVE (SRs)	0.63 ± 0.03	0.94 ± 0.12	$0.097^{+0.012}_{-0.010}$
(4)	ATLAS$^{\rm 3D}$ (SRs)	0.63 ± 0.03	0.48 ± 0.04	$0.115^{+0.016}_{-0.014}$

Table 5.2: Fit parameters for the Size-Luminosity relation, as defined by equation 5.5, in various galaxy samples. (1) All galaxies in the MASSIVE sample for which we report measured R_e and L from CFHT. (2) All galaxies in the ATLAS$^{\rm 3D}$ sample. (3) All galaxies in the MASSIVE sample which are classified as slow rotators by Veale et al. [104] for which we report measured R_e and L from CFHT. (4) All galaxies in the ATLAS$^{\rm 3D}$ sample which are classified as slow rotators by Emsellem et al. [7].

geometric radius of the half-light ellipse.

We consider a power-law SL relation of the form

$$\log \frac{R_{e,\rm circ}}{1\rm kpc} = b_{\rm SL} \log \frac{L}{10^{11.5} L_\odot} + a_{\rm SL}\,. \tag{5.5}$$

We further assume an intrinsic normal scatter in $\log(R_{e,\rm circ})$ about this relation with standard deviation $\epsilon_{\rm SL}$.

MASSIVE and ATLAS$^{\rm 3D}$ Galaxies

Our fit results are summarized in Table 5.2. For the galaxies within the MASSIVE survey for which we measured $R_{e,\rm circ}$ and L, our best-fit parameter values and associated uncertainties for the SL relation are listed in row (1) of Table 5.2. The uncertainties in $a_{\rm SL}$ and $b_{\rm SL}$ are strongly correlated. These fit results are summarized in the left panel of Figure 5.3. Linear relations corresponding to a number of samples from the posterior distribution are shown by the gray lines distributed about the best-fit relation.

One of the defining selection criteria for the MASSIVE survey is the absolute K-band magnitude selection, $M_K < -25.3$ mag, as measured in the 2MASS XSC. However, this limits the dynamic range over which we can study scaling relations. In order to extend this dynamic range, we compare with points from ATLAS$^{\rm 3D}$, a volume limited sample of early-type galaxies with $M_K < -21.5$. MASSIVE includes galaxies out to a distance of approximately 100 Mpc, while ATLAS$^{\rm 3D}$ includes galaxies out to 42 Mpc. The similarity in selection criteria makes ATLAS$^{\rm 3D}$ a natural comparison point to MASSIVE.

A fair comparison of the relations for MASSIVE and ATLAS$^{\rm 3D}$ galaxies requires consistent sets of measurements for the two surveys. For the half-light radii of ATLAS$^{\rm 3D}$ galaxies, we use the values reported by Cappellari et al. [151]. These radii were taken from the RC3 [152], where available, and from 2MASS otherwise. The RC3 values are based primarily on

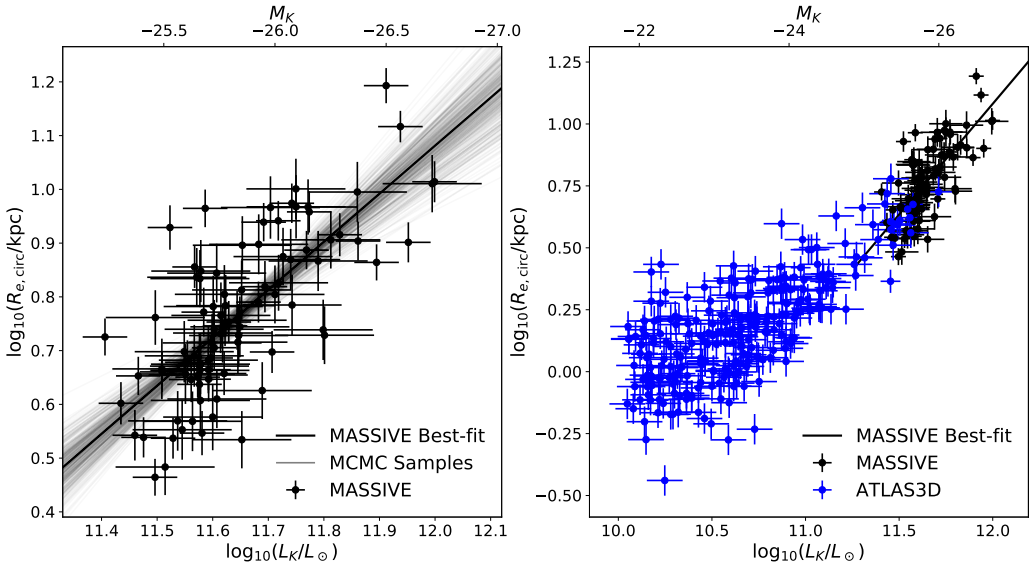

Figure 5.3: Size-luminosity relation for early-type galaxies in the MASSIVE survey (left) and the MASSIVE (black) and ATLAS^{3D} (blue) surveys together (right). The best-fit linear relation to the MASSIVE survey shown in black is described by the parameters listed in row (1) of Table 5.2. The grey lines represent MCMC draws from the posterior distribution over the parameters describing this linear relation. Low luminosity galaxies within the ATLAS^{3D} survey are clearly oversized compared to this linear relation.

B-band photoelectric photometry extrapolated to infinite aperture and the interpolated to find the equivalent circular aperture containing half the total light, without corrections for nearby contaminating sources. Cappellari et al. [151] find that the RC3 values are a factor of 1.7 times larger than 2MASS on average, with a scatter of 0.11 dex. The values from 2MASS were thus scaled up by a factor of 1.7. In order to directly compare with our radii as measured with CFHT, we take these radii, divide by a factor of 1.7, and then multiply by a factor of 1.18 (see Section 5.3) to agree with CFHT on average.

The K-band luminosities of ATLAS^{3D} galaxies were taken from 2MASS without corrections [151]. We apply a constant shift to these values of 0.27 magnitudes, such that they agree with the average offset between 2MASS and our CFHT magnitudes. We do not account for any deviation of the slope from unity in this relation. However, Schombert and Smith [140] found that the systematic offset in J-band 2MASS magnitudes is roughly constant over a wide range of apparent magnitude.

In the right panel of Figure 5.3, we plot the SL relation as determined from the MASSIVE data but overlay the points from ATLAS^{3D}. Above $M_K \sim -24$, the two appear to agree well, no visually obvious offset or change in slope. At around $M_K \sim -23$, the

ATLAS^{3D} galaxies exhibit a clear change in slope. This is qualitatively similar to the non-linear zone-of-exclusion observed in the size-mass plane in Cappellari et al. [153] using dynamically determined total stellar masses. Despite the clear non-linearity in ATLAS^{3D}, we report the best-fitting linear relation parameters in row (2) of Table 5.2 for completeness.

Fast and Slow Rotators

Elliptical galaxies have properties that vary significantly with stellar mass. More massive ellipticals tend to exhibit central cores, round shapes, boxy isophotes, and little or no rotation. Less massive ellipticals tend to have power law central surface brightness profiles, flattened shapes, disky isophotes, and significant rotation [e.g., 154, 155, 156].

In order to study these two populations of galaxies, we categorize our sample into fast rotators (FRs) and slow rotators (SRs). The exact classification scheme is described in Veale et al. [104]. Due to the tendency for more massive galaxies to exhibit less rotation, most of the MASSIVE galaxies are SRs. The left panel of Figure 5.4 shows the SL relation fit to only the SRs in MASSIVE. The FRs are plotted in red, but are not included in the fit. Some galaxies were not observed with the Mitchell IFU, and thus did not receive classifications - they do not appear in this figure. The fit to SRs alone results in the best-fit parameters and uncertainties listed in row (3) of Table 5.2. These values are consistent within their uncertainties with the values determined from fitting the full CFHT MASSIVE sample (row (1) of Table 5.2). Due to the small number of FRs within the MASSIVE sample, we do not attempt to measure a best-fit SL relation for the FRs alone.

Galaxies in the ATLAS^{3D} survey were classified as FRs and SRs in Emsellem et al. [7]. The classification scheme in Veale et al. [104] was based on that of Emsellem et al. [7], and the two differ only by relatively minor differences in the apertures used to measure the rotation. We adopt the classifications from Emsellem et al. [7] in order to compare SRs between the MASSIVE and ATLAS^{3D} samples. In the right panel of Figure 5.4, we plot the SL relation for MASSIVE combined with ATLAS^{3D}, but only for galaxies that are SRs. The SRs form a tight, continuous sequence within this plane. The best-fit linear relation for the ATLAS^{3D} SRs is described by the parameters given in row (4) of Table 5.2. There is a significant difference in slope between low luminosity (ATLAS^{3D}) and high luminosity (MASSIVE) galaxies.

5.6 Faber-Jackson Relation

The Faber-Jackson (FJ) relation describes an approximately power-law relationship between the central velocity dispersion and total luminosity of elliptical galaxies [14]. We consider a Faber-Jackson Relation of the form:

$$\log \frac{\sigma_c}{1\text{km s}^{-1}} = b_{\rm FJ} \log \frac{L}{10^{11.5} L_\odot} + a_{\rm FJ}. \tag{5.6}$$

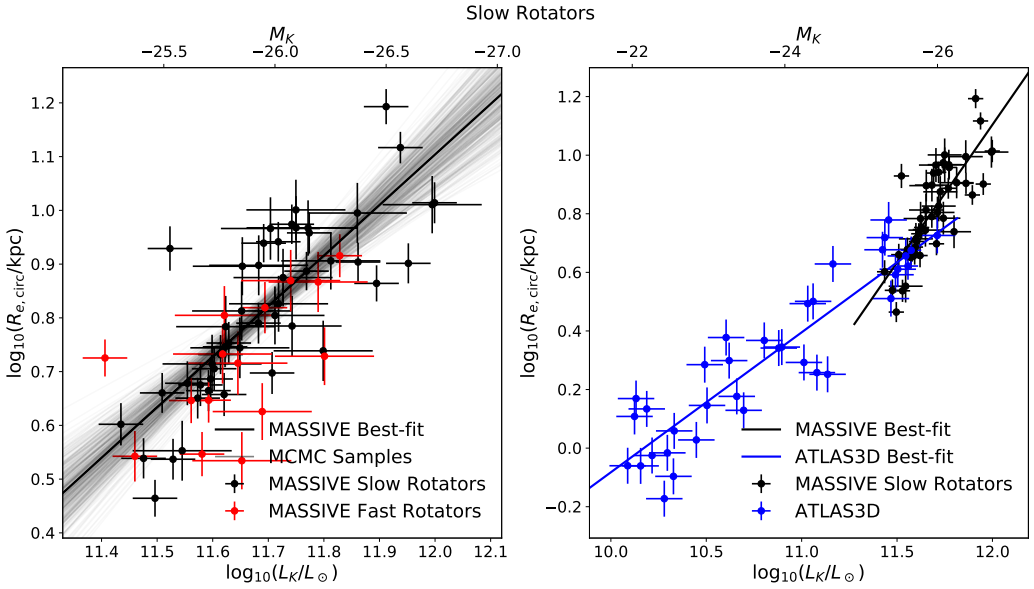

Figure 5.4: Size-luminosity relation for slow-rotator galaxies in the MASSIVE survey (left) and the MASSIVE (black) and ATLAS^{3D} (blue) surveys together (right). The fast-rotator galaxies in the MASSIVE survey are shown in red in the left panel, but are excluded from the fit. The best-fit linear relation to the slow-rotators in the MASSIVE survey shown in black is described by the parameters listed in row (3) of Table 5.2. The grey lines represent MCMC draws from the posterior distribution over the parameters describing this linear relation. Low luminosity galaxies within the ATLAS^{3D} survey are clearly oversized compared to this linear relation. The best-fit linear relation to the slow-rotators in the ATLAS^{3D} survey shown in blue is described by the parameters listed in row (4) of Table 5.2.

We further assume an intrinsic normal scatter in $\log(\sigma_c)$ about this relation with standard deviation ϵ_{FJ}.

Combined Sample

The FJ relation for the MASSIVE sample is shown in the right panel of Figure 5.5. The parameters describing the best-fit linear relation are given in row (1) of Table 5.3, along with their associated uncertainties. The uncertainties in a_{FJ} and b_{FJ} are strongly correlated. This best-fit relation is shown by the solid black line in Figure 5.5. Other relations described by samples from the posterior probability distribution are shown in grey.

As with the SL relation, the ATLAS^{3D} can be used to extend the dynamic range in total luminosity. We use the same luminosities as in Section 5.5. For central velocity dispersion, we adopt the value measured within a circular aperture of radius 1 kpc, as reported in Cappellari

	Sample	$a_{\rm FJ}$	$b_{\rm FJ}$	$\epsilon_{\rm FJ}$
(1)	MASSIVE	$2.399^{+0.011}_{-0.011}$	$0.22^{+0.06}_{-0.06}$	$0.049^{+0.005}_{-0.005}$
(2)	ATLAS$^{\rm 3D}$	2.445 ± 0.016	0.391 ± 0.017	$0.090^{+0.005}_{-0.005}$
(3)	MASSIVE (SRs)	2.415 ± 0.015	0.14 ± 0.07	$0.052^{+0.007}_{-0.006}$
(4)	ATLAS$^{\rm 3D}$ (SRs)	2.423 ± 0.02	$0.36^{+0.02}_{-0.03}$	$0.063^{+0.012}_{-0.011}$

Table 5.3: Fit parameters for the Faber-Jackson relation, as defined by equation 5.6, in various galaxy samples. (1) All galaxies in the MASSIVE sample for which we report measured R_e and L from CFHT. (2) All galaxies in the ATLAS$^{\rm 3D}$ sample. (3) All galaxies in the MASSIVE sample which are classified as slow rotators by Veale et al. [104] for which we report measured R_e and L from CFHT. (4) All galaxies in the ATLAS$^{\rm 3D}$ sample which are classified as slow rotators by Emsellem et al. [7].

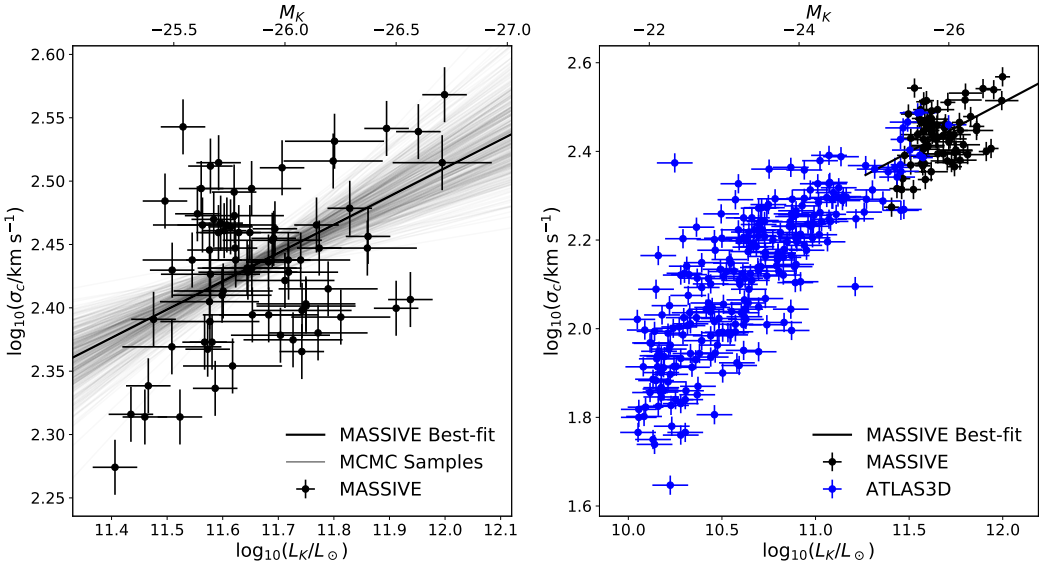

Figure 5.5: Faber-Jackson relation for early-type galaxies in the MASSIVE survey (left) and the MASSIVE (black) and ATLAS$^{\rm 3D}$ (blue) surveys together (right). The best-fit linear relation to the MASSIVE survey shown in black is described by the parameters listed in row (1) of Table 5.3. The grey lines represent MCMC draws from the posterior distribution over the parameters describing this linear relation. Low luminosity galaxies within the ATLAS$^{\rm 3D}$ survey clearly have lower velocity dispersion than would be predicted by this linear relation.

et al. [153]. This aperture is only moderately larger than the average aperture used for the MASSIVE galaxies which is typically between about 0.6 kpc and 1 kpc depending on the distance to the galaxy.

The FJ relation for the MASSIVE and ATLAS^{3D} samples is shown in the right panel of Figure 5.5. Above $M_K \sim -24$, the two samples appear to agree in terms of both slope and normalization. However, there is significant curvature at lower luminosities within the ATLAS^{3D} sample with lower luminosity galaxies having smaller central velocity dispersion than predicted from the linear relation from MASSIVE. This curvature is qualitatively similar to the change in slope of the mass-velocity dispersion relation reported in Cappellari et al. [153]. Despite the nonlinearity, our best-fit linear fit parameters for the ATLAS^{3D} sample are reported in row (2) of Table 5.3 for completeness.

Fast and Slow Rotators

The left panel of Figure 5.6 shows the Faber-Jackson relation for SRs in the MASSIVE survey. The FRs are shown in red, but are not included in the fit. The parameters associated with the best-fit linear relation for the MASSIVE SRs alone are given in row (3) of Table 5.3. The slope for the SRs alone is consistent with, but moderately shallower than, the slope for the complete sample.

As in the previous section, we can combine the SRs in the MASSIVE and ATLAS^{3D} samples in order to extend the dynamic range in L. When MASSIVE and ATLAS^{3D} are combined, the SRs form a thin sequence in the $\sigma_c - L$ plane (right panel of Figure 5.6). There is a significant change in slope between the two galaxy samples, with σ_c increasing less quickly at larger luminosities. The best-fit linear FJ relation parameters for the sample of SRs in ATLAS^{3D} are given in row (4) of Table 5.3.

Choice of Velocity Dispersion Aperture

The FJ relation has been studied using central velocity dispersions measured within various aperture sizes. In our case, the velocity dispersions are measured within the central fiber of the Mitchell IFU, corresponding to a radius of 2 arcseconds. These velocity dispersions are largely consistent with other measures of central velocity dispersion taken from the literature [157, 103].

Typically, these apertures are significantly smaller than the half-light radii of the galaxies. However, velocity dispersion is often measured within an aperture defined by the half-light radius of the galaxy. For our sample, Veale et al. [105] reported velocity dispersions measured by averaging the velocity dispersion for all Mitchell IFU fibres within a circularized half-light radius of the center. In this case, the half-light radii were taken from NSA. We used these σ_e values in order to check that our results are not sensitive to the precise aperture used to measure velocity dispersion.

For ATLAS^{3D} , Cappellari et al. [153] report velocity dispersions as measured within an aperture defined by the half-light elliptical isophote. In this case, the half-light isophote is

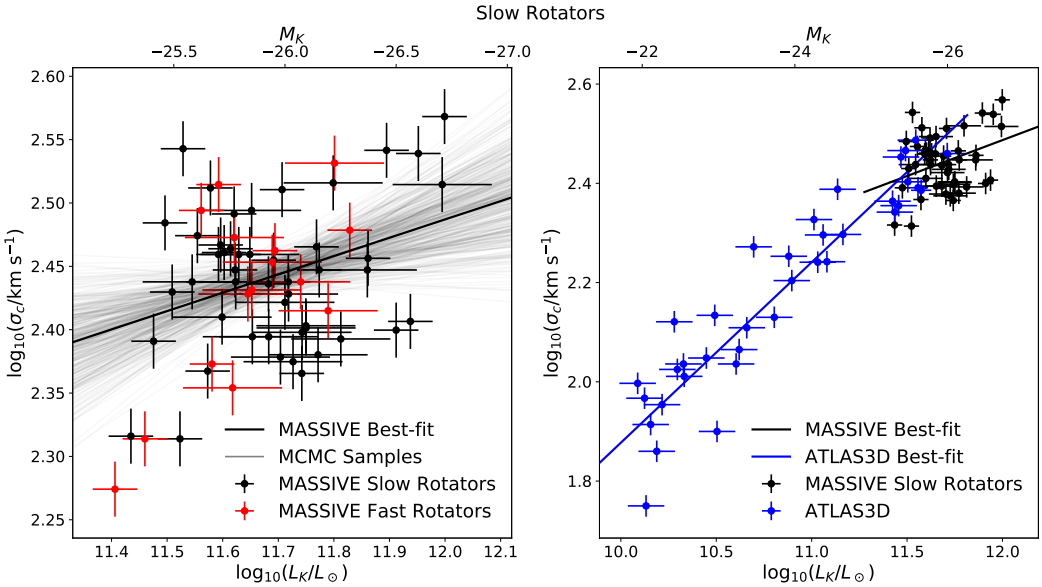

Figure 5.6: Faber-Jackson relation for slow-rotator galaxies in the MASSIVE survey (left) and the MASSIVE (black) and ATLAS^{3D} (blue) surveys together (right). The fast-rotator galaxies in the MASSIVE survey are shown in red in the left panel, but are excluded from the fit. The best-fit linear relation to the slow-rotators in the MASSIVE survey shown in black is described by the parameters listed in row (3) of Table 5.3. The grey lines represent MCMC draws from the posterior distribution over the parameters describing this linear relation. Low luminosity galaxies within the ATLAS^{3D} survey have lower dispersions than would be predicted by an extrapolation of the linear relation from MASSIVE. The best-fit linear relation to the slow-rotators in the ATLAS^{3D} survey shown in blue is described by the parameters listed in row (4) of Table 5.3.

determined from r-band photometry, scaled to match values from the RC3 catalog on average [152]. The semi-major axis of this elliptical aperture is thus larger than the half-light radii from 2MASS by an average factor of 1.7. The velocity dispersions for MASSIVE [taken from 105], are measured within an aperture scaled to agree with values from NSA on average, and are thus larger than those from 2MASS by a factor of 1.35 on average.

A further difference between these two velocity dispersion measurements is that the velocity dispersions from ATLAS^{3D} include the effects of rotation within the galaxy, while those from MASSIVE do not. To account for this, we plot only the SRs within each sample, where galaxy rotation has a negligible effect. The resulting FJ relation is shown in Figure 5.7, for the MASSIVE survey alone in the left panel and the MASSIVE and ATLAS^{3D} surveys together in the right panel.

After restricting to SRs, the situation is qualitatively similar when σ_e is used instead of

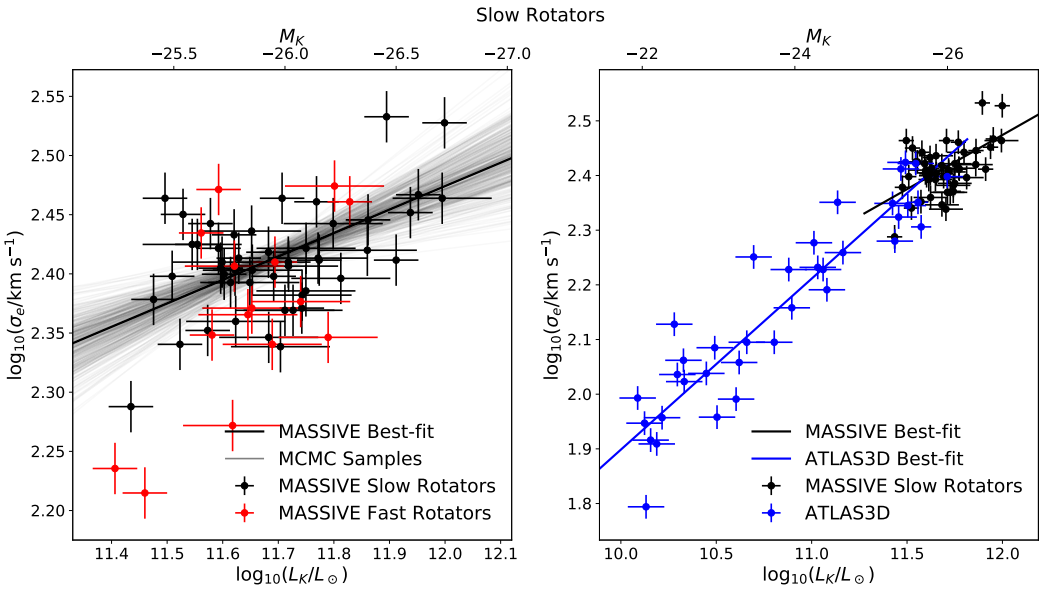

Figure 5.7: Faber-Jackson relation for slow-rotator galaxies in the MASSIVE survey (left) and the MASSIVE (black) and ATLAS^{3D} (blue) surveys together (right), but using the velocity dispersion measured within R_e instead of σ_c. The fast-rotator galaxies in the MASSIVE survey are shown in red in the left panel, but are excluded from the fit. The best-fit line for MASSIVE is given by the parameters $a_{\rm FJ} = 2.375 \pm 0.011$, $b_{\rm FJ} = 0.20 \pm 0.05$, and $\epsilon_{\rm FJ} = 0.032^{+0.006}_{-0.005}$. The grey lines represent MCMC draws from the posterior distribution over the parameters describing this linear relation. Low luminosity galaxies within the ATLAS^{3D} survey have lower dispersions than would be predicted by an extrapolation of the linear relation from MASSIVE. The best-fit line for ATLAS^{3D} is given by the parameters $a_{\rm FJ} = 2.368 \pm 0.019$, $b_{\rm FJ} = 0.31 \pm 0.02$, and $\epsilon_{\rm FJ} = 0.057^{+0.011}_{-0.009}$.

σ_c. There is a significantly shallower slope for the MASSIVE sample ($b_{\rm FJ} = 0.20 \pm 0.05$) than for the ATLAS^{3D} sample ($b_{\rm FJ} = 0.31 \pm 0.02$). The best-fit parameters are given in the caption of Figure 5.7. The slope and normalization for each sample are consistent within 1σ between the two choices of velocity dispersion. The intrinsic scatter, $\epsilon_{\rm FJ}$, is smaller for the MASSIVE SRs when σ_e is used (0.032 versus 0.052 dex), which is reasonable because the velocity dispersion over the effective radius gives a better tracer of the total mass. Regardless, we regard the fits in the previous subsection using the central velocity dispersion, σ_c, as our fiducial FJ relation due to its prevalence in the literature.

5.7 Discussion

In Sections 5.2 and 5.3, we described new CFHT imaging for a large sample of galaxies in the MASSIVE survey, and how we obtained accurate half-light radii and total luminosities from these images. In Sections 5.5 and 5.6, we used these photometric parameters along with other measurements from the literature to perform fits to the Size-Luminosity and Faber-Jackson relations for galaxies in the MASSIVE and ATLAS^{3D} surveys. In both cases, we found evidence of curvature in the relations. Further, this curvature was present in the relation for SRs alone.

Virial Mass Consistency Check

In Figure 5.8, we plot the $R_{e,\mathrm{circ}}\sigma_c^2$ which is a dynamical measure of mass if the galaxy has virialized. When plotted versus L, we see that all galaxies in both MASSIVE and ATLAS^{3D} lie on a single tight power-law relation. In this sense, the curvature in the SL and FJ relations cancel to give a single power law, suggesting that galaxies in both samples have virialized. This uniformity is also evidence that the curvature observed is not a consequence of the different definitions of σ_c and the corrections applied to $R_{e,\mathrm{circ}}$ and L for ATLAS^{3D} . The best-fit power-law relation shown in Figure 5.8 is given by:

$$\log \frac{R_{e,\mathrm{circ}}\ \sigma_c^2}{1\ \mathrm{kpc\ km^2\ s^{-2}}} = 1.21 \log \frac{L}{10^{11.5}\ L\odot} + 5.44. \tag{5.7}$$

This is consistent with a linear scaling of the mass with $\sigma_c^2 R_e$, given that $M/L \propto L^{0.2}$ for elliptical galaxies [e.g., 136, 158]. The data are consistent with a small intrinsic vertical scatter of 0.017 about the best-fit relation.

We now compare our observed relations with previously published scaling relations from the literature, and discuss their physical implications.

Size-Luminosity Relation

The SL relation has been observed in a wide variety of galaxy populations in different photometric bands. This is closely related to the Kormendy relation, which describes a correlation between the effective radius and surface brightness within the effective radius. The SL relation was studied in the SDSS survey for elliptical galaxies in Bernardi et al. [159], and re-analyzed with a particular focus on brightest cluster galaxies (BCGs) in Bernardi et al. [160]. The resulting scaling relations for r-band photometry reported in Bernardi et al. [160] were $R_e \propto L^{0.68}$ for elliptical galaxies as a whole and $R_e \propto L^{0.88}$ for BCGs alone. This is the same scaling we find for the full MASSIVE sample, as reported in Table 5.2, and the scaling does not change significantly, $R_e \propto L^{0.94}$, when we restrict the analysis to slow rotators. The SL relation for the bulge component of early-type galaxies SDSS was analyzed by Bernardi et al. [161], who found a power-law scaling relation of $R_e \propto L_{\mathrm{bulge}}^{0.85}$, with a comparable scaling in total luminosity among the most luminous early type galaxies. Thus,

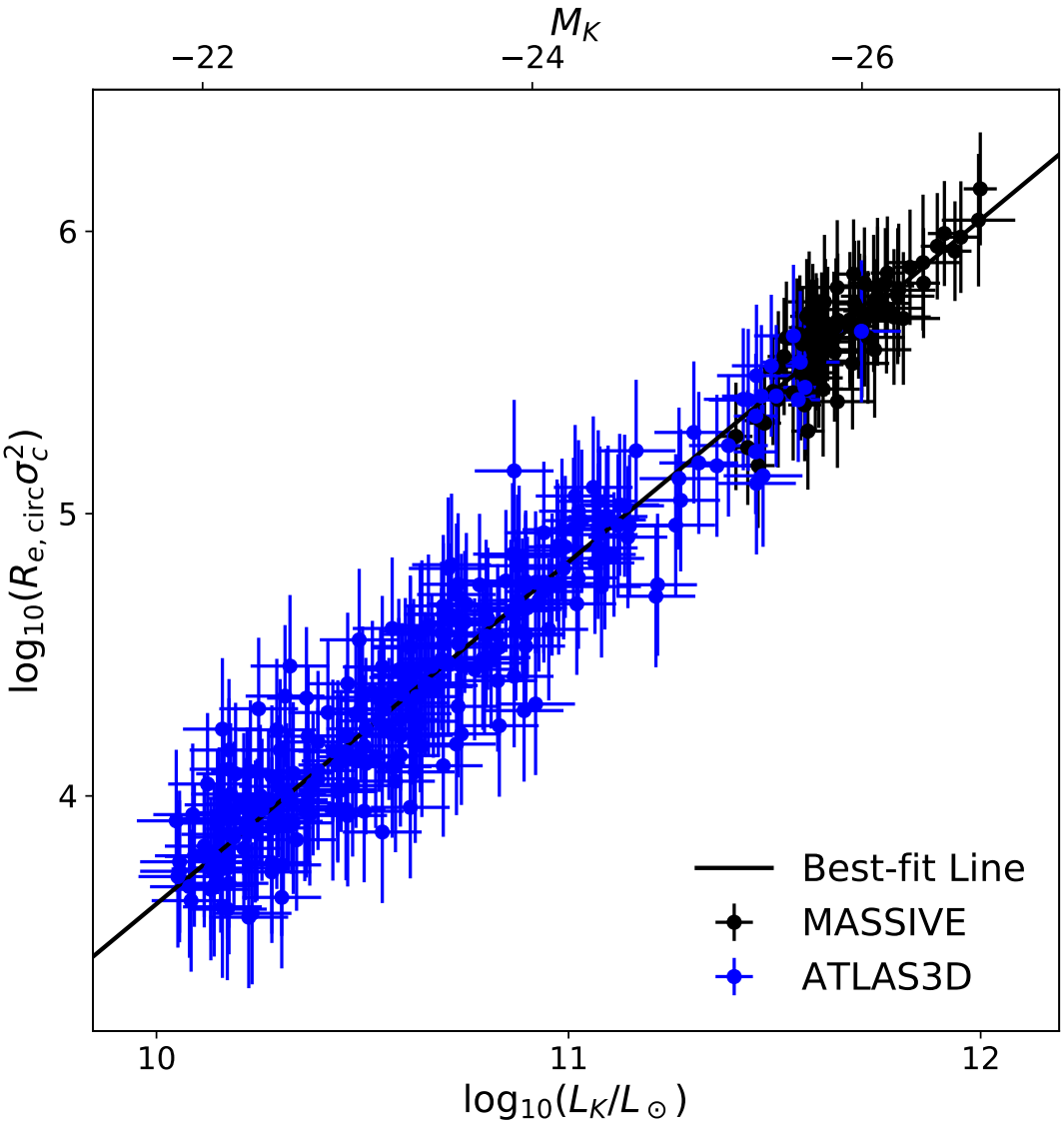

Figure 5.8: Relationship between dynamical mass ($M_{\rm dyn} \propto R_e\sigma^2$) and total luminosity for galaxies in the MASSIVE (black) and ATLAS$^{\rm 3D}$ (blue) surveys. The curvature in the SL and FJ relations cancel, leading to a relation that is well described by a single power-law. The black line shows a linear fit to the combined MASSIVE and ATLAS$^{\rm 3D}$ samples.

the K-band SL relation in the MASSIVE survey is consistent with the r-band relation from SDSS for BCGs and the bulge components of a broader range of early-type galaxies, but is significantly steeper than the r-band relation for early-type galaxies as a whole within SDSS. We have found that it is also steeper than the relation for low-luminosity slow rotators.

Among massive elliptical galaxies, curvature has been measured in the SL relation. For example, Graham and Guzmán [4] and Graham and Worley [162] demonstrate that a curved SL relation can result from two quantities having power law relationships with luminosity: the central surface brightness of an inward interpolation of the outer Sérsic profile and total magnitude, and the Sérsic index n. Similar curvature has also been suggested in the K-band in Forbes et al. [163], using 2MASS photometry. However, in this case, the half-light radii were calculated from the semi-major axes of the 20 mag/arcsec^2 isophote and an assumed Sérsic profile.

Further evidence for curvature in this relation for massive elliptical galaxies was presented in Bernardi et al. [160] and Bernardi et al. [161]. They suggested that this curvature may arise from an increased fraction of BCGs at high-luminosity, together with the fact that BCGs tend to have larger sizes than expected from global scaling relations for ellipticals. We further examine this picture in Section 5.7.

Faber-Jackson Relation

The FJ relation has also been studied in a wide variety of galaxy samples, since the introduction of the canonical $b_{\rm FJ} = 0.25$ ($L \propto \sigma^4$) relation in Faber and Jackson [14]. Our power-law slopes for this relation in the MASSIVE survey give a somewhat less steep scaling of σ with L compared to the canonical value, ranging from $b_{\rm FJ} = 0.22 \pm 0.06$ for the full sample, to $b_{\rm FJ} = 0.14 \pm 0.07$ for the SRs alone. The latter value corresponds to a steep luminosity scaling of $L \sim \sigma^7$, although with a wide uncertainty range.

The slope for the full MASSIVE sample ($b_{\rm FJ} = 0.22 \pm 0.06$) is consistent with previous K-band studies of the FJ relation from both Pahre, Carvalho, and Djorgovski [164] and La Barbera et al. [165], where the slopes were found to be 0.24 and 0.22 respectively. La Barbera et al. [165] also finds that the slope of the FJ relation is relatively constant over a range of wavelength bands. In the r-band, Bernardi [166] reports a slope of $b_{\rm FJ} = 0.25$ for early-type galaxies the SDSS, consistent with our measured K-band slope in MASSIVE.

Curvature in the FJ relation was suggested by Oegerle and Hoessel [167], with many more recent studies supporting this claim. Lauer et al. [6] finds an FJ relation of $L \sim \sigma^{(6.5\pm1.3)}$ for core galaxies and BCGs, consistent with our reported slopes. Our results are also consistent with the reported slopes for BCGS of $L \sim \sigma^{(5.32\pm0.37)}$ from Von Der Linden et al. [168] and $\sigma \sim L^{(0.16\pm0.01)}$ from Samir, Takey, and Shaker [169]. Such changes have also been predicted in simulations, leading to a flattening of the $\sigma - L$ relation [e.g., 170]. With K-band photometry from 2MASS, Batcheldor et al. [171] analyzed a sample of BCGs and found that there was no significant difference in the $\sigma - L$ distribution of BCGs when compared to other ellipticals. However, Lauer et al. [6] suggests that this may be due to 2MASS being insufficiently deep to recover accurate total magnitudes. In contrast, Von Der Linden et al.

[168] did find a flattening of σ with increasing L for BCGs using 2MASS K-band photometry, consistent with our results.

Environment

Throughout this paper, we have focused on the variation of galaxy properties with total luminosity. For elliptical galaxies, total luminosity is a strong predictor of both half-light radius and central velocity dispersion, and it is tightly coupled to a galaxy's evolutionary history. However, a galaxy's environment can also have a significant impact on its evolution. One common environmental classification criterion is whether a galaxy is the central dominant galaxy in the cluster, which is most often the same as the BCG. Scaling relations for BCGs have been studied in the literature [e.g., 161, 172, 173]

In order to classify galaxies within the MASSIVE survey, we use classifications from the high density contrast (HDC) group catalogue [174]. More specifically, we classify all galaxies as BCGs if they belong to a group of three or more members, and are the most luminous galaxy within that group. Being the brightest in their clusters, BCGs tend to be more massive than non-BCGs. Thus, BCGs are overrepresented within the MASSIVE survey, compared to their proportion among galaxies as a whole. Therefore, the curvature described in the previous sections could conceivably be attributed to differences between BCG and non-BCG populations, rather than a curvature in the relation itself. In order to distinguish between these scenarios, we have explored fitting separate linear relations to the BCG and non-BCG populations within MASSIVE.

For both the SL and FJ relations, we find that the parameters obtained for BCGs and non-BCGs individually were consistent with those obtained for the complete MASSIVE sample. We conclude that there is no evidence of different SL or FJ relations between BCGs and non-BCGs, and the curvature in the relations cannot be due to a changing fraction of BCGs with increasing luminosity.

Merger Histories

Our fits provide further evidence that the most luminous elliptical galaxies have larger radii and smaller velocity dispersions than predicted from power-law fits at lower luminosities. This can provide insight into the assembly history of these galaxies. Curvature in scaling relations for elliptical galaxies may indicate changes in the relative influence of different formation mechanisms with galaxy luminosity [6]. One example of this is the role of dissipation in galaxy mergers. Dissipation is thought to play a larger role in the merger history of lower mass, rotation dominated ellipticals and a smaller role for more massive, slow-rotating ellipticals [e.g., 175, 156, 176, 177].

The pre-merger galaxy trajectories may leave detailed imprints on the FJ and SL relations in dissipationless mergers. For example, Boylan-Kolchin, Ma, and Quataert [170] suggest that dissipationless mergers that occur along more radial trajectories lead to a steeper SL relation, and an FJ relation where σ increases less steeply with L. They also argue that

massive elliptical galaxies are preferentially formed by radial mergers due to mergers occuring along cosmological filaments [e.g., 178]. This suggests that both the SL and FJ relations should exhibit curvature, due to more massive galaxies forming on preferentially radial orbits, qualitatively consistent with what we observe. Bernardi et al. [138] provides an argument that a qualitatively similar change in slope will occur for dissipationless mergers of pairs of galaxies on parabolic orbits. Thus, our observed steepening of R_e and flattening of σ at large L may be interpreted as evidence of dissipationless merging playing a larger role for the assembly of the most massive elliptical galaxies.

The curvature in both relations is apparent in both the FJ and SL relations even when only SRs are included in the fits. Therefore, the curvature can not be attributed solely to a changing fraction of SRs and FRs. This suggests that SRs can not be considered a homologous population, but instead that high and low luminosity populations of SRs have distinct structures and formation physics.

Prior studies have suggested distinct populations of low and high mass SR elliptical galaxies based on other evidence. Krajnović et al. [179] showed that while the most massive ellipticals are cored, some less massive SRs can be core-less. Thus, the difference between low-mass core-less and high-mass cored galaxies is not simply related to angular momentum. The increased prevalence of cores among SRs occurs around a characteristic stellar dynamical mass of $2\times10^{11}\ M_\odot$, which would correspond to an absolute K magnitude ~ -24.9 mag using the stellar mass relation from Cappellari [180] together with the correction between 2MASS and CFHT magnitudes reported in Section 5.3. This characteristic luminosity is qualitatively consistent with what we observe in both the SL and FJ relations. Our observations of a change in slope of the SL and FJ relations is further evidence of a difference between high-mass and low-mass SR populations.

Central Black Hole Scaling

Black hole scaling relations are often used to predict SMBH masses in galaxies where they cannot be measured directly. Two of the most commonly used relations are the $M_{\rm BH}-\sigma$ [181, 182] and $M_{\rm BH}-L$ [158] relations. If σ and L are related by a simple power-law, then power-law fits to these two relations must be consistent with one another. However, if there is curvature in the relationship between σ and L, power-law fits to the $M_{\rm BH}-\sigma$ and $M_{\rm BH}-L$ relations will result in different predictions for black hole masses.

This is precisely what occurs at large luminosities: since the slope of σ flattens with respect to L, the $M_{\rm BH}-\sigma$ relation predicts smaller central black hole masses than the $M_{\rm BH}-L$ relation. This was outlined by Lauer et al. [6], who argue that the $M_{\rm BH}-L$ relation predicts the black hole mass more accurately for very luminous galaxies. If these galaxies form through dissipationless mergers, the central SMBHs grow primarily through mergers of the SMBHs in the progenitor galaxies. This maintains the $M_{\rm BH}-L$ relation, while σ may grow more slowly. There is evidence that the $M_{\rm BH}-\sigma$ relation does underpredict the highest SMBH masses [e.g., 38, 183], although this may be due to differing $M_{\rm BH}-\sigma$ relations for cored and non-cored galaxies [184], with a predominance of cored galaxies at the highest

luminosities. Further exploration of the scaling of SMBH mass with galaxy luminosity and structural parameters is needed at the high-mass end [e.g., 185].

5.8 Conclusions

We have presented CFHT WIRCam data for ~ 100 galaxies within the MASSIVE survey, and measured K-band total luminosities and half-light radii. The updated luminosities are systematically brighter by about 0.27 mag than those from the 2MASS XSC, similar to the offset found by Schombert and Smith [140] in the J band. The half-light radii are systematically larger than those from 2MASS by about 17%.

Using these measured values, we study the SL and FJ relations for the MASSIVE galaxies. For the SL relation, we find $R_e \sim L_K^{0.88\pm0.10}$. This is consistent with prior studies, and indicates a significant steepening of the SL relation at high luminosities. For SRs alone, ATLAS^{3D} and MASSIVE combine to form a tight continuous sequence in the $R_e - L$ plane, but once again, there is a significant steepening of the SL relation at luminosities $L_K \gtrsim 10^{11.5}\ M_\odot$.

For the FJ relation, we find $L \sim \sigma_c^{4.5}$ for the full MASSIVE sample. However, when we consider the SRs alone, the power law steepens to $L \sim \sigma_c^{7.1}$. Consistent with other studies, we find σ flattens as a function of luminosity for the most massive galaxies. This is likely related to the prevalence of central cores in these massive galaxies.

The curvature in these two relations is further evidence for a picture in which the most luminous elliptical galaxies grow largely through dissipationless "dry" mergers, with dissipation playing a larger role for less luminous galaxies. Even within a sample composed purely of slow rotators, there is a significant change in the slopes of the SL and FJ relations, suggesting different formation histories for low and high luminosity slow rotators. We have also separately explored the relations for the BCGs and non-BCGs in our sample. We find no evidence that the BCGs follow different relations from the general population of luminous early-type galaxies.

These results suggest that the curvature in the SL and FJ relations is not due to varying fractions of either BCGs or SRs, but is instead intrinsic to the relations for early-type galaxies. The curvature we observe is consistent with the picture put forth in Lauer et al. [6], suggesting that velocity dispersion plateaus as luminosity continues to increase through dry mergers, leading to an underprediction of central SMBH masses from the $M-\sigma$ relation. We are currently working to increase the number of dynamical black hole mass measurements in our sample and plan to explore this issue further.

Acknowledgements

We thank James Schombert for his assistance with the ARCHANGEL pipeline. Based on observations obtained with WIRCam, a joint project of CFHT, Taiwan, Korea, Canada,

France, at the Canada-France-Hawaii Telescope (CFHT) which is operated by the National Research Council (NRC) of Canada, the Institut National des Sciences de l'Univers of the Centre National de la Recherche Scientifique of France, and the University of Hawaii. We thank the staff of CFHT for their outstanding and always good-natured support during the course of this project. The MASSIVE survey is supported in part by NSF AST-1815417 and AST-1817100. J.P.B. is supported by NOIRLab, which is managed by the Association of Universities for Research in Astronomy (AURA) under a cooperative agreement with the National Science Foundation. C.-P.M. acknowledges support from the Heising-Simons Foundation and the Miller Institute for Basic Research in Science.

Chapter 6

Conclusion and Future Directions

This dissertation presented studies of several aspects of giant elliptical galaxies. Chapter 2 presented updates to the modeling code originally described in [59], along with an application of this code to axisymmetric models of NGC 1453. A fully triaxial version of this code was then presented in Chapter 3, and a new triaxial search strategy was outlined. This framework was then applied to NGC 1453, resulting in a simultaneous determination of the central black hole mass, mass-to-light ratio, dark matter halo mass, and triaxial shape.

In order to validate this code, a pipeline for generating photometric and kinematic data of realistic mock galaxies was described in Chapter 4. The ability for the orbit modeling code to recover galaxy parameters was tested for both axisymmetric and triaxial models. These tests demonstrate recovery of the intrinsic galaxy shape that is far more accurate than comparable tests of the original code version. Together, these chapters provide dramatic improvements on existing dynamical modeling frameworks, allowing for precise measurements of intrinsic galaxy shapes.

Chapter 5 presents measurements of K-band total magnitudes and half-light radii for a volume-limited sample of the $\sim$100 most massive nearby elliptical galaxies. The Faber-Jackson and luminosity-size relations are studied within this sample. The addition of these massive elliptical galaxies reveals curvature in these relations when compared with less massive ellipticals.

The updated code described in this dissertation can be used to infer triaxial shapes, mass distributions, and orbital distributions in elliptical galaxies. Specifically, this dissertation takes significant steps towards many of the science goals of the MASSIVE survey [88]. The updated code described in this dissertation can now be used to model this sample of massive elliptical galaxies for which photometric and spectroscopic observations have been made. A volume-limited sample of central black hole masses in the most massive nearby galaxies, together with the photometric parameters measured in Chapter 5, would give key insights into the local scaling relations and allow for a more complete understanding of how these galaxies formed.

Bibliography

[1] E. P. Hubble. "Extragalactic nebulae." In: *The Astrophysical Journal* 64 (Dec. 1926), pp. 321–369. DOI: 10.1086/143018.

[2] J. Kormendy. "Brightness distributions in compact and normal galaxies. II. Structure parameters of the spheroidal component." In: *The Astrophysical Journal* 218 (Dec. 1977), pp. 333–346. DOI: 10.1086/155687.

[3] J. L. Sérsic. "Influence of the atmospheric and instrumental dispersion on the brightness distribution in a galaxy". In: *Boletin de la Asociacion Argentina de Astronomia La Plata Argentina* 6 (Feb. 1963), pp. 41–43.

[4] Alister W. Graham and Rafael Guzmán. "HST Photometry of Dwarf Elliptical Galaxies in Coma, and an Explanation for the Alleged Structural Dichotomy between Dwarf and Bright Elliptical Galaxies". In: *The Astronomical Journal* 125.6 (June 2003), pp. 2936–2950. DOI: 10.1086/374992. arXiv: astro-ph/0303391 [astro-ph].

[5] Alister W. Graham et al. "A New Empirical Model for the Structural Analysis of Early-Type Galaxies, and A Critical Review of the Nuker Model". In: *The Astronomical Journal* 125.6 (June 2003), pp. 2951–2963. DOI: 10.1086/375320. arXiv: astro-ph/0306023 [astro-ph].

[6] Tod R. Lauer et al. "The Masses of Nuclear Black Holes in Luminous Elliptical Galaxies and Implications for the Space Density of the Most Massive Black Holes". In: *The Astrophysical Journal* 662.2 (2007), pp. 808–834. ISSN: 0004-637X. DOI: 10.1086/518223. arXiv: 0606739 [arXiv:astro-ph]. URL: http://stacks.iop.org/0004-637X/662/i=2/a=808.

[7] Eric Emsellem et al. "The ATLAS^{3D} project - III. A census of the stellar angular momentum within the effective radius of early-type galaxies: unveiling the distribution of fast and slow rotators". In: *Monthly Notices of the Royal Astronomical Society* 414.2 (June 2011), pp. 888–912. DOI: 10.1111/j.1365-2966.2011.18496.x. arXiv: 1102.4444 [astro-ph.CO].

[8] Charles F. Goullaud et al. "The MASSIVE Survey. IX. Photometric Analysis of 35 High-mass Early-type Galaxies with HST WFC3/IR". In: *The Astrophysical Journal* 856, 11 (Mar. 2018), p. 11. DOI: 10.3847/1538-4357/aab1f3.

[9] David Carter. "The structure of the isophotes of elliptical galaxies". In: *Monthly Notices of the Royal Astronomical Society* 182 (Mar. 1978), p. 797. DOI: 10.1093/mnras/182.4.797.

[10] Robert I. Jedrzejewski. "CCD surface photometry of elliptical galaxies - I. Observations, reduction and results." In: *Monthly Notices of the Royal Astronomical Society* 226 (June 1987), pp. 747–768. DOI: 10.1093/mnras/226.4.747.

[11] R. Bender. "Velocity anisotropies and isophote shapes in elliptical galaxies." In: *Astronomy and Astrophysics* 193 (Mar. 1988), pp. L7–L10.

[12] Frank C. van den Bosch et al. "Hubble Space Telescope Photometry of the Central Regions of Virgo Cluster Elliptical Galaxies. II. Isophote Shapes". In: *The Astronomical Journal* 108 (Nov. 1994), p. 1579. DOI: 10.1086/117179.

[13] M. Cappellari et al. "The SAURON project - IV. The mass-to-light ratio, the virial mass estimator and the Fundamental Plane of elliptical and lenticular galaxies". In: *Monthly Notices of the Royal Astronomical Society* 366 (Mar. 2006), pp. 1126–1150. DOI: 10.1111/j.1365-2966.2005.09981.x. eprint: arXiv:astro-ph/0505042.

[14] S. M. Faber and R. E. Jackson. "Velocity dispersions and mass-to-light ratios for elliptical galaxies." In: *The Astrophysical Journal* 204 (Mar. 1976), pp. 668–683. DOI: 10.1086/154215.

[15] S. Djorgovski and Marc Davis. "Fundamental Properties of Elliptical Galaxies". In: *The Astrophysical Journal* 313 (Feb. 1987), p. 59. DOI: 10.1086/164948.

[16] Patrick Morrissey et al. "The Keck Cosmic Web Imager Integral Field Spectrograph". In: *The Astrophysical Journal* 864.1, 93 (Sept. 2018), p. 93. DOI: 10.3847/1538-4357/aad597. arXiv: 1807.10356 [astro-ph.IM].

[17] P. Jakobsen et al. "The Near-Infrared Spectrograph (NIRSpec) on the James Webb Space Telescope. I. Overview of the instrument and its capabilities". In: *Astronomy and Astrophysics* 661, A80 (May 2022), A80. DOI: 10.1051/0004-6361/202142663. arXiv: 2202.03305 [astro-ph.IM].

[18] Roeland P. van der Marel and Marijn Franx. "A New Method for the Identification of Non-Gaussian Line Profiles in Elliptical Galaxies". In: *The Astrophysical Journal* 407 (Apr. 1993), p. 525. DOI: 10.1086/172534.

[19] J. Binney. "Elliptical galaxies: prolate, oblate or triaxial?" In: *Comments on Astrophysics* 8.2 (Jan. 1978), pp. 27–36.

[20] A.-M. Weijmans et al. "The ATLAS ^{3D} project - XXIV. The intrinsic shape distribution of early-type galaxies". In: *Monthly Notices of the Royal Astronomical Society* 444 (Nov. 2014), pp. 3340–3356. DOI: 10.1093/mnras/stu1603. arXiv: 1408.1099.

[21] James Binney. "Testing for triaxiality with kinematic data". In: *Monthly Notices of the Royal Astronomical Society* 212.4 (1985), pp. 767–781. ISSN: 0035-8711. DOI: 10.1093/mnras/212.4.767. eprint: http://oup.prod.sis.lan/mnras/article-pdf/212/4/767/3792766/mnras212-0767.pdf.

[22] Tim de Zeeuw. "Elliptical galaxies with separable potentials". In: *Monthly Notices of the Royal Astronomical Society* 216.2 (Sept. 1985), pp. 273–334. ISSN: 0035-8711. DOI: 10.1093/mnras/216.2.273. eprint: http://oup.prod.sis.lan/mnras/article-pdf/216/2/273/3500591/mnras216-0273.pdf.

[23] Martin Schwarzschild. "Self-consistent Models for Galactic Halos". In: *The Astrophysical Journal* 409 (June 1993), p. 563. DOI: 10.1086/172687.

[24] Jordi Miralda-Escude and M. Schwarzschild. "On the Orbit Structure of the Logarithmic Potential". In: *The Astrophysical Journal* 339 (Apr. 1989), p. 752. DOI: 10.1086/167333.

[25] Monica Valluri, David Merritt, and Eric Emsellem. "Difficulties with Recovering the Masses of Supermassive Black Holes from Stellar Kinematical Data". In: *The Astrophysical Journal* 602.1 (2004), pp. 66–92. DOI: 10.1086/380896. arXiv: astro-ph/0210379 [astro-ph].

[26] Marijn Franx and Garth D. Illingworth. "A Counterrotating Core in IC 1459". In: *The Astrophysical Journal, Letters* 327 (Apr. 1988), p. L55. DOI: 10.1086/185139.

[27] Irina Ene et al. "The MASSIVE Survey - X. Misalignment between kinematic and photometric axes and intrinsic shapes of massive early-type galaxies". In: *Monthly Notices of the Royal Astronomical Society* 479.2 (2018), pp. 2810–2826. DOI: 10.1093/mnras/sty1649. eprint: /oup/backfile/content_public/journal/mnras/479/2/10.1093_mnras_sty1649/1/sty1649.pdf. URL: http://dx.doi.org/10.1093/mnras/sty1649.

[28] Karl Gebhardt et al. "A Relationship between Nuclear Black Hole Mass and Galaxy Velocity Dispersion". In: *The Astrophysical Journal, Letters* 539.1 (Aug. 2000), pp. L13–L16. DOI: 10.1086/312840. arXiv: astro-ph/0006289 [astro-ph].

[29] E. E. Salpeter. "Accretion of Interstellar Matter by Massive Objects." In: *The Astrophysical Journal* 140 (Aug. 1964), pp. 796–800. DOI: 10.1086/147973.

[30] Ya. B. Zel'dovich. "The Fate of a Star and the Evolution of Gravitational Energy Upon Accretion". In: *Soviet Physics Doklady* 9 (Sept. 1964), p. 195.

[31] Gravity Collaboration et al. "A geometric distance measurement to the Galactic center black hole with 0.3% uncertainty". In: *Astronomy and Astrophysics* 625, L10 (May 2019), p. L10. DOI: 10.1051/0004-6361/201935656. arXiv: 1904.05721 [astro-ph.GA].

[32] John Kormendy and Luis C. Ho. "Coevolution (Or Not) of Supermassive Black Holes and Host Galaxies". In: (2013). DOI: 10.1146/annurev-astro-082708-101811. arXiv: 1304.7762. URL: http://arxiv.org/abs/1304.7762%20http://dx.doi.org/10.1146/annurev-astro-082708-101811.

[33] Event Horizon Telescope Collaboration et al. "First M87 Event Horizon Telescope Results. I. The Shadow of the Supermassive Black Hole". In: *The Astrophysical Journal, Letters* 875.1, L1 (Apr. 2019), p. L1. DOI: 10.3847/2041-8213/ab0ec7. arXiv: 1906.11238 [astro-ph.GA].

[34] Event Horizon Telescope Collaboration et al. "First Sagittarius A* Event Horizon Telescope Results. I. The Shadow of the Supermassive Black Hole in the Center of the Milky Way". In: *The Astrophysical Journal, Letters* 930.2, L12 (May 2022), p. L12. DOI: 10.3847/2041-8213/ac667410.3847/2041-8213/ac6675.

[35] Event Horizon Telescope Collaboration et al. "First M87 Event Horizon Telescope Results. VI. The Shadow and Mass of the Central Black Hole". In: *The Astrophysical Journal, Letters* 875.1, L6 (Apr. 2019), p. L6. DOI: 10.3847/2041-8213/ab1141. arXiv: 1906.11243 [astro-ph.GA].

[36] Event Horizon Telescope Collaboration et al. "First Sagittarius A* Event Horizon Telescope Results. IV. Variability, Morphology, and Black Hole Mass". In: *The Astrophysical Journal, Letters* 930.2, L15 (May 2022), p. L15. DOI: 10.3847/2041-8213/ac667410.3847/2041-8213/ac667210.3847/2041-8213/ac6736.

[37] John Kormendy and Douglas Richstone. "Inward Bound—The Search For Supermassive Black Holes In Galactic Nuclei". In: *Annual Review of Astronomy and Astrophysics* 33 (Jan. 1995), p. 581. DOI: 10.1146/annurev.aa.33.090195.003053.

[38] N. J. McConnell and C.-P. Ma. "Revisiting the Scaling Relations of Black Hole Masses and Host Galaxy Properties". In: *The Astrophysical Journal* 764, 184 (Feb. 2013), p. 184. DOI: 10.1088/0004-637X/764/2/184. arXiv: 1211.2816 [astro-ph.CO].

[39] Massimo Gaspari, Francesco Tombesi, and Massimo Cappi. "Linking macro-, meso- and microscales in multiphase AGN feeding and feedback". In: *Nature Astronomy* 4 (Jan. 2020), pp. 10–13. DOI: 10.1038/s41550-019-0970-1. arXiv: 2001.04985 [astro-ph.GA].

[40] Li-Ming Yu et al. "Calibration of the virial factor f in supermassive black hole masses of reverberation-mapped AGNs". In: *Monthly Notices of the Royal Astronomical Society* 488.2 (Sept. 2019), pp. 1519–1534. DOI: 10.1093/mnras/stz1766. arXiv: 1907.00315 [astro-ph.GA].

[41] James Binney and Scott Tremaine. *Galactic Dynamics, 2nd edition, p. 75.* 2008.

[42] Michele Cappellari et al. "The ATLAS^{3D} project - XV. Benchmark for early-type galaxies scaling relations from 260 dynamical models: mass-to-light ratio, dark matter, Fundamental Plane and Mass Plane". In: *Monthly Notices of the Royal Astronomical Society* 432.3 (July 2013), pp. 1709–1741. DOI: 10.1093/mnras/stt562. arXiv: 1208.3522 [astro-ph.CO].

[43] Michele Cappellari. "Measuring the inclination and mass-to-light ratio of axisymmetric galaxies via anisotropic Jeans models of stellar kinematics". In: *Monthly Notices of the Royal Astronomical Society* 390.1 (Oct. 2008), pp. 71–86. DOI: 10.1111/j.1365-2966.2008.13754.x. arXiv: 0806.0042 [astro-ph].

[44] Michele Cappellari. "Efficient solution of the anisotropic spherically aligned axisymmetric Jeans equations of stellar hydrodynamics for galactic dynamics". In: *Monthly Notices of the Royal Astronomical Society* 494.4 (June 2020), pp. 4819–4837. DOI: 10.1093/mnras/staa959. arXiv: 1907.09894 [astro-ph.GA].

[45] M. Schwarzschild. "A numerical model for a triaxial stellar system in dynamical equilibrium". In: *The Astrophysical Journal* 232 (Aug. 1979), pp. 236–247. DOI: 10.1086/157282.

[46] Hans-Walter Rix et al. "Dynamical Modeling of Velocity Profiles: The Dark Halo around the Elliptical Galaxy NGC 2434". In: *The Astrophysical Journal* 488.2 (Oct. 1997), pp. 702–719. DOI: 10.1086/304733. arXiv: astro-ph/9702126 [astro-ph].

[47] Roeland P. van der Marel et al. "Improved Evidence for a Black Hole in M32 from HST/FOS Spectra. II. Axisymmetric Dynamical Models". In: *The Astrophysical Journal* 493.2 (Jan. 1998), pp. 613–631. DOI: 10.1086/305147. arXiv: astro-ph/9705081 [astro-ph].

[48] N. Cretton et al. "Axisymmetric Three-Integral Models for Galaxies". In: *The Astrophysical Journal, Supplement* 124.2 (Oct. 1999), pp. 383–401. DOI: 10.1086/313264. arXiv: astro-ph/9902034 [astro-ph].

[49] M. Cappellari et al. "The Counterrotating Core and the Black Hole Mass of IC 1459". In: *The Astrophysical Journal* 578.2 (Oct. 2002), pp. 787–805. DOI: 10.1086/342653. arXiv: astro-ph/0202155 [astro-ph].

[50] E. K. Verolme et al. "A SAURON study of M32: measuring the intrinsic flattening and the central black hole mass". In: *Monthly Notices of the Royal Astronomical Society* 335 (Sept. 2002), pp. 517–525. DOI: 10.1046/j.1365-8711.2002.05664.x. arXiv: astro-ph/0201086 [astro-ph].

[51] Kristen L. Shapiro et al. "The black hole in NGC 3379: a comparison of gas and stellar dynamical mass measurements with HST and integral-field data". In: *Monthly Notices of the Royal Astronomical Society* 370.2 (Aug. 2006), pp. 559–579. DOI: 10.1111/j.1365-2966.2006.10537.x. arXiv: astro-ph/0605479 [astro-ph].

[52] Davor Krajnović et al. "Determination of masses of the central black holes in NGC 524 and 2549 using laser guide star adaptive optics". In: *Monthly Notices of the Royal Astronomical Society* 399.4 (Nov. 2009), pp. 1839–1857. DOI: 10.1111/j.1365-2966.2009.15415.x. arXiv: 0907.3748 [astro-ph.GA].

[53] Karl Gebhardt et al. "Axisymmetric, Three-Integral Models of Galaxies: A Massive Black Hole in NGC 3379". In: *The Astronomical Journal* 119.3 (Mar. 2000), pp. 1157–1171. DOI: 10.1086/301240. arXiv: astro-ph/9912026 [astro-ph].

[54] Karl Gebhardt et al. "Axisymmetric Dynamical Models of the Central Regions of Galaxies". In: *The Astrophysical Journal* 583.1 (Jan. 2003), pp. 92–115. DOI: 10.1086/345081. arXiv: astro-ph/0209483 [astro-ph].

[55] Monica Valluri et al. "The Low End of the Supermassive Black Hole Mass Function: Constraining the Mass of a Nuclear Black Hole in NGC 205 via Stellar Kinematics". In: *The Astrophysical Journal* 628.1 (July 2005), pp. 137–152. DOI: 10.1086/430752. arXiv: astro-ph/0502493 [astro-ph].

[56] Christos Siopis et al. "A Stellar Dynamical Measurement of the Black Hole Mass in the Maser Galaxy NGC 4258". In: *The Astrophysical Journal* 693.1 (Mar. 2009), pp. 946–969. DOI: 10.1088/0004-637x/693/1/946.

[57] Juntai Shen and Karl Gebhardt. "The Supermassive Black Hole and Dark Matter Halo of NGC 4649 (M60)". In: *The Astrophysical Journal* 711.1 (Mar. 2010), pp. 484–494. DOI: 10.1088/0004-637X/711/1/484. arXiv: 0910.4168 [astro-ph.CO].

[58] Karl Gebhardt et al. "The Black Hole Mass in M87 from Gemini/NIFS Adaptive Optics Observations". In: *The Astrophysical Journal* 729.2, 119 (Mar. 2011), p. 119. DOI: 10.1088/0004-637X/729/2/119. arXiv: 1101.1954 [astro-ph.CO].

[59] R. C. E. van den Bosch et al. "Triaxial orbit based galaxy models with an application to the (apparent) decoupled core galaxy NGC 4365". In: *Monthly Notices of the Royal Astronomical Society* 385 (Apr. 2008), pp. 647–666. DOI: 10.1111/j.1365-2966.2008.12874.x. arXiv: 0712.0113.

[60] Remco C. E. van den Bosch and Glenn van de Ven. "Recovering the intrinsic shape of early-type galaxies". In: *Monthly Notices of the Royal Astronomical Society* 398.3 (Sept. 2009), pp. 1117–1128. DOI: 10.1111/j.1365-2966.2009.15177.x. arXiv: 0811.3474 [astro-ph].

[61] G. van de Ven, P. T. De Zeeuw, and R. C. E. Van Den Bosch. "Recovery of the internal orbital structure of galaxies". In: *Monthly Notices of the Royal Astronomical Society* 385.2 (Feb. 2008), pp. 614–646. ISSN: 0035-8711. DOI: 10.1111/j.1365-2966.2008.12873.x. eprint: http://oup.prod.sis.lan/mnras/article-pdf/385/2/614/18226009/mnras0385-0614.pdf.

[62] Ling Zhu et al. "The stellar orbit distribution in present-day galaxies inferred from the CALIFA survey". In: *Nature Astronomy* 2 (Jan. 2018), pp. 233–238. DOI: 10.1038/s41550-017-0348-1. arXiv: 1711.06728 [astro-ph.GA].

[63] Adriano Poci et al. "Combining stellar populations with orbit-superposition dynamical modelling: the formation history of the lenticular galaxy NGC 3115". In: *Monthly Notices of the Royal Astronomical Society* 487.3 (Aug. 2019), pp. 3776–3796. DOI: 10.1093/mnras/stz1154. arXiv: 1904.11605 [astro-ph.GA].

[64] Katja Fahrion et al. "Constraining nuclear star cluster formation using MUSE-AO observations of the early-type galaxy FCC 47". In: *Astronomy and Astrophysics* 628, A92 (Aug. 2019), A92. DOI: 10.1051/0004-6361/201935832. arXiv: 1907.01007 [astro-ph.GA].

[65] Yunpeng Jin et al. "SDSS-IV MaNGA: Internal mass distributions and orbital structures of early-type galaxies and their dependence on environment". In: *Monthly Notices of the Royal Astronomical Society* 491.2 (Jan. 2020), pp. 1690–1708. DOI: 10.1093/mnras/stz3072. arXiv: 1911.00777 [astro-ph.GA].

[66] Remco C. E. van den Bosch and P. Tim de Zeeuw. "Estimating black hole masses in triaxial galaxies". In: *Monthly Notices of the Royal Astronomical Society* 401.3 (Jan. 2010), pp. 1770–1780. DOI: 10.1111/j.1365-2966.2009.15832.x. arXiv: 0910.0844 [astro-ph.CO].

[67] J. L. Walsh et al. "A Stellar Dynamical Mass Measurement of the Black Hole in NGC 3998 from Keck Adaptive Optics Observations". In: *The Astrophysical Journal* 753, 79 (July 2012), p. 79. DOI: 10.1088/0004-637X/753/1/79. arXiv: 1205.0816.

[68] A. Feldmeier-Krause et al. "Triaxial orbit-based modelling of the Milky Way Nuclear Star Cluster". In: *Monthly Notices of the Royal Astronomical Society* 466.4 (Apr. 2017), pp. 4040–4052. DOI: 10.1093/mnras/stw3377. arXiv: 1701.01583 [astro-ph.GA].

[69] Mark den Brok et al. "Dynamical modelling of the twisted galaxy PGC 046832". In: *Monthly Notices of the Royal Astronomical Society* 508.4 (Dec. 2021), pp. 4786–4805. DOI: 10.1093/mnras/stab2852. arXiv: 2109.14640 [astro-ph.GA].

[70] Anil C. Seth et al. "A supermassive black hole in an ultra-compact dwarf galaxy". In: *Nature* 513.1 (2014), p. 398. DOI: 10.1038/nature13762.

[71] J. L. Walsh et al. "The Black Hole in the Compact, High-dispersion Galaxy NGC 1271". In: *The Astrophysical Journal* 808, 183 (Aug. 2015), p. 183. DOI: 10.1088/0004-637X/808/2/183. arXiv: 1506.05129.

[72] J. L. Walsh et al. "A 5 x 10^9 Msun Black Hole in NGC 1277 from Adaptive Optics Spectroscopy". In: *The Astrophysical Journal* 817, 2 (Jan. 2016), p. 2. DOI: 10.3847/0004-637X/817/1/2. arXiv: 1511.04455.

[73] J. L. Walsh et al. "A Black Hole Mass Determination for the Compact Galaxy Mrk 1216". In: *The Astrophysical Journal* 835, 208 (Feb. 2017), p. 208. DOI: 10.3847/1538-4357/835/2/208. arXiv: 1612.02015.

[74] C. P. Ahn et al. "The Black Hole in the Most Massive Ultracompact Dwarf Galaxy M59-UCD3". In: *The Astrophysical Journal* 858, 102 (May 2018), p. 102. DOI: 10.3847/1538-4357/aabc57. arXiv: 1804.02399.

[75] Yunpeng Jin et al. "Evaluating the ability of triaxial Schwarzschild modelling to estimate properties of galaxies from the Illustris simulation". In: *Monthly Notices of the Royal Astronomical Society* 486.4 (July 2019), pp. 4753–4772. DOI: 10.1093/mnras/stz1170. arXiv: 1904.12942 [astro-ph.GA].

[76] Ricardo Herbonnet et al. "Brightest cluster galaxies trace weak lensing mass bias and halo triaxiality in the three hundred project". In: *Monthly Notices of the Royal Astronomical Society* 513.2 (June 2022), pp. 2178–2193. DOI: 10.1093/mnras/stac997. arXiv: 2109.01673 [astro-ph.CO].

[77] M. Meneghetti et al. "The MUSIC of CLASH: Predictions on the Concentration-Mass Relation". In: *The Astrophysical Journal* 797.1, 34 (Dec. 2014), p. 34. DOI: 10.1088/0004-637X/797/1/34. arXiv: 1404.1384 [astro-ph.CO].

[78] Matthew E. Quenneville, Christopher M. Liepold, and Chung-Pei Ma. "Dynamical Modeling of Galaxies and Supermassive Black Holes: Axisymmetry in Triaxial Schwarzschild Orbit Superposition Models". In: *The Astrophysical Journal, Supplement* 254.2, 25 (June 2021), p. 25. DOI: 10.3847/1538-4365/abe6a0. arXiv: 2005.00542 [astro-ph.GA].

[79] D. Pfenniger. "The velocity fields of barred galaxies." In: *Astronomy and Astrophysics* 141 (Dec. 1984), pp. 171–188.

[80] D. O. Richstone and S. Tremaine. "A general method for constructing spherical galaxy models". In: *The Astrophysical Journal* 286 (Nov. 1984), pp. 27–37. DOI: 10.1086/162572.

[81] D. O. Richstone and S. Tremaine. "Dynamical models of M 87 without a central black hole." In: *The Astrophysical Journal* 296 (Sept. 1985), pp. 370–378. DOI: 10.1086/163455.

[82] J. Thomas et al. "Mapping stationary axisymmetric phase-space distribution functions by orbit libraries". In: *Monthly Notices of the Royal Astronomical Society* 353.2 (Sept. 2004), pp. 391–404. ISSN: 0035-8711. DOI: 10.1111/j.1365-2966.2004.08072.x. eprint: http://oup.prod.sis.lan/mnras/article-pdf/353/2/391/3858810/353-2-391.pdf.

[83] R. C. E. van den Bosch and P. T. de Zeeuw. "Estimating black hole masses in triaxial galaxies". In: *Monthly Notices of the Royal Astronomical Society* 401 (Jan. 2010), pp. 1770–1780. DOI: 10.1111/j.1365-2966.2009.15832.x. arXiv: 0910.0844 [astro-ph.CO].

[84] A. Feldmeier-Krause et al. "Triaxial orbit-based modelling of the Milky Way nuclear star cluster". In: *Monthly Notices of the Royal Astronomical Society* 466.4 (2017), pp. 4040–4052. DOI: 10.1093/mnras/stw3377. eprint: /oup/backfile/content_public/journal/mnras/466/4/10.1093_mnras_stw3377/4/stw3377.pdf.

[85] Eugene Vasiliev and Monica Valluri. "A New Implementation of the Schwarzchild Method for Constructing Observationally Driven Dynamical Models of Galaxies of All Morphological Types". In: *The Astrophysical Journal* 889.1, 39 (Jan. 2020), p. 39. DOI: 10.3847/1538-4357/ab5fe0. arXiv: 1912.04288 [astro-ph.GA].

[86] C. L. Joseph et al. "The Nuclear Dynamics of M32. I. Data and Stellar Kinematics". In: *The Astrophysical Journal* 550.2 (Apr. 2001), pp. 668–690. DOI: 10.1086/319781. arXiv: astro-ph/0005530 [astro-ph].

[87] Christopher M. Liepold et al. "The MASSIVE Survey. XV. A Stellar Dynamical Mass Measurement of the Supermassive Black Hole in Massive Elliptical Galaxy NGC 1453". In: *The Astrophysical Journal* 891.1 (Feb. 2020), p. 4. DOI: 10.3847/1538-4357/ab6f71.

[88] C.-P. Ma et al. "The MASSIVE Survey. I. A Volume-limited Integral-field Spectroscopic Study of the Most Massive Early-type Galaxies within 108 Mpc". In: *The Astrophysical Journal* 795, 158 (Nov. 2014), p. 158. DOI: 10.1088/0004-637X/795/2/158. arXiv: 1407.1054.

[89] G. Heiligman and M. Schwarzschild. "On the nonexistence of three-dimensional tube orbits around the intermediate axis in a triaxial galaxy model." In: *The Astrophysical Journal* 233.3 (Nov. 1979), pp. 872–876. DOI: 10.1086/157449.

[90] J. Binney and D. Spergel. "Spectral stellar dynamics. II - The action integrals". In: *Monthly Notices of the Royal Astronomical Society* 206 (Jan. 1984), pp. 159–177. DOI: 10.1093/mnras/206.1.159.

[91] Jorrit H. J. Hagen, Amina Helmi, and Maarten A. Breddels. "Axisymmetric Schwarzschild models of an isothermal axisymmetric mock dwarf spheroidal galaxy". In: *Astronomy and Astrophysics* 632, A99 (Dec. 2019), A99. DOI: 10.1051/0004-6361/201936196. arXiv: 1907.00156 [astro-ph.GA].

[92] S. Sridhar and J. Touma. "Stellar dynamics around black holes in galactic nuclei". In: *Monthly Notices of the Royal Astronomical Society* 303.3 (Mar. 1999), pp. 483–494. DOI: 10.1046/j.1365-8711.1999.02218.x. arXiv: astro-ph/9811304 [astro-ph].

[93] S. Sridhar and Jihad R. Touma. "Stellar dynamics around a massive black hole – I. Secular collisionless theory". In: *Monthly Notices of the Royal Astronomical Society* 458.4 (Mar. 2016), pp. 4129–4142. ISSN: 0035-8711. DOI: 10.1093/mnras/stw542. URL: https://doi.org/10.1093/mnras/stw542.

[94] Monica Valluri et al. "A Unified Framework for the Orbital Structure of Bars and Triaxial Ellipsoids". In: *The Astrophysical Journal* 818.2, 141 (Feb. 2016), p. 141. DOI: 10.3847/0004-637X/818/2/141. arXiv: 1512.03467 [astro-ph.GA].

[95] Lars Hernquist. "An Analytical Model for Spherical Galaxies and Bulges". In: *The Astrophysical Journal* 356 (June 1990), p. 359. DOI: 10.1086/168845.

[96] Julio F. Navarro, Carlos S. Frenk, and Simon D. M. White. "The Structure of Cold Dark Matter Halos". In: *The Astrophysical Journal* 462 (May 1996), p. 563. DOI: 10.1086/177173. arXiv: astro-ph/9508025 [astro-ph].

[97] F. Pedregosa et al. "Scikit-learn: Machine Learning in Python". In: *Journal of Machine Learning Research* 12 (2011), pp. 2825–2830.

[98] Matthew E. Quenneville, Christopher M. Liepold, and Chung-Pei Ma. "Triaxial Orbit-based Dynamical Modeling of Galaxies with Supermassive Black Holes and an Application to Massive Elliptical Galaxy NGC 1453". In: *The Astrophysical Journal* 926.1, 30 (Feb. 2022), p. 30. DOI: 10.3847/1538-4357/ac3e68. arXiv: 2111.06904 [astro-ph.GA].

[99] M. Franx, G. Illingworth, and T. de Zeeuw. "The ordered nature of elliptical galaxies - Implications for their intrinsic angular momenta and shapes". In: *The Astrophysical Journal* 383 (Dec. 1991), pp. 112–134. DOI: 10.1086/170769.

[100] E. Emsellem et al. "The SAURON project - IX. A kinematic classification for early-type galaxies". In: *Monthly Notices of the Royal Astronomical Society* 379 (Aug. 2007), pp. 401–417. DOI: 10.1111/j.1365-2966.2007.11752.x. eprint: arXiv:astro-ph/0703531.

[101] M. Cappellari. "Structure and Kinematics of Early-Type Galaxies from Integral Field Spectroscopy". In: *Annual Review of Astronomy and Astrophysics* 54 (Sept. 2016), pp. 597–665. DOI: 10.1146/annurev-astro-082214-122432. arXiv: 1602.04267.

[102] C. Foster et al. "The SAMI Galaxy Survey: the intrinsic shape of kinematically selected galaxies". In: *Monthly Notices of the Royal Astronomical Society* 472.1 (Nov. 2017), pp. 966–978. DOI: 10.1093/mnras/stx1869. arXiv: 1709.03585 [astro-ph.GA].

[103] Melanie Veale et al. "The MASSIVE Survey - V. Spatially resolved stellar angular momentum, velocity dispersion, and higher moments of the 41 most massive local early-type galaxies". In: *Monthly Notices of the Royal Astronomical Society* 464 (Jan. 2017), pp. 356–384. DOI: 10.1093/mnras/stw2330. arXiv: 1609.00391 [astro-ph.GA].

[104] Melanie Veale et al. "The MASSIVE Survey - VII. The relationship of angular momentum, stellar mass and environment of early-type galaxies". In: *Monthly Notices of the Royal Astronomical Society* 471 (Oct. 2017), pp. 1428–1445. DOI: 10.1093/mnras/stx1639. arXiv: 1703.08573 [astro-ph.GA].

[105] Melanie Veale et al. "The MASSIVE survey - VIII. Stellar velocity dispersion profiles and environmental dependence of early-type galaxies". In: *Monthly Notices of the Royal Astronomical Society* 473 (Feb. 2018), pp. 5446–5467. DOI: 10.1093/mnras/stx2717. arXiv: 1708.00870 [astro-ph.GA].

[106] D. Krajnović et al. "A quartet of black holes and a missing duo: probing the low end of the M_{BH}-σ relation with the adaptive optics assisted integral-field spectroscopy". In: *Monthly Notices of the Royal Astronomical Society* 477 (July 2018), pp. 3030–3064. DOI: 10.1093/mnras/sty778. arXiv: 1803.08055.

[107] Irina Ene et al. "The MASSIVE Survey XIV—Stellar Velocity Profiles and Kinematic Misalignments from 200 pc to 20 kpc in Massive Early-type Galaxies". In: *The Astrophysical Journal* 891.1, 65 (Mar. 2020), p. 65. DOI: 10.3847/1538-4357/ab7016. arXiv: 2001.11046 [astro-ph.GA].

[108] Tuan Do et al. "Relativistic redshift of the star S0-2 orbiting the Galactic Center supermassive black hole". In: *Science* 365.6454 (Aug. 2019), pp. 664–668. DOI: 10.1126/science.aav8137. arXiv: 1907.10731 [astro-ph.GA].

[109] Gigi Y. C. Leung et al. "The EDGE-CALIFA survey: validating stellar dynamical mass models with CO kinematics". In: *Monthly Notices of the Royal Astronomical Society* 477.1 (June 2018), pp. 254–292. DOI: 10.1093/mnras/sty288. arXiv: 1803.02259 [astro-ph.GA].

[110] Ling Zhu et al. "Orbital decomposition of CALIFA spiral galaxies". In: *Monthly Notices of the Royal Astronomical Society* 473.3 (Jan. 2018), pp. 3000–3018. DOI: 10.1093/mnras/stx2409. arXiv: 1709.06649 [astro-ph.GA].

[111] Meng Yang et al. "Mapping the dark matter halo of early-type galaxy NGC 2974 through orbit-based models with combined stellar and cold gas kinematics". In: *Monthly Notices of the Royal Astronomical Society* 491.3 (Jan. 2020), pp. 4221–4231. DOI: 10.1093/mnras/stz3293. arXiv: 1911.11058 [astro-ph.GA].

[112] Tim de Zeeuw and Marijn Franx. "Kinematics of Gas in a Triaxial Galaxy". In: *The Astrophysical Journal* 343 (Aug. 1989), p. 617. DOI: 10.1086/167735.

[113] Michele Cappellari. "Efficient multi-Gaussian expansion of galaxies". In: *Monthly Notices of the Royal Astronomical Society* 333.2 (2002), pp. 400–410. DOI: 10.1046/j.1365-8711.2002.05412.x. eprint: /oup/backfile/content_public/journal/mnras/333/2/10.1046_j.1365-8711.2002.05412.x/2/333-2-400.pdf. URL: http://dx.doi.org/10.1046/j.1365-8711.2002.05412.x.

[114] Stefano de Nicola et al. "Non-parametric triaxial deprojection of elliptical galaxies". In: *Monthly Notices of the Royal Astronomical Society* 496.3 (Aug. 2020), pp. 3076–3100. DOI: 10.1093/mnras/staa1703. arXiv: 2006.05971 [astro-ph.GA].

[115] Marijn Franx. "The projection of galaxy models with a Staeckel potential". In: *Monthly Notices of the Royal Astronomical Society* 231 (Mar. 1988), pp. 285–308. DOI: 10.1093/mnras/231.2.285.

[116] I. Ene et al. "The MASSIVE Survey XIII. Spatially Resolved Stellar Kinematics in the Central 1 kpc of 20 Massive Elliptical Galaxies with the GMOS-North Integral Field Spectrograph". In: *The Astrophysical Journal* 878, 57 (June 2019), p. 57. DOI: 10.3847/1538-4357/ab1f04. arXiv: 1904.08929.

[117] Joseph B. Jensen et al. "Infrared Surface Brightness Fluctuation Distances for MASSIVE and Type Ia Supernova Host Galaxies". In: *The Astrophysical Journal, Supplement* 255.2, 21 (Aug. 2021), p. 21. DOI: 10.3847/1538-4365/ac01e7. arXiv: 2105.08299 [astro-ph.CO].

[118] Mathias Lipka and Jens Thomas. "A novel approach to optimize the regularization and evaluation of dynamical models using a model selection framework". In: *Monthly Notices of the Royal Astronomical Society* (Apr. 2021). DOI: 10.1093/mnras/stab1092. arXiv: 2104.10168 [astro-ph.GA].

[119] M. D. McKay, R. J. Beckman, and W. J. Conover. "A Comparison of Three Methods for Selecting Values of Input Variables in the Analysis of Output from a Computer Code". In: *Technometrics* 21.2 (1979), pp. 239–245. ISSN: 00401706. URL: http://www.jstor.org/stable/1268522.

[120] Jared L. Deutsch and Clayton V. Deutsch. "Latin hypercube sampling with multidimensional uniformity". In: *Journal of Statistical Planning and Inference* 142.3 (2012), pp. 763–772. ISSN: 0378-3758. DOI: https://doi.org/10.1016/j.jspi.2011.09.016. URL: https://www.sciencedirect.com/science/article/pii/S0378375811003776.

[121] Sahil Moza. *sahilm89/lhsmdu: Latin Hypercube Sampling with Multi-Dimensional Uniformity (LHSMDU): Speed Boost minor compatibility fixes*. Version 1.1.1. July 2020. DOI: 10.5281/zenodo.3929531. URL: https://doi.org/10.5281/zenodo.3929531.

[122] A. S. Eddington. "The distribution of stars in globular clusters". In: *Monthly Notices of the Royal Astronomical Society* 76 (May 1916), pp. 572–585. DOI: 10.1093/mnras/76.7.572.

[123] L. P. Osipkov. "Spherical systems of gravitating bodies with ellipsoidal velocity distribution." In: *Pisma v Astronomicheskii Zhurnal* 5 (Feb. 1979), pp. 77–80.

[124] D. Merritt. "Spherical stellar systems with spheroidal velocity distributions". In: *The Astronomical Journal* 90 (June 1985), pp. 1027–1037. DOI: 10.1086/113810.

[125] C. Hunter and Edward Qian. "Two-integral distribution functions for axisymmetric galaxies." In: *Monthly Notices of the Royal Astronomical Society* 262 (May 1993), pp. 401–428. DOI: 10.1093/mnras/262.2.401.

[126] E. E. Qian et al. "Axisymmetric galaxy models with central black holes, with an application to M32". In: *Monthly Notices of the Royal Astronomical Society* 274.2 (May 1995), pp. 602–622. DOI: 10.1093/mnras/274.2.602. arXiv: astro-ph/9412067 [astro-ph].

[127] H. Dejonghe and D. Laurent. "Abel models for triaxial systems." In: *Monthly Notices of the Royal Astronomical Society* 252 (Oct. 1991), pp. 606–636. DOI: 10.1093/mnras/252.4.606.

[128] A. Mathieu and H. Dejonghe. "Triaxial dynamical models of elliptical galaxies using Stackel potentials". In: *Monthly Notices of the Royal Astronomical Society* 303.3 (Mar. 1999), pp. 455–465. DOI: 10.1046/j.1365-8711.1999.02199.x.

[129] C. Hunter and P. T. de Zeeuw. "Triaxial Galaxy Models with Thin Tube Orbits". In: *The Astrophysical Journal* 389 (Apr. 1992), p. 79. DOI: 10.1086/171190.

[130] Subrahmanyan Chandrasekhar. *Ellipsoidal figures of equilibrium*. Yale University Press, 1969.

[131] Tim de Zeeuw and Daniel Pfenniger. "Potential-density pairs for galaxies." In: *Monthly Notices of the Royal Astronomical Society* 235 (Dec. 1988), pp. 949–995. DOI: 10.1093/mnras/235.3.949.

[132] Carl Edward Rasmussen and Christopher K. I. Williams. *Gaussian Processes for Machine Learning*. 2006.

[133] Sabine Thater et al. "On the robustness of triaxial Schwarzschild modelling: The effects of correcting the orbit mirroring". In: *arXiv e-prints*, arXiv:2205.04165 (May 2022), arXiv:2205.04165. arXiv: 2205.04165 [astro-ph.GA].

[134] Jacob D. Pilawa et al. "The MASSIVE Survey. XVII. A Triaxial Orbit-based Determination of the Black Hole Mass and Intrinsic Shape of Elliptical Galaxy NGC 2693". In: *The Astrophysical Journal* 928.2, 178 (Apr. 2022), p. 178. DOI: 10.3847/1538-4357/ac58fd. arXiv: 2111.13699 [astro-ph.GA].

[135] Davor Krajnović et al. "Dynamical modelling of stars and gas in NGC 2974: determination of mass-to-light ratio, inclination and orbital structure using the Schwarzschild method". In: *Monthly Notices of the Royal Astronomical Society* 357.4 (Mar. 2005), pp. 1113–1133. DOI: 10.1111/j.1365-2966.2005.08715.x. arXiv: astro-ph/0412186 [astro-ph].

[136] S. M. Faber et al. "Global Scaling Relations for Elliptical Galaxies and Implications for Formation". In: *Nearly Normal Galaxies. From the Planck Time to the Present*. Ed. by Sandra M. Faber. Jan. 1987, p. 175.

[137] Brant Robertson et al. "The Fundamental Scaling Relations of Elliptical Galaxies". In: *The Astrophysical Journal* 641.1 (Apr. 2006), pp. 21–40. DOI: 10.1086/500360. arXiv: astro-ph/0511053 [astro-ph].

[138] Mariangela Bernardi et al. "Curvature in the colour-magnitude relation but not in colour-σ: major dry mergers at $M_* > 2 \times 10^{11} M_\odot$". In: *Monthly Notices of the Royal Astronomical Society* 412.1 (Mar. 2011), pp. 684–704. DOI: 10.1111/j.1365-2966.2010.17984.x. arXiv: 1005.3770 [astro-ph.CO].

[139] Meng Gu et al. "The MASSIVE Survey. XVI. The Stellar Initial Mass Function in the Center of MASSIVE Early-type Galaxies". In: *The Astrophysical Journal* 932.2, 103 (June 2022), p. 103. DOI: 10.3847/1538-4357/ac69ea. arXiv: 2110.11985 [astro-ph.GA].

[140] J. Schombert and A. K. Smith. "The Structure of Galaxies I: Surface Photometry Techniques". In: *Publications of the Astronomical Society of Australia* 29.2 (Apr. 2012), pp. 174–192. DOI: 10.1071/AS11059. arXiv: 1203.2578 [astro-ph.IM].

[141] John P. Huchra et al. "The 2MASS Redshift Survey—Description and Data Release". In: *The Astrophysical Journal, Supplement* 199.2, 26 (Apr. 2012), p. 26. DOI: 10.1088/0067-0049/199/2/26. arXiv: 1108.0669 [astro-ph.CO].

[142] Pascal Puget et al. "WIRCam: the infrared wide-field camera for the Canada-France-Hawaii Telescope". In: *Ground-based Instrumentation for Astronomy*. Ed. by Alan F. M. Moorwood and Masanori Iye. Vol. 5492. Society of Photo-Optical Instrumentation Engineers (SPIE) Conference Series. Sept. 2004, pp. 978–987. DOI: 10.1117/12.551097.

[143] Stephen D J Gwyn. "WIRwolf : A Pipeline for Calibrating and Stacking CFHT WIRCam Data". In: 485 (2014), pp. 387–390.

[144] Emmanuel Bertin et al. "The TERAPIX Pipeline". In: *Astronomical Data Analysis Software and Systems XI*. Ed. by David A. Bohlender, Daniel Durand, and Thomas H. Handley. Vol. 281. Astronomical Society of the Pacific Conference Series. Jan. 2002, p. 228.

[145] E. Bertin and S. Arnouts. "SExtractor: Software for source extraction." In: *Astronomy and Astrophysics, Supplement* 117 (June 1996), pp. 393–404. DOI: 10.1051/aas:1996164.

[146] J. Schombert. "ARCHANGEL Galaxy Photometry System". In: (2007). arXiv: 0703646 [astro-ph]. URL: http://arxiv.org/abs/astro-ph/0703646.

[147] Emmanuel Ríos-López et al. "2D surface brightness modelling of large 2MASS galaxies - I: photometry and structural parameters". In: *Monthly Notices of the Royal Astronomical Society* 507.4 (Nov. 2021), pp. 5952–5973. DOI: 10.1093/mnras/stab2321. arXiv: 2108.04461 [astro-ph.GA].

[148] Ronald Läsker, Laura Ferrarese, and Glenn Van De Ven. "Supermassive black holes and their host galaxies. I. Bulge luminosities from dedicated near-infrared data". In: *Astrophysical Journal* 780.1 (2014). ISSN: 15384357. DOI: 10.1088/0004-637X/780/1/69. arXiv: 1311.1530.

[149] Brandon C. Kelly. "Some Aspects of Measurement Error in Linear Regression of Astronomical Data". In: *The Astrophysical Journal* 665.2 (Aug. 2007), pp. 1489–1506. DOI: 10.1086/519947. arXiv: 0705.2774 [astro-ph].

[150] Hiroaki Aihara et al. "The Eighth Data Release of the Sloan Digital Sky Survey: First Data from SDSS-III". In: *The Astrophysical Journal, Supplement* 193.2, 29 (Apr. 2011), p. 29. DOI: 10.1088/0067-0049/193/2/29. arXiv: 1101.1559 [astro-ph.IM].

[151] Michele Cappellari et al. "The ATLAS3Dproject - I. A volume-limited sample of 260 nearby early-type galaxies: Science goals and selection criteria". In: *Monthly Notices of the Royal Astronomical Society* 413.2 (2011), pp. 813–836. ISSN: 00358711. DOI: 10.1111/j.1365-2966.2010.18174.x. arXiv: 1012.1551.

[152] Gerard de Vaucouleurs et al. *Third Reference Catalogue of Bright Galaxies*. 1991.

[153] Michele Cappellari et al. "The ATLAS3D project-XX. Mass-size and mass-σ distributions of early-type galaxies: Bulge fraction drives kinematics, mass-to-light ratio, molecular gas fraction and stellar initial mass function". In: *Monthly Notices of the Royal Astronomical Society* 432.3 (2013), pp. 1862–1893. ISSN: 00358711. DOI: 10.1093/mnras/stt644. arXiv: 1208.3523.

[154] R. Bender et al. "Isophote shapes of elliptical galaxies. II. Correlations with global optical, radio and X-ray properties." In: *Astronomy and Astrophysics* 217 (June 1989), pp. 35–43.

[155] R. Bender. "Sub-Components in Elliptical Galaxies and Their Formation". In: *Morphological and Physical Classification of Galaxies*. Ed. by G. Longo, M. Capaccioli, and G. Busarello. Vol. 178. Astrophysics and Space Science Library. Jan. 1992, p. 357. DOI: 10.1007/978-94-011-2522-2_28.

[156] John Kormendy and Ralf Bender. "A Proposed Revision of the Hubble Sequence for Elliptical Galaxies". In: *The Astrophysical Journal, Letters* 464 (June 1996), p. L119. DOI: 10.1086/310095.

[157] Jenny E. Greene et al. "The MASSIVE Survey. II. Stellar Population Trends Out to Large Radius in Massive Early-type Galaxies". In: *The Astrophysical Journal* 807.1, 11 (July 2015), p. 11. DOI: 10.1088/0004-637X/807/1/11. arXiv: 1504.02483 [astro-ph.GA].

[158] John Magorrian et al. "The Demography of Massive Dark Objects in Galaxy Centers". In: *The Astronomical Journal* 115.6 (June 1998), pp. 2285–2305. DOI: 10.1086/300353. arXiv: astro-ph/9708072 [astro-ph].

[159] Mariangela Bernardi et al. "Early-Type Galaxies in the Sloan Digital Sky Survey. III. The Fundamental Plane". In: *The Astronomical Journal* 125.4 (2003), pp. 1866–1881. ISSN: 00046256. DOI: 10.1086/367794. arXiv: 0301626 [astro-ph]. URL: http://stacks.iop.org/1538-3881/125/i=4/a=1866.

[160] Mariangela Bernardi et al. "The Luminosities, Sizes, and Velocity Dispersions of Brightest Cluster Galaxies: Implications for Formation History". In: *The Astronomical Journal* 133.4 (Apr. 2007), pp. 1741–1755. DOI: 10.1086/511783. arXiv: astro-ph/0607117 [astro-ph].

[161] M. Bernardi et al. "Systematic effects on the size-luminosity relations of early- and late-type galaxies: dependence on model fitting and morphology". In: *Monthly Notices of the Royal Astronomical Society* 443.1 (Sept. 2014), pp. 874–897. DOI: 10.1093/mnras/stu1106.

[162] Alister W. Graham and C. Clare Worley. "Inclination- and dust-corrected galaxy parameters: bulge-to-disc ratios and size-luminosity relations". In: *Monthly Notices of the Royal Astronomical Society* 388.4 (Aug. 2008), pp. 1708–1728. DOI: 10.1111/j.1365-2966.2008.13506.x. arXiv: 0805.3565 [astro-ph].

[163] Duncan A. Forbes et al. "Uniting old stellar systems: from globular clusters to giant ellipticals". In: *Monthly Notices of the Royal Astronomical Society* 389.4 (Oct. 2008), pp. 1924–1936. DOI: 10.1111/j.1365-2966.2008.13739.x. arXiv: 0806.1090 [astro-ph].

[164] Michael a. Pahre, Reinaldo R. de Carvalho, and S. G. Djorgovski. "Near-Infrared Imaging of Early-Type Galaxies. IV. The Physical Origins of the Fundamental Plane Scaling Relations". In: *The Astronomical Journal* 116.4 (1998), pp. 1606–1625. ISSN: 00046256. DOI: 10.1086/300545. arXiv: 9806326 [astro-ph].

[165] F. La Barbera et al. "SPIDER - II. The Fundamental Plane of early-type galaxies in grizYJHK". In: *Monthly Notices of the Royal Astronomical Society* 408.3 (Nov. 2010), pp. 1335–1360. DOI: 10.1111/j.1365-2966.2010.17091.x. arXiv: 0912.4558 [astro-ph.CO].

[166] Mariangela Bernardi. "The σ-L Correlation in Nearby Early-Type Galaxies". In: *The Astronomical Journal* 133.5 (May 2007), pp. 1954–1961. DOI: 10.1086/512611. arXiv: astro-ph/0609301 [astro-ph].

[167] William R. Oegerle and John G. Hoessel. "Fundamental Parameters of Brightest Cluster Galaxies". In: *The Astrophysical Journal* 375 (July 1991), p. 15. DOI: 10.1086/170165.

[168] Anja Von Der Linden et al. "How special are brightest group and cluster galaxies?" In: *Monthly Notices of the Royal Astronomical Society* 379.3 (Aug. 2007), pp. 867–893. DOI: 10.1111/j.1365-2966.2007.11940.x. arXiv: astro-ph/0611196 [astro-ph].

[169] R. M. Samir, A. Takey, and A. A. Shaker. "The fundamental plane of brightest cluster galaxies and isolated elliptical galaxies". In: *Astrophysics and Space Science* 365.8, 142 (Aug. 2020), p. 142. DOI: 10.1007/s10509-020-03857-8.

[170] Michael Boylan-Kolchin, Chung Pei Ma, and Eliot Quataert. "Red mergers and the assembly of massive elliptical galaxies: The fundamental plane and its projections". In: *Monthly Notices of the Royal Astronomical Society* 369.3 (2006), pp. 1081–1089. ISSN: 00358711. DOI: 10.1111/j.1365-2966.2006.10379.x. arXiv: 0601400 [astro-ph].

[171] Dan Batcheldor et al. "How Special Are Brightest Cluster Galaxies? The Impact of Near-Infrared Luminosities on Scaling Relations for BCGs". In: *The Astrophysical Journal, Letters* 663.2 (July 2007), pp. L85–L88. DOI: 10.1086/520338. arXiv: astro-ph/0610264 [astro-ph].

[172] Tod R. Lauer et al. "Brightest Cluster Galaxies at the Present Epoch". In: *The Astrophysical Journal* 797.2, 82 (Dec. 2014), p. 82. DOI: 10.1088/0004-637X/797/2/82. arXiv: 1407.2260 [astro-ph.GA].

[173] R. M. Samir, A. Takey, and A. A. Shaker. "The fundamental plane of brightest cluster galaxies and isolated elliptical galaxies". In: *Astrophysics and Space Science* 365.8, 142 (Aug. 2020), p. 142. DOI: 10.1007/s10509-020-03857-8.

[174] Aidan C. Crook et al. "Groups of Galaxies in the Two Micron All Sky Redshift Survey". In: *The Astrophysical Journal* 655.2 (Feb. 2007), pp. 790–813. DOI: 10.1086/510201. arXiv: astro-ph/0610732 [astro-ph].

[175] Ralf Bender, David Burstein, and S. M. Faber. "Dynamically Hot Galaxies. I. Structural Properties". In: *The Astrophysical Journal* 399 (Nov. 1992), p. 462. DOI: 10.1086/171940.

[176] S. M. Faber et al. "The Centers of Early-Type Galaxies with HST. IV. Central Parameter Relations." In: *The Astronomical Journal* 114 (Nov. 1997), p. 1771. DOI: 10.1086/118606. arXiv: astro-ph/9610055 [astro-ph].

[177] Thorsten Naab, Sadegh Khochfar, and Andreas Burkert. "Properties of Early-Type, Dry Galaxy Mergers and the Origin of Massive Elliptical Galaxies". In: *The Astrophysical Journal, Letters* 636.2 (Jan. 2006), pp. L81–L84. DOI: 10.1086/500205. arXiv: astro-ph/0509667 [astro-ph].

[178] John Dubinski. "The Origin of the Brightest Cluster Galaxies". In: *The Astrophysical Journal* 502.1 (July 1998), pp. 141–149. DOI: 10.1086/305901. arXiv: astro-ph/9709102 [astro-ph].

[179] Davor Krajnović et al. "The ATLAS^{3D} Project - XXIII. Angular momentum and nuclear surface brightness profiles". In: *Monthly Notices of the Royal Astronomical Society* 433.4 (Aug. 2013), pp. 2812–2839. DOI: 10.1093/mnras/stt905. arXiv: 1305.4973 [astro-ph.CO].

[180] Michele Cappellari. "Effect of environment on galaxies' mass-size distribution: Unveiling the transition from outside-in to inside-out evolution". In: *Astrophysical Journal Letters* 778.1 (2013). ISSN: 20418205. DOI: 10.1088/2041-8205/778/1/L2. arXiv: 1309.1136.

[181] Laura Ferrarese and David Merritt. "A Fundamental Relation between Supermassive Black Holes and Their Host Galaxies". In: *The Astrophysical Journal, Letters* 539.1 (Aug. 2000), pp. L9–L12. DOI: 10.1086/312838. arXiv: astro-ph/0006053 [astro-ph].

[182] Karl Gebhardt et al. "A Relationship between Nuclear Black Hole Mass and Galaxy Velocity Dispersion". In: *The Astrophysical Journal, Letters* 539.1 (Aug. 2000), pp. L13–L16. DOI: 10.1086/312840. arXiv: astro-ph/0006289 [astro-ph].

[183] Jens Thomas et al. "A 17-billion-solar-mass black hole in a group galaxy with a diffuse core". In: *Nature* 532.7599 (Apr. 2016), pp. 340–342. DOI: 10.1038/nature17197. arXiv: 1604.01400 [astro-ph.GA].

[184] Nandini Sahu, Alister W. Graham, and Benjamin L. Davis. "Revealing Hidden Substructures in the M $_{BH}$-σ Diagram, and Refining the Bend in the L-σ Relation". In: *The Astrophysical Journal* 887.1, 10 (Dec. 2019), p. 10. DOI: 10.3847/1538-4357/ab50b7. arXiv: 1908.06838 [astro-ph.GA].

[185] Kianusch Mehrgan et al. "A 40 Billion Solar-mass Black Hole in the Extreme Core of Holm 15A, the Central Galaxy of Abell 85". In: *The Astrophysical Journal* 887.2, 195 (Dec. 2019), p. 195. DOI: 10.3847/1538-4357/ab5856. arXiv: 1907.10608 [astro-ph.GA].

[186] Jason L. Sanders and James Binney. "A fast algorithm for estimating actions in triaxial potentials". In: *Monthly Notices of the Royal Astronomical Society* 447.3 (Mar. 2015), pp. 2479–2496. DOI: 10.1093/mnras/stu2598. arXiv: 1412.2093 [astro-ph.GA].

[187] Nicolas Cretton and Eric Emsellem. "On the reliability of the black hole mass and mass-to-light ratio determinations with Schwarzschild models". In: *Monthly Notices of the Royal Astronomical Society* 347.2 (Jan. 2004), pp. L31–L35. DOI: 10.1111/j.1365-2966.2004.07374.x. arXiv: astro-ph/0312307 [astro-ph].

[188] John Magorrian. "Constraining black hole masses from stellar kinematics by summing over all possible distribution functions". In: *Monthly Notices of the Royal Astronomical Society* 373.1 (Nov. 2006), pp. 425–434. DOI: 10.1111/j.1365-2966.2006.11054.x. arXiv: astro-ph/0609238 [astro-ph].

Appendix A

Criterion for Existence of Long-axis Tubes (Appendix for Chapter 2)

We use Stäckel potentials to gain insights into the existence of long-axis tubes. A potential is said to be in Stäckel form if it can be written as:

$$V(\lambda,\mu,\nu) = -\frac{F(\lambda)}{(\lambda-\mu)(\lambda-\nu)} - \frac{F(\mu)}{(\mu-\nu)(\mu-\lambda)} - \frac{F(\nu)}{(\nu-\lambda)(\nu-\mu)}, \tag{A.1}$$

for some function $F(\tau)$ where (λ,μ,ν) are ellipsoidal coordinates defined as the roots of τ in the equation

$$\frac{x^2}{\tau+\alpha} + \frac{y^2}{\tau+\beta} + \frac{z^2}{\tau+\gamma} = 1\,, \tag{A.2}$$

such that $-\gamma \leq \nu \leq -\beta \leq \mu \leq -\alpha \leq \lambda$. Here, (α,β,γ) are constants that define the coordinate system. Such a potential is said to be separable in these coordinates. When a density corresponding to a Stäckel potential is projected in any direction to give a 2D surface density, it will have no isophotal twists [115]. Thus, we can use the viewing angles (θ,ϕ,ψ) of Binney [21] to define the relationship between the primary axes of the projected and intrinsic densities. This set of viewing angles imposes a constraint on the allowed values of (α,β,γ) given by:

$$\frac{\sqrt{\beta-\alpha}}{\sqrt{\gamma-\beta}} = \sqrt{\frac{\sin^2\theta}{\cot 2\psi \sin 2\phi \cos\theta + \cos^2\phi(\cos^2\theta+1)-1}}. \tag{A.3}$$

This expression follows from Equation (B9) of Franx [115]. Orbital structure in Stäckel potentials has been well studied [22]. This structure is what motivated the x-z start space described in Schwarzschild [23]. Long axis tube orbits pass through the x-z start-space above the focal curve, defined by

$$\frac{z^2}{\gamma-\beta} + \frac{x^2}{\alpha-\beta} = 1\,. \tag{A.4}$$

For large x, this curve is approximately a line given by $z \approx x\frac{\sqrt{\gamma-\beta}}{\sqrt{\beta-\alpha}}$. Therefore, the angle that this line forms with the z axis can be written simply in terms of the viewing angles as

$$\tan\eta = \sqrt{\frac{\sin^2\theta}{\cot 2\psi \sin 2\phi \cos\theta + \cos^2\phi(\cos^2\theta+1) - 1}}\,. \tag{A.5}$$

Any orbits launched initially between the focal curve and the positive z-axis in the x-z plane will be long axis tubes which violate axisymmetry. To effectively achieve axisymmetry, the angle η must be small enough for no orbits to be sampled above the focal curve. Since the line defined by the angle η is a lower bound to this curve, if all initial orbits in the positive x-z quadrant are launched outside of the approximate angular region between the z-axis and the angle η, there will be no long-axis tubes in the model.

This expression is derived for Stäckel potentials. However, in the absence of isophotal twists, we expect it to apply reasonably well to more realistic models as they can often be locally approximated by a Stäckel potential [186]. A central SMBH is inconsistent with a Stäckel potential and can thus destroy the ordered orbital structure. However, we suggest that Equation (A.5) could give a rough rule-of-thumb for where the boundary between long-axis and short-axis tubes will exist in models from the code, particularly at radii far from the SMBH.

The stellar mass distribution is represented by an MGE in our models. Each gaussian component is stratified on similar ellipsoids, and can thus be related to its deprojection via the equations given in Binney [21]. These equations can be rearranged to give

$$\frac{T}{1-T} = \frac{\sin^2\theta}{\cot 2\psi \sin 2\phi \cos\theta + \cos^2\phi(\cos^2\theta+1) - 1}, \tag{A.6}$$

where $T = (1-p^2)/(1-q^2)$ of each MGE component. For an MGE with no isophotal twists, each MGE component has the same triaxiality parameter, T. Thus, in this case, the angle, η, can be written simply as:

$$\eta = \tan^{-1}\sqrt{\frac{T}{1-T}}\,, \tag{A.7}$$

where T is the triaxiality parameter for each MGE component. Two examples of triaxial start spaces for NGC 1453 models are shown in Figure A.1. The boundary between long-axis tubes and short-axis tubes is well approximated by the angle η for a wide range of galaxy shapes.

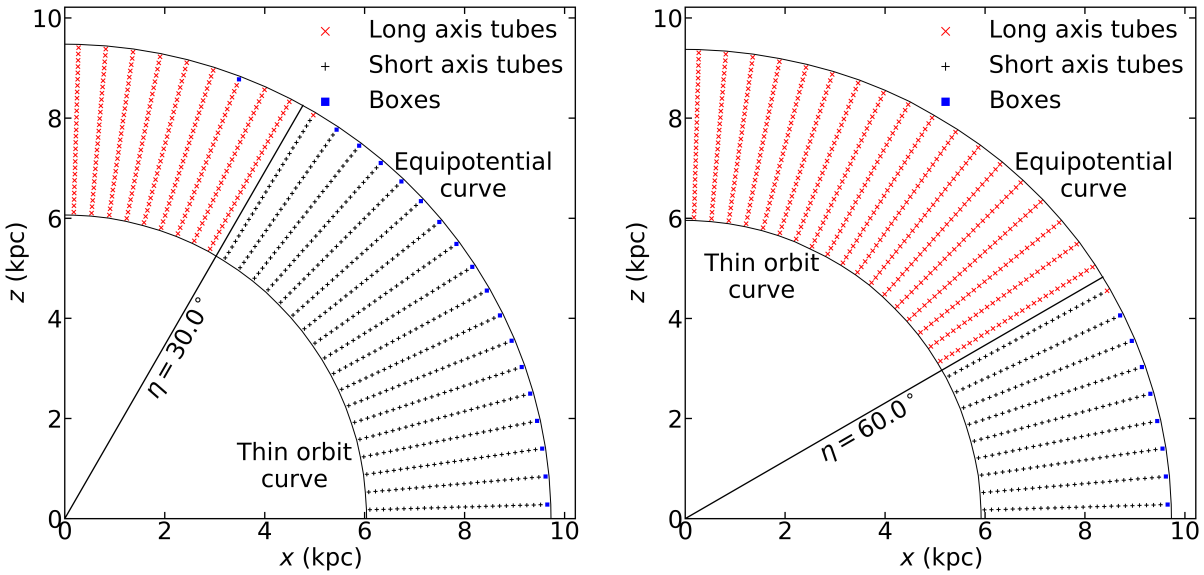

Figure A.1: Same as Figure 2.1 but for two additional mass models with larger triaxiality: (left) triaxiality parameter $T = 0.25$, (luminosity averaged) shape parameters $(u, p, q) = (0.96, 0.95, 0.77)$, and viewing angles $(\theta, \phi, \psi) = (67.62°, -28.38°, 86.61°)$, and (right) $T = 0.75$, $(u, p, q) = (0.96, 0.85, 0.79)$, and $(\theta, \phi, \psi) = (48.74°, -51.33°, 67.15°)$. The diagonal black line in each panel represents the angle η given in Equation (2.2). As in Figure 2.1, this angle approximates well the boundary separating long-axis (red symbols) and short-axis (black symbols) tube orbits in the x-z start space.

Appendix B

Thin Orbit Finding (Appendix for Chapter 2)

The TriOS code uses the thin orbit curve to construct its start space. This curve has to be found numerically in the x-z plane. For a given angle in this plane, the thin orbit radius is found by integrating test orbits starting at different radii. For each orbit, the radius of the orbit is recorded each time it passes through the x-z plane. The thin orbit radius is found by minimizing the difference between the maximum and minimum of these radii.

This algorithm should work for triaxial models but needs some revision in the axisymmetric case, particularly when there is no central density cusp or mass concentration. In this case, when close enough to the center, the potential should be well approximated by a harmonic oscillator. When the potential is axisymmetric, the motion can be regarded as two separate contributions: an oscillation in the z-axis and a closed elliptical orbit about the z-axis. Since the x-y motion constitutes a closed ellipse centered on the z axis, all orbits will pass through the x-z plane at a fixed x value, with some z value. The orbit width is then simply set by the maximum and minimum z values. Thus, for a given ray in the x-z plane, the orbital width in this plane can be minimized by simply taking the initial radius to be as small as possible. To solve this issue when running an axisymmetric model, we instead record radii when passing through the x-y plane. Closed ellipses will have a finite width in this plane while all thin orbits should pass through this plane in a circle of 0 width.

It is unclear how much this issue should affect the resulting orbit libraries. If orbits are sampled starting at the origin instead of the thin orbit, the result should be a less uniform sampling of angular momentum. There should also be some range of energies where the thin orbit radius is not estimated to be 0 or the correct value, but rather somewhere in between. This would result in a significantly non-uniform sampling of angular momentum since orbits passing through the x-z plane within this radius will be undersampled relative those that do not. This issue should be essentially resolved outside of the axisymmetric limit, or if a black hole or density cusp is included. However, axisymmetric studies that use this code with no central cusp may be affected [91].

Appendix C

Michie-like Mock Recovery Tests (Appendix for Chapter 2)

In 2, we demonstrated that our changes to the TriOS code result in a consistent, non-zero SMBH mass estimate for our NGC 1453 dataset. Here, we show that the changes correctly recover the SMBH mass in a mock dataset with known parameter values. Mock tests have been performed within various other Schwarzschild codes [e.g. 25, 187, 188, 56, 85].

For our mock galaxy, we use a flattened version of the spherical potential introduced in Siopis et al. [56]. These models have an axisymmetric gravitational potential given by

$$\Phi(R,z) = \frac{1}{2}V_c^2 \ln\left(\frac{R^2 + z^2/q_\Phi^2}{1\ \mathrm{pc}^2}\right) - \frac{GM_{\mathrm{BH}}}{\sqrt{R^2+z^2}}, \tag{C.1}$$

where q_Φ is the flattening of the potential due to the extended mass distribution. The stellar DF is chosen to have a Michie-like form:

$$f = A \exp\left\{-\left[\frac{E + L_z^2/(2r_a^2)}{\sigma^2}\right]\right\} L_z^{2N} \sqcap (E_1, E, E_2), \tag{C.2}$$

where A is the normalization, and r_a, N, σ, E_1, and E_2 are parameters of the model: r_a is an anisotropy distance, N controls the L_z dependence, σ is a characteristic velocity dispersion, and E_1 and E_2 are energy cutoffs. The symbol $\sqcap$ denotes a step function defined by

$$\sqcap(E_1, E, E_2) = \begin{cases} 1, & \text{if } E_1 \le E \le E_2 \\ 0, & \text{otherwise.} \end{cases} \tag{C.3}$$

Because L_z only enters Eq. (C.2) in even powers, there is additional freedom in how f differs for positive and negative values of L_z. Here, we set a fixed fraction of stars to rotate in each positive direction. In this model, the stars are essentially regarded as massless tracers of the underlying potential in eq. C.2. Even when the potential is chosen to be spherical, the stellar distribution function can be axisymmetric.

We use the same potential parameters as Siopis et al. [56], with $V_c = 220$ km s^{-1} and $M_{\rm BH} = 1.126 \times 10^8\ M_\odot$. We generated two models: one model with a spherical potential ($q_\Phi = 1$) to compare with Siopis et al. [56], and one model with a flattened potential ($q_\Phi = 0.95$). The models both have a sphere of influence of about 10 pc. We also use the same two component DF parameters as Siopis et al. [56]: the first component is a non-rotating nearly spherical bulge-like component which has $\sigma = 160$ km s^{-1}, $r_a = 600$ pc, $N = 0$, $E_1 = \Phi(10\,\mathrm{pc})$, $E_2 = \Phi(1000\,\mathrm{pc})$ with equal numbers of stars having positive and negative L_z; the second component is a rotating disk-like component w has $\sigma = 120$ km s^{-1}, $r_a = 200$ pc, $N = 2$, $E_1 = \Phi(10$ pc), $E_2 = \Phi(1000$ pc) with 3/4 of the stars having positive L_z and 1/4 having negative L_z. The two components have equal numbers of stars.

We draw points in phase space from this distribution function for each star to generate mock data. We use a nearly edge-on projection, with an inclination of $\theta = 89°$. For the model with the flattened potential, we convolve the projected positions with a circular gaussian PSF with standard deviation 5 pc. We bin the stars into mock IFU data with a resolution of 10 pc, with a square FOV of 1000 pc. We fit an MGE to the projected surface brightness. We then run Voronoi binning on all bins with central radii > 20 pc, resulting in 12 inner unbinned kinematic points and 108 larger outer bins. In order to keep the bins between the two models fixed, we use the Voronoi bins derived from the spherical potential. Each LOSVD is fit with a Gauss-Hermite expansion up to h_{12}. Gaussian noise is added to each LOSVD bin, resulting in a scatter of about 0.03 in each moment and about $0.03\sqrt{2}\sigma$ in the average velocity and velocity dispersion for each bin. We draw 20 realizations of this noise, and run the updated TriOS code for each realization.

Figure C.1 shows the resulting constraint on $M_{\rm BH}$ for each noise realization. The left panel is for the mock in the spherical potential, while the right panel is for the mock in the flattened potential. The kinematic contribution to the reduced χ^2 in these realizations ranges from 0.81 to 0.94 for the spherical potential and 0.71 to 0.84 for the flattened potential, indicating a good fit to the projected kinematics for all realizations.

The average SMBH masses and corresponding sample standard deviations from these combined 20 runs are $M_{\rm BH} = (1.17 \pm 0.09) \times 10^8\ M_\odot$ for the spherical potential, and $M_{\rm BH} = (1.18 \pm 0.13) \times 10^8\ M_\odot$ for the flattened potential. In both test cases, the estimated $M_{\rm BH}$ values are in excellent agreement with the true value of $M_{\rm BH} = 1.126 \times 10^8 M_\odot$.

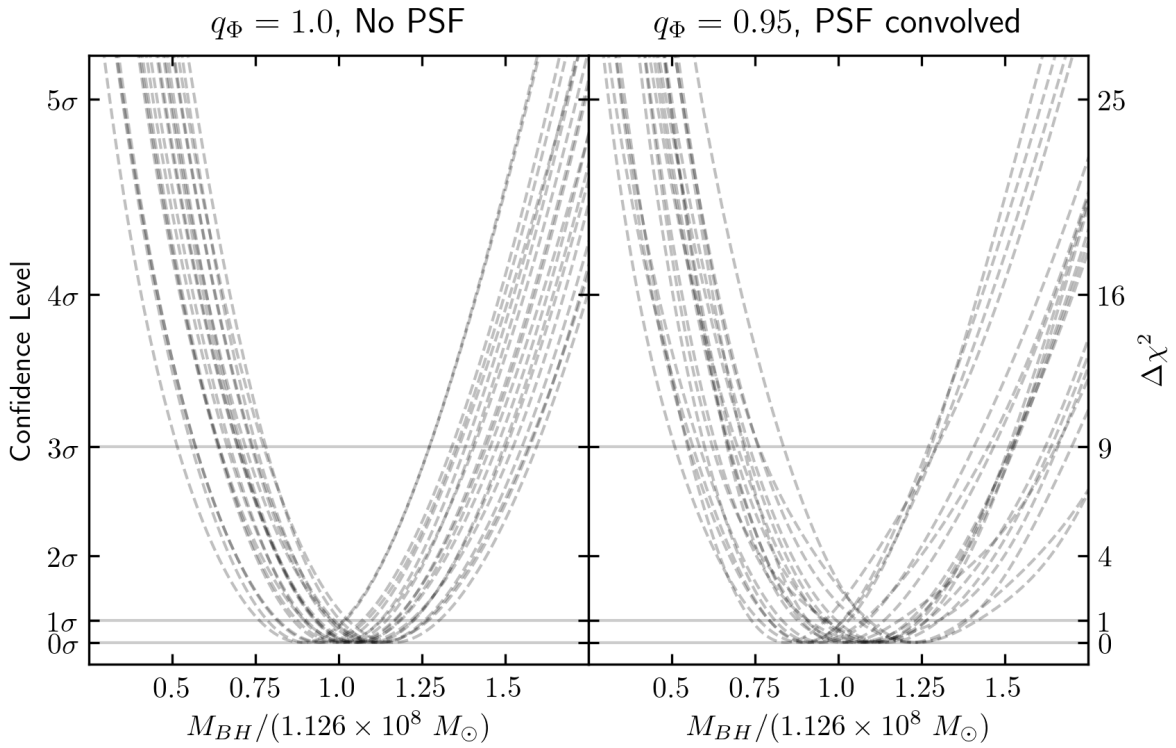

Figure C.1: Illustration of the $M_{\rm BH}$ constraints for the mock datasets described in the text. Each dashed curve represents a separate realization of the noise.

In the left panel, the potential is spherical, no PSF convolution is performed and each DF component has 5×10^8 stars. In the right panel, the model is flattened, projected stellar positions are convolved with a circular gaussian PSF with a standard deviation of 5 pc, and each DF component has 5×10^9 stars. The 1D χ^2 curves are obtained by marginalizing over V_c in the smoothed 2D χ^2 landscape generated by Gaussian Process regression with a squared-exponential covariance function [97].

Appendix D

Relating new and old parameters (Appendix for Chapter 3)

The expressions given in Equation (3.8) can be written in a simpler form when expressed sequentially:

$$\begin{aligned} \cos^2\theta &= T_{\rm min}(1 - TT_{\rm maj})\,, \\ \sin^2\phi &= \frac{(1-T_{\rm maj})(1-T_{\rm min})}{\sin^2\theta}\,, \\ \tan\psi &= \frac{-(1-T_{\rm min})\cos\theta}{(T_{\rm min}-\cos^2\theta)\tan\phi}\,. \end{aligned} \tag{D.1}$$

The inverse expressions are then

$$\begin{aligned} T &= \frac{\sin^2\theta}{\cos\theta\sin 2\phi\cot 2\psi + \cos^2\phi - \cos^2\theta\sin^2\phi}\,, \\ T_{\rm maj} &= 1 - \sin^2\phi(1 - \cos\theta\cot\phi\cot\psi)\,, \\ T_{\rm min} &= 1 - \sin^2\theta(1 - \cos\theta\cot\phi\cot\psi)^{-1}\,. \end{aligned} \tag{D.2}$$

The deprojection equations, giving the intrinsic shape in terms of the projected flattening and angles (θ, ϕ, ψ) are given by [113]:

$$\begin{aligned} 1 - q^2 &= \frac{\delta'[2\cos 2\psi + \sin 2\psi(\sec\theta\cot\phi - \cos\theta\tan\phi)]}{2\sin^2\theta[\delta'\cos\psi(\cos\psi + \cot\phi\sec\theta\sin\psi) - 1]} \\ p^2 - q^2 &= \frac{\delta'[2\cos 2\psi + \sin 2\psi(\cos\theta\cot\phi - \sec\theta\tan\phi)]}{2\sin^2\theta[\delta'\cos\psi(\cos\psi + \cot\phi\sec\theta\sin\psi) - 1]} \\ u^2 &= \frac{1}{q'}\sqrt{p^2\cos^2\theta + q^2\sin^2\theta(p^2\cos^2\phi + \sin^2\phi)}, \end{aligned} \tag{D.3}$$

where $\delta' = 1 - q'^2$. While [113] presents these expressions in the context of the MGE formalism, they are more broadly applicable to all densities that are stratified on similar

concentric ellipsoids. This is demonstrated in de Zeeuw and Franx [112]. The first two expressions in equation D.3 are listed as their equation A8. The third expression giving the projection axis ratio, u, follows from expressions in this paper as well. Following appendix A of this paper, combining their equations 3.37, 3.38, and 3.49 gives:

$$\begin{aligned} a'^2 + b'^2 &= 2c^2 + (a^2 - c^2)(\sin^2\phi + \cos^2\phi\cos^2\theta) + (b^2 - c^2)(\cos^2\phi + \sin^2\phi\cos^2\theta) \\ (a'^2 - b'^2)^2 &= [(a - c^2)(\sin^2\phi - \cos^2\phi\cos^2\theta) + (b^2 - c^2)(\cos^2\phi - \sin^2\phi\cos^2\theta)]^2 \\ &\quad + 4(a^2 - b^2)^2 \sin^2\phi\cos^2\phi\cos^2\theta. \end{aligned} \tag{D.4}$$

Here, (α, β, γ) in the original expressions have been set to $(-a^2, -b^2, -c^2)$ in order to consider a perfect ellipsoid. The first of these expressions is explicitly given in equation A6 of the original paper. Squaring the first expression and subtracting the second gives (after significant simplification):

$$4a'^2b'^2 = 4a^2b^2\cos^2\theta + 4a^2c^2\sin^2\phi\sin^2\theta + 4b^2c^2\cos^2\phi\sin^2\theta. \tag{D.5}$$

Substituting the definitions of the axis ratios reduces this expression to the third line of equation D.3 above.

Equation 3.8 follows from equations 3.39 and 3.42 of de Zeeuw and Franx [112], together with the definitions given in equation 3.4. Equation 3.7 then follows from equation D.3, together with equation 3.8. As in appendix A1 of de Zeeuw and Franx [112], while these expressions are derived in the context of a perfect ellipsoid, the results are independent of the assumed profile and are thus valid for all densities stratified on similar concentric ellipsoids.